Tommy Karlsson

Simulations of 2D dynamic brittle fracture by the Element-free Galerkin method and linear fracture mechanics

Doctoral thesis
for the degree of doktor ingeniør

Trondheim, July 2006

Norwegian University of
Science and Technology
Faculty of Engineering Science and Technology
Department of Structural Engineering

NTNU
Innovation and Creativity

NTNU
Norwegian University of Science and Technology

Doctoral thesis
for the degree of doktor ingeniør

Faculty of Engineering Science and Technology
Department of Structural Engineering

ISBN 82-471-8011-1 (printed ver.)
ISBN 82-471-8010-3 (electronic ver.)
ISSN 1503-8181

Doctoral Theses at NTNU, 2006:125

Printed by Tapir Uttrykk

Tommy Karlsson

Simulations of 2D dynamic brittle fracture by the Element-free Galerkin method and linear fracture mechanics

Dr.ing. thesis

Department of Structural Engineering
Norwegian University of Scenic and Technology
N-7491 Trondheim

September 2006

Laila, Rebecca, Pernilla og Sandra Karlsson

Takkes spesielt for å ha gjort det mulig
å gjennomføre arbeidet med avhandlingen.
Deres tålmodighet og toleranse i denne
prosessen er imponerende.

Takk jentene mine!

Abstract

The research presented in this thesis is addressing the Element Free Galerkin method and the dynamic linear fracture mechanics theory to investigate their capabilities of solving crack propagation problems.

The element-free Galerkin (EFG) method is a particle method, because it needs only a set of nodes and a description of a domain boundary to obtain an approximate solution. Every node in the model has a surrounding domain that describes its connectivity, called the domain of influence. In the Element Free Galerkin method the displacement approximation is described by shape functions derived from the Moving Least Square (MLS) technique, minimizing a weighted quadratic difference between the local displacement approximations and the nodal parameters. The discrete equations are established in the same manner as for the finite element method with respect to the displacement approximations. The special connectivity description of the Element Free Galerkin method enables rational modeling of for local discontinuities in numerical simulations.

A prototype code based on the Element Free Galerkin method and dynamic linear fracture mechanics where developed on a MATLAB platform. The code solves two dimensional general crack propagation problems. The material must behave linearly elastic. The code can handle relatively general geometries and it allows two arbitrary cracks to propagate within a prescribed sub-domain of the numerical model. The explicit Newmark algorithm is adopted for solving the discrete equations in the time domain. The developed code was verified by running two examples of general brittle crack growth: the pendulum experiment by John, R. and S. P. Shah (1990) on concrete beams and the experiment performed by Kalthoff and Winkler (1987). A comprehensive parameter study was performed on a modified pendulum experiment. This was done to understand how the model parameters are influencing the results of brittle crack growth.

Experiments in the structural laboratory are performed for validation. Since the EFG code is restricted to calculations of two dimensional numerical models the experiment must also have this limitation. A shear wall structure is thus chosen as model for the experiments. Crack patterns should arise from stress waves generated from shock wave loading. The load is applied to one of the shear wall edges as an impact from a projectile. The applied force is thus in the shear wall plane. The shear wall is supported at each side of the edge opposite to the loading. The experiments show that the numerical tools based on linear fracture mechanics and the Element Free Galerkin method are suited for solving dynamic brittle fracture.

The main conclusions from this thesis is that the numerical tools based on the Element Free Galerkin method and the dynamic linear fracture mechanics work properly for predicting general brittle crack propagation. The work presented in the thesis demonstrates one possible way of predicting the crack initiation and finial crack pattern for brittle fracture.

Acknowledgements

I would like to express my gratitude to my advisor Professor Svein Remseth for professional supervision and support during the study.

This work was made possible by a scholarship from the Norwegian University of Science and Technology and by financial support from Forsvarsbygg.

I am also very thankful for all support from friends and colleagues.

Table of content

List of figures

List of tables

Notation, symbols and abbreviations

Roman symbol:

a	crack area
a_i	discrete crack segment
a	coefficients which are functions of the spatial co-ordinates
A	integration domain enclosing the crack tip
A_I, A_{II}	universal function of crack tip speed for mode I and mode II deformation
∂A	complete contour of the integration domain A
b	vector of body forces per unit volume
$\mathbf{B}_I$	strain-displacement matrix
C_{ijkl}	components of the elastic stiffness tensor
C_0	outer contour of the integration domain A
C_+, C_-	straight crack faces in the integration domain A
C_R	Rayleigh surface wave speed
C_{xI}, C_{yI}	distances between the nodes in x and y direction respectively (only for regular mesh)
Cxg	matrix with the information of the Gauss points inside the xcrack region
d	side of the quadratic J-integral domain
d_{max}	scaling factor (e.g. $d_{mlx} = d_{max} \cdot C_{xI}$ and $d_{mly} = d_{max} \cdot C_{yI}$)
d_{mlx}, d_{mly}	the domain of influence range zone in x- and y- direction respectively
D(v)	the quantity $4\alpha_d\alpha_s - (1+\alpha_s^2)^2$, a function of crack tip speed
D	symmetric matrix of material stiffness for plane stress and plane strain
E	Young's modulus
F(Γ)	energy flux into Γ
F	load vector
$\mathbf{G}_s$	matrix with information of each Gauss integration cell
J	weighted quadratic form
K	stiffness matrix
K_I	mode I stress intensity factor
K_{Iaux}	mode I auxiliary stress intensity factor
K_{Ic}	value of stress intensity factor at crack initiation (fracture toughness)
K_{II}	mode II stress intensity factor
K_{IIaux}	mode II auxiliary stress intensity factor
K_{III}	mode III stress intensity factor
L	kinetic energy density
$\dot{L}$	time derivative of the kinetic energy density
Lc	a matrix describing the coordinates of the main points in a predefined crack path
Ln	defines the number of time increments between checking of the crack propagating criterion
m_i	component i of the normal vector to C_0
M	diagonal mass matrix (diagonalized by the row sum technique)
n_i	component i of the normal vector to Γ

N_I^{EFG}	shape function related to node I in the MLS approximation
$\mathbf{N}^{EFG}$	vector of EFG shape functions
N_I^{FE}	shape function related to node I in the finite element approximation
N_I^{enr}	shape function based on the enriched basis related to node I in the MLS approximation
N_I^{lin}	shape function based on the linear basis related to node I in the MLS approximation
N_I^{IF}	shape function related to node I in the interface approximation
N_I	shape function related to node I for all approximations
$\tilde{N}_I$	shape function related to node I in the transition and enriched EFG domain
N_{en}	number of element nodes
NN	NN=N for the EFG domain and the interface domain, and NN=N_{en} for the FE domain
$\mathbf{p}$	functional basis (e.g. linear basis: $\mathbf{p}^T=[1,x,y]$)
$\mathbf{P}$	square matrix of basis functions evaluated at nodes N
q	arbitrary smooth function that is equal to unity on Γ
r_x, r_y	normalized distances between the x and y co-ordinates of $\mathbf{x}$ and $\mathbf{x}_I$ respectively
R	ramp function (defined using the sum of the finite element shape functions on the EFG boundary)
$S_{x\rightarrow x_I}$	set of all points on the straight line from $\mathbf{x}$ to $\mathbf{x}_I$
t	time
$\bar{\mathbf{t}}$	tractions
Δt	discrete time increment
Δt_{crit}	the lowest discrete time increment to ensure stable solution
$\mathbf{x}$	spatial co-ordinates (x=[x y])
$\mathbf{x}_I$	coordinates of node I
xcrack	defines the model region where the crack can propagate arbitrarily
u	displacement function
$\mathbf{u}$	displacement vector
u^{enr}	displacement approximation based on an enriched basis
u^{lin}	displacement approximation based on a linear basis
u^h_{EFG}	displacement approximation based on the EFG method
u^h_{FE}	displacement approximation based on the FE method
u^h_{IF}	hybrid displacement approximation in the interface domain
u_I	nodal parameter associated with node I
$\dot{u}$	velocity function
$\dot{\mathbf{u}}$	velocity vector
$\ddot{u}$	acceleration function
$\ddot{\mathbf{u}}$	acceleration vector
v	crack velocity

v_c	anticipated crack velocity
w	weight function covering the circular domain of influence
W	stress work density
$\dot{W}$	time derivative of the stress work density
$\mathbf{W}$	diagonal matrix of weight functions evaluated at nodes N
w_x, w_y	weight function covering the rectangular domain of influence in x- and y-direction respectively

Greek symbol:

α_d, α_s	the quantities $\alpha_d = \sqrt{1-\frac{v^2}{c_d^2}}$, and $\alpha_s = \sqrt{1-\frac{v^2}{c_s^2}}$
β_1	general newmark integration variable
β_2	general newmark integration variable (β_2=0, explicit type)
δ_{ii}	Cronecker delta
$\mathcal{G}$	rate of change in the potential energy, $\prod$, with the crack area a (energy release rate)
ε	strain vector ($\varepsilon^T = \left[\varepsilon_{xx}\ \varepsilon_{yy}\ \varepsilon_{xy}\right]$)
Ω	domain of the whole numerical model
Ω_{EFG}	EFG sub-domain
Ω_{FE}	FE sub-domain
Ω_{IF}	interface sub-domain
Ω_I	nodes in Ω with $w(\mathbf{x}_I-\mathbf{x})>0$
Ω_I^{VIS}	points on a straight line between $\mathbf{x}$ and $\mathbf{x}_I$ without any intersection of Γ
Ω^{DI}	nodes that satisfy $\Omega_I^{DI} = \Omega_I^{VIS} \cap \Omega_I$
ν	Poisson's ratio
$\prod$	potential energy
ρ	mass density
σ	stress vector ($\sigma^T = \left[\sigma_{xx}\ \sigma_{yy}\ \sigma_{xy}\right] = \left[\sigma_{11}\ \sigma_{22}\ \sigma_{12}\right]$)
σ_c	critical stress for the material
σ_{ij}	stress component ij
$\sigma_{\theta\theta}$	circumferential stress
$\sigma_{\theta\theta max}$	maximum circumferential stress
$\sigma_{r\theta}$	shear stress
θ	the angle between the x_1-axis and the line from the crack tip to the evaluation point
θ_c	crack growth direction
Γ	crack tip contour

Γ_c	complete boundary of the total domain, including any interior surfaces (corresponding to cavities and crack edges in this study)
Γ_{EFG}	boundary between interface domain and EFG domain
Γ_{FE}	boundary between interface domain and FE domain
Γ_u	prescribed displacement boundary
Γ_t	prescribed traction boundary

Operators

$\delta(\bullet)$	indicate that $(\bullet)$ is a variation

Subscript:

i	co-ordinate x (i=1) and y (i=2)
I	node number
j	co-ordinate x (i=1) and y (i=2)
J	node number
n	discrete time instant
, (•)	derivative with respect to (•)

Superscript:

(1)	association to the auxiliary field of mode I
(2)	association to the auxiliary field of mode II
e	refer to a finite element
h	h indicate that $(\bullet)^h$ is an approximation of (•)
m	number of terms in the functional basis
N	total number of nodes with influence domain $w(\mathbf{x}-\mathbf{x}_I,t)\geq 0$ at the evaluation point $\mathbf{x}$

Abbreviations:

CT	crack tip
EFG	element-free Galerkin
FE	finite element
MLS	moving least square
SIF	stress intensity factor

Chapter 1 Introduction

1.1 Background for the thesis work

When this thesis work started, a need for assessment of the vulnerability and safety of underground rock caverns subjected to explosive loading was requested. Some results from full scale experiments were available. These results would be very useful for the assessment together with numerical modelling of the behaviour of the rock surrounding a cavern exposed to explosive loading. Numerical computations are necessary to trace the shock wave propagation from the location of the explosion through the rock mass and predict the response of the rock in the vicinity of the cavern.

It is of particular interest to predict the rock response close to the cavern when the shock waves pass and are reflected. In this area it must be possible to predict spalling and cracking and also the level and characteristics of vibration on the cavern surface.

Figure 1.1 illustrates a possible case for which numerical wave propagation and response analyses should give reliable estimates of the behaviour during an explosive loading. Three different domains are illustrated in the figure. Different numerical methods of analysis will be required to efficiently obtain response estimates with sufficient accuracy in the three domains. The explosion takes place in Domain 1. This domain is limited by an idealized spherical boundary outside which the rock has not been disintegrated, but can be modelled as a continuum. Domain 2 is surrounding the rock cavern. In this domain fracture and spalling may be expected for sufficiently high explosion load levels.

As Domain 3 is considered to be a continuum it can conveniently be modelled with the Finite Element method. The material behaviour may be elastic or elasto-plastic, but without dominant local discontinuities.

Numerical estimation of the response to the loading on the outer boundary of this domain will not be considered in this study. It must be available from separate numerical analyses.

For Domain 2 the rock masses will have local discontinuities with crack growth and possible spalling at the cavern surface. Available numerical methods to model this type of behaviour have been reviewed. The Element Free Galerkin (EFG) method seemed promising for estimation of crack growth in arbitrary directions according to the state of stress and material properties. Local discontinuities can conveniently be handled by the EFG method as its connectivity description is only associated with nodes in the numerical model. General discontinuities, such as crack faces, can easily be included without any remeshing during a numerical simulation. This represents a major distinction in properties between the Element Free Galerkin method and the Finite Element method.

A description of the EFG method can be found in Belytschko (1994).

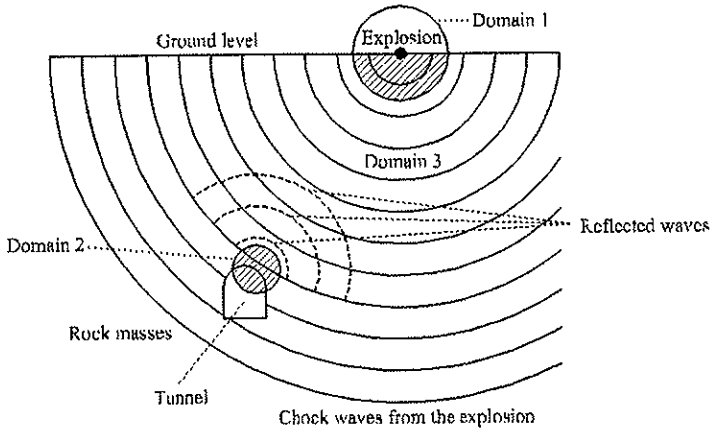

Figure 1.1: Illustration of a rock cavern subjected to explosion from ground level

1.2 Objectives and scope

The contribution from the present study towards the solution of the rock cavern problem will be concentrated on possible achievements of the Element Free Galerkin method. The problem as illustrated in Figure 1.1 will be addressed as a guide to required capabilities of the numerical method.

No commercial codes with the Element Free Galerkin method included were available. The performance and limitations of the method could thus only be studied by developing a prototype code. This code had to be verified and as far as possible validated through comparisons with experimental results for brittle material failure with crack propagation.

The rock cavern problem will require the code to handle coupling of the Finite Element method with the EFG method to be efficient for simulation of elastic wave propagation between the explosion area and the cavern area. The code has been developed on the MATLAB platform for solving two-dimensional problems. This will limit the code development work and still be satisfactory for modelling of the rock cavern problem when the distance between the explosion area and the cavern allow approximation of plane stress waves in the cavern area.

Dynamic and linearly elastic fracture mechanics is the tool for describing the crack propagation. It means that the material behaves linearly elastic up to the initiation of cracking. The traditional dynamic linear elastic fracture mechanics is well suited to combine with the connectivity description in the Element Free Galerkin method.

Even if this study was initiated in connection with the rock cavern problem, other dynamic brittle fracture problems that can be modelled in 2D can easily adopted also for different materials as concrete and metals.

1.3 Organization of the report

The report is organized in the following chapters:

Chapter 2 describes the basics of the Element Free Galerkin method. The governing equations for describing linear elasto-dynamic behaviour in two dimensions, is established both for the Element Free Galerkin method separately and coupled with the Finite Element method. A simple method for describing discontinuous behavior is outlined through the visibility criterion. To improve computations of the crack tip field variables, the enriched Element Free Galerkin basis is adopted.

In Chapter 3 the basis of the mixed mode dynamic fracture modelling is outlined. This is the basis for the numerical integration of the J-integral which gives the value of the stress intensity factors. These factors are the main control parameters for the crack criterion.

One major part of the work with this theses has been the development of the 2D prototype code for solving the dynamic linear elastic fracture problems. The basis and the features of the code are listed in Chapter 4.

Chapter 5 gives some examples for verification of the present code against results reported in the literature.

In Chapter 6 a setup for experiments is proposed on the basis of pre-calculations by the prototype code. The test specimens are concrete slabs mounted as shear walls and subjected to an impact loading. The impacting projectile causes a pressure pulse to propagate. This pulse will reflect, and if the reflected tension stress wave is strong enough, it can cause various crack patterns in the test specimen.

Chapter 7 gives the results from the experiments, and numerical recalculation with updated model parameters corresponding to the experiments.

Conclusions of the study and suggestions for further work are finally given in Chapter 8.

Chapter 2 The Element Free Galerkin method

2.1 Introduction

The element-free Galerkin (EFG) method is a particle method, because it needs only a set of nodes and a description of a domain boundary to obtain an approximate solution. Every node in the model has a surrounding domain that describes its connectivity, called the domain of influence. Inside this domain a function describing the weight of the influence from the actual node on a material point is defined. This is called the weight function. In the finite element (FE) method the displacement approximation is described by shape functions between nodal values. In the EFG method a similar description with shape functions is adopted. The EFG shape functions are derived from the Moving Least Square (MLS) technique, minimizing a weighted quadratic difference between the local displacement approximations and the nodal parameters. The set of nodal parameters are in general not equal to the nodal displacements. The EFG displacement approximation is treated in the same manner as the FE displacement approximation by inserting the displacement approximations into the weak form of the problem to generate discrete equations that calculate the model behaviour. To obtain the discrete equations a numerical integration is performed in the same manner as for the FE method.

A main advantage with the EFG method is its general capability of describing moving discontinuities as for instance crack growth. This feature lies in the easiness to update the domain of influence for the nodes during an analysis. A drawback is an increased requirement of computer time. Computational efficiency may be improved through models combining an EFG domain and a FE domain where modeling of discontinuities are not required.

In Section 2.1 the displacement approximation is established by the moving least square (MLS) technique, followed by Section 2.2 were the discrete equations for the computational model are derived. Further, in Section 2.3 coupling between the FE

method and the EFG method is defined. The discontinuity approximation method, the visibility criterion, follows in Section 2.4.

2.2 *Moving least square approximation*

In the EFG method the displacement function u(**x**,t) is approximated by

$$u^h(\mathbf{x},t) = \sum_{i=1}^{m} p_i(\mathbf{x}) a_i(\mathbf{x},t) = \mathbf{p}^T(\mathbf{x})\mathbf{a}(\mathbf{x},t), \tag{2.1}$$

where the superscript h indicates that $u^h(\mathbf{x},t)$ is an approximation of u(**x**,t). m is the number of terms in the functional basis $\mathbf{p}^T(\mathbf{x})$ and **a**(**x**,t) contains the coefficients which are functions of the spatial co-ordinates (**x**=[x y] in 2D) and the time t. Examples of bases in two dimensions are:

$$\mathbf{p}^T = [1, x, y], \qquad (m = 3, \text{ linear}), \tag{2.2}$$

$$\mathbf{p}^T = \left[1, x, y, \sqrt{r}\right], \qquad (m = 4, \text{ enriched}). \tag{2.3}$$

Equation (2.2) is a linear basis, while Eq. (2.3) is a radially enriched basis containing a term with the square root of the distance from the crack tip in addition to the linear terms (see Flemming, M. A (1997)). This last basis will be advantageous for solving problems with asymptotic crack tip fields. For multiple cracks, additional terms must be added for each crack. More details on the radially enriched basis are found in Section 2.7.

The coefficients **a**(**x**,t) are obtained at any point **x**, by using the moving least-square (MLS) technique (see Lancaster and Salkauskas (1981)). The approximate displacement function $u^h(\mathbf{x},t)$, are called the MLS interpolants. The MLS technique is minimizing the weighted quadratic difference between the local approximation and the

nodal parameters for every node with influence domain different from zero at **x**. The weighted quadratic form is given by

$$J = \sum_{I=1}^{N} w(\mathbf{x} - \mathbf{x}_I, t)\left[\mathbf{p}^T(\mathbf{x}_I)\mathbf{a}(\mathbf{x}, t) - u_I\right]^2 \tag{2.4}$$

where $w(\mathbf{x}-\mathbf{x}_I,t)$ is a weight function covering the domain of influence for node I, see Section 2.2.1. $\mathbf{x}_I$ are the coordinates of node I. u_I is a nodal parameter associated with node I, while N is the total number of nodes with influence domain $w(\mathbf{x}-\mathbf{x}_I,t)\geq 0$ at the evaluation point **x**, Flemming, M. (1997).

2.2.1 Weight function descriptions

For EFG the weight function, $w(\mathbf{x}-\mathbf{x}_I,t)$, is a monotonically decreasing function as $\|\mathbf{x}-\mathbf{x}_I\|$ increases. The weight function is nonzero over a small domain in the neighbourhood of node I, called the domain of influence for node I, and zero elsewhere, see Figure 2.1. The continuity requirements of the MLS interpolants are the same as for the weight functions. If $w(\mathbf{x}-\mathbf{x}_I)$ is C^1 continuous, then the shape function in the MLS interpolants will be C^1 continuous.

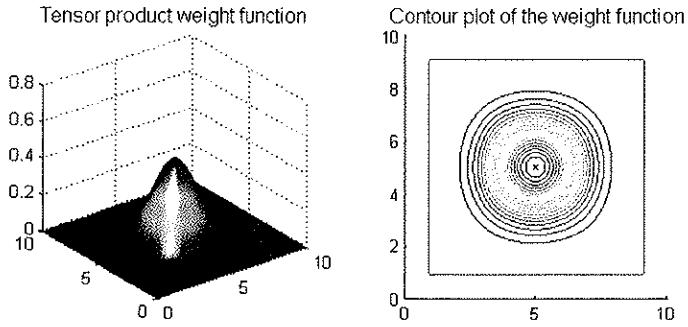

Figure 2.1: Illustration of the domain of influence for node I, were the weight function in the figure shows a tensor product weight with a cubic spline function. See Eq. (2.5).

The choice of the shape of the domain of influence may be arbitrary. Rectangular domains are chosen in the following. The weight function for the rectangular domain at any given point is called a tensor product weight, Dolbow and Belytschko 1998, and is given by

$$w(\mathbf{x}-\mathbf{x}_I,t) = w(r_x,t)\cdot w(r_y,t) = w_x \cdot w_y \tag{2.5}$$

The weight functions, as cubic splines in the normalized distance r from node I are:

$$w(r,t) = \begin{cases} \frac{2}{3} - 4r^2 + 4r^3 & \text{for } r \le \frac{1}{2}, \\ \frac{4}{3} - 4r + 4r^2 - \frac{4}{3}r^3 & \text{for } \frac{1}{2} < r \le 1, \\ 0 & \text{for } r > 1. \end{cases} \tag{2.6}$$

For the tensor product weight, r is replaced by r_x and r_y respectively. r_x and r_y are defined as:

$$r_x = \frac{\|x - x_I\|}{d_{mIx}} \text{ and } r_y = \frac{\|y - y_I\|}{d_{mIy}} \tag{2.7}$$

where

$$d_{mIx} = d_{max}\cdot C_{xI} \text{ and } d_{mIy} = d_{max}\cdot C_{yI} \tag{2.8}$$

d_{max} is a scaling factor and C_{xI} and C_{yI} are determined at a particular node by searching for enough adjacent nodes in x and y directions respectively to satisfy the basis in both directions. This requirement is necessary to be able to invert the **A** matrix see eq.(2.18). If the nodes are uniformly distributed the values C_{xI} and C_{yI} are the distances between the nodes in x and y direction respectively, see Figure 2.2.

The derivatives of the tensor product weight function are:

$$w_{,x} = \frac{dw_x}{dx} \cdot w_y \tag{2.9}$$

$$w_{,y} = \frac{dw_y}{dy} \cdot w_x \tag{2.10}$$

where

$$\frac{dw_x}{dx} = \frac{dw_x}{dr}\frac{dr}{dx} = \begin{Bmatrix} (-8r+12r^2)\text{sign}(x-x_I) & \text{for } r \le \frac{1}{2} \\ (-4+8r-4r^2)\text{sign}(x-x_I) & \text{for } \frac{1}{2} < r \le 1 \\ 0 & \text{for } r > 1 \end{Bmatrix} \tag{2.11}$$

$$\frac{dw_y}{dy} = \frac{dw_y}{dr}\frac{dr}{dy} = \begin{Bmatrix} (-8r+12r^2)\text{sign}(y-y_I) & \text{for } r \le \frac{1}{2} \\ (-4+8r-4r^2)\text{sign}(y-y_I) & \text{for } \frac{1}{2} < r \le 1 \\ 0 & \text{for } r > 1 \end{Bmatrix} \tag{2.12}.$$

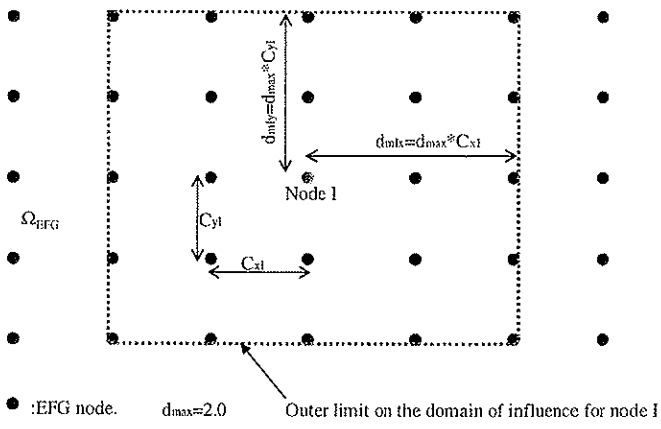

Figure 2.2: Definition of the EFG variables related to tensor product weights.

2.2.2 Shape functions

The EFG shape functions are derived by the MLS technique. Equation (2.4) is minimized with respect to $\mathbf{a}(\mathbf{x},t)$. The weighted quadratic form of Eq. (2.4) can be rewritten as:

$$J = (\mathbf{Pa} - \mathbf{u}_N)^T \mathbf{W} (\mathbf{Pa} - \mathbf{u}_N), \tag{2.13}$$

where the vector $\mathbf{u}_N$ contains the nodal parameters for all the nodes with the evaluation point $\mathbf{x}$ inside their influence domain,

$$\mathbf{u}_N{}^T = [u_1, u_2, u_3, ..., u_N]. \tag{2.14}$$

The square matrix $\mathbf{P}$ is given by:

$$\mathbf{P} = \begin{bmatrix} p_1(\mathbf{x}_1) & p_2(\mathbf{x}_1) & \cdots & p_m(\mathbf{x}_1) \\ p_1(\mathbf{x}_2) & p_2(\mathbf{x}_2) & \cdots & p_m(\mathbf{x}_2) \\ \vdots & \vdots & \ddots & \vdots \\ p_1(\mathbf{x}_N) & p_2(\mathbf{x}_N) & \cdots & p_m(\mathbf{x}_N) \end{bmatrix}. \tag{2.15}$$

$\mathbf{W}$ is a diagonal matrix of weight functions

$$\mathbf{W} = \begin{bmatrix} w(\mathbf{x}-\mathbf{x}_1, t) & 0 & \cdots & 0 \\ 0 & w(\mathbf{x}-\mathbf{x}_2, t) & \cdots & 0 \\ \vdots & \vdots & \ddots & \vdots \\ 0 & 0 & \cdots & w(\mathbf{x}-\mathbf{x}_N, t) \end{bmatrix}. \tag{2.16}$$

Minimizing the weighted quadratic form, Eq. (2.4), with respect to the functional basis coefficient vector, **a**, requires

$$\frac{\partial J}{\partial \mathbf{a}} = \frac{\partial}{\partial \mathbf{a}}\left(\left(\mathbf{Pa}-\mathbf{u}_N\right)^T \mathbf{W}\left(\mathbf{Pa}-\mathbf{u}_N\right)\right) = \mathbf{P}^T\mathbf{WPa}-\mathbf{P}^T\mathbf{Wu}_N = 0. \tag{2.17}$$

Now define $\mathbf{P}^T\mathbf{WP}=\mathbf{A}(\mathbf{x},t)$ and $\mathbf{P}^T\mathbf{W}=\mathbf{C}(\mathbf{x},t)$. Then insert these definitions into Eq. (2.17), and rewrite as an expression for the coefficients of the functional basis

$$\mathbf{a}(\mathbf{x},t) = \mathbf{A}^{-1}(\mathbf{x},t)\mathbf{C}(\mathbf{x},t)\mathbf{u}_N(t). \tag{2.18}$$

Substituting Eq. (2.18) into Eq. (2.1) gives the MLS approximated displacement function, $u^h(\mathbf{x},t)$, in terms of nodal parameters:

$$u^h(\mathbf{x},t) = \mathbf{p}^T(\mathbf{x})\mathbf{a}(\mathbf{x},t) = \mathbf{P}^T(\mathbf{x})\mathbf{A}^{-1}(\mathbf{x},t)\mathbf{C}(\mathbf{x},t)\mathbf{u}_N(t) \tag{2.19}$$

In the finite element method the displacement approximation is given in terms of shape functions interpolating between nodal values. A similar form can be adopted for EFG by rewriting Eq. (2.19) as:

$$u^h(\mathbf{x},t) = \mathbf{P}^T(\mathbf{x})\mathbf{A}^{-1}(\mathbf{x},t)\mathbf{C}(\mathbf{x},t)\mathbf{u}_N(t) = \mathbf{N}^{EFG}(\mathbf{x},t)\mathbf{u}_N(t) = \sum_{I=1}^{N} N_I^{EFG}(\mathbf{x},t)u_I(t), \tag{2.20}$$

where $\mathbf{N}^{EFG}(\mathbf{x},t)$ then can be defined as the shape functions related to node I in the MLS approximation. N is the total number of nodes influencing the evaluation point **x** ($\omega(\mathbf{x}-\mathbf{x}_I)\geq 0$). Note that the domain of influence may vary during an analysis. This will for example be the case during a dynamic crack growth simulation. Time dependent shape functions, are thus required (see Section 2.5.1 for further discussions).

Displacement gradients are then calculated from

$$u_{,i}^{h}(\mathbf{x},t) = \mathbf{N}_{I,i}^{EFG}(\mathbf{x},t)\mathbf{u}_N(t), \tag{2.21}$$

where

$$\mathbf{N}_{I,i}^{EFG} = \mathbf{p}_{,i}^{T}\mathbf{A}^{-1}\mathbf{C} + \mathbf{p}^{T}(\mathbf{A}_{,i}^{-1}\mathbf{C} + \mathbf{A}^{-1}\mathbf{C}_{,i}). \tag{2.22}$$

The comma notation denotes the spatial derivatives.

It should be noted that the EFG shape function in general does not satisfy the Cronecker delta criterion $\mathbf{N}^{EFG}(\mathbf{x}_I,t) \neq \delta_{iI}$. This feature makes the imposition of the essential boundary condition more complicated in the EFG method than in the FE method. In Section 2.4 a method for coupling the EFG description to the FE description is introduced. This coupling enables the use of finite elements along the essential boundaries and takes advantage of imposing the boundary conditions directly as nodal values at the finite element nodes.

2.3 *Elasto dynamics*

I this Section the discrete equations is established based on the governing equations in elasto dynamics. The work presented in this thesis is based on the assumption of elastic material behaviour surrounding possible cracks.

2.3.1 Governing equations

The strong form of the momentum equation for elasto dynamics is given by:

$$\nabla^T \sigma + \mathbf{b} = \rho \ddot{\mathbf{u}} \quad \text{in } \Omega, \tag{2.23}$$

where ρ is the mass density, σ is the stress vector, $\mathbf{b}$ is the vector of body forces per unit volume, and Ω is the domain of the model (see Figure 2.3). The definitions of ∇, σ, $\mathbf{b}$, and $\ddot{\mathbf{u}}$ is listed below together with the stress - strain relationships and the strain - displacement relationships for the case of small displacement and plane stress as

$$\nabla = \begin{bmatrix} \frac{\partial}{\partial x} & 0 \\ 0 & \frac{\partial}{\partial y} \\ \frac{\partial}{\partial y} & \frac{\partial}{\partial x} \end{bmatrix}, \quad \varepsilon = \begin{bmatrix} \varepsilon_{xx} \\ \varepsilon_{yy} \\ \varepsilon_{xy} \end{bmatrix} = \nabla \mathbf{u}, \quad \sigma = \begin{bmatrix} \sigma_{xx} \\ \sigma_{yy} \\ \sigma_{xy} \end{bmatrix}, \quad \mathbf{b} = \begin{bmatrix} f_x \\ f_y \end{bmatrix}, \quad \text{and } \ddot{\mathbf{u}} = \begin{bmatrix} \ddot{u}_x \\ \ddot{u}_y \end{bmatrix} = \frac{d^2}{dt^2} \begin{bmatrix} u_x \\ u_y \end{bmatrix} \tag{2.24}$$

$$\sigma = \mathbf{D}\varepsilon, \quad \mathbf{D} = \left\{ \underbrace{\frac{E}{1-\nu^2} \begin{bmatrix} 1 & \nu & 0 \\ \nu & 1 & 0 \\ 0 & 0 & \frac{1-\nu}{2} \end{bmatrix}}_{\text{Plane stress}}, \underbrace{\frac{E}{(1+\nu)(1-2\nu)} \begin{bmatrix} (1-\nu) & \nu & 0 \\ \nu & (1-\nu) & 0 \\ 0 & 0 & \frac{1-2\nu}{2} \end{bmatrix}}_{\text{Plane strain}} \right\} \tag{2.25}$$

E is the Young's modulus and ν is the Poisson's ratio.

The boundary- and initial- conditions are given by:

$$\mathbf{u} = \bar{\mathbf{u}} \qquad \text{on } \Gamma_u, \tag{2.26}$$

$$\sigma\mathbf{n} = \bar{\mathbf{t}} \qquad \text{on } \Gamma_t, \tag{2.27}$$

$$\mathbf{u}(\mathbf{x},0) = \mathbf{u}_0(\mathbf{x}) \quad \text{for } \mathbf{x} \in \Omega, \tag{2.28}$$

$$\dot{\mathbf{u}}(\mathbf{x},0) = \dot{\mathbf{u}}_0(\mathbf{x}) \quad \text{for } \mathbf{x} \in \Omega. \tag{2.29}$$

Γ_u is the prescribed displacement boundary. Γ_t is the prescribed traction boundary and $\bar{\mathbf{t}}$ are the tractions. The weak form of the momentum equation and the traction boundary condition is given by:

$$\int_\Omega \rho\delta\mathbf{u}^T\ddot{\mathbf{u}}d\Omega + \int_\Omega \delta\varepsilon^T\sigma d\Omega = \int_{\Gamma_t} \delta\mathbf{u}^T\mathbf{t}d\Gamma_t + \int_\Omega \delta\mathbf{u}^T\mathbf{b}d\Omega \tag{2.30}$$

where δ indicate that the following variable is a variation.

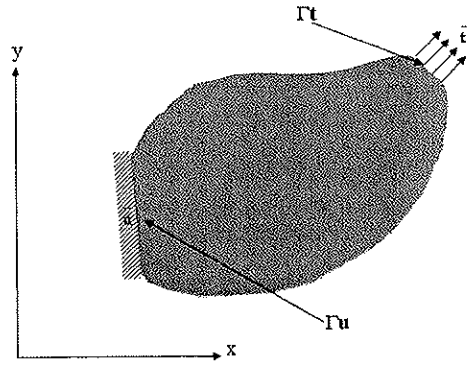

Figure 2.3: General 2D model.

2.3.2 Discrete equations

The discrete equations are obtained from the weak form Eq. (2.30) by inserting the displacement approximation (2.20), and its variation, given by:

$$\mathbf{u}^h(\mathbf{x},t)=\sum_I N_I^{EFG}(\mathbf{x},t)\mathbf{u}_I(t)=\sum_I N_I^{EFG}(\mathbf{x},t)\begin{bmatrix}u_{xI}(t)\\ u_{yI}(t)\end{bmatrix},\quad \text{for } \mathbf{x}\in\Omega. \tag{2.31}$$

$$\delta\mathbf{u}^h(\mathbf{x},t)=\sum_I N_I^{EFG}(\mathbf{x},t)\delta\mathbf{u}_I(t)=\sum_I N_I^{EFG}(\mathbf{x},t)\begin{bmatrix}\delta u_{xI}(t)\\ \delta u_{yI}(t)\end{bmatrix},\quad \text{for } \mathbf{x}\in\Omega. \tag{2.32}$$

$$\delta\boldsymbol{\varepsilon}=\delta\nabla\mathbf{u}=\begin{bmatrix}\dfrac{\partial \mathbf{N}^{EFG}(\mathbf{x},t)}{\partial x} & 0\\ 0 & \dfrac{\partial \mathbf{N}^{EFG}(\mathbf{x},t)}{\partial y}\\ \dfrac{\partial \mathbf{N}^{EFG}(\mathbf{x},t)}{\partial y} & \dfrac{\partial \mathbf{N}^{EFG}(\mathbf{x},t)}{\partial x}\end{bmatrix}\delta\mathbf{u}_I(t) \tag{2.33}$$

For arbitrary displacement variation the weak form gives the equations of motion

$$\mathbf{M}\ddot{\mathbf{u}}+\mathbf{K}\mathbf{u}=\mathbf{F} \tag{2.34}$$

The matrix elements are obtained from

$$M_{II}=\sum_J\int_\Omega \rho N_I^{EFG}N_J^{EFG}d\Omega,\qquad M_{IJ(I\neq J)}=0, \tag{2.35}$$

$$K_{IJ}=\int \mathbf{B}_I\mathbf{D}\mathbf{B}_J d\Omega, \tag{2.36}$$

$$\mathbf{F}_I=\int_{\Gamma_{\bar{t}}} N_I^{EFG}\bar{\mathbf{t}}d\Gamma_{\bar{t}}+\int_\Omega N_I^{EFG}\mathbf{b}d\Omega, \tag{2.37}$$

$\mathbf{B}_I$ in Eq. (2.36) is defined by

$$\mathbf{B}_I = \begin{bmatrix} N^{EFG}_{I,x} & 0 \\ 0 & N^{EFG}_{I,y} \\ N^{EFG}_{I,y} & N^{EFG}_{I,x} \end{bmatrix}. \tag{2.38}$$

In this study the mass matrix in Eq.(2.34) is diagonalized by the row sum technique. (The modification of the shape functions in dynamic fracture problems are illustrated in Section 2.5.) Possible modification of the mass matrix for time dependence is neglected in the present work.

2.3.3 Numerical integration

In the EFG method, numerical integration of the matrices in the equations of motion is performed by using a background mesh or cell structure, without correspondence to their support boundaries (see Figure 2.4). A source of inaccuracy in the EFG method is that the background cells do not align with the boundary of influence domain of the shape functions or their intersections. This can be remedied by using the tensor product weight function with equally spaced nodes or modification of the integration cell domain with the bonding box technique for rectangular domains (see Dolbow (1998)). For circular support the construction of integration cells with the above properties is more difficult. The misalignment between the integration boundaries and the support boundaries will then affect the accuracy and the rate of convergence of the EFG method. If regular mesh or integration cell modification is not possible or convenient, higher order Gauss quadrature may be also combined with refinement of the integration cells is required to maintain the desired level of accuracy. This leads, however, to a considerable increase in computation time. Detailed information and examples on this topic is found in Dolbow (1998).

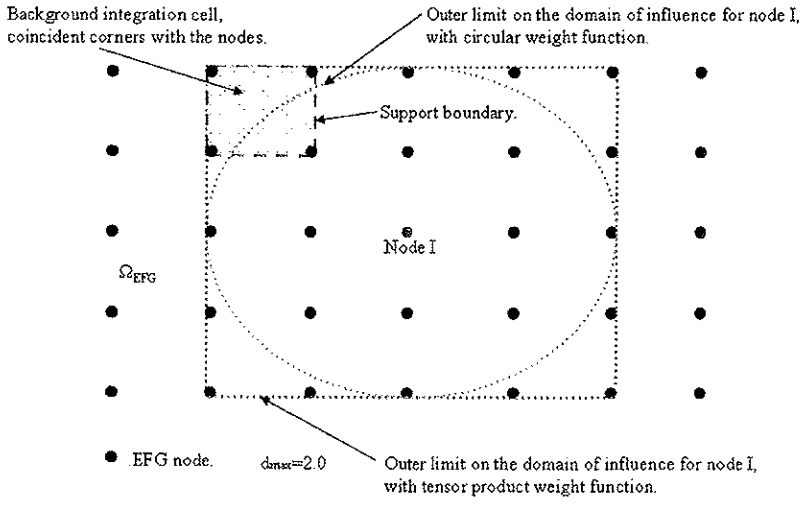

Figure 2.4: Integration cell and support boundaries for tensor product weight function with equally spaced nodes and radial weight function.

2.4 *Time discretisation - explicit integration.*

The time discretization is based on the Newmark family algorithm, for the solution of the equations of motion. Displacements and velocities at successive discrete times, t_n, are found respectively from

$$\mathbf{u}_{n+1} = \mathbf{u}_n + \Delta t\dot{\mathbf{u}}_n + \frac{\Delta t^2}{2}(1-\beta_2)\ddot{\mathbf{u}}_n + \frac{\Delta t^2}{2}\beta_2\ddot{\mathbf{u}}_{n+1} \tag{2.39}$$

and

$$\dot{\mathbf{u}}_{n+1} = \dot{\mathbf{u}}_n + \Delta t(1-\beta_1)\ddot{\mathbf{u}}_n + \Delta t\beta_1\ddot{\mathbf{u}}_{n+1} \tag{2.40}$$

The time step is denoted Δt, and thus $t_n = n\Delta t$.

In the following derivation β_2=0, this is corresponding to the explicit integration since **M** is a diagonal matrix. β_1 is chosen to be 0.99 for all analyses performed in this thesis, except when the influence on the result of varying the parameter from 0.5 (corresponding to the well known central difference algorithm) to 0.99 is investigated. 0.99 is adopted because it introduces artificial algorithm damping of high frequencies. The high frequencies are introduced by the discretization process of the semi discrete structural equations.

The expressions for displacements and velocities, together with the equations of motion satisfied at the end of time step t_n,

$$\mathbf{M}\ddot{\mathbf{u}}_{n+1} + \mathbf{K}\mathbf{u}_{n+1} = \mathbf{F}_{n+1} \tag{2.41}$$

allows the two unknowns $\dot{\mathbf{u}}_{n+1}$ and $\ddot{\mathbf{u}}_{n+1}$ to be determined (since by using β_2=0, $\mathbf{u}_{n+1}$ is already known). First it is convenient to solve for $\ddot{\mathbf{u}}_{n+1}$ by inserting Equation (2.39) into Equation (2.41), to get

$$\ddot{\mathbf{u}}_{n+1} = \mathbf{M}^{-1}\left[\mathbf{F}_{n+1} - \mathbf{K}\left(\mathbf{u}_n + \Delta t\dot{\mathbf{u}}_n + \frac{\Delta t^2}{2}\ddot{\mathbf{u}}_n\right)\right] \tag{2.42}$$

Further, $\dot{\mathbf{u}}_{n+1}$ can be obtained by inserting Equation (2.42) into Equation(2.40), to obtain the expression

$$\dot{\mathbf{u}}_{n+1} = \dot{\mathbf{u}}_n + \Delta t(1-\beta_1)\ddot{\mathbf{u}}_n + \Delta t\beta_1\mathbf{M}^{-1}\left[\mathbf{F}_{n+1} - \mathbf{K}\left(\mathbf{u}_n + \Delta t\dot{\mathbf{u}}_n + \frac{\Delta t^2}{2}\ddot{\mathbf{u}}_n\right)\right] \tag{2.43}$$

The above algorithm is repeated for each time increment of the total time range. To ensure that this explicit Newmark algorithm does not depart from the true solution, the stability of the algorithm must be considered. The critical time increment, Δt_{crit}, is given by the Courant condition: Δt_{crit} =h/c, where h is set to the minimum distance between nodes (FE or EFG) and c is the dilatational wave speed in the material. The above critical time increment is conservative for the EFG method (Belytshko, Organ, and Krongauz (1995)).

2.5 *Model combining finite elements and element free Galerkin domains*

As mention in the introduction, the EFG method offers considerable advantages over the FE method for many problems. This is particularly true for problems with moving discontinuities, such as in the case of crack propagation. On the other hand the EFG method is today more computer demanding than the FE method when comparing analysis of the same continues problems with both methods. It may then be beneficial to use the EFG method in subdomains where that method is favorable compared to the FE method, but use the FE method in the remainder of the domain. By this separation of the local domain into an "EFG"- and a "FE"- domain, one can efficiently analyze moving discontinuities that was almost impossible or very difficult by using the finite element method. Another advantage of the domain partitioning is that the essential boundary conditions can be imposed in a FE domain at the boundaries (without any extra effort, as would be the case with the EFG method).

2.5.1 Shape functions

The coupling methodology between the EFG method and the FE method presented in this section has been published by Belytshko, Organ, and Krongauz (1995). The thesis by Organ (1996) also includes a detailed description of the coupling procedure. The coupling is performed in an interface domain by interface elements (see Figure 2.5). In these interface elements, a hybrid displacement approximation is defined that satisfies displacement continuity across the interface boundaries.

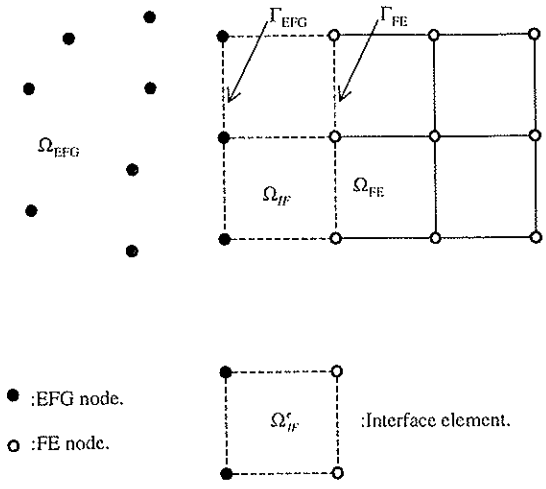

Figure 2.5: Coupling between EFG-domain and FE-domain by interface elements.

Figure 2.5 illustrates the coupling procedure, with the transition region between the EFG- and the FE-domain. In the EFG-domain, Ω_{EFG}, the displacement at a point is approximated according to Eq. (2.20)

$$u^h_{EFG}(\mathbf{x},t) = \sum_{I=1}^{N} N_I^{EFG}(\mathbf{x},t)u_I(t), \quad \text{for } \mathbf{x} \in \Omega_{EFG}. \tag{2.44}$$

In the FE-domain, Ω_{FE}, the displacement at a point is approximated by the finite element interpolation

$$u^h_{FE}(\mathbf{x},t) = \sum_{I=1}^{Nen} N_I^{FE}(\xi(\mathbf{x}),\eta(\mathbf{x}))u_I(t), \quad \text{for } \mathbf{x} \in \Omega^e_{FE}. \tag{2.45}$$

This equation is employed in each finite element subdomain, Ω^e_{FE}. N_{en} is the number of element nodes, and $N_I^{FE}(\xi(\mathbf{x}),\eta(\mathbf{x}))$ is the standard bilinear shape function for a 4-node quadrilateral element given by:

$$N_i^{FE}(\xi(\mathbf{x}),\eta(\mathbf{x})) = \frac{1}{4}(1+\xi_i\xi)(1+\eta_i\eta), \tag{2.46}$$

where $\xi(\mathbf{x})$ and $\eta(\mathbf{x})$ are the standard mapping function from the physical domain to the $\xi\eta$ reference domain. In the interface domain, Ω_{IF}, the displacement at a point is approximated by the hybrid displacement formulation:

$$u_{IF}^{h}(\mathbf{x},t)=\left[1-R(\mathbf{x})\right]u_{FE}^{h}(\mathbf{x},t)+R(\mathbf{x})u_{EFG}^{h}(\mathbf{x},t), \tag{2.47}$$

where R(x) is a ramp function. It is defined using the sum of the finite element shape functions on the EFG boundary. The ramp function varies linearly along the interface element boundaries, and is given by:

$$R(\mathbf{x})=\sum_{\substack{J\\ x_J\in\Gamma_{EFG}}} N_J(\mathbf{x}). \tag{2.48}$$

Note that at the boundaries, Γ_{EFG} and Γ_{FE}, the ramp function Eq. (2.48), reduces to 1 and 0 respectively. This ensures that the displacement approximations on these boundaries reduces to $u_{EFG}^{h}(\mathbf{x},t)$ and $u_{FE}^{h}(\mathbf{x},t)$ respectively. Equation (2.47) can be rewritten with a standard FE notation. The hybrid shape function is multiplied by the nodal parameters, and the EFG and the FE displacement approximations from Eq. (2.44) and Eq. (2.45) are substituted into Eq.(2.47) to get

$$\begin{aligned} u_{IF}^{h}(\mathbf{x},t)&=\left[1-R(\mathbf{x})\right]\sum_{I=1}^{Nen} N_I^{FE}(\xi(\mathbf{x}),\eta(\mathbf{x}))u_I(t)+R(\mathbf{x})\sum_{I=1}^{N} N_I^{EFG}(\mathbf{x})u_I(t)\\ &=\sum_{I=1}^{N} N_I^{IF}(\mathbf{x})u_I(t) \quad \text{for } \mathbf{x}\in\Omega_{IF}^{e}. \end{aligned} \tag{2.49}$$

The interface shape functions $N_I^{IF}(\mathbf{x})$ are given by

$$N_I^{IF}(\mathbf{x})=\begin{cases}\left[1-R(\mathbf{x})\right]N_I^{FE}(\xi(\mathbf{x}),\eta(\mathbf{x}))+R(\mathbf{x})N_I^{EFG}(\mathbf{x}), & \text{for } \mathbf{x}\in\Omega_{IF}^{e},\\ R(\mathbf{x})N_I^{EFG}(\mathbf{x}) & \text{for } \mathbf{x}\notin\Omega_{IF}^{e}.\end{cases} \tag{2.50}$$

The first expression in Eq. (2.50) gives the interface shape function for the interface element nodes, and the second expression gives the interface shape function for the

nodes outside the interface element and inside the EFG domain. Note that the EFG shape function contribution to the interface shape function expression is not time dependent. This is because local discontinuities in the interface domain are not allowed since the location of the domain is arbitrary. The shape function material derivatives are given by:

$$N_{I,i}^{IF}(\mathbf{x}) = \begin{cases} -R_{,i}N_I^{FE} + [1-R]N_{I,i}^{FE} + R_{,i}N_I^{EFG} + RN_{I,i}^{EFG} & \text{for } \mathbf{x} \in \Omega_{IF}^{e}, \\ R_{,i}N_I^{EFG} + RN_{I,i}^{EFG} & \text{for } \mathbf{x} \notin \Omega_{IF}^{e}, \end{cases} \tag{2.51}$$

where

$$R_{,i} = \sum_{\substack{J \\ x_J \in \Gamma_{EFG}}} N_{J,i}(\mathbf{x}). \tag{2.52}$$

The derivative of the interface shape function (2.51) is discontinuous across Γ_{EFG} and Γ_{FE}, since $R_{,i}$ contributes to the derivative of the interface shape function. To satisfy continuous first order derivatives across Γ_{EFG} and Γ_{FE}, a quadratic ramp function given by

$$R_{quad}(\mathbf{x}) = 3R^2(\mathbf{x}) - 2R^3(\mathbf{x}), \tag{2.53}$$

may be adopted. By inserting R_{quad} for R in Eq. (2.50), and with $R_{,i}$ replaced by

$$R_{quad,i}(\mathbf{x}) = (R(\mathbf{x}) - R^2(\mathbf{x}))6R_{,i}(\mathbf{x}), \tag{2.54}$$

the first order derivative of the hybrid displacement functions across boundaries Γ_{EFG} and Γ_{FE} are satisfied. The interface shape functions depend on which nodes are included for the EFG approximation in Ω_{IF}.

A compact form of the displacement approximation for the total domain Ω, can be obtained by a combination of Equations (2.44), (2.45) and (2.49). The compact displacement approximation will then be:

$$u^h(\mathbf{x},t) = \sum_{I=1}^{NN} N_I(\mathbf{x},t)u_I(t), \quad \text{for } \mathbf{x} \in \Omega, \tag{2.55}$$

where

$$N_I(\mathbf{x},t) = \begin{cases} N_I^{FE}(\mathbf{x}) & \text{for } \mathbf{x} \in \Omega_{FE} \\ N_I^{EFG}(\mathbf{x},t) & \text{for } \mathbf{x} \in \Omega_{EFG} \\ N_I^{IF}(\mathbf{x}) & \text{for } \mathbf{x} \in \Omega_{IF} \end{cases} \tag{2.56}$$

The summation limit in Eq. (2.55), is NN =N for the EFG domain, and the interface domain, Ω_{IF}, and NN=N_{en} for the FE domain. The compact form of the displacement approximation, Eq. (2.55), inserted in the weighted residual (weak form of the momentum equation, Eq. (2.30)) results in the set of discrete equations describing the combined behaviour of the three domains similarly as for Equations (2.31) to (2.38).

2.6 *Discontinuous approximation by the visibility criterion*

In this Section a method to handle discontinuities such as cracks, cavities and other non-convex boundaries is treated. The method is based on the visibility criterion, first introduced by Organ, Flemming, Terry and Belytschko (1996). The visibility criterion is a simple approach, more sophisticated methods such as the diffraction method and the transparency method are shown in Organ, Flemming, Terry and Belytschko (1996), Organ (1996), and Flemming (1997).

2.6.1 The Visibility Criterion

The visibility criterion is used to define the domain of influence in the vicinity of cavities, cracks and other non-convex domains. In the visibility criterion approach, the point $\mathbf{x}$ is within the domain of influence of node $\mathbf{x}_I$ if $\mathbf{x}$ is within the region where the weight function $w(\mathbf{x}_I-\mathbf{x})>0$. The point $\mathbf{x}$ is visible to an observer at node I. These conditions can be defined as follows:

$$\Omega_I = \{\mathbf{x} | \mathbf{x} \in \Omega, w(\mathbf{x}_I - \mathbf{x}) > 0\}, \quad \Omega_I^{VIS} = \{\mathbf{x} | S_{x \to x_I} \cap \Gamma_c = \emptyset\}, \tag{2.57}$$

where $S_{x \to x_I}$ is the set of all points on the straight line from $\mathbf{x}$ to $\mathbf{x}_I$ and Γ_c is the complete boundary of the total domain, including any interior surfaces (corresponding to cavities and crack edges in this study). The domain of influence Ω^{DI} is then defined by the intersection expression

$$\Omega_I^{DI} = \Omega_I^{VIS} \cap \Omega_I \tag{2.58}$$

The effect of this definition can be seen in Figure 2.6. For a rectangular cavity, the domain of influence is truncated by the ray from the node which just grazes the rectangular cavity (the corners in this case).

The domain of influence Ω^{DI} is shown by grey dashed lines. Consequently, the weight function is discontinuous along the lines AB, AC and CD in Figure 2.6. Similar domain visualization is included for a circular cavity. For a crack, the domain of influence Ω^{DI} is illustrated by grey dashed lines, and with discontinuities along the lines AB and BC in Figure 2.6. The discontinuous weight functions for these examples are illustrated in Figure 2.7, Figure 2.8 and Figure 2.9 respectively. The displacement approximation can then be found from the same procedure as described in Section 2.1.2, by using the domain of influence as given by Eq. (2.58).

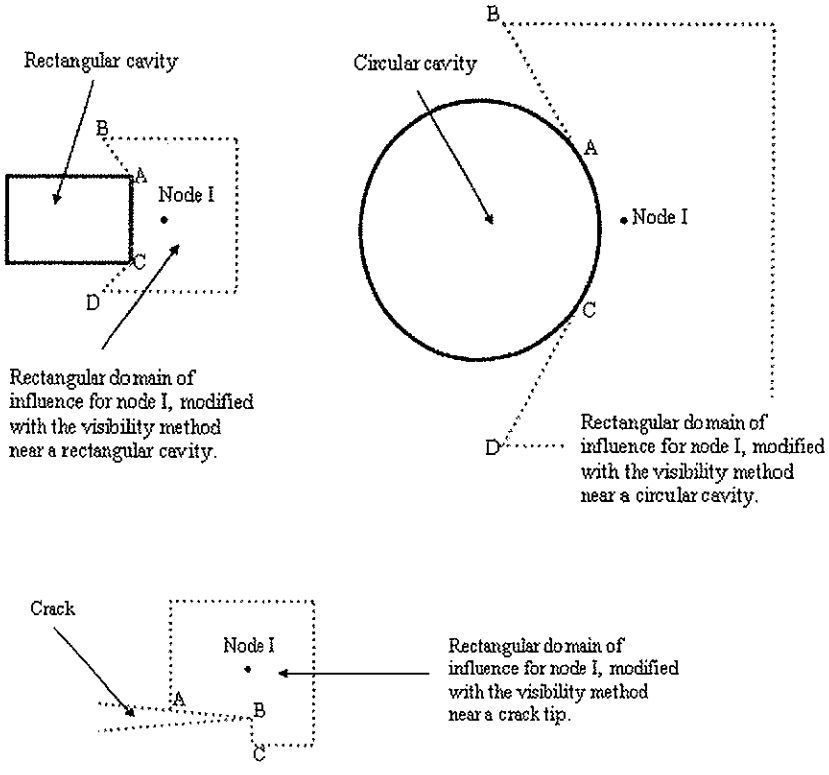

Figure 2.6: Domain of influence near an interior rectangular and circular cavity, and a crack tip.

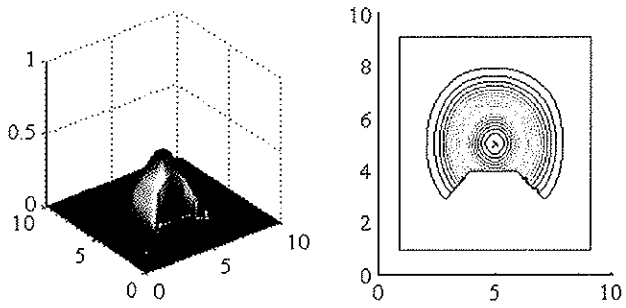

Figure 2.7: Illustration of a discontinuous 3D weight function in the case of a rectangular cavity, and with a contour plot to the right.

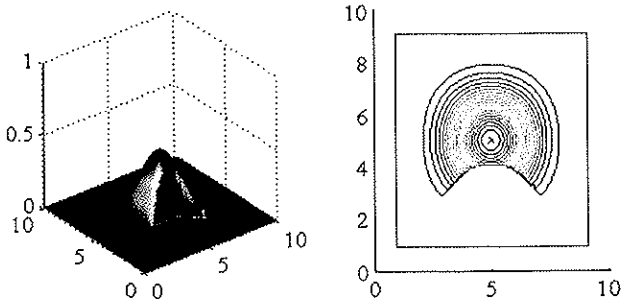

Figure 2.8: Illustration of a discontinuous 3D weight function in the case of a circular cavity, and with a contour plot to the right.

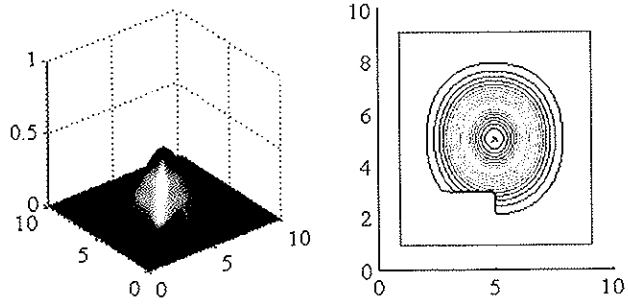

Figure 2.9: Illustration of a discontinuous 3D weight function in the vicinity of crack tip, and with a contour plot to the right.

2.7 *Enriched EFG basis for crack tip fields*

In fracture mechanics simulations it is necessary with high accuracy in the calculations of the crack tip fields in order to obtain reliable results in the estimates of the stress intensity factors, K_I and K_{II}. For a two dimensional problem intrinsic enrichment is one approach to obtain this. Enrichment functions are added to the EFG basis in a sub-domain around the crack tip. The enriched terms in the basis should reflect the behaviour of the expected crack tip field fully or partly, to capture the main behaviour. One advantage of the method is that no extra nodes are needed.

The method is presented in Sections 2.7.1 and 2.7.2.

2.7.1 Intrinsic radial basis enrichment for crack tip fields

In the EFG method the approximation can be improved by expanding the basis with functions related to the actual field of interest. In fracture mechanics the basis can be extended with the radial term $\sqrt{r}$, which evolves from the asymptotic crack tip field as shown in Appendix A. Further improvement can be performed by including more terms in the basis to represent the asymptotic crack tip field fully (see Flemming, Chu, Moran, and Belytshko (1997)).

In the following the intrinsic radial enrichment of the basis is adopted. The expression of the basis is then:

$$\mathbf{p}^T = \left[1, x, y, \sqrt{r}\right], \quad (m = 4, \text{enriched}) \tag{2.59}$$

where r is the radial distance from the crack tip to the calculating point (x,y), see Figure 2.10. The advantage of the radial enriched basis is that the basis is only extended with one term in comparison with the fully enriched basis extended with 4 terms. This means a significant saving of computer time related to the calculation of the inverse of matrix $\mathbf{A}(\mathbf{x})$ of Eq. (2.18).

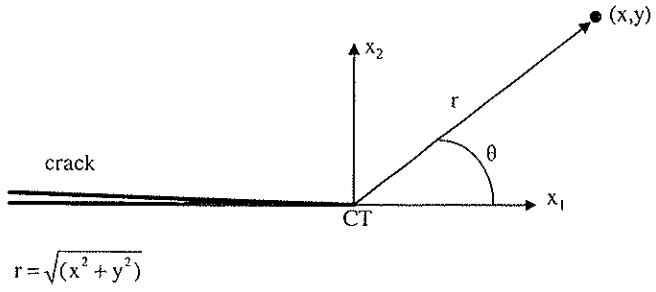

Figure 2.10: Description of crack tip variables.

2.7.2 Coupling of radially enriched and linear approximations

An enriched basis is not required for the entire domain. The crack tip singularity field is a small area. It would be favorable to have an enriched approximation in this area and the linear approximation elsewhere. By a coupling procedure, like the coupling between FE and EFG in Section 2.5, it is possible to enrich the approximation in the area close to the crack tip.

The method described in this section couples linearly the enriched approximation with the linear approximation over a transition area. The displacement approximation in the transition area is defined as:

$$u^h(\mathbf{x}) = Ru^{enr}(\mathbf{x}) + (1-R)u^{lin}(\mathbf{x}), \tag{2.60}$$

where $u^{enr}(\mathbf{x})$ is the enriched displacement approximation and $u^{lin}(\mathbf{x})$ is the linear displacement approximation. R is a ramp function. Two different ramp functions, a linear one and a quintic one are defined by

$$R = \begin{cases} 1-\xi & \text{linear ramp} \\ 1-10\xi^3+15\xi^4-6\xi^5 & \text{quintic ramp} \end{cases}. \tag{2.61}$$

Here $\xi = (r-r_1)/(r_2-r_1)$. R is 1.0 on the enriched boundary ($r=r_1$) and equal to zero on the linear boundary ($r=r_2$), see Figure 2.11. The coupled displacement approximation in the transition region, can be defined as a shape function interpolation between nodal parameters as in the standard FE notation

$$u^h(\mathbf{x}) = \sum_{I=1}^{n} \tilde{N}_I u_I \tag{2.62}$$

where

$$\tilde{N}_I = RN_I^{enr} + (1-R)N_I^{lin} \tag{2.63}$$

N_I^{enr} is the shape function based on the enriched basis, Eq. (2.59) and N_I^{lin} is the shape function based on the linear basis, Eq. (2.2). This method will sustain compatibility in displacements, but only the quintic ramp function ensures compatibility in strains. The size of the enriched domain (r_1) is rather arbitrary. It can actually be zero, but the outer radius, r_2, must be outside the singularity dominated zone around the crack tip (Flemming (1997)).

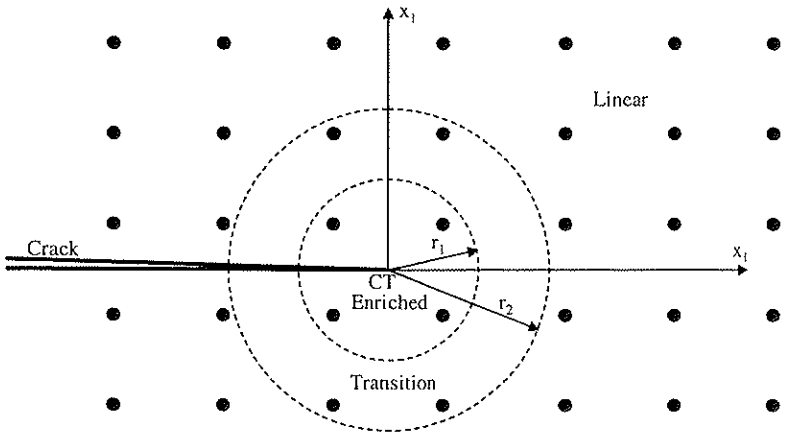

Figure 2.11: Illustration of the coupling between linear and radial enriched bases.

Chapter 3 Linear dynamic fracture mechanics

3.1 Introduction

It is well known in the linear elastic fracture mechanics theory (isotropic linear elastic material behaviour), that the near tip stress fields for in plane loading is dominated by the term $1/\sqrt{r}$. The field of every fracture mode is known, and it is characterized by its respective stress intensity factors. The influence on the field from the crack propagating velocity is established in Freund (1998). Thus, in linear elastic dynamic fracture problems, the stress fields near the crack tip reduces to calculation of the stress intensity factors, K_I, K_{II}, and K_{III} in the general 3D domain. In a crack propagating simulation, a simple crack propagation criterion could be dependent of the stress intensity factors and the residence of the material only. Then it is important to establish a robust method to calculate the stress intensity factors, to obtain a reliable solution of the problem.

This chapter deals with how to handle numerical calculation of the fracture parameters in dynamic crack propagation problems, and how to numerically solve the cracking process. Only 2D problems are studied. The derivation considers only the opening mode, denoted mode I, and the shearing mode, denoted mode II (see Figure 3.1). The tearing mode, denoted mode III, is naturally of no interest in a 2D problem.

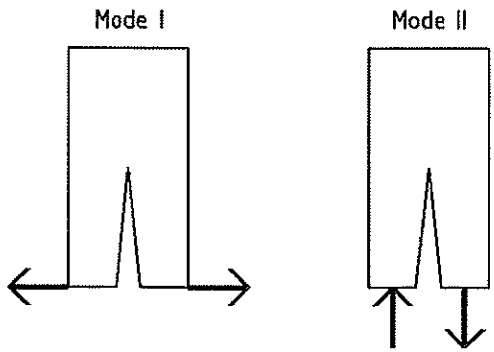

Figure 3.1: Illustration of the crack opening mode I, and the shearing mode II.

In Sections 3.2 to 3.7 of a procedure for numerical calculation of the stress intensity factors K_I and K_{II} in an elastic dynamic crack propagation problem is established. The method is based on the path independent energy release rate $\mathcal{G}$. The classic contour integral is transformed to a domain integral to simplify the numerical calculation in the EFG context. Mixed mode stress intensity factors are derived by using an auxiliary field. With this technique, separate expressions of the stress intensity factors are obtained.

Section 3.8 discusses how the dynamic fracture is handled numerically in the EFG method. This includes the procedure to calculate stress intensity factors, the crack propagation criterion and the implementation of the variable crack propagation velocity. The asymptotic crack tip field and the auxiliary field terms in the interaction integral are listed in Appendix A.

3.2 General mechanical energy balance on integral form

The derivation of the general mechanical energy balance in integral form starts with the equation of motion (neglecting the body forces):

$$\sigma_{ij,j} = \rho \ddot{u}_i \tag{3.1}$$

Taking the inner product with the material velocity, $\dot{u}_i$, gives:

$$\sigma_{ij,j}\dot{u}_i = \rho \ddot{u}_i \dot{u}_i \tag{3.2}$$

Rewriting the left hand side of Eq. (3.2) by using $(\sigma_{ij}\dot{u}_i)_{,j} = \sigma_{ij,j}\dot{u}_i + \sigma_{ij}\dot{u}_{i,j}$, gives:

$$(\sigma_{ij}\dot{u}_i)_{,j} = \sigma_{ij}\dot{u}_{i,j} + \rho \ddot{u}_i \dot{u}_i \tag{3.3}$$

The first term on the right hand side is recognized as the time derivative of the stress work density

$$\sigma_{ij}\dot{u}_{i,j} = \dot{W} \tag{3.4}$$

as

$$W = \int_{-\infty}^{t} \sigma_{ij}\dot{u}_{i,j}dt \tag{3.5}$$

The second term on the right hand side can be identified as the time derivative of the kinetic energy density

$$\rho\ddot{u}_i\dot{u}_i = \dot{L} \tag{3.6}$$

where

$$L = \frac{1}{2}\rho\dot{u}_i\dot{u}_i \tag{3.7}$$

Inserting Eq. (3.6) and Eq. (3.4) into Eq. (3.3) gives:

$$(\sigma_{ij}\dot{u}_i)_{,j} = \dot{W} + \dot{L} \tag{3.8}$$

Equation (3.8) states the mechanical energy balance on differential form. The mechanical energy balance for a general 3D volume can be obtained by integrating Eq. (3.8) to get

$$\int_V (\sigma_{ij}\dot{u}_i)_{,j}dV = \int_V (\dot{W} + \dot{L})dV \tag{3.9}$$

Rewriting Eq. (3.9) by applying the divergence theorem to the left hand side and the Reynolds transport theorem to the right hand side, the integral form of the mechanical energy balance results as

$$\int_{\partial V} \sigma_{ij}\dot{u}_i m_j dA = \frac{d}{dt}\int_V (W+L)dV - \int_{\partial V} (W+L)v_i m_i dA \qquad (3.10)$$

3.3 Mechanical energy balance of a domain surrounding a crack tip

The general integral form of the mechanical energy balance was established in Section 3.2. In this section the mechanical energy balance for the special case with a crack in two dimensions is developed. A local coordinate system is defined, where the origin is located at the crack tip with the local x_1 axis oriented in the direction of the crack growth aligned with the crack faces. The local coordinate system is moving with the crack tip, see Figure 3.2.

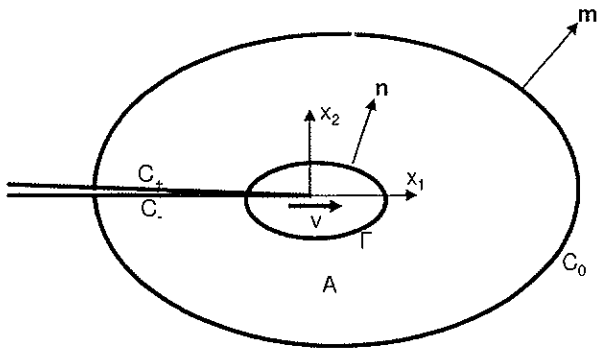

Figure 3.2: Propagating crack tip with the velocity v. The local coordinate system, the different contours, the domain A, and the normal vectors are illustrated.

For this configuration, the integral form of the mechanical energy balance, Eq. (3.10), becomes

$$\int_{\partial A} \sigma_{ij}\dot{u}_i m_j dS = \frac{d}{dt}\int_A (W+L)dA - \int_{\partial A} (W+L)v_i m_i dS \tag{3.11}$$

where $\partial A = C_0 \cup C_+ \cup C_- \cup \Gamma$. For simplification of Eq. (3.11), the following assumptions are made:

- Straight crack faces within the integration domain A.
- Traction free crack faces $\Rightarrow \quad \sigma_{ij}m_j = 0 \quad$ on $C_+ \cup C_-$.
- C_0 is stationary $\Rightarrow \quad v_i = 0 \quad$ on $\quad C_0$.
- Γ moves with the crack tip $\Rightarrow \quad v_1 = v$ and $v_2 = 0 \quad$ on Γ (see 3.2).

With these assumptions the mechanical energy balance, Eq. (3.11), for a 2D domain surrounding a crack tip can be expressed as

$$\int_{C_0} \sigma_{ij}\dot{u}_i m_j dS + \int_{\Gamma} \sigma_{ij}\dot{u}_i m_j dS + \overbrace{\int_{C_+\cup C_-} \sigma_{ij}\dot{u}_i m_j dS}^{=0 \Rightarrow \sigma_{ij}m_j = 0 \text{ on } C_+\cup C_-} = \frac{d}{dt}\int_{\partial A} (W+L)dA$$
$$- \overbrace{\int_{C_+\cup C_-} (W+L)v_i m_2 dS}^{\Rightarrow m_1 = 0 \text{ (straight crack faces)}} - \overbrace{\int_{\Gamma} (W+L)v_i m_1 dS}^{vm_1 \Rightarrow v = ve_1 \text{ on } \Gamma} - \overbrace{\int_{C_0} (W+L)v_i m_j dS}^{=0 \Rightarrow v_i = 0 \text{ on } C_0} \tag{3.12}$$

The mechanical energy balance for the particular problem illustrated in Figure 3.2, is found by rewriting Eq. (3.12) in th form

$$\overbrace{\int_{C_0} \sigma_{ij}\dot{u}_i m_j dS}^{\text{rate of traction work}} = \overbrace{\frac{d}{dt}\int_{\partial A} (W+L)dA}^{\text{rate of change of tot. mech. energy}}$$
$$- \overbrace{\int_{C_+\cup C_-} (W+L)v_i m_2 dS}^{\text{energy flux through crack faces}} - \overbrace{\int_{\Gamma} \left((W+L)v_i m_1 + \sigma_{ij}\dot{u}_i m_j\right) dS}^{\text{energy flux through } \Gamma} \tag{3.13}$$

3.4 Crack tip energy flux

The last term in Eq. (3.13), is the energy flux through Γ. By use of the relation **m**=-**n** on Γ, the crack tip energy flux integral is:

$$F(\Gamma) = \int_{\Gamma} \left((W + L) v \delta_{1j} + \sigma_{ij} \dot{u}_i \right) n_j dS \tag{3.14}$$

The integral in Eq. (3.14) is not necessarily independent of the integration path Γ, but in the limit as $\Gamma \to 0$ and shrinks towards the crack tip, the flux is independent of the shape of Γ. Then the definition of the crack tip energy flux is

$$F(\Gamma) = \lim_{\Gamma \to 0} \int_{\Gamma} \left((W + L) v \delta_{1j} + \sigma_{ij} \dot{u}_i \right) n_j dS \tag{3.15}$$

3.5 Energy release rate

Griffith defined G (energy release rate) which is the amount of energy, per unit length along a crack edge, that is supplied by the elastic energy in the body and by the loading system creating the new fracture surface. Irwin obtained the important relationship between the energy release rate and the stress intensity factor. The energy release rate is given by:

$$\mathcal{G} = -\frac{d\Pi}{da} \tag{3.16}$$

where $\mathcal{G}$ is the rate of change in the potential energy, $\prod$, with the crack area, a. For the preceding case the energy release rate can be expressed by the crack propagation, vdt, during the infinitesimal time dt and the energy flux F (in which is the change of potential energy). This gives the expression of the energy release rate as:

$$\mathcal{G} = \frac{F\mathrm{d}t}{v\mathrm{d}t} = \frac{F}{v} \tag{3.17}$$

By inserting Eq. (3.15) into Eq. (3.17), the general expression for the energy release rate can be obtained. The displacement rate expressed by the crack velocity, v, follows from time differentiation of the displacement in the x_1-direction

$$\dot{u}_i = \frac{\partial u}{\partial t} - v\frac{\partial u_i}{\partial x_1} \tag{3.18}$$

With steady state conditions, the first term in Eq. (3.18) is zero. For non steady state conditions the second term in Eq. (3.18) will still be dominating because of the large displacement gradients in the crack tip area. Then the material time derivative of the displacement can be simplified as

$$\dot{u}_i = -v\frac{\partial u_i}{\partial x_1} = -vu_{i,1} \tag{3.19}$$

Equation (3.19) is inserted into Eq. (3.15) to give an expression of the crack tip energy flux as:

$$\mathcal{F}(\Gamma) = \lim_{\Gamma\to 0}\int_{\Gamma}\left((W+L)v\delta_{1j} - \sigma_{ij}vu_{i,1}\right)n_j\mathrm{d}S \tag{3.20}$$

With Eq. (3.20) inserted into Eq. (3.17) the dynamic energy release rate becomes

$$\mathcal{G}(\Gamma) = \lim_{\Gamma\to 0}\int_{\Gamma}\left((W+L)\delta_{1j} - \sigma_{ij}u_{i,1}\right)n_j\mathrm{d}S \tag{3.21}$$

3.6 Energy release rate domain integral

The following derivation is performed with the aim of establishing an expression for the energy release rate that is simple to calculate numerically. The derivation starts with the dynamic energy release rate given by Eq. (3.21), and the definition of a quantity

$$H_{1j} = (W + L)\delta_{1j} - \sigma_{ij}u_{i,1} \tag{3.22}$$

to simplify successive expressions. The dynamic energy release rate can now be rewritten as:

$$\mathcal{G}(\Gamma) = \lim_{\Gamma \to 0} \int_{\Gamma} H_{1j} n_j dS \tag{3.23}$$

Further, an integral of a product of $H_{1j}n_j$ and a function q is introduced. Integration over the domain boundary, ∂A, is related to the domain integration by using the divergence theorem with the result

$$\int_{\partial A} H_{1j} q m_j dS = \int_{A} (H_{1j} q_{,j} + H_{1j,j} q) dA \tag{3.24}$$

Then the contour ∂A is separated into (see Figure 3.2) $\partial A = C_0 \cup C_+ \cup C_- \cup \Gamma$ to get:

$$\begin{aligned} \int_{\partial A} H_{1j} q m_j dS &= \int_{\Gamma} H_{1j} q m_j dS + \int_{C_+ \cup C_-} H_{1j} q m_j dS + \int_{C_0} H_{1j} q m_j dS \\ &= \int_{A} (H_{1j} q_{,j} + H_{1j,j} q) dA \end{aligned} \tag{3.25}$$

Next, the relationship **m=-n** on the contour Γ is used. The expression (3.25) can now be rewritten to give the left hand side as the contour integral on Γ

$$\int_{\Gamma} H_{1j} q n_j dS = \int_{C_+ \cup C_-} H_{1j} q m_j dS + \int_{C_0} H_{1j} q m_j dS - \int_{A} (H_{1j} q_{,j} + H_{1j,j} q) dA \tag{3.26}$$

For the case q=1 on Γ, the relationship between Eq. (3.26) and Eq. (3.23) is:

$$\overbrace{\lim_{\Gamma\to 0}\int_{\Gamma} H_{1j}qn_j dS}^{\text{as }\Gamma\to 0} = \overbrace{\lim_{\Gamma\to 0}\int_{\Gamma} H_{1j}n_j dS}^{q=1 \text{ on } \Gamma} = \lim_{\Gamma\to 0}\int_{\Gamma} H_{1j}n_j dS = \mathcal{G}(\Gamma) \tag{3.27}$$

where q is defined as follows:

$$q = \begin{Bmatrix} 1.0 & \text{on } \Gamma \\ 0 & \text{on } C_0 \\ \text{arbitrary} & \text{elsewhere} \end{Bmatrix} \tag{3.28}$$

With this definition of q, the contour integral on C_0 in Eq. (3.26) will disappear. The resulting form of the dynamic energy release rate will then be

$$\mathcal{G} = \lim_{\Gamma\to 0}\int_{\Gamma} H_{1j}qn_j dS = \int_{C_+\cup C_-} H_{1j}qm_j dS - \int_{A}(H_{1j}q_{,j} + H_{1j,j}q)dA \tag{3.29}$$

where A is the area enclosed by the contour C_0, and Γ is shrinked to the crack tip. The expressions H_{1j} and $H_{1j,j}$ are given by:

$$H_{1j} = (W + L)\delta_{1j} - \sigma_{ij}u_{i,1} \tag{3.30}$$

and

$$\begin{aligned} H_{1j,j} &= (W_{,1} + L_{,1}) - \sigma_{ij,j}u_{i,1} - \sigma_{ij}u_{i,1j} \\ &= \sigma_{ij}\varepsilon_{ij,1} + \rho\dot{u}_i\dot{u}_{i,1} - \underbrace{\rho\ddot{u}_i u_{i,1}}_{\text{Since } \sigma_{ij,j}=\rho\ddot{u}_i} - \underbrace{\sigma_{ij}\varepsilon_{ij,1}}_{\text{Since } u_{i,1j}=\varepsilon_{ij,1}} = \rho\dot{u}_i\dot{u}_{i,1} - \rho\ddot{u}_i u_{i,1} \end{aligned} \tag{3.31}$$

If Eq. (3.30) and Eq. (3.31) are inserted into Eq. (3.29), the dynamic energy release rate takes the form:

$$\begin{aligned} \mathcal{G} = &\int_{C_+\cup C_-}\left((W + L)\delta_{1j} - \sigma_{ij}u_{i,1}\right)qm_j dS \\ &- \int_{A}\left((W + L)\delta_{1j} - \sigma_{ij}u_{i,1}\right)q_{,j}dA - \int_{A}(\rho\dot{u}_i\dot{u}_{i,1} - \rho\ddot{u}_i u_{i,1})qdA \end{aligned} \tag{3.32}$$

By assuming straight crack faces, the term (W+L) will vanish since $m_1=0$ on $C_+ \cup C_-$, and it is assumed that the crack faces are traction free such that $\sigma_{ij}=0$ on $C_+ \cup C_-$. Thus the contour integral disappears, and the dynamic energy release rate can finally be expressed as:

$$\mathcal{G} = -\int_A \left((W+L)\delta_{1j} - \sigma_{ij}u_{i,1}\right)q_{,j}dA - \int_A (\rho\dot{u}_i\dot{u}_{i,1} - \rho\ddot{u}_i u_{i,1})qdA \tag{3.33}$$

3.7 Mixed mode stress intensity factors

By inserting the stress component formulas for the asymptotic crack tip field (Appendix A) into the energy release rate given by Eq. (3.21), the energy release rate is expressed in terms of the stress intensity factors K_I and K_{II}. K_I is the stress intensity factor related to the in plane opening mode of the crack, and K_{II} is the stress intensity factor related to the in plane shearing mode of the crack. For the special case of plane stress condition in a two-dimensional domain, the energy release rate is given by (Freund 1998):

$$\mathcal{G} = \frac{1-\nu}{E}\left(A_I(v)K_I^2 + A_{II}(v)K_{II}^2\right) \tag{3.34}$$

The quantities A_I and A_{II} are defined by

$$A_I(v) = \frac{v^2\alpha_d}{(1-\nu)c_s^2 D}, \qquad A_{II}(v) = \frac{v^2\alpha_s}{(1-\nu)c_s^2 D} \tag{3.35}$$

where

$$\alpha_d = \sqrt{1-\frac{v^2}{c_d^2}}, \qquad \alpha_s = \sqrt{1-\frac{v^2}{c_s^2}} \tag{3.36}$$

and

$$D(v) = 4\alpha_d\alpha_s - (1+\alpha_s^2)^2 \tag{3.37}$$

Expression (3.34) is a generalization of the Irwin relationship, which relates the stress intensity factors and the energy release rate under equilibrium conditions in an elastic material.

In some cases it is convenient to have separate expressions for each of the stress intensity factors K_I and K_{II}. These relationships are developed by introduction of an auxiliary stress field with stress intensity factors K_{Iaux} and K_{IIaux}. For mode I, the resulting stress intensity factor is then $K_I = K_I + K_{Iaux}$ and for mode II $K_{II} = K_{II} + K_{IIaux}$. Inserting into Eq. (3.34) with K_{IIaux}=0 gives:

$$\begin{aligned} \mathcal{G}_{total}^{(1)} &= \frac{1-\nu}{E}\left(A_I(K_I + K_{Iaux})^2 + A_{II}K_{II}^2\right) \\ &= \frac{1-\nu}{E}\left(A_I K_I^2 + A_{II}K_{II}^2 + A_I K_{Iaux}^2 + 2A_I K_I K_{Iaux}\right) \\ &= \underbrace{\frac{1-\nu}{E}\left(A_I K_I^2 + A_{II}K_{II}^2\right)}_{\mathcal{G}} + \underbrace{\frac{1-\nu}{E}\left(A_I K_{Iaux}^2\right)}_{\mathcal{G}_{aux}} + \underbrace{\frac{1-\nu}{E}\left(2A_I K_I K_{Iaux}\right)}_{\mathcal{G}_{int}} \end{aligned} \tag{3.38}$$

The superindex (1) for the total dynamic energy release rate is associated with the auxiliary field of mode I. From Eq. (3.38) the relations between K_I and $\mathcal{G}_{int}^{(1)}$ can directly be identified as:

$$K_I = \left(\frac{E}{1-\nu^2}\right)\frac{\mathcal{G}_{int}^{(1)}}{2A_I} \tag{3.39}$$

when K_{Iaux} is chosen equal to 1.0.

The same approach will give the relationship between K_{II} and $\mathcal{G}_{int}^{(2)}$ by introducing K_{Iaux}=0 og K_{IIaux}=1 into Eq. (3.34) gives:

$$K_{II} = \left(\frac{E}{1-\nu^2}\right)\frac{\mathcal{G}_{int}^{(2)}}{2A_{II}} \tag{3.40}$$

The superscript (2) is related to the auxiliary field from mode II.

3.8 Energy release rate expressions for numerical calculations

To be able to calculate the stress intensity factors Eq. (3.39) and Eq. (3.40), expressions of $\mathcal{G}_{\text{int}}^{(1)}$ and $\mathcal{G}_{\text{int}}^{(2)}$ that are convenient for numerical calculations have to be derived. The derivations follow the same pattern that was described in Section 3.6. The quantities of the dynamic energy release expression, Eq. (3.21), are inserted with the auxiliary parts.

In the following, the super index notation $(\,)^{(1)}$ indicates that the auxiliary field is from mode I. The derivation starts with the mode I auxiliary field to obtain the interaction energy release rate expression. An auxiliary part is added to every term in Eq. (3.21). The stress work density, W, is inserted as:

$$W = \frac{1}{2}\sigma_{ij}\varepsilon_{ij} \tag{3.41}$$

in Eq. (3.21). Auxiliary parts are added to the stress and strain fields as:

$$\sigma_{ij}^{\text{total}} = \sigma_{ij} + \sigma_{ij}^{(1)} \tag{3.42}$$

$$\varepsilon_{ij}^{\text{total}} = \varepsilon_{ij} + \varepsilon_{ij}^{(1)} \tag{3.43}$$

With these expressions inserted into Eq. (3.41) the total stress work density is divided into W, the interaction part, W^{int}, and the auxiliary part, W^{aux}:

$$\begin{aligned} W^{\text{total}} &= \frac{1}{2}(\sigma_{ij} + \sigma_{ij}^{(1)})(\varepsilon_{ij} + \varepsilon_{ij}^{(1)}) \\ &= \frac{1}{2}(\sigma_{ij}\varepsilon_{ij} + \sigma_{ij}\varepsilon_{ij}^{(1)} + \sigma_{ij}^{(1)}\varepsilon_{ij} + \sigma_{ij}^{(1)}\varepsilon_{ij}^{(1)}) \\ &= \underbrace{\frac{1}{2}\sigma_{ij}\varepsilon_{ij}}_{W} + \underbrace{\frac{1}{2}(\sigma_{ij}\varepsilon_{ij}^{(1)} + \sigma_{ij}^{(1)}\varepsilon_{ij})}_{W^{\text{int}}} + \underbrace{\frac{1}{2}\sigma_{ij}^{(1)}\varepsilon_{ij}^{(1)}}_{W^{\text{aux}}} \end{aligned} \tag{3.44}$$

The next term of Eq. (3.21) is the kinetic energy density

$$L = \frac{1}{2}\rho \dot{u}_i \dot{u}_i \tag{3.45}$$

Adding an auxiliary part to $\dot{u}_i$, gives:

$$\dot{u}_i = (\dot{u}_i + \dot{u}_i^{(1)}) \tag{3.46}$$

With Eq. (3.46) inserted into Eq. (3.45), the total kinetic energy density is divided into L, an interaction part, L^{int}, and an auxiliary part L^{aux}

$$\begin{aligned} L^{total} &= \frac{1}{2}\rho(\dot{u}_i + \dot{u}_i^{(1)})(\dot{u}_i + \dot{u}_i^{(1)}) \\ &= \frac{1}{2}\rho(\dot{u}_i\dot{u}_i + \dot{u}_i^{(1)}\dot{u}_i + \dot{u}_i\dot{u}_i^{(1)} + \dot{u}_i^{(1)}\dot{u}_i^{(1)}) \\ &= \underbrace{\frac{1}{2}\rho\dot{u}_i\dot{u}_i}_{L} + \underbrace{\frac{1}{2}\rho(\dot{u}_i^{(1)}\dot{u}_i + \dot{u}_i\dot{u}_i^{(1)})}_{L^{int}} + \underbrace{\frac{1}{2}\rho\dot{u}_i^{(1)}\dot{u}_i^{(1)}}_{L^{aux}} \end{aligned} \tag{3.47}$$

Finally, auxiliary fields are added to the last term in Eq. (3.21), to get:

$$\begin{aligned} \left(\sigma_{ij}u_{i,l}\right)_{total} &= (\sigma_{ij} + \sigma_{ij}^{(1)})(u_{i,l} + u_{i,l}^{(1)}) \\ &= \underbrace{\sigma_{ij}u_{i,l}}_{\text{ordernary}} + \underbrace{\sigma_{ij}u_{i,l}^{(1)} + \sigma_{ij}^{(1)}u_{i,l}}_{\text{interaction}} + \underbrace{\sigma_{ij}^{(1)}u_{i,l}^{(1)}}_{\text{auxilary}} \end{aligned} \tag{3.48}$$

The expressions of Eq. (3.44), Eq. (3.47) and Eq. (3.48) are then inserted into Eq. (3.21).

The interaction part of the dynamic energy release rate integral is then obtained as:

$$\begin{aligned} \mathcal{G}_{int}^{(1)} &= \lim_{\Gamma\to 0}\int_{\Gamma}\left((W^{int} + L^{int})\delta_{1j} - (\sigma_{ij}u_{i,1}^{(1)} + \sigma_{ij}^{(1)}u_{i,1})\right)n_j dS \\ &= \lim_{\Gamma\to 0}\int_{\Gamma}\left((\sigma_{ij}\varepsilon_{ij}^{(1)} + \rho\dot{u}_i\dot{u}_i^{(1)})\delta_{1j} - (\sigma_{ij}u_{i,1}^{(1)} + \sigma_{ij}^{(1)}u_{i,1})\right)n_j dS \end{aligned} \tag{3.49}$$

Here δ_{ij} is the Cronecker delta function. Linear elastic material behaviour has been assumed in the preceding derivation.

For the mode II auxiliary field the interaction part of the dynamic energy release rate integral analogously becomes

$$\mathcal{G}_{int}^{(2)} = \lim_{\Gamma \to 0} \int_{\Gamma} \left((\sigma_{ij}\varepsilon_{ij}^{(2)} + \rho \dot{u}_i \dot{u}_i^{(2)})\delta_{1j} - (\sigma_{ij}u_{i,1}^{(2)} + \sigma_{ij}^{(2)}u_{i,1}) \right) n_j dS \tag{3.50}$$

Since the aim of this derivation is to obtain expressions for convenient numerical calculations Eq. (3.49) and Eq. (3.50) are transformed into sub-domain integrals. The same procedure as described in Section 3.5 is used for the following derivation, starting with the expression for $\mathcal{G}_{int}^{(1)}$ in Eq. (3.49). For the purpose of clarity define

$$f_j = (\sigma_{ij}\varepsilon_{ij}^{(1)} + \rho \dot{u}_i \dot{u}_i^{(1)})\delta_{1j} - (\sigma_{ij}u_{i,1}^{(1)} + \sigma_{ij}^{(1)}u_{i,1}) \tag{3.51}$$

Then consider the integration of the product of f_j the corresponding component, m_j, of an outward normal vector and an arbitrary function q over the contour ∂A shown in Figure 3.2:

$$\begin{aligned} \int_{\partial A} f_j q m_j dS &= \int_{\Gamma} f_j q m_j dS + \int_{C_+ \cup C_-} f_j q m_j dS + \int_{C_0} f_j q m_j dS \\ &= \int_A (f_j q_{,j} + f_{j,j} q) dA \end{aligned} \tag{3.52}$$

The divergence theorem has been used to transform the contour integral into a domain integral. Then introduce q=0 on C_0, **m=-n** (Figure 3.2) and q=1 on Γ. In the limit as $\Gamma \to 0$ Eq. (3.52) can be rewritten as:

$$\lim_{\Gamma \to 0} \int_{\Gamma} f_j n_j dS = \mathcal{G}_{int}^{(1)} = \int_{C_+ \cup C_-} f_j q m_j dS - \int_A (f_j q_{,j} + f_{j,j} q) dA \tag{3.53}$$

With the expression for f_j from Eq. (3.51), f_j and $f_{j,j}$ are inserted into Eq. (3.53) to give:

$$\begin{aligned}
\mathcal{G}_{int}^{(I)} = & \int_{C_+ \cup C_-} \left(\underbrace{(\sigma_{ij}\varepsilon_{ij}^{(I)} + \rho\dot{u}_i\dot{u}_i^{(I)})\delta_{1j}}_{=0 \Rightarrow m_I=0 \text{ på } C_+ \cup C_-} - \underbrace{(\sigma_{ij}^{(I)}u_{i,1} + \sigma_{ij}u_{i,1}^{(I)})}_{=0 \text{ no traction on } C_+ \cup C_-} \right) qm_j dS \\
& - \int_A \left((\sigma_{ij}\varepsilon_{ij}^{(I)} + \rho\dot{u}_i\dot{u}_i^{(I)})\delta_{1j} - (\sigma_{ij}^{(I)}u_{i,1} + \sigma_{ij}u_{i,1}^{(I)}) \right) q_{,j} dA \\
& - \int_A (\sigma_{ij,j}\varepsilon_{ij}^{(I)} + \sigma_{ij}\varepsilon_{ij,1}^{(I)} + \rho\dot{u}_{i,j}\dot{u}_i^{(I)} + \rho\dot{u}_i\dot{u}_i^{(I)})\delta_{1j} q dA \\
& + \int_A (\sigma_{ij,j}^{(I)}u_{i,1} + \sigma_{ij}^{(I)}u_{i,1j} + \sigma_{ij,j}u_{i,1}^{(I)} + \sigma_{ij}u_{i,1j}^{(I)}) q dA
\end{aligned} \tag{3.54}$$

The expression (3.54) is simplified by introducing the momentum equation, the condition $m_I=0$ on the crack faces, and the assumption of no traction forces on the crack faces. Accordingly Eq. (3.54) can be rewritten as:

$$\begin{aligned}
\mathcal{G}_{int}^{(I)} = & - \int_A \left((\sigma_{ij}\varepsilon_{ij}^{(I)} + \rho\dot{u}_i\dot{u}_i^{(I)})\delta_{1j} - (\sigma_{ij}^{(I)}u_{i,1} + \sigma_{ij}u_{i,1}^{(I)}) \right) q_{,j} dA \\
& - \int_A (\sigma_{ij,1}\varepsilon_{ij}^{(I)} + \sigma_{ij}\varepsilon_{ij,1}^{(I)} + \rho\dot{u}_{i,1}\dot{u}_i^{(I)} + \rho\dot{u}_i\dot{u}_i^{(I)}) q dA \\
& + \int_A (\rho\ddot{u}_i^{(I)}u_{i,1} + \sigma_{ij}^{(I)}\varepsilon_{ij,1} + \rho\ddot{u}_i u_{i,1}^{(I)} + \sigma_{ij}\varepsilon_{ij,1}^{(I)}) q dA
\end{aligned} \tag{3.55}$$

Since linear elastic material properties are assumed, further simplification can be obtained from the following relationships $\sigma_{ij}^{(I)}\varepsilon_{ij,1} = C_{ijkl}\varepsilon_{kl}^{(I)}\varepsilon_{ij,1} = (C_{klij}\varepsilon_{ij})_{,1}\varepsilon_{kl}^{(I)} = \sigma_{kl,1}\varepsilon_{kl}^{(I)}$. The resulting domain integral of the interaction energy release rate, $\mathcal{G}_{int}^{(I)}$, associated with the mode I auxiliary field is then

$$\begin{aligned}
\mathcal{G}_{int}^{(I)} = & \int_A \left(-(\sigma_{ij}\varepsilon_{ij}^{(I)} + \rho\dot{u}_i\dot{u}_i^{(I)})q_{,1} + (\sigma_{ij}^{(I)}u_{i,1} + \sigma_{ij}u_{i,1}^{(I)})q_{,j} \right) dA \\
& + \int_A \left(\ddot{u}_i^{(I)}u_{i,1} + \ddot{u}_i u_{i,1}^{(I)} - \dot{u}_{i,1}\dot{u}_i^{(I)} - \dot{u}_i\dot{u}_{i,1}^{(I)} \right) \rho q dA
\end{aligned} \tag{3.56}$$

A similar derivation gives the interaction energy release rate, $\mathcal{G}_{int}^{(2)}$, associated with the mode II auxiliary field:

$$\begin{aligned}\mathcal{G}_{int}^{(2)} = &\int_A \left(-(\sigma_{ij}\varepsilon_{ij}^{(1)} + \rho\dot{u}_i\dot{u}_i^{(2)})q_{,1} + (\sigma_{ij}^{(2)}u_{i,1} + \sigma_{ij}u_{i,1}^{(2)})q_{,j}\right)dA \\ &+ \int_A \left(\ddot{u}_i^{(2)}u_{i,1} + \ddot{u}_i u_{i,1}^{(2)} - \dot{u}_{i,1}\dot{u}_i^{(2)} - \dot{u}_i\dot{u}_{i,1}^{(2)}\right)\rho q dA\end{aligned} \tag{3.57}$$

The stress intensity factors K_I and K_{II}, can now readily be calculated from Eq. (3.39) and (3.40).

3.9 Numerical implementation of the linear elastic dynamic fracture criterion

3.9.1 The maximum circumferential stress criterion

To decide if a crack would propagate, and in what direction, the maximum circumferential stress criterion is adopted. It states that the growth direction, θ_c, from the crack tip is in the direction of the maximum circumferential stress, $\sigma_{\theta\theta}$. Under general mixed mode loading, the near-tip circumferential stress and shear stress is given as

$$\begin{Bmatrix}\sigma_{\theta\theta}\\ \sigma_{r\theta}\end{Bmatrix} = \frac{K_I}{4\sqrt{2\pi r}}\begin{Bmatrix}3\cos(\theta/2)+\cos(3\theta/2)\\ \sin(\theta/2)+\sin(3\theta/2)\end{Bmatrix} + \frac{K_{II}}{4\sqrt{2\pi r}}\begin{Bmatrix}-3\sin(\theta/2)-3\sin(3\theta/2)\\ \cos(\theta/2)+3\cos(3\theta/2)\end{Bmatrix} \tag{3.58}$$

Here r is the radial distance from the crack tip to the evaluation point and θ is the angle between the x_1-axis and the line from the crack tip to the evaluation point (see Figure 3.3). K_I and K_{II} are the stress intensity factors for crack modes I and II respectively. The circumferential stress in the direction of the crack propagation is a principal stress.

As the shear stress is then equal to zero, it follows that the growth direction will be

$$\theta_c = 2\arctan\frac{1}{4}(K_I / K_{II} \pm \sqrt{(K_I / K_{II})^2 + 8}) \tag{3.59}$$

When the maximum hoop stress, $\sigma_{\theta\theta max}$, normal to the critical growth direction, θ_c, exceeds the critical stress for the material, σ_c, it is stated that the crack begins to propagate. The critical stress, σ_c, can be obtained from pure mode I experiments on the material under considerations. With $K_I=K_{Ic}$, $K_{II}=0$ and $\theta=0$ inserted in Eq. (3.58) the relationship between material strength and the mode I stress intensity factor results in

$$\sigma_c = \frac{K_{Ic}}{\sqrt{2\pi r}} \tag{3.60}$$

As stated above the crack starts propagating when:

$$\sigma_{\theta\theta max} \geq \sigma_c \tag{3.61}$$

Now inserting for $\sigma_{\theta\theta max} = \sigma_{\theta\theta}(\theta_c)$ and σ_c from Eq. (3.60) into Eq. (3.61) the propagation condition becomes

$$\begin{aligned} \sigma_{\theta\theta max} &= \frac{K_I}{4\sqrt{2\pi r}}(3\cos(\theta_c/2) + \cos(3\theta_c/2)) - \frac{3K_{II}}{4\sqrt{2\pi r}}(\sin(\theta/2) + \sin(3\theta_c/2)) \\ &\geq \sigma_c = \frac{K_{Ic}}{\sqrt{2\pi r}} \end{aligned} \tag{3.62}$$

This criterion is independent of the behaviour in the radial direction. The propagation thus starts when

$$\frac{K_I}{4}(3\cos(\theta_c/2) + \cos(3\theta_c/2)) - \frac{3K_{II}}{4}(\sin(\theta_c/2) + \sin(3\theta_c/2)) \geq K_{Ic} \tag{3.63}$$

3.9.2 Numerical integration of the integrals giving the energy release rate

The development of the interaction integrals has assumed straight crack segments inside the domain of integration. Only one crack segment can thus be inside the integration domain. It is further supposed that the local x_1-coordinate is aligned with the crack faces (see Figure 3.3), forcing the integration domain to rotate with the crack faces as the crack advances.

The integration domain is chosen to be rectangular, with the side lengths 2d (see Figure 3.3). The magnitude of d is prescribed and kept constant during the numerical simulation of the crack propagation. The crack tip coincides with the center of the integration domain for crack segments $a_i \geq d$. For crack segments with $a_i < d$ the crack tip is shifted so that 95% of the crack segment is inside the integration domain (see Figure 3.4). In order to obtain accurate values for the interaction integrals, the integration domain should include an area big enough to enclose the near tip dominated field and the crack tip centered as close to the center of the integration domain as possible. This gives restrictions on the size of a_i. Experience indicates that $a_i > d/2$ gives reliable results (see Organ (1996)).

Choice of location for the integration points in the numerical integration procedure is important with respect to obtainable accuracy. If the same integration points as used for calculation of the stiffness matrix are applied to perform the numerical integration of the interaction integrals, the results are reliable and the integration procedure is robust and gives accurate results when compared to reference or theoretical solutions. Inaccuracies are likely to occur if the integration points are chosen independently in the integration domain. One explanation of this deviation from the correct solution can be related to the discussion on the misalignment in the domain of the numerical integration cells with the domain of influence of the shape functions (see Section 2.3.3).

Figure 3.5 illustrates an advancing crack. During one time increment Δt the crack propagates a line segment Δtv. This is repeated until the line segment is larger than the minimum suggested size d/2 or larger than a prescribed limit. Then the maximum hoop stress criterion (see Section 3.7.1) is used to control the further advancement of the propagating crack. A new crack segment starts, and if the maximum

hoop stress criterion predicts further propagation of the crack, it will move the incremental distance Δtv in the calculated direction and with the crack propagation speed, v.

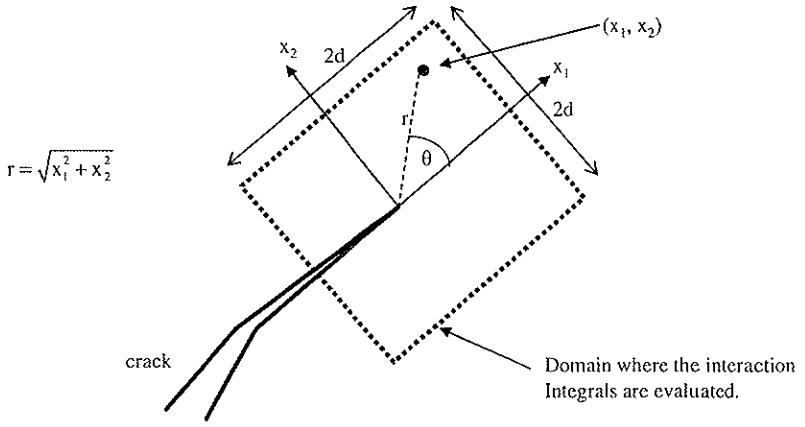

Figure 3.3: Integration domain for numerical integration of the interaction integrals.

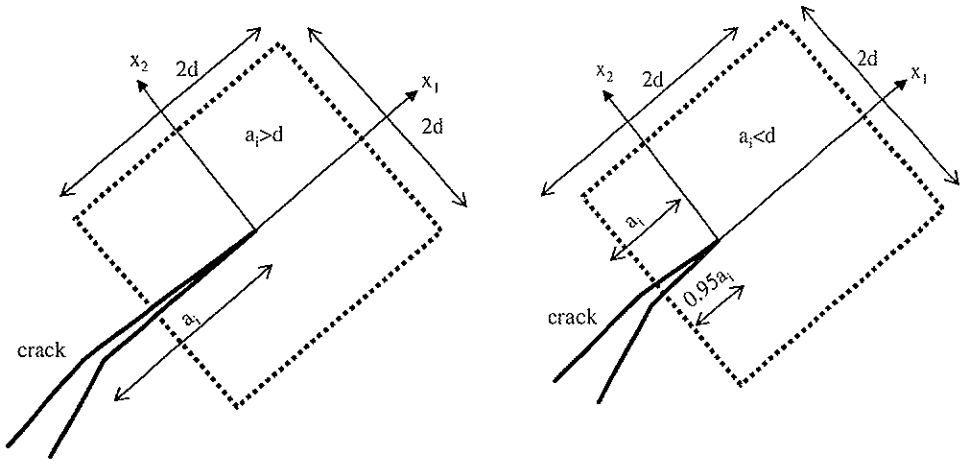

Figure 3.4: Placement of the crack tip based on the length of the crack segment with respect to the domain variable d.

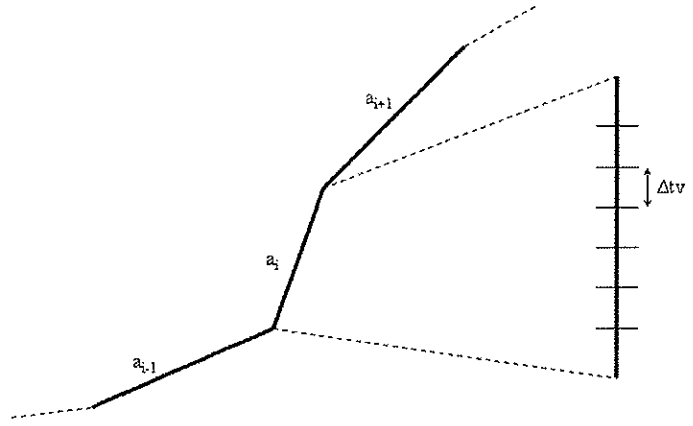

Figure 3.5: The crack is modeled as a series of line segments. During each time increment the crack is moving a distance Δtv.

3.9.3 Arbitrary crack propagating velocity

When a variable propagation velocity is used in a numerical simulation, the crack segments a_i (see Figure 3.4) could be larger or smaller than for a constant crack propagation velocity. For the development of the crack the same criterion and rules as for the constant crack propagation velocity is adopted, except that the requirement $a_i>d/2$ is relaxed.

When the crack criterion is satisfied, the crack propagation velocity is calculated by scaling the Rayleigh surface wave speed, C_R, by the coefficient of the difference between the maximum hoop stress, $\sigma_{\theta\theta max}$, and the critical stress for the material, σ_c divided by the critical stress σ_c

$$v = \frac{\sigma_{\theta\theta max} - \sigma_c}{\sigma_c} C_R \tag{3.64}$$

The Rayleigh surface wave speed is the highest theoretical velocity of a propagating crack.

Inserting the hoop stress from Eq. (3.58) and the critical stress from Eq. (3.60) into Eq. (3.64), gives and expression for the variable crack propagation velocity as

$$v = \frac{\left(\frac{K_I}{4}(3\cos(\theta_c/2)+\cos(3\theta_c/2)) - \frac{3K_{II}}{4}(\sin(\theta_c/2)+\sin(3\theta_c/2))\right) - K_{Ic}}{K_{Ic}} C_R \qquad (3.65)$$

In the present study K_{Ic} is supposed to be constant with respect to the crack propagation velocity.

Chapter 4 Brief description of the MATLAB code and its capabilities

4.1 Introduction

As described in the introduction to this thesis, available codes based on the finite element method were not suited to solve the general crack propagation simulations. Neither were codes based on meshless methods available. Consequently one major part of this thesis work, had to deal with development of a prototype program for dynamic fracture mechanics analyses. The prototype computer program can simulate 2D general crack propagation in a linearly elastic material. The code is based on MATLAB. This choice is made to simplify the coding part, and as computational efficiency is not a primary goal. The main structure and the main routines can easily be converted to other languages if that will be of interest in other contexts.

Section 4.2 discusses the main capabilities of the MATLAB program for solving 2D crack propagation problems. Section 4.3 outlines the code structure with references to Appendix B where the main subroutines are listed in more detail.

Reference is made to Dolbow and Belytshko (1998) who presented a very simple linearly elastic static 2D calculation procedure by the EFG method.

4.2 Description of the MATLAB code capabilities

4.2.1 Geometry modeling and mesh specification

The prototype code can handle rectangular two dimensional (2D) models. An expansion to more general model geometries is simple, but this is not given priority in this thesis work in order to limit the program development work. The outer boundary on the numerical model is limited by the height D (y direction), the length Lb (x direction) and the thickness t_h of the plate (see Figure 4.1).

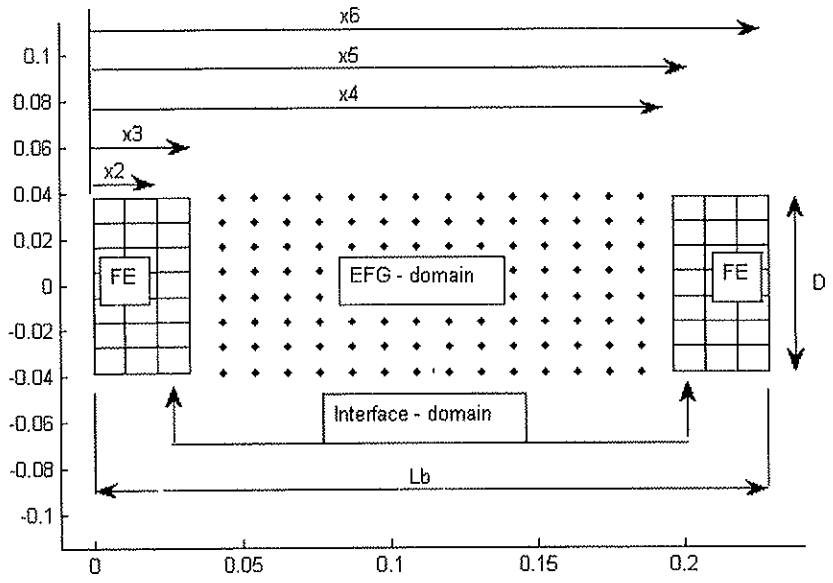

Figure 4.1: Illustration of the model geometry, and the variables related to it. The black rectangular "boxes" are the FE domain, the red rectangular "boxes" are the interface domain and the black dots represent the EFG domain.

The whole model domain can be divided into three subdomains: the FE-domain, where the material behaviour is described by the Finite Element method; the EFG-domain, where the material behaviour is described by the Element Free Galerkin method and the

interface-domain, where the material behaviour is described by a linear combination of the FE method and the EFG method (see Section 2.5). The different domains are bounded as illustrated in Figure 4.1. The domain boundaries are identified by the variables x_1 to x_6. To illustrate the possibilities with this description, some examples are listed: to describe the whole model by the EFG method, set x_3=0 and x_4=Lb (Figure 4.2 A); to describe the whole model by the FE method, set x_2=Lb (Figure 4.2 B); All combinations between the two previously described alternatives are possible. Figure 4.2 C shows a model where the left part is described by the FE method and the right part is described by the EFG method. Similarly Figure 4.2 D shows a model where the FE and EFG are exchanged compared with Figure 4.2 C.

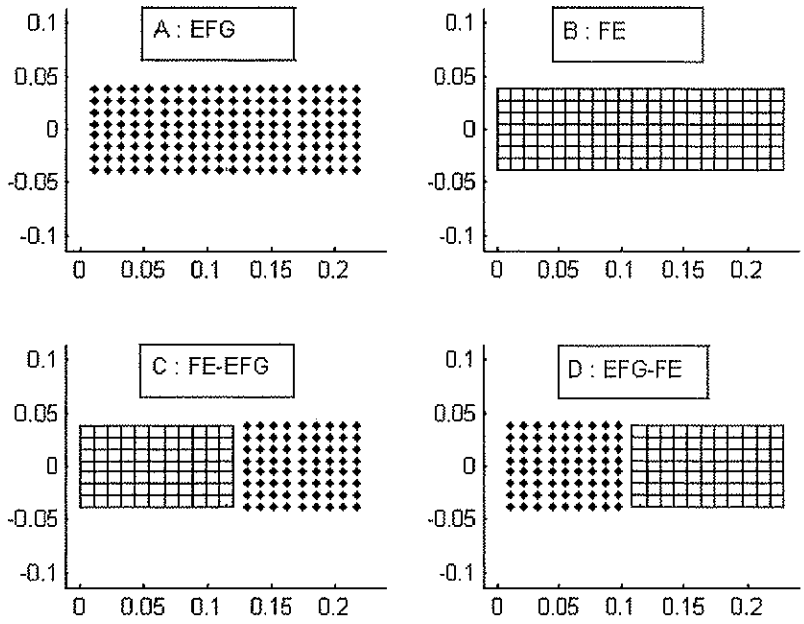

Figure 4.2: Illustration of four different methods describing the material behaviour of the same model geometry, A: the whole model described by the EFG method. B: the whole model described by the FE method. C: the left part of the model described by the FE method and the right part of the model described by the EFG method. D: the same as C but with a reversed order of the FE and EFG domains.

The mesh density is given globally by xdiv and ydiv, which is the number of intervals between nodes in x- and y- direction respectively. This results in a regular mesh. The material behaviour is linearly elastic with the material constants: Young's modules, Poisson's ratio and mass density. Plain stress or plain strain can be chosen as the 2D model simplification. In the EFG domain the size of the domain of influence is given by dmax (see Section 2.2.1).

4.2.2 Loading and prescribed motion

There are several alternatives for load application and prescribed motion: distributed load along a predefined line; this type of load can be inserted into any domain of the model. Two example cases of uniformly distributed load are shown in Figure 4.4, where the numerical model consists of a FE mesh and an EFG mesh. The uniformly distributed load (step traction with intensity 1.0 in Figure 4.3) is inserted on the line between points (Lb,-D/4) to (Lb,D/4). Figure 4.4 shows the undeformed mesh and the deformed mesh (scaled deformations) of this numerical model. Concentrated loads can be applied to any point in the FE domain. The intensity of the distributed loads and the concentrated loads can be modeled as a mathematical function with respect to the variables t (time), x and y (material coordinates).

Prescribed displacements, velocities and accelerations can be inserted along predefined lines, or directly on predefined degrees of freedom in the FE domain and on the interface boundary along the FE domain. An example where a uniform velocity field (step velocity with intensity 1.0 in Figure 4.5) is inserted on the FE elements along the line with endpoints (Lb/2-Lb/10, D/2) and (Lb/2+Lb/10, D/2) is shown in Figure 4.6. The undeformed and deformed (scaled deformations) meshes are plotted in the upper part of the figure. Since in general the EFG method do not satisfy the Dirac delta criterion (see Section 2.2.2), this type of specified motion is not an option for the EFG domain or the interface boundary nodes along the EFG domain. Nevertheless, if it is required to apply this type of specified motion along a row on the EFG domain boundary, the code can handle this by introducing a row with interface elements on the actual boundary. The same example as described previously, but with part of the FE

domain replaced with an EFG domain and the prescribed velocities on a row of interface elements is also shown in Figure 4.6. The intensity of this type of loading can be described mathematically as in the case of distributed loads or concentrated loads.

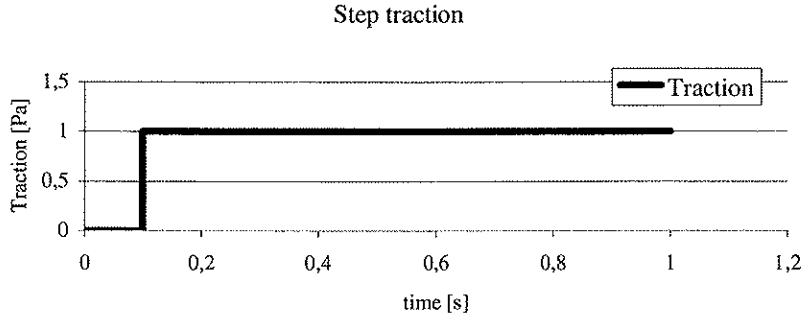

Figure 4.3: Plot of the step traction applied to the model plotted in Figure 4.4.

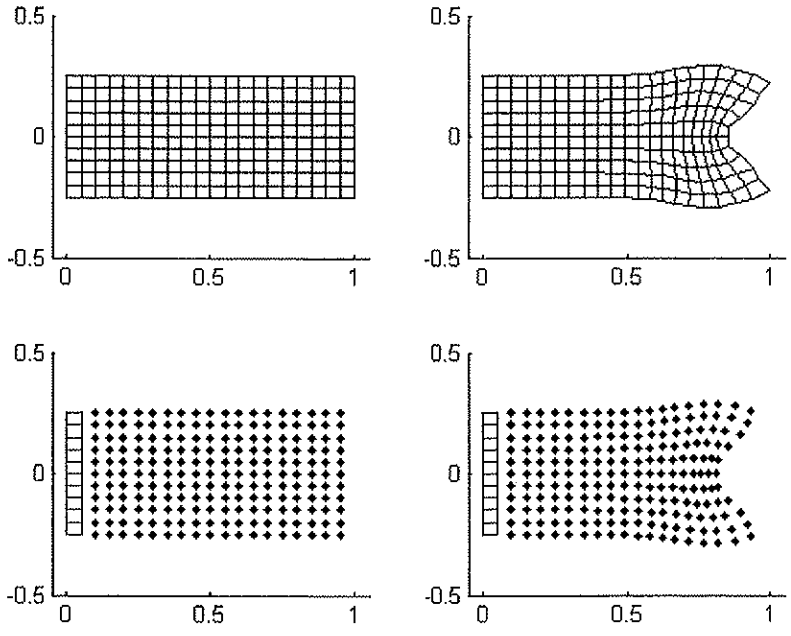

Figure 4.4: Illustration of uniformly distributed load on FE boundary and EFG boundary. The left hand figures show undeformed meshes and the right hand figures the corresponding deformed meshes.

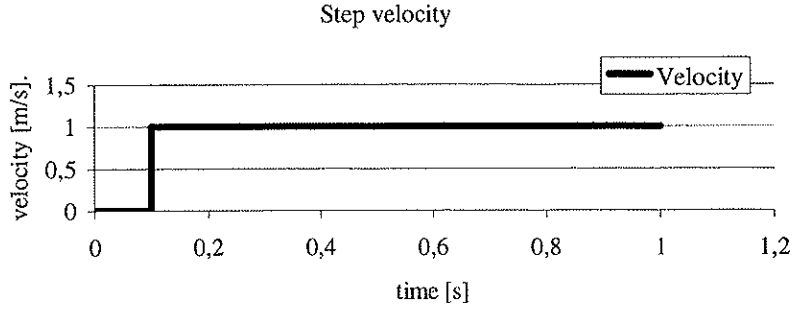

Figure 4.5: Plot of the step velocity applied to the model plotted in Figure 4.6.

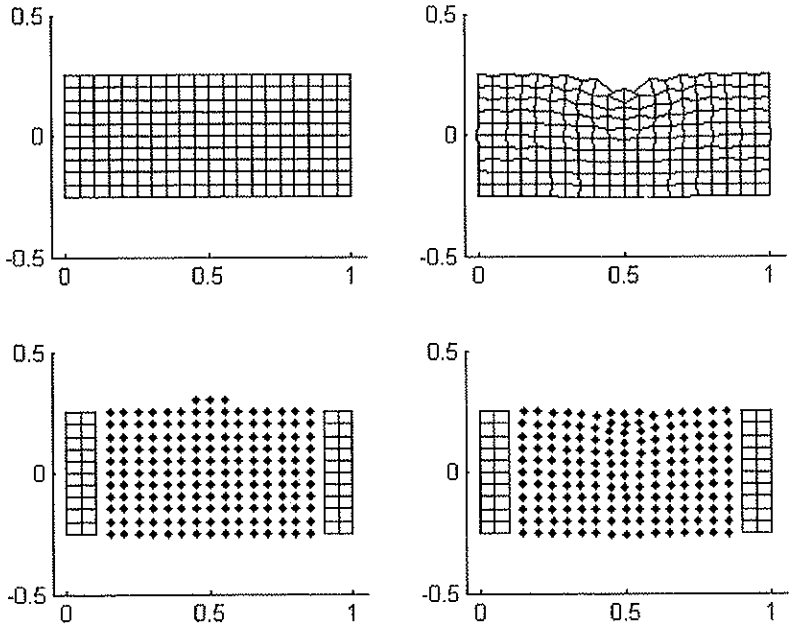

Figure 4.6: Illustration of applied velocities on a FE boundary and EFG (interface) boundary. The left hand figures show undeformed meshes and the right hand figures the corresponding deformed meshes.

4.2.3 The possibilities to include cavities in the numerical model

Inside the EFG domain of the numerical model, it is possible to insert a rectangular or circular cavity. The different cavities can be modelled as follows: each cavity domain can overlap each other or be separate; the basic shapes are limited to rectangular or circular; it is possible with an EFG boundary through the cavities.

The rectangular cavity is identified by the coordinates at the lower left corner and the upper right corner. The circular cavity is identified by the coordinates of the circle center and the radius of the circle. The code also allow crack propagation into the boundary of the cavities and cracks can start from the cavity boundary.

Figure 4.7 illustrates four different cavities with respective shapes of a rectangle, a circle, a typical tunnel cross section and symmetric case of a tunnel cross section. The tunnel cavity form combines the rectangle and the circle.

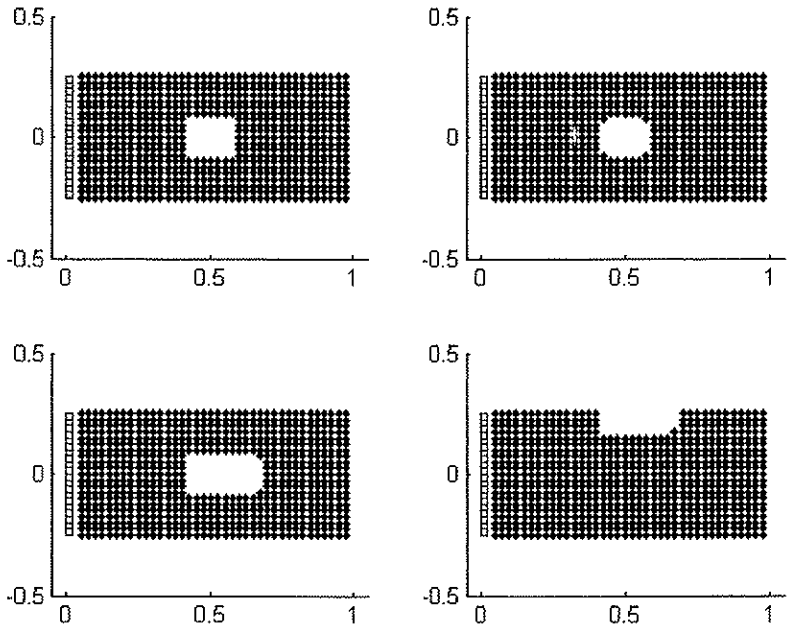

Figure 4.7: Illustration of four different cavity shapes.

4.2.4 Time integration of the equations of motion

The integration in time is performed with the explicit algorithm (β_2=0, and diagonal mass matrix), as a algorithm belonging to the Newmark families formula on displacements and velocities (see Section 2.4)

$$\mathbf{u}_{n+1} = \mathbf{u}_n + \Delta t\dot{\mathbf{u}}_n + \frac{\Delta t^2}{2}(1-\beta_2)\ddot{\mathbf{u}}_n + \frac{\Delta t^2}{2}\beta_2\ddot{\mathbf{u}}_{n+1}$$

and

$$\dot{\mathbf{u}}_{n+1} = \dot{\mathbf{u}}_n + \Delta t(1-\beta_1)\ddot{\mathbf{u}}_n + \Delta t\beta_1\ddot{\mathbf{u}}_{n+1}$$

The parameters β_1 and β_2 can in general be defined by the user. The standard explicit time integration scheme, the central difference method results with β_2=0. The time increment Δt can be specified in the input file as a factor multiplied with the critical time increment Δt_{crit}, which is given from the Courant condition (see Section 2.4):

$$\Delta t = f_{inp}\Delta t_{crit} \tag{3.1}$$

where f_{inp} is given in the input file. In order to obtain convergent solutions the validity domain is limited to $f_{inp} \in [0,1]$.

4.2.5 Description of fracture mechanics input parameters, and the cracking possibilities in the program.

When a numerical simulation of mixed mode fracture is to be performed, a predefined crack region where the crack can propagate must be defined. The crack can propagate from both ends of the predefined (piece vise) line. The predefined line (initial crack) can consist a single line, or multiple lines to define the crack. The crack can develop arbitrarily inside the predefined region within the EFG domain in the numerical model.

In a crack propagation simulation it is necessary to calculate the stress intensity factors, which define the evolution of the crack (see Section 3.9.1). The stress intensity factors are calculated on the basis of results from the numerical model in the vicinity of the crack tip (see Section 3.8). The code includes an enhanced basis in the crack tip area to improve the accuracy of the calculation of the stress intensity factors.

In the following, all the input parameters that are controlling the crack propagation in a simulation are listed and explained:

- $\text{xcrack} = \begin{bmatrix} x_1 & x_2 \\ y_1 & y_2 \end{bmatrix}$ is defining the model region where the crack can propagate arbitrarily. Point 1 is the lower left corner and point 2 is the upper right corner defining a rectangular subdomain inside the EFG domain in the numerical model, (see Figure 4.8). The stiffness contribution from this domain is updated during the analysis. Thus the stiffness modification due to a propagating crack is taken into account. It should be noticed that the size of this sub-domain is a considerable source of computer time requirement during a crack propagation simulation.
- $\text{Lc} := \begin{bmatrix} x_1 & y_1 \\ \vdots & \vdots \\ x_n & y_n \end{bmatrix}$ is a matrix describing the coordinates of the main points in a predefined crack. Straight lines are assumed between successive points. Lc must consist of two or more points (see Figure 4.8).
- K_{Ic} is obtained from pure mode I experiments on the material under consideration.
- v_c is the assumed crack propagating velocity, which is used for crack propagating simulations with constant crack velocity.
- Ln defines the number of time increments between checking of the crack propagating criterion (the maximum circumferential stress criterion (see Section 3.9.1).
- d defines the size of the domain integral in the crack tip area, for calculation of the stress intensity factors (see Section 3.9.2).

- nc is the number of time increments between updating of the stiffness matrix to include the effect of the crack growth. nc is normally less than Ln (never larger). Since checking of the maximum circumferential stress criterion requires considerable computer time, it is calculated as seldom as possible. If nc is to large, however, numerical pulses will result when the crack advances too far during a time step.
- Cvar(14) defines if an enriched basis (see Section 2.7) should be used in the vicinity of the crack tip. If so, the domain where the enriched basis is to be used must be defined. This domain is circular, and it is defined with the radius r_2 (outer radius). The inner radius is by default set to $r_1=r_2/2$.

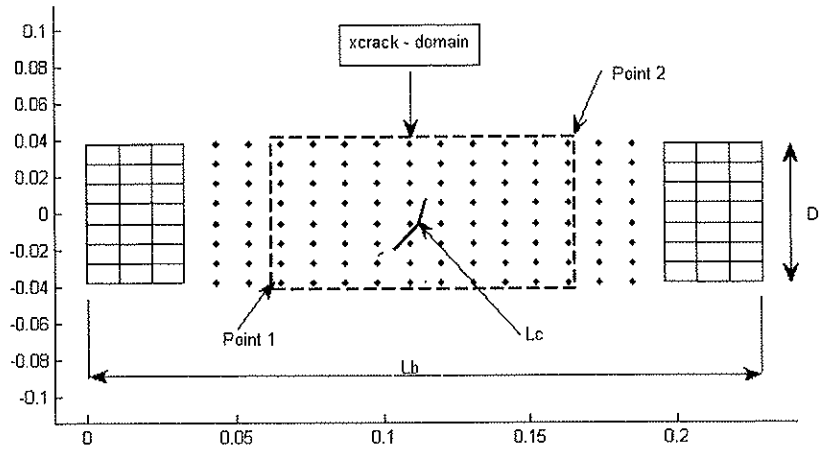

Figure 4.8: An example of a numerical model with illustration of the xcrack - domain (defined by the corner points 1 and 2) and the predefined crack path Lc.

4.2.6 Output of computed results

The code includes several possibilities of presenting results from the numerical calculations. The main output capabilities of the code are listed below as follows:

1. Location for desired time plots of displacement, velocities, accelerations, reaction forces and stresses are defined by coordinates. The number of points is arbitrary. The user may also define the total number of time logging points of the variables described above. By default the logging points are uniformly distributed over the total analysis time range.

2. Displacements and stresses can be plotted at every point in the numerical model, for a number of predefined time increments, as a surface above the mesh. The value of the variable defines the height of the surface above the plane of the mesh.

3. In crack propagation simulations, the stress intensity factors and the critical propagation angle can be plotted similarly as for the items above. The total crack path is plotted on the undeformed mesh.

4. Undeformed and deformed meshes of the numerical model can be plotted. The number of plots is predefined and at equal time intervals as default.

4.3 Brief description of the structure of the MATLAB code

An overview of the structure of the code, and a brief description of some of the main subroutines are listed in this section. The main subroutines are described in more detail in Appendix B. The main structure of the code is listed in the same sequence as the calculations are carried out

1. Reading the input file.
2. Initiating all variables of the actual analysis.
3. Generating the matrix with coordinates for each node and the matrix with information of each Gauss integration cell, respectively as:

$$\mathbf{x} = \begin{bmatrix} x_1 & \cdots & x_n \\ y_1 & \cdots & y_n \end{bmatrix}, \quad \mathbf{G}_s = \begin{bmatrix} x_{g1} & \cdots & x_{gn} \\ y_{g1} & \cdots & y_{gn} \\ w_{g1} & \cdots & w_{gn} \\ J_{g1} & \cdots & J_{gn} \\ C_1 & \cdots & C_{ngc} \end{bmatrix},$$

   Here n is the number of nodes in the first matrix, and the number of Gauss points in the second matrix. C_i refers to the Gauss cell number i. The weighting of a Gauss point is denoted w and J is the Jacobean at the same point.
4. Constructing the load vector, **f**, in the routine BC.m. If the load is time dependent, this dependency is ensured in the time integration scheme. The localization of the nodes on the predefined displacement boundaries is performed in routines BC.m and Bload.m.
5. Creating the stiffness matrix, **K**, on the basis of the Gauss points that contribute to the part of the model with no crack propagation (outside the xcrack domain, see Figure 4.8). If the numerical model includes a xcrack domain, a matrix, **Cxg**, with the information of the Gauss points inside the region xcrack is initiated

$$\mathbf{Cxg} = \begin{bmatrix} x_{g1} & \cdots & x_{gn} \\ y_{g1} & \cdots & y_{gn} \\ w_{g1} & \cdots & w_{gn} \\ J_{g1} & \cdots & J_{gn} \end{bmatrix},$$ where n is the total number of Gauss points inside the xcrack domain. **K** and **Cxg** is created in the routine Kmat.m (see Appendix B).
6. The consistent mass matrix, **M**, is established in the routine Mmat.m.
7. If the numerical model consists of one or more cavities, the degree of freedom inside the cavities (respective roads and columns in matrixes **K** and **M**) will be removed. This operation is done in the routine RemoveDOFs.m.
8. The time stepping is the main part of the code, it starts at time increment 1 and steps until the total time is reached. A brief description of the time stepping process is listed below, (together with the main routines that is called during the time stepping).

for n = 1 **to** *the number of time increments:* $\dfrac{\text{T(total time)}}{\Delta t}$

$t = n\Delta t$, *(the analysis time)*

if (*crack analysis = ok*) **&** (n = 1 or tc = 1)

kEFGc=CGKmat(...), *the routine CGKmat returns the stiffness matrix related to the xcrack domain. In Appendix B the routine is described in more detail.*

Ktot = K + kEFGc, *where Ktot is the total stiffness matrix of the whole numerical model, and K is the precalculated stiffness matrix of the model except for the xcrack domain.*

tc = -1, *tc is a variable that tells (this part) if the crack has advanced, and the stiffness matrix needs to be updated.*

end if

$\mathbf{F}(t) = g(t)\mathbf{f}$, *g(t) is the specified time variation of the load (***f** *is predefined in BC.m)*

The time stepping equations:

$$\mathbf{u}_{n+1} = \mathbf{u}_n + \Delta t\dot{\mathbf{u}}_n + \frac{\Delta t^2}{2}(1-\beta_2)\ddot{\mathbf{u}}_n + \frac{\Delta t^2}{2}\beta_2\ddot{\mathbf{u}}_{n+1}$$

$$\ddot{\mathbf{u}}_{n+1} = \mathbf{M}^{-1}(\mathbf{f} - \mathbf{K}_{tot}\mathbf{u}_{n+1})$$

$$\dot{\mathbf{u}}_{n+1} = \dot{\mathbf{u}}_n + \Delta t(1-\beta_1)\ddot{\mathbf{u}}_n + \Delta t\beta_1\ddot{\mathbf{u}}_{n+1}$$

nc = nc + 1

if nc ≥ Ln **&** (*crack analysis = ok*)

[Lc,tc,...] = CG(.....) , *CG.m returns results of the crack propagation criterion. If tc=1, the crack will propagate according to the criterion. Lc is updated with the new crack path. In Appendix B the routine is described in more detail.*

nc = 0

end if

Saving the predefined output variables.

end for

Chapter 5 Verification examples

5.1 Introduction

This chapter reports results from numerical simulations. The simulations are compared with results from the literature and results from the FE computations using (ABAQUS Version 6.5). The examples will constitute a major part of the verification of the computer code developed during this study.

In Section 5.2 the influence on the results and the use of computer time by varying different EFG parameters are investigated by numerical calculation of a 3-point bending of a concrete beam. For simplicity the same concrete beam that is investigated and reported in Section 5.3 is adopted also for this parametric study. An advantage of this choice is that a thorough investigation and optimization of the input parameters for the analyses of the 3-point bending of the concrete beam make the comparison with the result obtained by Organ (1996) more reliable.

Section 5.3 reports the results from numerical simulations of the pendulum experiment by John, R. and S. P. Shah (1990) on concrete beams. The numerical example employs a coupling procedure between the EFG and the FE domains (see Section 2.5) and the mixed mode fracture mechanics procedures (see Chapter 3). This makes the example suited as a verification of the main section of the computer code. The numerical results are directly comparable with the numerical results reported by Organ (1996), who uses the same theory to solve a pendulum experiment.

Section 5.4 covers numerical simulations of the experiment performed by Kalthoff and Winkler (1987). This experiment consisted of a free plate of high strength steel, with two initial edge cracks and loading from a projectile that crashes into the plate.

5.2 Optimization of the EFG parameters in analyses of 3-point bending of a concrete beam

5.2.1 Introduction

In this section the influence on the results and requirement of computer time by varying different EFG parameters are investigated by numerical calculation of a 3-point bending of a concrete beam. The concrete beam, material parameters, boundary conditions and load are equal to what will be studied in Section 5.3, except that unsymmetrical cracks will then be studied. A numerical model allowing only a centrically propagating crack is chosen to reduce the analyses computer time compared with the model consisting of a centric and an excentric crack. The computer time decrease is related to the reduction of the domain allowing general crack propagation, which in this case is only a narrow column enveloping the expected centric crack path. This is because the number of Gauss points for checking if a crack influencing the capability is reduced to a few points in a small domain.

The EFG parameters to be varied is the J integral size (d), the size of the time increment (Δt), the influence domain, d_{max}, the extended basis in the vicinity of the crack tip versus linear basis in the same domain, the number of Gauss integration cells and linear contra quadratic coupling of the EFG and FE displacements in the transition (interface) domain.

5.2.2 Description of the numerical model

In this section the numerical model is described. The geometry of the beam is shown in Figure 5.1. The length of the beam is 9 inches; the height of the beam is 3 inches and the thickness is 1 inch. The distance between the vertical supports (y-direction) on each side of the beam is 8 inches. The motion of the beam is not constrained in the x-direction.

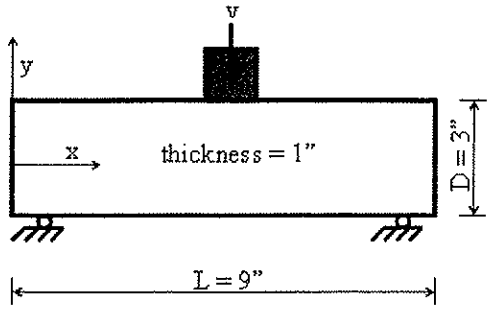

Figure 5.1: Illustration of the 3-point concrete beam bending beam used for the numerical investigation.

The material parameters used in the numerical simulations are: density $\rho = 2400\ \mathrm{kg/m^3}$; Young's Modulus $E = 31.37\ \mathrm{GPa}$; Poisson's ratio $\nu = 0.20$; and dynamic fracture toughness $K_{Ic} = 0.8\ \mathrm{MPa}\sqrt{\mathrm{m}}$.

The load in the numerical model is imposed as velocity on the interface elements (see Section 2.5) at the top of the beam. The load is centered in the longitudinal direction with a width of 0.0282m. It covers 10 nodes in the numerical model (see Figure 5.2). The load intensity is given as:

$$v_0(t) = \begin{cases} v_1 t / t_1, & \text{for } t \le t_1 \\ v_1, & \text{for } t > t_1 \end{cases}$$

where $v_1 = 0.06\ \mathrm{m/s}$ and $t_1 = 196\ \mu\mathrm{s}$.

The model is discretized with 74 nodes in the x-direction and 25 nodes in the y-direction. Rectangular Gauss cells are defined for the numerical integration, the number of Gauss cells are varied in subsequent analyses. In the FE domains 1x1 Gauss integration is applied, while the 4x4 rule is applied for the EFG- and interface- domains. The influence domain, d_{max}, is varied between 2.5 and 5.5 nodal distances (see Section 2.2).

The numerical model has one pre-crack that is running in y-direction at the midspan cross section. The pre-crack goes from the bottom of the beam and has a length of 3/32 inches.

The J-domain is the area where the interaction integral is calculated (see Section 3.6). It is a square domain and its area is varied. The domain is centered around the crack tip. Before the crack started to evolve the J-domain was reduced, since the predefined crack line is small and therefore limits the J-domain so that the crack tip is placed in the center of the domain. All the integration points inside the J-domain are used in the calculation of the stress intensity factors KI and KII.

The numerical model, model I, shown in Figure 5.2 is used for all the analyses, except those where linear and quadratic coupling between EFG and FE domains and the extended basis (see Section 2.7) are studied (see Tables 5.6 and 5.7). The latter analyses are based on the numerical model, model II, shown in Figure 5.3.

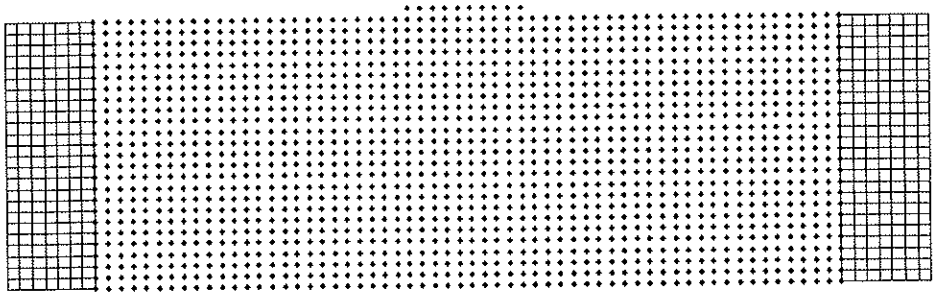

Figure 5.2: Illustration of numerical model I.

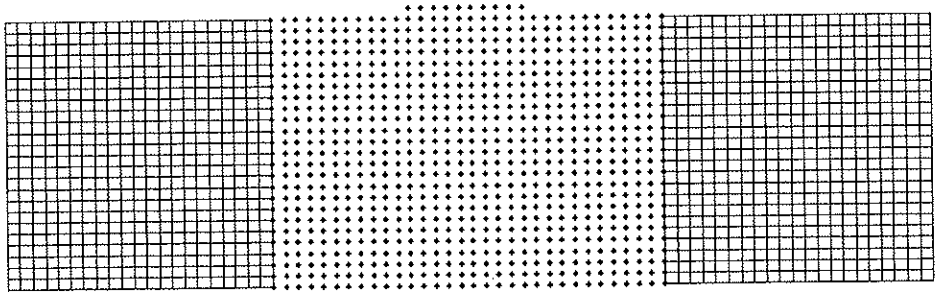

Figure 5.3: Illustration of numerical model II.

5.2.3 Specification of the simulation scheme

In this section the simulation scheme is listed. The simulation Sim-A is described by the following parameters:

Analyse	d	Δt	d_{max}	Gauss cell	updating K	Coupling
Sim-A	1.5dx	1/30 Δt_{crit}	3.5dx	0.5dx	300Δt	linear

This simulation is used as a reference solution. The variables d, Δt, dmax, Gauss cell (length of the quadratic sides), updating K (how often the stiffness matrix is updated for the crack path information), coupling (the type of coupling between the EFG domain and the FE domain in the numerical model), linear versus extended basis and the Newmark variable β_1 are varied in different series of analyses. Δt_{crit} is defined in Section 2.4 by the Courant condition, $\Delta t_{crit}=h/c$. The fracture criterion is checked every 1500Δt, except for the series where the time increment is varied. For this simulation the frequency of fracture criterion check is listed in the column with the updating of K. The simulation scheme of the simulation series is listed in Table 5.1 to Table 5.8.

Table 5.1: Listing of the parameters applied when the size of the J integral domain is varied.

Analyse	d	Δt	d_{max}	Gauss cell	updating K	Coupling
Sim-01	0.5dx	1/30 Δt_{crit}	3.5dx	1.0dx	300Δt	linear
Sim-02	1.0dx	1/30 Δt_{crit}	3.5dx	1.0dx	300Δt	linear
Sim-03	1.5dx	1/30 Δt_{crit}	3.5dx	1.0dx	300Δt	linear

Table 5.2: Listing of the parameters applied when the size of the time increment Δt is varied.

Analyse	d	Δt	d_{max}	Gauss cell	updating K	Coupling
Sim-04	1.5dx	0.5 Δt_{crit}	3.5dx	1.0dx	14dt/140Δt	linear
Sim-05	1.5dx	1/8 Δt_{crit}	3.5dx	1.0dx	60dt/600Δt	linear
Sim-06	1.5dx	1/15 Δt_{crit}	3.5dx	1.0dx	120dt/1200Δt	linear
Sim-03	1.5dx	1/30 Δt_{crit}	3.5dx	1.0dx	300dt/1500Δt	linear

Table 5.3: Listing of the parameters applied when the size of the domain of influence, d_{max}, is varied.

Analyse	d	Δt	d_{max}	Gauss cell	updating K	Coupling
Sim-07	1.5dx	1/30 Δt_{crit}	2.5dx	1.0dx	300Δt	linear
Sim-03	1.5dx	1/30 Δt_{crit}	3.5dx	1.0dx	300Δt	linear
Sim-08	1.5dx	1/30 Δt_{crit}	4.5dx	1.0dx	300Δt	linear
Sim-09	1.5dx	1/30 Δt_{crit}	5.5dx	1.0dx	300Δt	linear

Table 5.4: Listing of the parameters applied when the size of the quadratic sides of the Gauss cell are varied.

Analyse	d	Δt	d_{max}	Gauss cell	updating K	Coupling
Sim-A	1.5dx	1/30 Δt_{crit}	3.5dx	0.5dx	300Δt	linear
Sim-03	1.5dx	1/30 Δt_{crit}	3.5dx	1.0dx	300Δt	linear

Table 5.5: Listing the parameters applied when the frequency of updating the stiffness matrix is varied.

Analyse	d	Δt	d_{max}	Gauss cell	updating K	Coupling
Sim-10	1.5dx	1/30 Δt_{crit}	3.5dx	1.0dx	50Δt	linear
Sim-11	1.5dx	1/30 Δt_{crit}	3.5dx	1.0dx	100Δt	linear
Sim-03	1.5dx	1/30 Δt_{crit}	3.5dx	1.0dx	300Δt	linear
Sim-12	1.5dx	1/30 Δt_{crit}	3.5dx	1.0dx	500Δt	linear
Sim-13	1.5dx	1/30 Δt_{crit}	3.5dx	1.0dx	750Δt	Linear

Table 5.6: Listing of the parameters applied when linear or quadratic coupling between the EFG domain and the FE domain is applied.

Analyse	d	Δt	d_{max}	Gauss cell	updating K	Coupling
Sim-14	1.5dx	1/30 Δt_{crit}	3.5dx	1.0dx	300Δt	Linear
Sim-15	1.5dx	1/30 Δt_{crit}	3.5dx	1.0dx	300Δt	Quadratic

Table 5.7: Listing of the parameters applied when linear or extended basis in the vicinity of the crack tip is applied.

Analyse	d	Δt	d_{max}	Gauss	updating K	Coupling	Basis
Sim-14	1.5dx	1/30 Δt_{crit}	3.5dx	1.0dx	300Δt	linear	Linear
Sim-16	1.5dx	1/30 Δt_{crit}	3.5dx	1.5dx	300Δt	linear	Extended

Table 5.8: Listing of the parameters applied when the Newmark integration parameter β_1 is varied.

Analyse	d	Δt	d_{max}	Gauss cell	updating K	β_1
Sim-17	1.5dx	1/30 Δt_{crit}	3.5dx	1.0dx	300Δt	0.5
Sim-18	1.5dx	1/30 Δt_{crit}	3.5dx	1.0dx	300Δt	0.75

5.2.4 Plot of the mode I stress intensity factors for each analyses

The mode I stress intensity factor (SIF) is plotted for the different analyses given in Table 5.1 to 5.8 in Figure 5.4 to 5.10. To calculate the stress intensity factor all the basic routines that is implemented in this work is included in such a simulation, which then makes the calculation of stress intensity well suited for comparison and validation of results. The conclusions given below are based on the fact that a set of parameters for this special case is to be chosen, so that a solution will probably converge with a minimum use of CPU time and still give a satisfactory level of accuracy.

The influence on the mode I stress intensity factor from the size of the area where the J-integral is integrated is shown in Figure 5.4. If the variable d (2d is the length of one side in the quadratic integration domain) is 0.5dx (Sim-01) the result is diverging from the other two solutions and the stress intensity peaks are under estimated. Based on these results, d should be greater than or equal to 1.0dx, to get a converging solution.

The size of the time increments versus the mode I stress intensity factor results is plotted in Figure 5.5. The shape and peak of the results from the analysis with Δt equal to 1/30 Δt_{crit} (Sim-03) is similar to the Sim-A analysis. The propagation of the crack starts later. For a larger time increment the solution is diverging from the two analyses described above. Based on these results, the time increment should be smaller or equal to 1/30 Δt_{crit}, to get a converging solution.

Variation of d_{max}, the size of the influence domain, is influencing the results significantly. Figure 5.6 shows how the mode I stress intensity factor is influenced by this parameter. A small d_{max} (2.5dx) and a large d_{max} (5.5dx) give diverging results. Based on these results d_{max} between 3.5dx and 4.5dx should be adopted to obtain a converging solution.

The Gauss cell size is varied in two analyses. One with 0.5dx quadratic sides in Sim-A and one with 1.0dx in Sim-03. The results are plotted in Figure 5.7, where the mode I stress intensity factor is shown for both analyses. The shape and peak values for the mode I stress intensity factor for the Gauss cell refinement solution (Sim-A) show similar behaviour as for Sim-03, but the crack propagation starts earlier for the refined analysis. Based on these results the Gauss cell size 1.0dx can be adopted to obtain a converging solution.

The influence on the mode I stress intensity factor from the frequency of updating the stiffness matrix with respect to the crack path is shown in Figure 5.8. The updating frequency has minor influence on the mode I stress intensity factor, but as will be shown in Section 5.2.5 larger time intervals between updating of the stiffness matrix will introduce artificial oscillations.

The mode I stress intensity factor shows only small variations from improving the coupling from linear to quadratic between the EFG domain and the FE domain. Equal shape but reduced magnitude is observed for the analysis Sim-16. Figure 5.9 shows curves of the mode I stress intensity factor for linear and quadratic coupling together with the analysis Sim-16 which has extended basis in the vicinity of the crack tip.

The mode I stress intensity factor shows small variation from varying the Newmark β_1 variable as can be observed in Figure 5.10.

Figures 5.11 and 5.12 show the final crack paths for analyses Sim-A and Sim-16. The zigzag pattern is more distinet for the simulation with use of extended basis versus the analyses with use of linear basis. The mean crack path direction is virtually the same for both analyses. The local difference results from more exact calculations of the stress intensity factors with the use of extended basis contra linear basis.

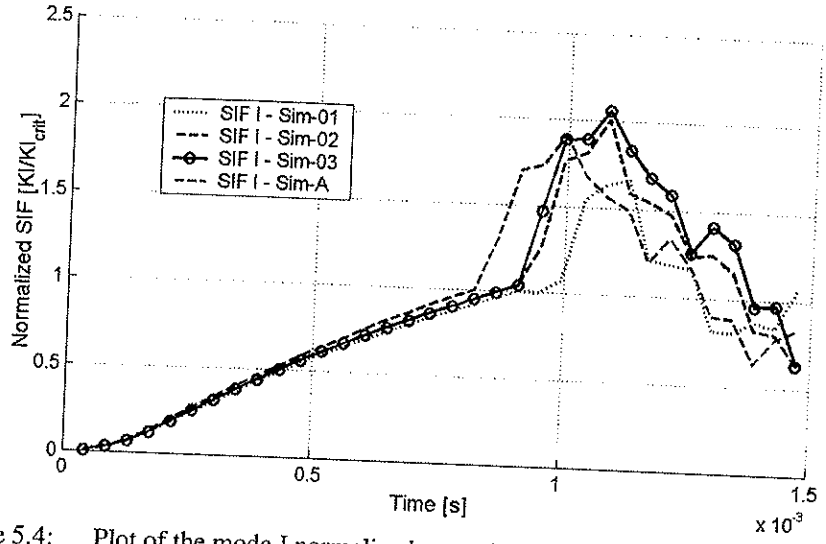

Figure 5.4: Plot of the mode I normalized stress intensity factor for different areas where the J-integral is calculated.

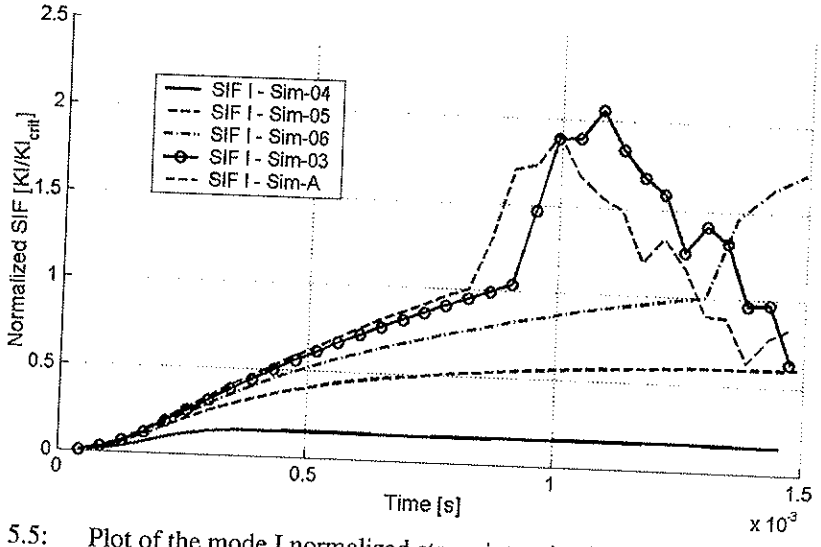

Figure 5.5: Plot of the mode I normalized stress intensity factor for different time increments.

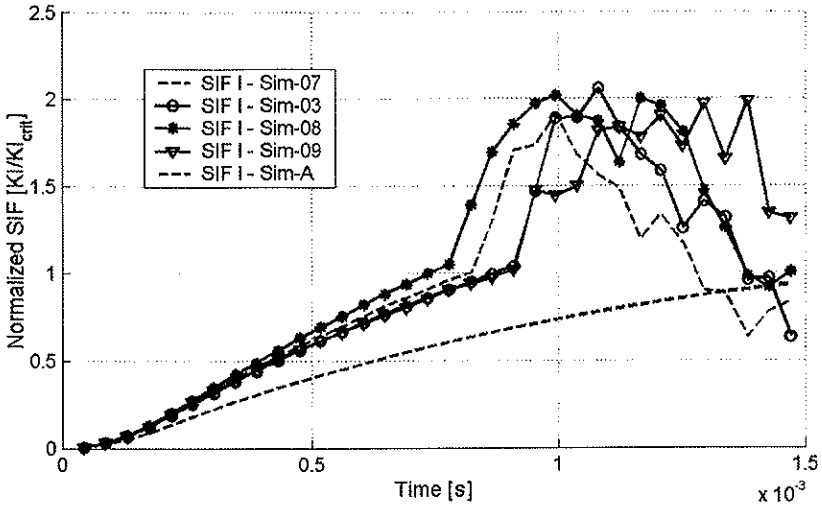

Figure 5.6: Plot of the mode I normalized stress intensity factor for different d_{max}.

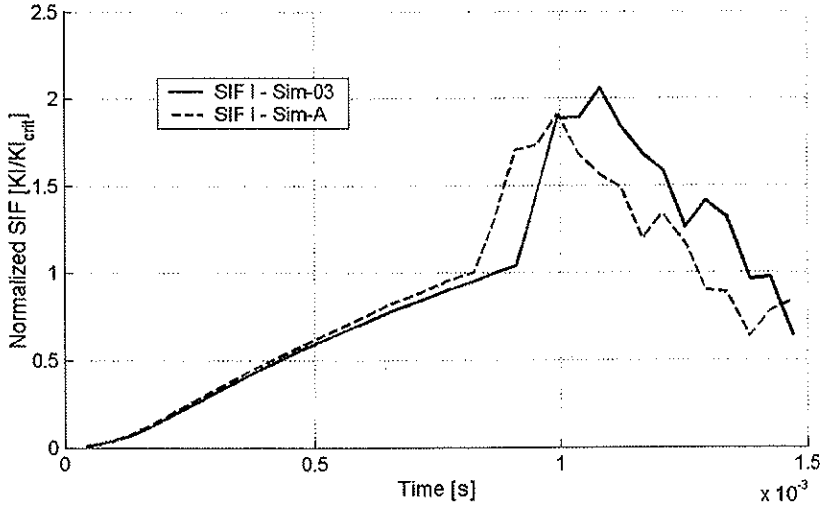

Figure 5.7: Plot of the mode I normalized stress intensity factor for different Gauss cells area.

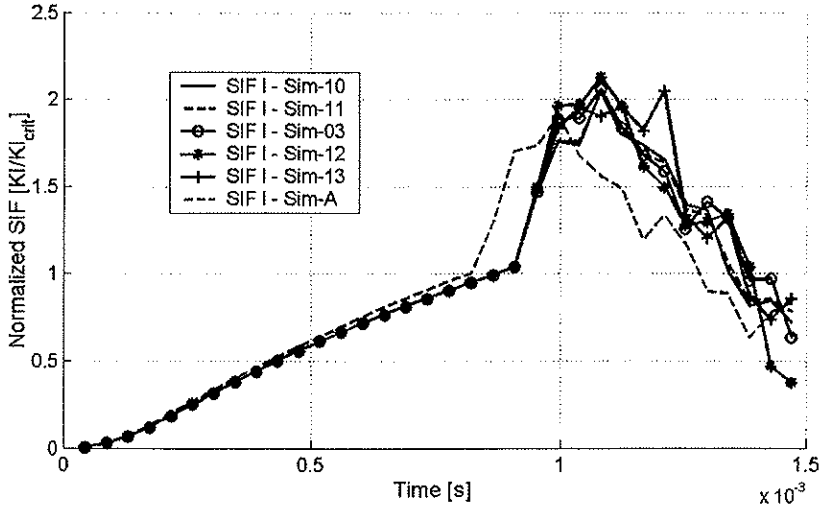

Figure 5.8: Plot of the mode I normalized stress intensity factor for different updating frequency interval of the stiffness matrix.

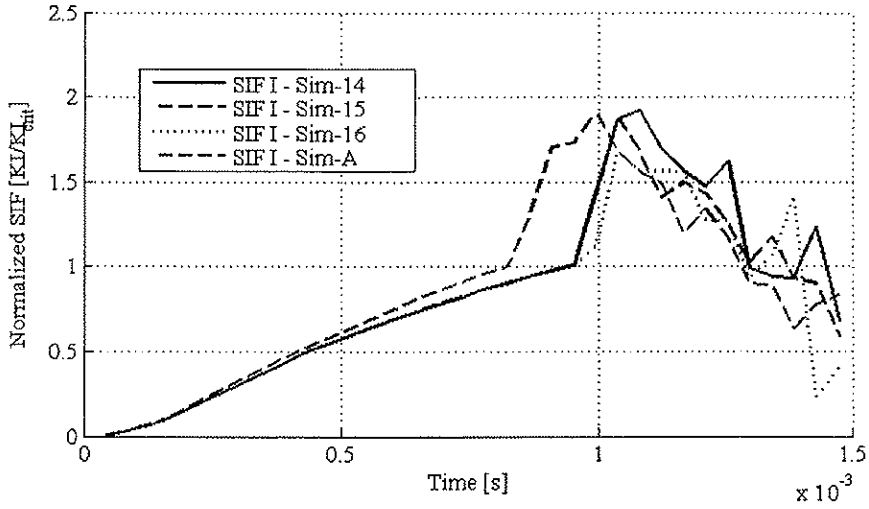

Figure 5.9: Plot of the mode I normalized stress intensity factor for linear and quadratic coupling of the EFG domain and the FE domain of the numerical model, together with linear and extended basis in the vicinity of the crack tip

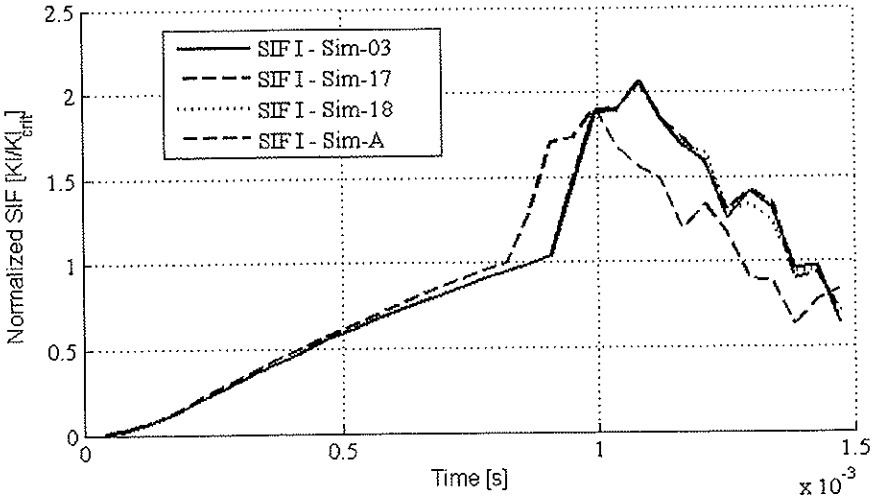

Figure 5.10: Plot of the mode I normalized stress intensity factor for variation of the Newmark integration parameter β_1

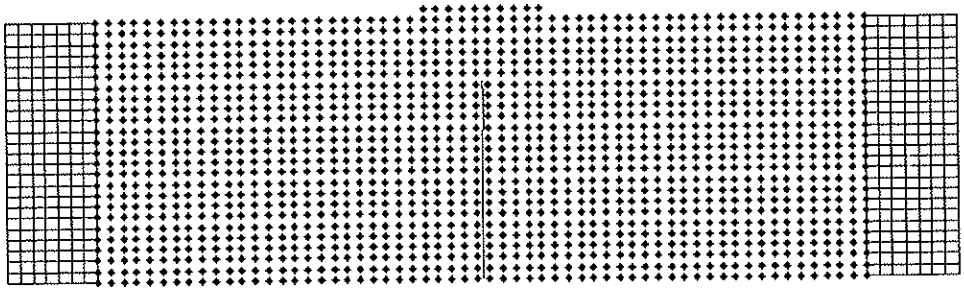

Figure 5. 11: Plot of the finial crack path from analysis Sim-A.

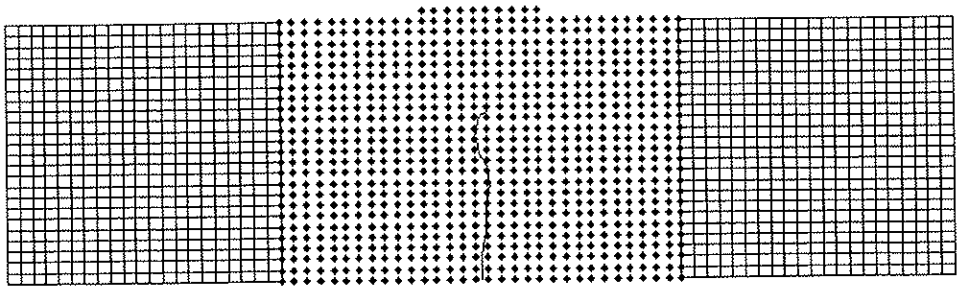

Figure 5.12: Plot of the finial crack path from analysis Sim-16.

5.2.5 Artificial numerically induced oscillations

Artificial numerically induced oscillations in this context are the oscillations caused by the release of stresses related to the process of adding a new line segment to the existing crack path. The new line segment is added to the existing crack path at a specific time increment, where the length is dependent on the crack propagation speed and the updating frequency of the stiffness matrix. This process releases stresses that act over the actual line segment. The effect is artificial numerical induced oscillations that can be observed as stress waves in the numerical model. These oscillations start simultaneously with the start of the first crack propagation. The frequency and intensity of the oscillations depend on how often the stiffness matrix is updated for the crack path.

Figure 5.13 shows curves for the total left hand reaction force for Sim-10 (updating K every 50Δt) and Sim-13 (updating K every 750Δt). The input parameters for the analyses are given in Table 5.13. The results emphasize that the oscillation intensity is strongly dependent on the updating frequency of the stiffness matrix. More infrequent updating of the stiffness matrix induces higher intensity oscillations.

Figure 5.14 to Figure 5.16 show 3D surface plots of the stress in x-direction (S11) for Sim-10 (updating K every 50Δt) and Sim-13 (updating K every 750Δt). Figure 5.14 shows the stress S11 at the simulation time 0.0008s, which is shortly before the crack propagation starts. At this time the 3D surface plot shows that there are no artificial oscillations in the model, as should be expected. Figure 5.15 and Figure 5.16 show the stress S11 at the simulation time 0.00105s, which is after the crack propagation has started. The artificial oscillations are now seen all over the whole numerical model. The intensities of the S11 oscillations are higher in Figure 5.15 (Sim-13) than in Figure 5.16 (Sim-10), but the level is still considerably lower than the actual stress intensities close to the crack tip. In this area the asymptotic stress field is dominating.

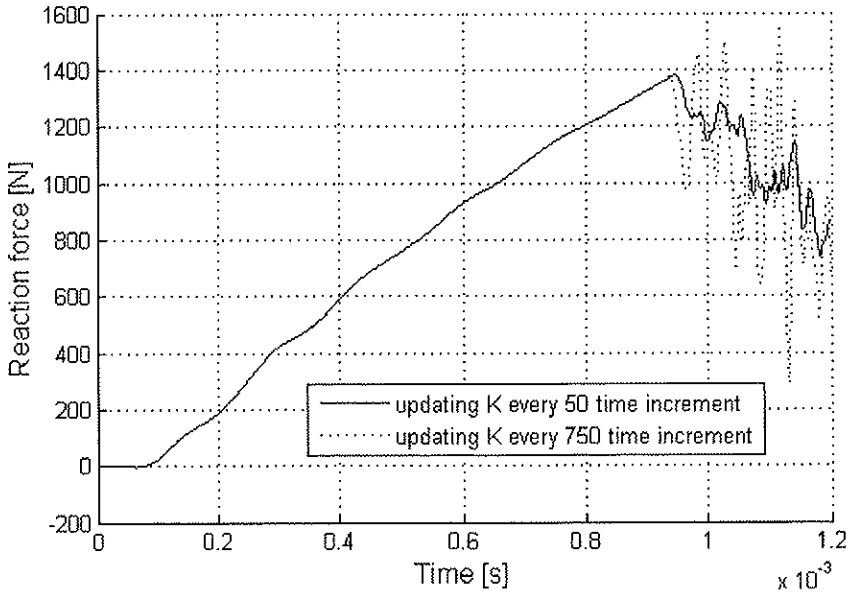

Figure 5.13: Plot of the total left hand reaction force for Sim-10 (updating K every 50Δt) and Sim-13 (updating K every 750Δt).

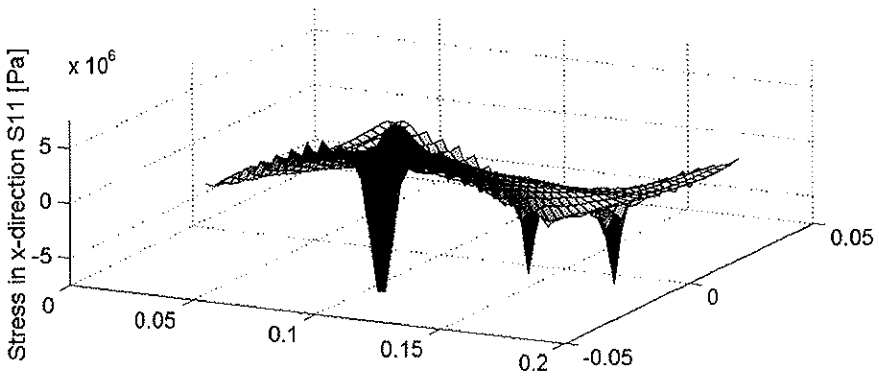

Figure 5.14: 3D surface plot of the stress in x-direction (S11) for Sim-10 (updating K every 50Δt) and Sim-13 (updating K every 750Δt) at the simulation time 0.0008s (the simulations are identical before the crack propagation starts).

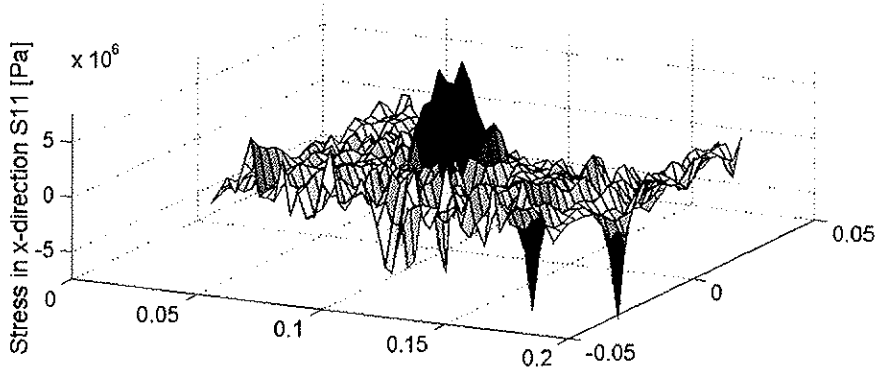

Figure 5.15: 3D surface plot of the stress in x-direction (S11) for Sim-13 (updating K every 750Δt) at the simulation time 0.00105s.

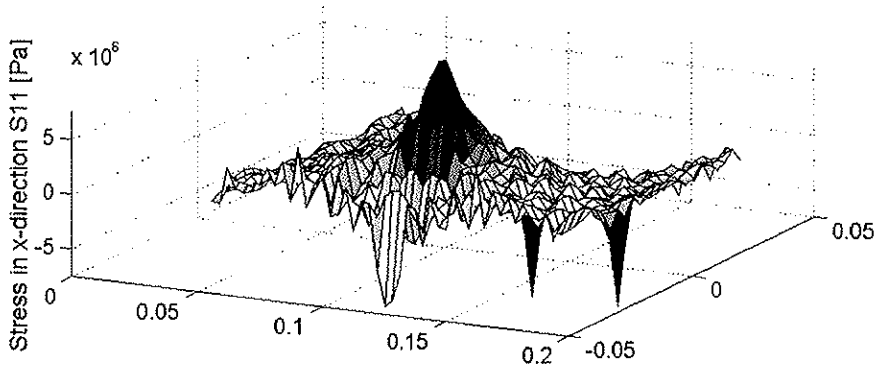

Figure 5.16: 3D surface plot of the stress in x-direction (S11) for Sim-10 (updating K every 50Δt) at the simulation time 0.00105s.

5.2.6 Verification of the J integral computation by FE analysis

The results from the EFG calculation of the stress intensity factor for the 3-point bending of the concrete beam with a centric crack investigated in this section is compared with stress intensity factors calculated by the FE code ABAQUS with implicit time integration (ABAQUS Version 6.5). The numerical FE model uses the same input data as described in Section 5.2.2. The FE model is discretized by 200 elements in the x-direction and 135 elements in the y-direction. The numerical FE model is shown in Figure 5.17, where the support, symmetric boundary condition at the center of the beam and the implied velocities at the top are indicated by orange color. Figure 5.18 shows the deformed numerical model at the time instant t=0.0015s, with a magnification factor of 10. ABAQUS offers calculation of stress intensity factors for the symmetric case, as utilized in this calculation.

ABAQUS can only calculate stress intensity factors at a crack tip point (2D) or line (3D). No crack propagation can be combined with the calculation of stress intensity factors. This limitation makes the comparison of the stress intensity factors valid only up to the point where the crack starts to propagate. Figure 5.19 shows the calculated mode I stress intensity factor for the ABAQUS analysis together with the Sim-A and Sim-03 analyses. The EFG reference analysis, Sim-A, shows relatively good agreement with the path evolution and the start of crack propagation point for the ABAQUS analysis.

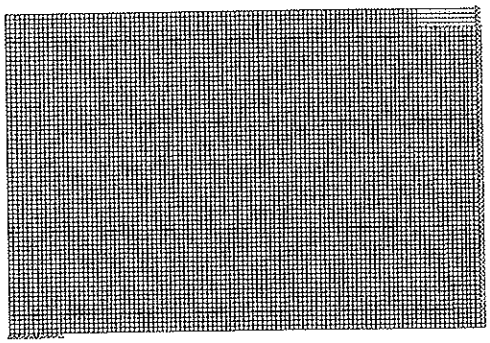

Figure 5.17: Illustration of the symmetric FE-model of the 3 point bending modelled by the FE-program ABAQUS. Orange color indicates the support, symmetric boundary conditions at mid cross section of the beam and the forced velocities at the top.

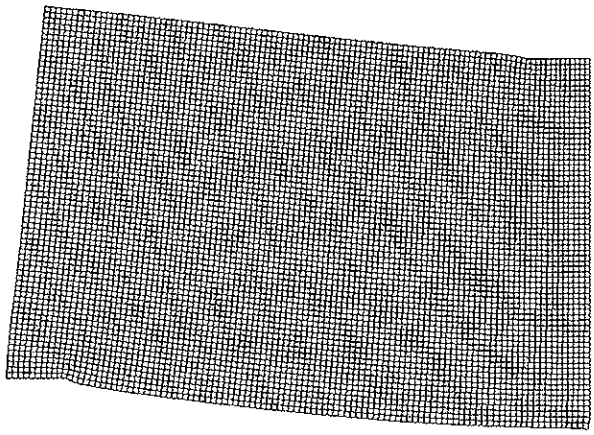

Figure 5. 18: Illustration of the deformed symmetric FE-model of the 3 point bending modelled by the FE-program ABAQUS. The deformed plot is at the time instant t=0.0015s, with a magnification factor of 10.

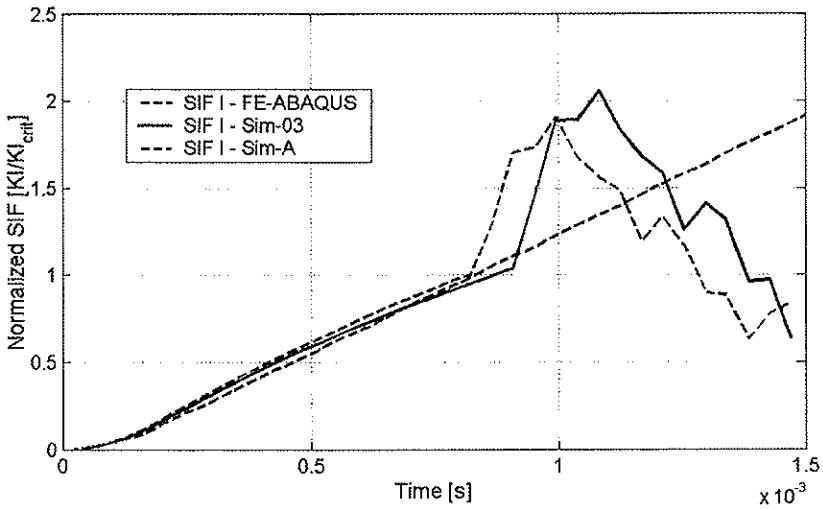

Figure 5.19: Plot of the mode I stress intensity factor at the crack tip in the FE-model, together with corresponding results for the EFG simulations Sim-03 and Sim-A.

5.2.7 Parameter influence on the required computer time

The column diagram shown in Figure 5.20 compares the consumption of computer time for all the reported analyses in this section (see Tables 5.1 to 5.8). The computer time is normalized with respect to the computer time for analysis Sim-03.

The columns Sim-01 to Sim-03 are approximately identical except for a little less total computer time for analysis Sim-01. The deviation is related to a diverging solution (see Figure 5.4), which estimates a lower mode I stress intensity factor with less crack propagation and computer time consumption as a consequence. This illustrate that the size of the J integral domain is not influencing the total computer time of an analysis significantly.

For analyses Sim-04 to Sim-06 the time increment is increased compared with Sim-03. This results in a lower estimate of the mode I stress intensity factor and no (or little) crack propagation (see Figure 5.5). These are of course a much less time consuming analyses as can be seen in Figure 5.20.

For columns Sim-07 to Sim-09 in Figure 5.20 the variation of the domain of influence, d_{max}, on the consumption of computer time is illustrated. The total computer time is dramatically increased with increased domain of influence. This is related to the extra cost of handling a lot more nodes in the MLS approximation.

Columns Sim-10 to Sim-13 illustrate the influence on computer time from how frequent the stiffness matrix is updated with respect to the crack path. It can be observed a very large reduction in computer time for an analysis with less frequent updated stiffness matrix.

Columns Sim-14 to Sim-16 are a little lower than the column for Sim-03. This is because the initiation of the numerical model is faster since it consists of more finite elements and a smaller EFG domain (see Figures 5.2 and 5.3). These columns represent the variation from linear to quadratic coupling in the interface domain and the influence of extended basis in the vicinity of the crack tip. The variation can be seen in Figure 5.20 to have minor influence on the computer time.

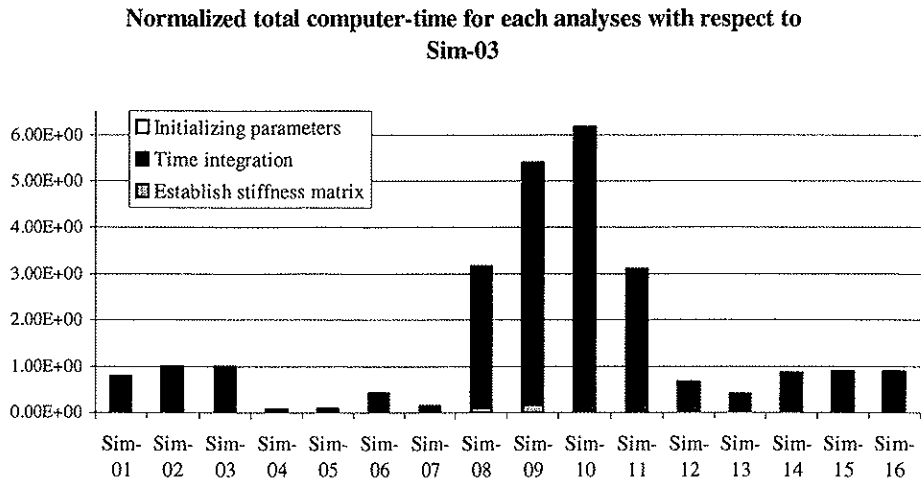

Figure 5.20: The column diagram shows the consumption of computer time for all the reported analyses in this section. The computer time is normalized with respect to the computer time for analysis Sim-03.

5.2.8 Conclusive remarks

The main objective of the analyses performed within this section was to thoroughly investigate and optimize the input parameters and its influence on the results for the calculation of the 3-point bending of a concrete beam. The main goal of the optimization was to establish a set of input parameters that gives a satisfactory level of accuracy with a minimum consumption of computer time.

The validation of the level of accuracy of the results from the calculations is based on comparison with results from a FE calculation with the code ABAQUS (ABAQUS Version 6.5), and a superficial comparison with results obtained by Organ (1996). The results obtained by Organ are not directly comparable, since the numerical model studied in this section has only a centric crack and not a combination of a centric crack with a non-centric crack as was the case in Organ (1996).

Reliable results and time effective simulations can be obtained if the parameters given in Table 5.9 are adopted. The parameter range listed in Table 5.9 for Sim-accu shows the parameters that should give converged solutions.

As shown in this section the input parameters that have significant influence on the consumption of computer time is the size of the domain of influence and how frequent the stiffness matrix is updated with respect to the crack path. The later is strongly related to the artificial oscillations in the solution, i.e. high level of the oscillations with more seldom updating of the stiffness matrix. The parameters listed for Sim-effec in Table 5.9 is the parameter combination that is likely to give the most computational effective simulations for an acceptable level of accuracy.

Based on the calculations in this section the input parameters Sim-effec are recommended to use in the succeeding computations, where numerical simulations of the pendulum experiment by John, R. and S. P. Shah (1990) on concrete beams are performed.

Table 5.9: Input parameters for analyses Sim-accu and Sim-effec.

Analyses	**d**	**dt**	**d_{max}**	**Gauss cell**	**updating K**
Sim-accu	1.5dx	1/30 $\Delta t_{crit<}$	3.5-4.5dx	1.0dx<	300dt<
Sim-effec	1.5dx	1/30 Δt_{crit}	3.5dx	1.0dx	300dt

5.3 Mixed-mode dynamic fracture of 3-point bending of concrete beam

5.3.1 Description of the numerical model

The geometry of the beam is shown in Figure 5.21. The length of the beam is 9 inches, the height is 3 inches and the thickness is 1 inch. The distance between the vertical supports (y-direction) 8 inches. The motion of the beam is not constrained in the x-direction.

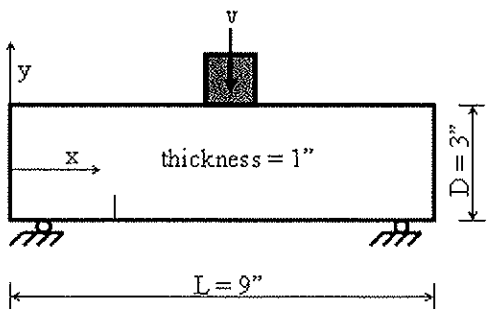

Figure 5.21: Illustration of the concrete 3-point bending beam used for the numerical investigation.

The material parameters used in the numerical simulations are: density $\rho = 2400\ \mathrm{kg/m^3}$; Young's Modulus $E = 31.37\ \mathrm{GPa}$; Poisson's ratio $\nu = 0.20$; and dynamic fracture toughness $K_{Ic} = 0.8\ \mathrm{MPa}\sqrt{\mathrm{m}}$.

The load in the numerical model is imposed as velocity on the interface elements (see Section 2.5) at the top of the beam. The load is centered in the x-direction and with an extension of 0.0282m. It covers 10 nodes in the numerical model (see Figure 5.22). The load intensity is given by:

$$v_0(t) = \begin{cases} v_l t / t_l, & \text{for } t \le t_l \\ v_l, & \text{for } t > t_l \end{cases}$$

where $v_l = 0.06\ \mathrm{m/s}$ and $t_l = 196\ \mu\mathrm{s}$.

The model is discretized with 74 nodes in the x-direction and 25 nodes in the y-direction. The number of nodes in the x-direction is chosen such that the precracks in the model are located between vertical rows of nodes to avoid unnecessary disturbance from nearby nodes. The model is divided into three domains, with different types of discretisation. The finite element domain, covers the areas: $x \in [0, 0.0188]$, $y \in [-D/2, D/2]$ and $x \in [0.2098, Lb]$, $y \in [-D/2, D/2]$. The element free Galerkin domain covers the area: $x \in [0.0251, 0.2067]$, $y \in [-D/2, D/2]$ and the interface domains which couple the EFG and FE domains cover: $x \in [0.0188, 0.0251]$, $y \in [-D/2, D/2]$ and $x \in [0.2067, 2098]$, $y \in [-D/2, D/2]$. Rectangular Gauss cells are defined for the numerical integration, with the nodes limiting the cell areas. In the FE domains 1x1 Gauss integration is applied, while the 4x4 rule is applied for the EFG- and interface- domains. The influence domain is limited by d_{max}=3.5 (see Section 2.2).

The numerical model has two predefined cracks. One crack is running in the y-direction at the midspan cross section and from the bottom of the beam with a length of 3/32 inches. This crack is chosen equal to ¼ of the maximum aggregate size. Imperfections of this size are typical in concrete. The midspan crack is in the following discussion named crack line 1 (CL1). The location of the second crack is given by the parameter γ which is defined as the distance to the crack from midspan divided by the distance from the midspan to the center of the support. Also the second crack starts from the lower side of the beam, normal to the beam axis and with a length of ¾ of an inch. This crack is in the following named crack line 2 (CL2).

The J-domain is the area where the interaction integral is calculated, see Section 3.6. This area is square and covers 9 integration cells. The domain is centered around the crack tip. Before CL1 started to evolve, the J-domain was reduced, since the predefined CL1 is small and therefore limits the J-domain so that the crack tip is located at the center of the domain. All the integration points inside the J-domain are used in the calculation of the stress intensity factors KI and KII.

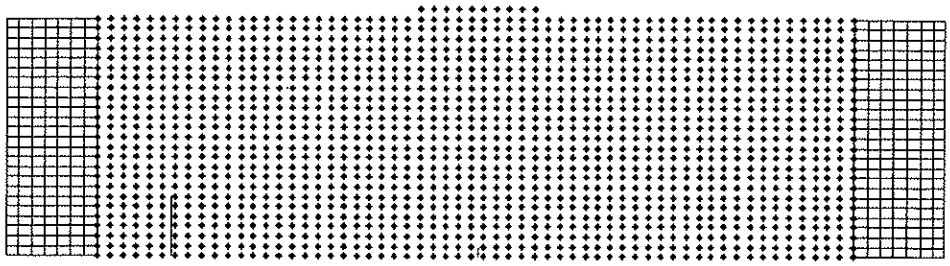

Figure 5.22: Illustration of the numerical model used to simulate the 3-point bending beam experiment.

5.3.2 Specification of the simulation scheme

Since the numerical simulations of the 3-point bending beam are performed in order to verify the computer code, the different analyses are chosen equal to those reported in Organ (1996). Table 5.10 gives the different cases: location of crack line 2 defined by the parameter γ, the crack propagation velocity (constant or variable) and the identification of the different simulations.

Table 5.10: Name, crack location, and variable or constant crack propagation velocities for the different numerical simulations reported.

Simulation name:	**Crack location, γ:**	**Propagation velocity:**
G0734C	0.734	Constant
G0705C	0.705	Constant
G0672C	0.672	Constant
G0672V	0.672	Variable

5.3.3 Numerical results

Four different simulations are performed as defined in Table 5.10. In Table 5.11 crack propagation angle information is given for all simulations. This information consists of initial crack angle, final crack angle and the range of the crack propagation angle during the crack advancement. The angle is measured from the positive x-direction counterclockwise. The analyses with constant crack propagation velocity are in reasonable agreement with Organ (1996) for the initial angle values. The final angle values and the range during the crack propagation do not show the same conformity. The difference in the results is related to the relatively high level of oscillations in the solution during the crack propagation phase. Before the crack propagation starts there are no oscillations in the solution and thus the initial crack angles are in good agreement with the solution given by Organ (1996). The oscillations during the crack propagation can be reduced by updating the stiffness matrix more frequently with respect to the crack propagation (see Section 5.2.5) and by replacing the visibility criterion with the diffraction method (see Organ, Flemming, Terry and Belytschko (1996)).

Table 5.11: Crack propagation angles for every simulation; initial, final and range of crack propagation angle during the simulations.

Analyses name - Crack		Initial angle - Final angle		Range of the angles
G0672C	Notch	70	90	55-90
G0705C	Notch	58	72	57-72
	Midspan	90	96	65-100
G0734C	Midspan	90	86	72-112
G0734V	Notch	65	40	35-80

The finial crack configurations of the simulations: G0672C, G0705C, G0734C, and G0734V are shown in Figure 5.23. It can be seen that the crack at the notch have the same curvature, and the path ends up with less than one node interval deviation. At midspan the crack for G0734C runs in a zig-zag pattern straight up to the loading location in the midspan as expected. For simulation G0705C the midspan crack path deviates somewhat from the center line of the beam. This is also reported by Organ (1996). Illustrations of the crack path evolution during the simulations are plotted for the cases: G0672C, G0705C, G0734C, and G0734V respectively in Figure 5.28 to 5.31. It can be shown that the crack path from the notch in simulation G0734V turns towards the loading point. This is an improvement from the solutions with constant crack propagation velocity when compared with the experimental results by John (1988). Similar results are also reported by Organ (1996).

Time history plot of the stress intensity factors for the simulations: G0672C, G0705C, G0734C, and G0734V are given in Figures 5.24a, 5.25a, 5.26a, and 5.27a. Comparison of the stress intensity factors for the simulations with constant crack velocity with the results given by Organ (1996), indicates a good agreement with the main form of the time history plot. The results from this study show more oscillations than reported by Organ. The source of these oscillations could be that the stiffness matrix is updated less frequently (see Section 5.2.5). This explanation is also supported by the stress plots related to simulation G0734V (see Appendix C), where less oscillation after the start of the crack growth can be seen for the simulations with constant crack velocity. Detailed information about the analyses performed by Organ is, however, required to conclude on the differences in results.

The simulation with variable crack velocity, G0734V, tends to move the transition region against higher values of γ. The transition region represents the value of γ, where on the lower side the crack propagation starts at the notch and at the higher side the crack propagation starts from the midpoint of the beam. This corresponds to the results by Organ (1996), and the experiments by John (1988). The time history plot of the stress intensity factors, are shown in Figure 5.27. One can notice that the mode I stress intensity factor for the notch oscillates around the fracture toughness of the material, KIc, rather than continuing to increase as it did for the constant velocity cases. A time history plot of the crack propagation velocity is given in Figure 5.27b. This velocity starts at zero, and increases when the crack propagation starts. The average peak value is close to 570m/s. This is 24% of the Rayleigh velocity. This result is higher but still in relatively good agreement with the results reported by Organ (1996), who got a velocity of 19% of the Rayleigh velocity. Again more detailed information of the basis for the analyses performed by Organ is needed to explain differences in these results.

Time history plot of the reaction forces for the simulations: G0672C, G0705C, and G0734C are given in Figures 5.24b, 5.25b, 5.26b. The reaction forces of the simulations are decreasing when the crack starts to propagate and the peak load is close to 4000 N which is approximately the same as reported by Organ (1996). The oscillations in the time history plot of the reaction forces, come from the same source as described previously in Section 5.2.5 (artificial oscillations).

In Appendix C several deformation plots of the numerical model are given, together with plots of the normal stress component σ_{xx} in the form of a surface level above the beam model and a contour plot of the stress surface below the beam model. These types of plots are given for the simulations: G0672C, G0705C, G0734C, and G0734V.

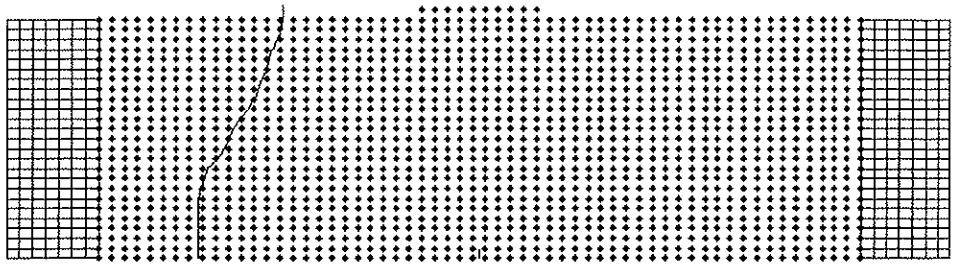

(a) Final crack configuration - G0672C

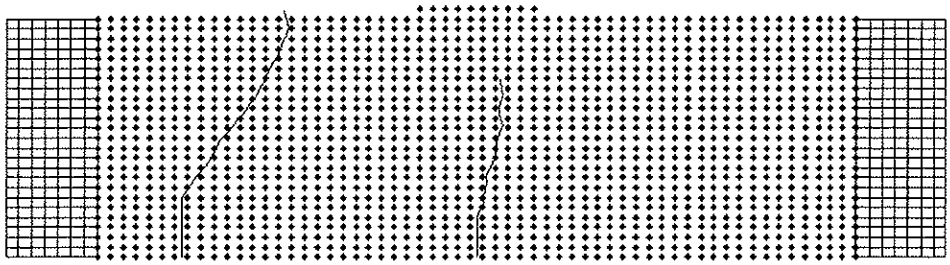

(b) Final crack configuration - G0705C

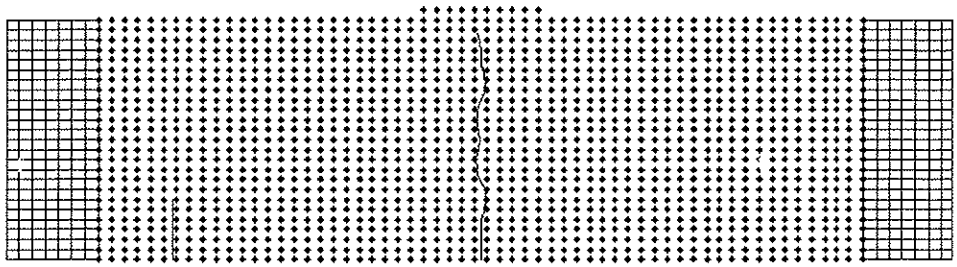

(c) Final crack configuration - G0734C

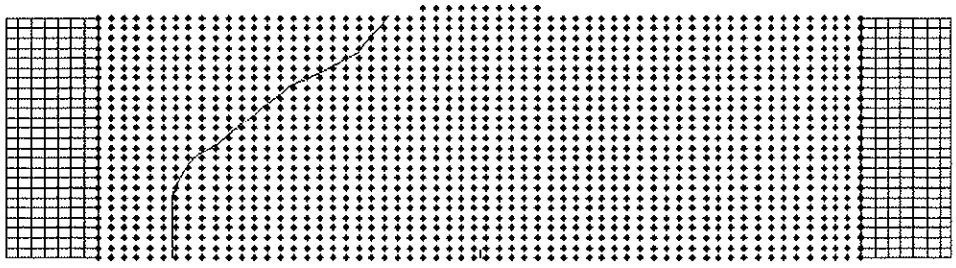

(d) Final crack configuration - G0734V

Figure 5.23: Illustration of the final crack configurations for the simulations: G0672C, G0705C, G0734C, and G0734V.

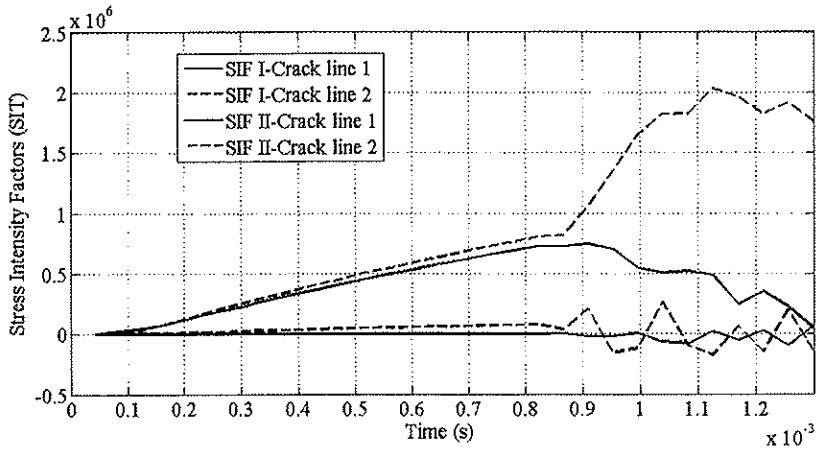

(a) Stress intensity factors - G0672C.

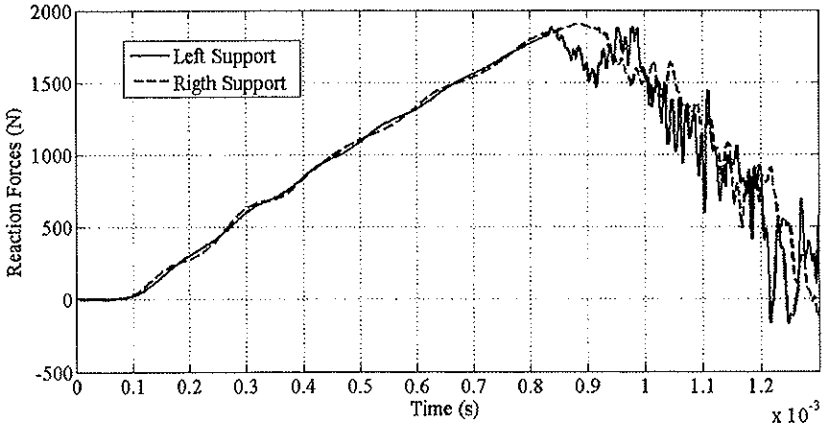

(b) Reaction Forces - G0672C.

Figure 5.24: Time history plot of the stress intensity factors and the reaction forces for the simulation G0672C.

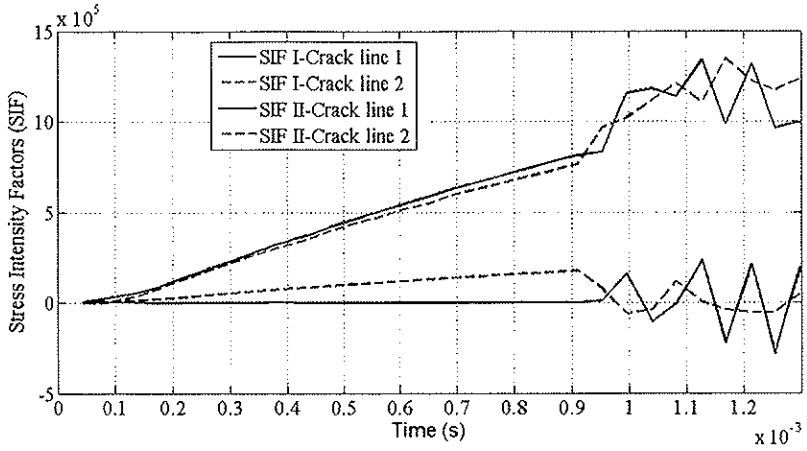

(a) Stress intensity factors - G0705C.

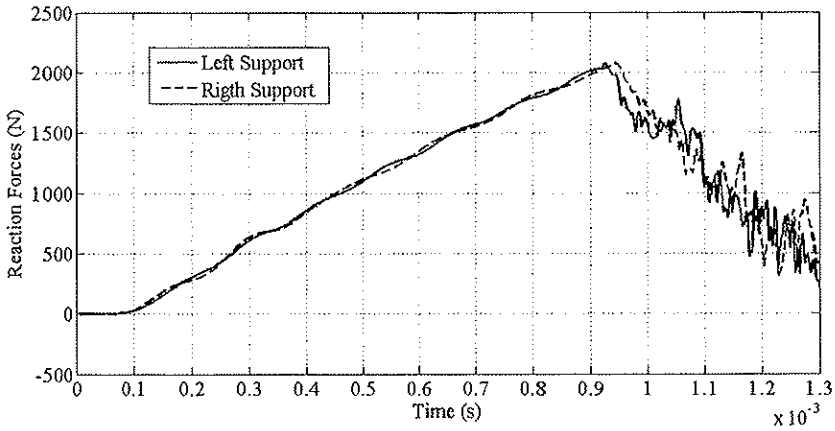

(b) Reaction Forces - G0705C.

Figure 5.25: Time history plot of the stress intensity factors and the reaction forces for the simulation G0705C.

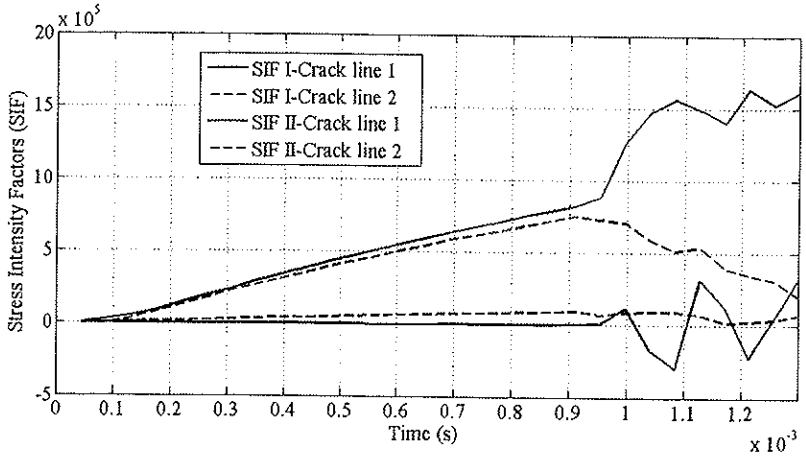

(a) Stress intensity factors - G0734C.

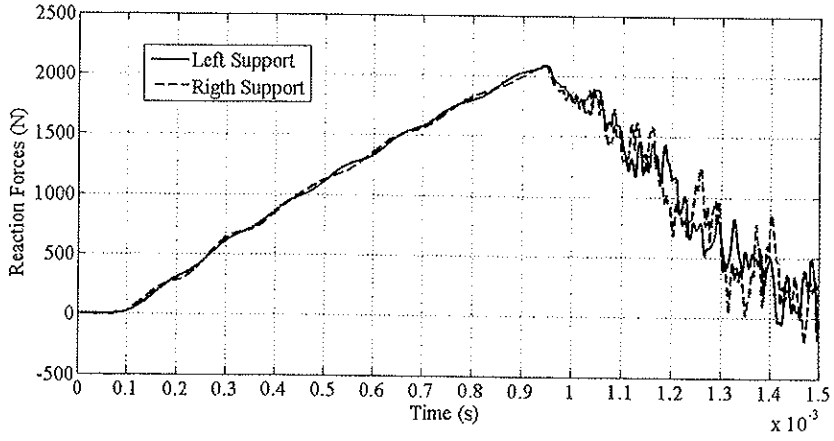

(b) Reaction Forces - G0734C.

Figure 5.26: Time history plot of the stress intensity factors and the reaction forces for the simulation G0734C.

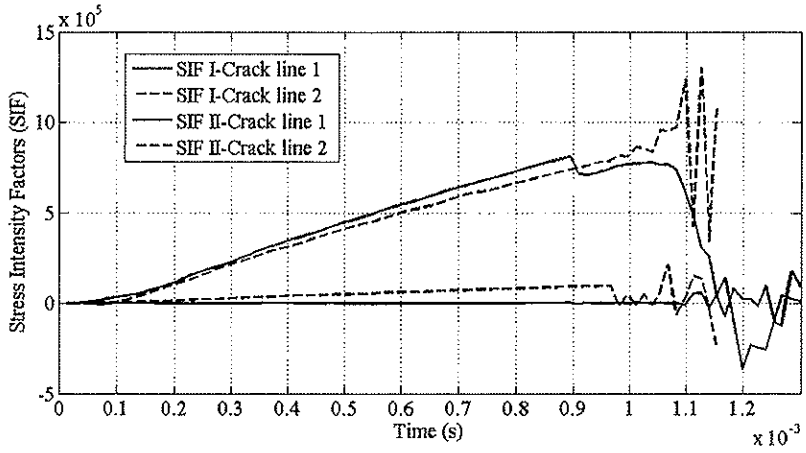

(a) Stress intensity factors - G0734V.

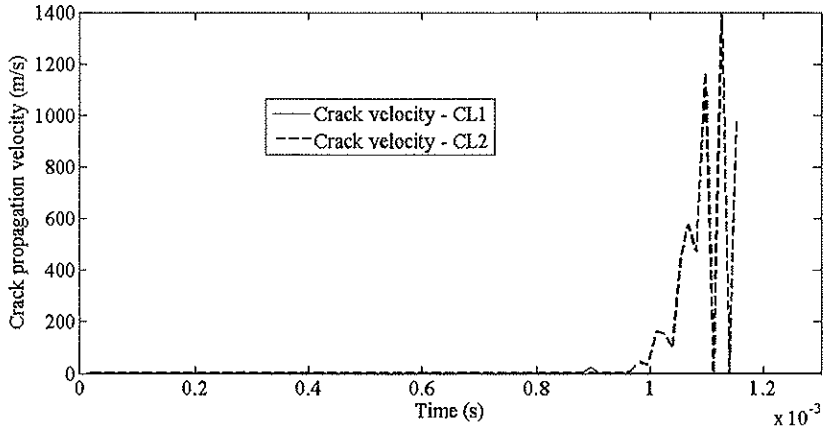

(b) Crack propagation velocity - G0734V.

Figure 5.27: Time history plot of the stress intensity factors and the crack propagation velocity for the simulation G0734V.

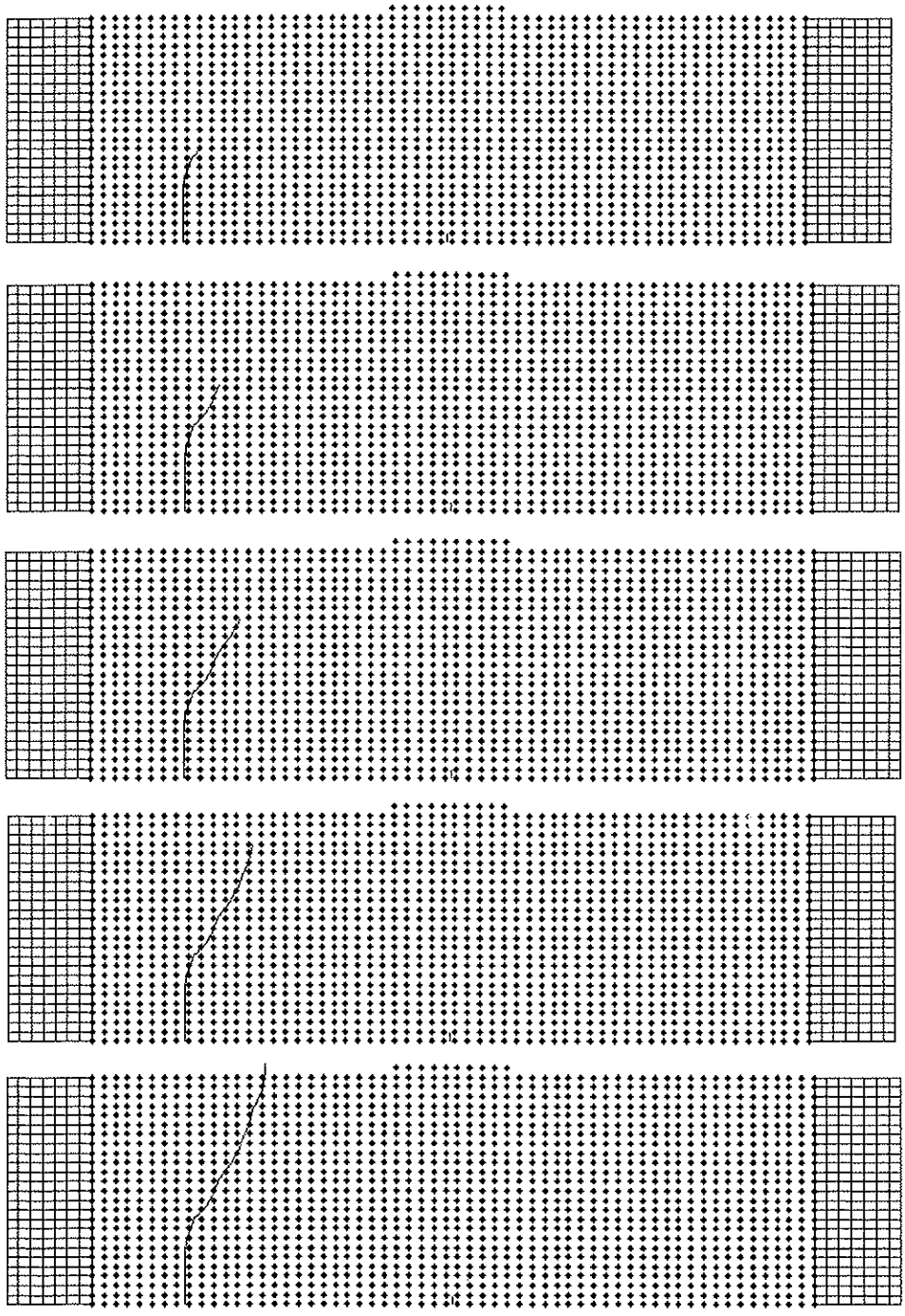

Figure 5.28: Illustration of the crack evolution for the simulation G0672C.

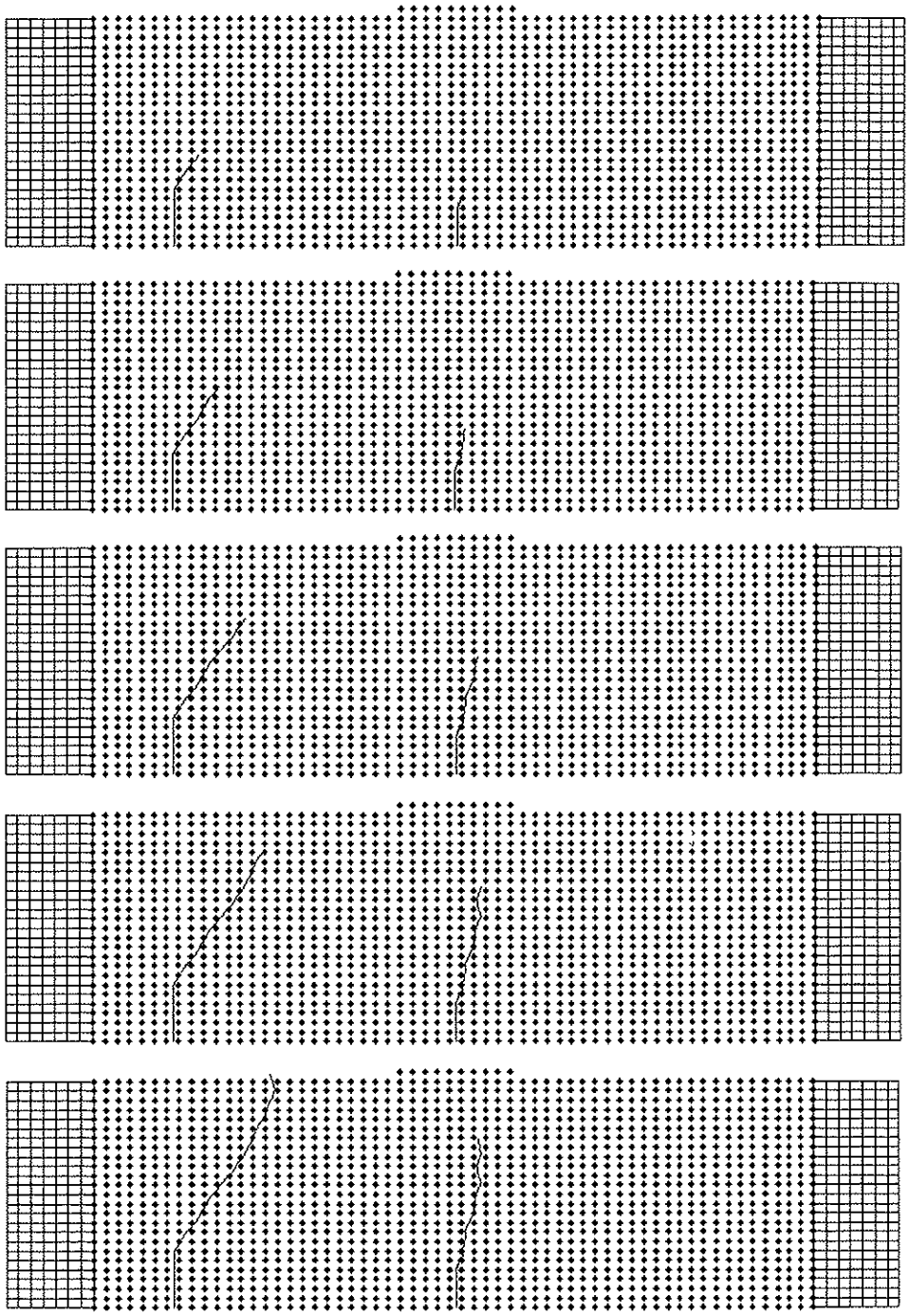

Figure 5.29: Illustration of the crack evolution for the simulation G0705C.

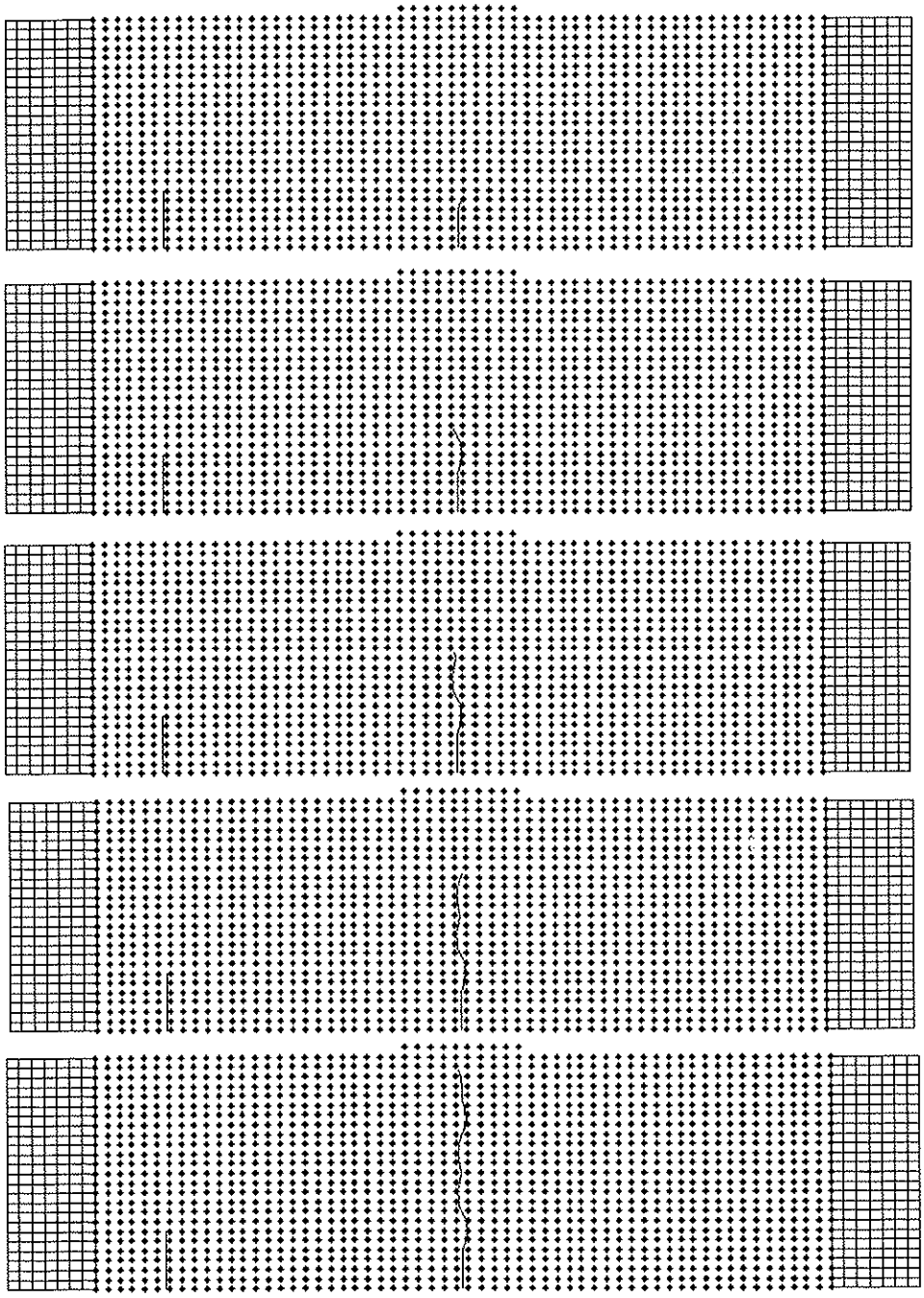

Figure 5.30: Illustration of the crack evolution for the simulation G0734C.

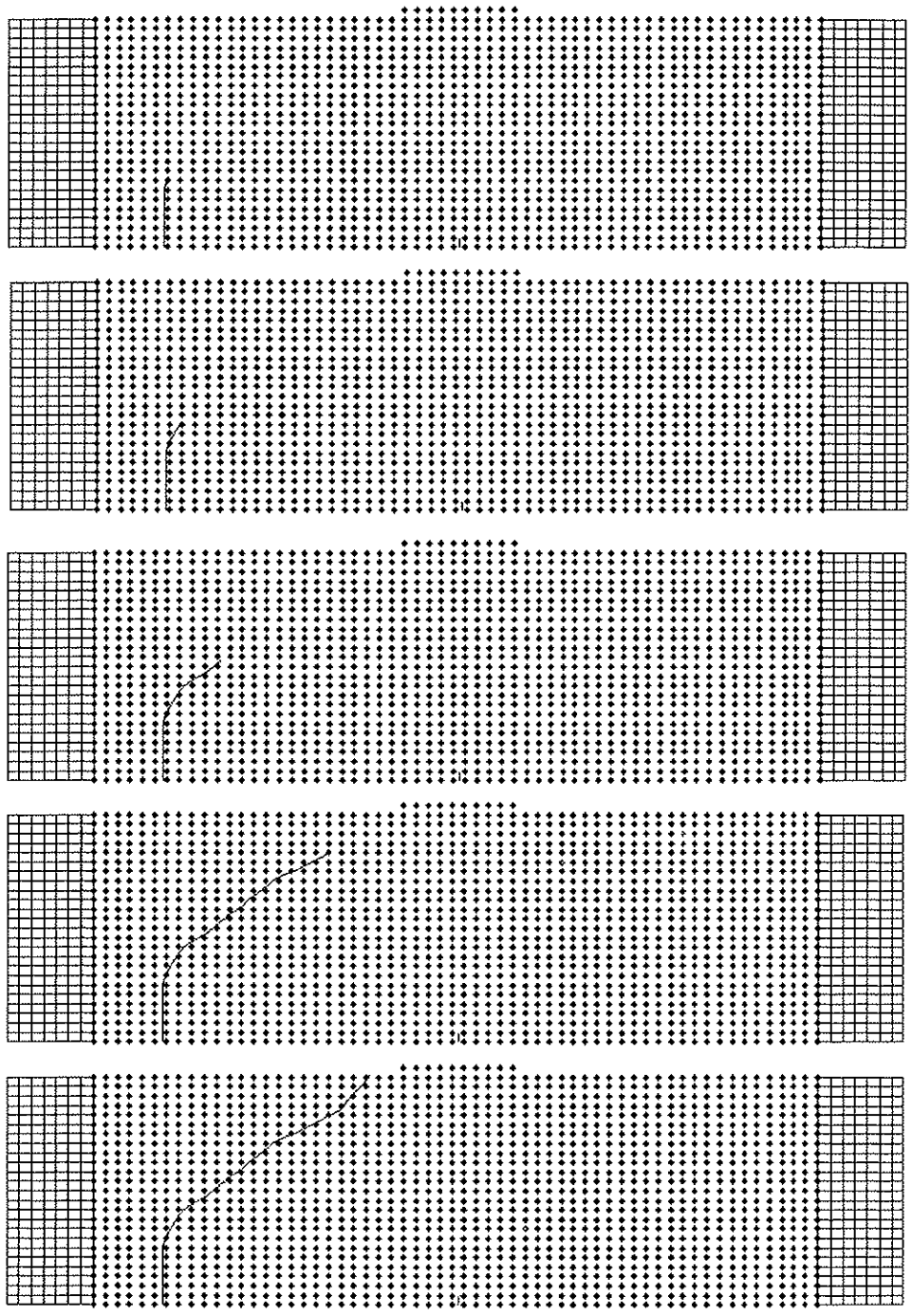

Figure 5.31: Illustration of the crack evolution for the simulation G0734V.

5.4 Numerical example of crack growth in an edge-cracked plate

5.4.1 Introduction

This example compares the numerical results obtained by the EFG simulations by Organ (1996) of the experiment performed by Kalthoff and Winkler (1987) with the numerical results from the EFG analysis performed in this study. The experiment consisted of a free plate of high strength steel, with to initial edge cracks and loading from a projectile that hits the plate (see Figure 5.32).

The simulation is performed for the experiment case with small strain rates, where the crack propagates with a crack angle about 70 degrees with respect on the initial crack line.

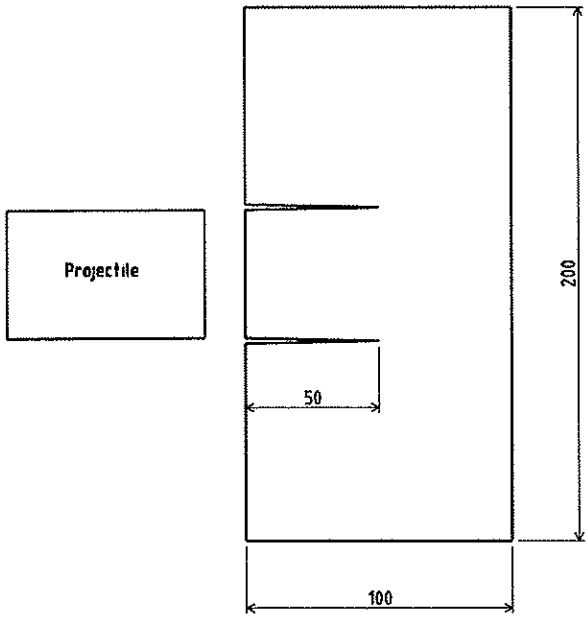

Figure 5.32: Illustration of the experiment performed by Kalthoff and Winkler (1987). A projectile that crashes into a free plate of steel.

5.4.2 Description of the numerical model

By using the symmetry in the experiment, only the upper half of the plate is modelled. The geometry of the numerical model is given by: the length of the plate (x-direction) = 100mm; the height of the plate (y-direction) = 100mm. The origin is placed at the center of the complete plate (see Figure 5.33). The plate is only supported at x=0 by symmetry conditions.

The material parameters used in the numerical simulation are: density ρ = 8000 kg/m^3; Young's modulus E = 190 GPa; Poisson's ratio ν = 0.30; and dynamic fracture toughness $K_{Ic} = 68\ \mathrm{MPa}\sqrt{\mathrm{m}}$.

The loading of the plate is prescribed velocity on the interface elements (see Section 2.5), imposed at the edge y = D/2 and in the range of $x \in [\Delta x, 25\mathrm{mm}]$. The reason that the x-range of the interface elements starts at $x = \Delta x = \dfrac{L}{\text{number of nodes} - 1}$, is that the present EFG code does not include interface elements at corners. This introduces a small error since the first node at x = 0 and y = D/2, should also be subjected to the imposed velocity trough an interface element at the top. In the following it is supposed that this source of error does not disturb significantly the results of interests (the error can be ignored as the element size becomes small). The velocity at the top nodes of the interface elements (FE nodes), is constant during the simulation with the value of v_0 = 16.5 m/s

Four EFG simulations have been performed for this problem. The analyses differ in the node densities: 31x31 nodes, 76x76 nodes, 101x101 nodes and 151x151 nodes. Rectangular Gauss cells are used for the numerical integration with the nodes limiting the cell areas. A 4x4 Gauss rule in the EFG- and interface- domain is adopted. The influence domain is limited by d_{max}=3.5 (see Section 2.2).

The numerical model has one predefined crack. The crack starts at the top of the plate at (x, y) = (25, 50) mm, and goes straightly down to (x, y) = (25, 0) mm. Then it goes a length of Δx in the negative y-direction by an angle of 70 degrees with the y-axes (see Figure 5.33).

The J-domain was square and covered an area equal to 4 Gauss integration cells. The crack tip is located in the center of the J-domain. All integration points inside the J-domain are used in the calculation of the stress intensity factors KI and KII.

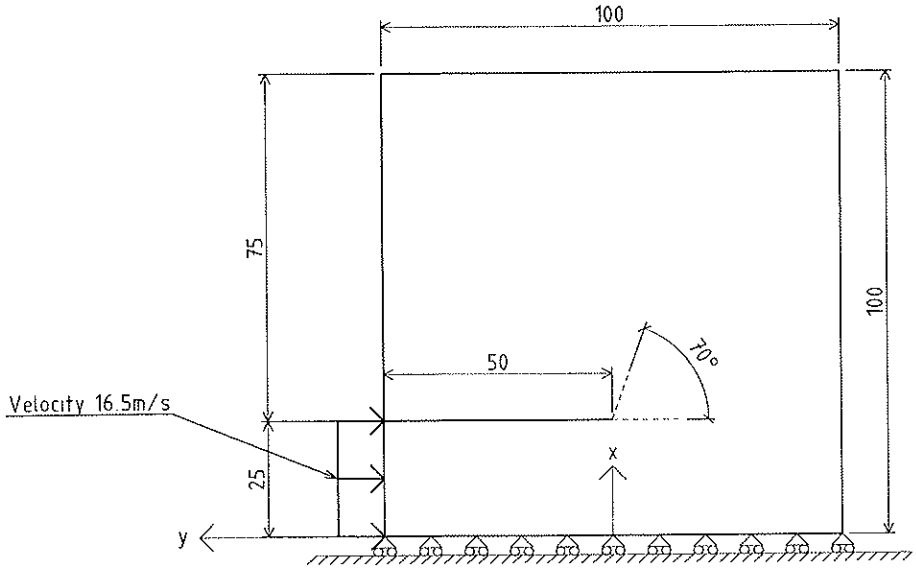

Figure 5.33: Illustration of the numerical model of the experiment performed by Kalthoff and Winkler (1987), with the geometry, origin location and boundary conditions plotted.

5.4.3 Specification of the simulation scheme

Since the numerical simulations of the plate are performed to verify the present code, the three analyses with the highest node densities are chosen to have the same node densities as reported in Organ (1996).

Table 5.12 gives the name of the different simulations and the node densities.

Table 5.12: Listing of identification and node densities of the different simulations.

Simulation name:	**Node density:**
M30	31 x 31 nodes
M75	76 x 76 nodes
M100	101 x 101 nodes
M150	151 x 151 nodes

5.4.4 Numerical results

The average angel of the crack path is defined as the angel between the predefined crack line and the line from the start of the crack propagation to the end point of the crack. Results of average crack path angles from the numerical simulations are given in Table 5.13. The results are in accordance with the results obtained by Organ (1996), which also tends towards higher angles compared with the experiment performed by Kalthoff and Winkler (1987) where the observed angle was 70°.

Figure 5.34 shows curves of normalized stress intensity factors for analyses M30, M75, M100 and M150. The drop of mode I stress intensity factor below zero at the beginning of the analyses is caused by the fact that the crack faces overlap each other at the beginning of the simulations. The plot of the stress intensity factors, given in Figure 5.34, converges towards similar curves of stress intensity factors reported in Organ (1996). Negative stress intensity factors at the beginning of the simulation are more pronounced in Organ than the simulations performed in this study. This is caused by the larger J-integral domain and the omitted pre-notch at an angle of 70° in the work by Organ. With larger J-integral domains and only a straight predefined crack path, more of the integrated domain contains overlapped crack faces.

In Figure 5.35, plots of the final crack paths for all analyses are shown. It can be observed that the M30 final crack path diverges slightly from the other solutions, which

also is emphasized by the deviation of the M30 stress intensity factors from the others shown in Figure 5.34.

Table 5.14 gives the number of crack segments and the range of the segment angle to the predefined crack line for all the analyses.

Figure 5.36 illustrates the crack path and the deformed numerical model of the experiment performed by Kalthoff and Winkler (1987) for analysis M75. The overlap of crack faces (caused of not having a contact description) is after some time dominating the numerical model, which then will diverge from the experimental result.

Table 5.13: Listing of identification and average crack angle for the different simulations.

Analyses:	**Average angle:**
M30	72.1
M75	75.2
M100	76.6
M150	75.4

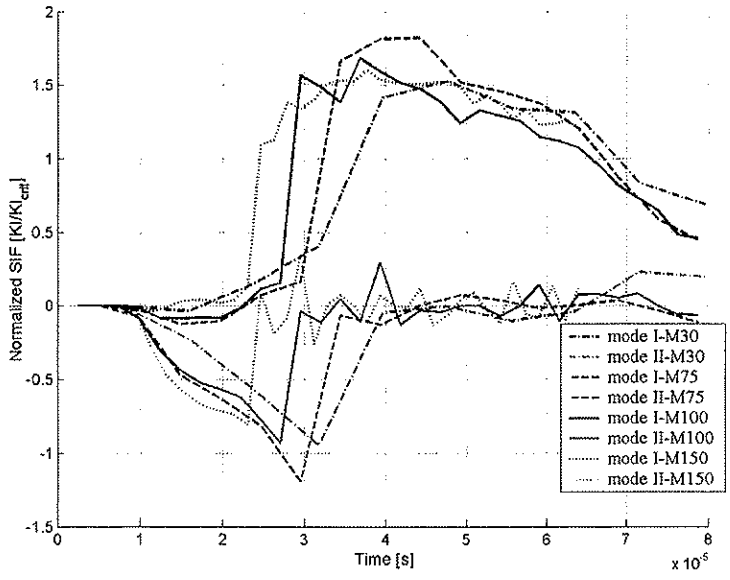

Figure 5.34: Stress intensity factor of mode I and mode II, for the four different simulations M30, M75, M100 and M150. The stress intensity factors are normalized with respect to the dynamic fracture toughness.

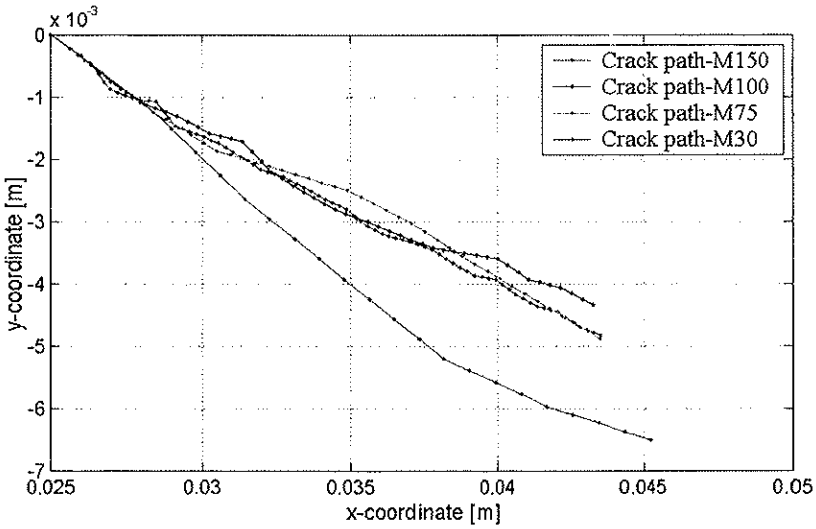

Figure 5.35: Plot of the final crack paths for all simulations of the experiment performed by Kalthoff and Winkler (1987)

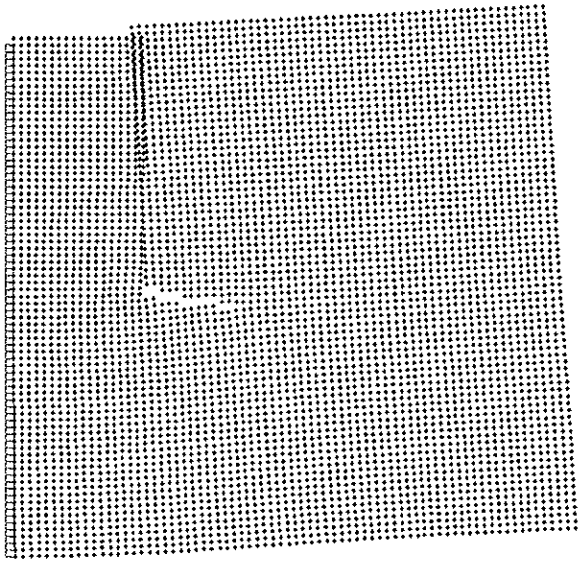

Figure 5.36: Illustration of the deformed numerical model, (magnification factor 10), of the experiment performed by Kalthoff and Winkler (1987) for simulation M75.

Table 5.14: Listing of identification, range of crack segment angle and number of crack segments for the numerical simulations.

Analyses:	**Range of crack segment angle:**	**Number of crack segments:**
M30	65.4 - 81.3	22
M75	69.2 - 81.8	42
M100	63.7 - 86.0	50
M150	59.5 - 85.4	77

5.5 Conclusive remarks

The numerical simulations performed in this chapter, are the basis for the verification procedure of the present code.

In Section 5.2 numerical simulations of a modified pendulum experiment by John, R. and Shah S. P. (1990) for concrete beams where studied. The 3-point bending of the concrete beam had one pre notch at the bottom of the mid span cross section. This differs from the experiment which in addition had another pre notch between the mid span and one of the supports. The numerical simulations provides the relationships between the different input variables of the analyses and the simulated results. In particular, the parameter that controls the frequency of updating of the stiffness matrix with respect to the crack path should be mentioned. Less frequent updating of the stiffness matrix results in an increase in the level of the oscillations in the simulated results. It should also be mentioned which variables that will considerably increase the consumption of computer time. The size of the domain of influence, d_{max}, and how frequent the stiffness matrix is updated during the simulation with respect to the propagating crack are the variables that mostly influence the required computer time. In addition the size of the predefined area where the crack propagation is allowed, will also considerably influence computer time. The node densities were fixed during the parameter study, but if the node densities were increased, the consumed computer time will of course increase. The parameter study performed in this section is useful to assess the results from the numerical simulation of the pendulum experiment by John, R. and Shah S. P. (1990) (see Section 5.3).

The numerical results of the analyses of the pendulum experiment were compared with numerical results from Organ (1996). The comparison of results was in relatively good agreement. It should be mention that the numerical results from this study showed more oscillations than reported by Organ (1996). The source of increased oscillations are likely to be the frequency of updating of the stiffness matrix with respect on the crack propagation (see Section 5.2.5). More detailed information on the input parameters for the analyses by Organ is needed for definite conclusion on this.

The verification example, reported in Section 5.4, was the numerical simulation of the experiment performed by Kalthoff and Winkler (1987). The experiment consisted of a free plate of high strength steel, with two initial edge cracks and loading from a

projectile that hits the plate. Organ (1996) has also simulated results with the EFG method for this experiment. The comparison of results showed relatively good agreement. It should be mentioned that the numerical results from this study showed slower convergence in the stress intensity factors than reported by Organ. The main reason is likely to be the use of lower order Gauss integration (4x4 compared with 6x6). Another possible reason of deviations is the use of more sophisticated representation of the stresses in the vicinity of the crack tip by Organ. Detailed information about this would be needed for a definite conclusion.

Since the comparison gave satisfactory results, it can, be concluded that the implemented code seems to work as it should, and that the theory implemented in the code is suited for this type of problems.

Chapter 6 Simulations prior to experimental study

6.1 Introduction

As discussed in the introduction of this thesis, the main aim of the work is to be able to simulate crack propagation in brittle materials. The previous chapter has demonstrated some of the capabilities of the present EFG code in simulation of brittle fracture.

In this chapter initial simulations prior to experiment are performed. The results of the simulations constitute the basis of the experimental set up. The purpose of the initial calculations is to define the experiments in the structural laboratory, such that the tests can produce crack patterns in brittle materials from dynamic load which can be compared with results from numerical simulations.

Since the EFG code is restricted to calculations of two dimensional numerical models the experiment must also have this limitation. A shear wall structure is thus chosen as model of investigation for the experiments. The crack pattern should arise from stress waves with relatively short durations, to be of relevance to cracking of unreinforced concrete from shock wave loading. The load is applied to one of the shear wall edges as an impact from a projectile. The applied force is thus in the shear wall plane. The shear wall is supported at each side of the edge opposite to the loading.

6.2 Experimental set-up

The experiment is performed in the structural laboratory at the Department of Structural Engineering, NTNU. A compressive pulse is applied to a concrete shear wall in the plane of the wall to obtain 2D conditions for crack propagation. Depending on the material, model geometry, pulse shape and magnitudes the compressive pulse can cause different crack patterns. The shear wall will behave according to plane stress theory. The experiment set up is illustrated in Figure 6.1. A compressive pulse is imposed by a projectile from a gas gun, see Figure 6.1. This will give a normal impact at the top

surface of the shear wall. The impact velocity range for this setup is 20 – 60 m/s, and the projectile mass will be in the range 100 – 230 grams.

Contact impact analysis has not been implemented in the present EFG code, but this analysis is done in the ABAQUS computer program. The result from the analysis is the time history of the contact pressure at the top of the shear wall. This excitation is then applied to the numerical model in the EFG simulation as a boundary time-force relationship. The simulations estimate the pulse magnitude that gives the desired crack pattern. Recalculations with ABAQUS give by tuning the projectile mass and impact velocity the contact pressure as a force time history to be applied in the EFG simulation.

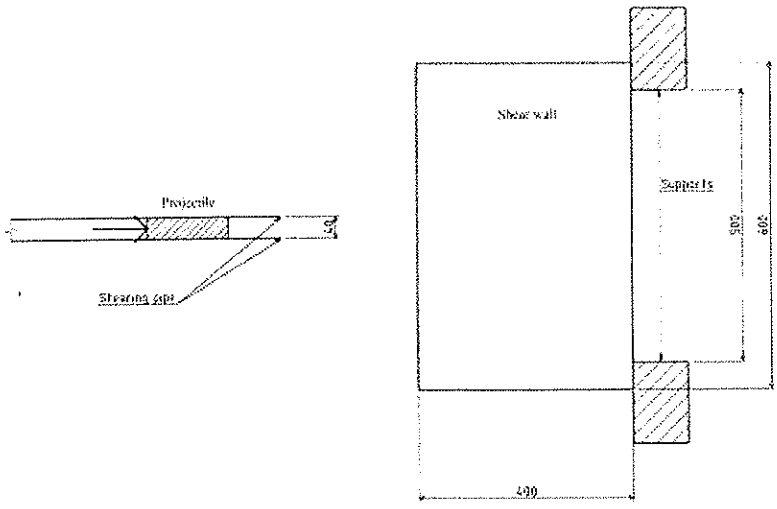

Figure 6.1: Illustration of the experimental set up.

6.3 Numerical simulation of elastic projectile impact

The intensity and duration of the contact pressure between a steel projectile and the concrete shear wall is to be calculated. In order to avoid (reduce) crushing of the concrete where the projectile hits the wall, a steel bar is placed on the top surface of the shear wall. The diameter of the projectile is fixed at 40mm, since the experiment should

be 2D the thickness of the shear wall is also chosen to be 40mm. This first pre calculation is considering shear walls with length 600mm and height 400mm and 250mm.The shear walls are supported at the bottom over a length of 50mm on both sides (the length and height of the steel bar at the top of the shear wall is 300mm and 10mm). Figure 6.2 shows the numerical models.

The concrete material parameters are: density $\rho = 2400 kg/m^3$; Young's Modulus $E = 30GPa$; Poisson's ratio $\nu = 0.2$. The steel material parameters are: density $\rho = 7850 kg/m^3$; Young's Modulus $E = 210GPa$; Poisson's ratio $\nu = 0.3$. The projectile mass and impact velocity is varied in the different analyses. The parameters are listed in Table 6.1 for both numerical models (height 400mm and height 250mm).

The peak stress level in an element at the center of the top boundary of the shear wall (location where projectile is hitting) versus projectile mass for the numerical model with height 400mm and height 250mm are plotted in Figure 6.3 and Figure 6.4 respectively.

Figure 6.5 and Figure 6.7 show correspondingly the time history plots of the vertical stress pulse from analyses a1 to a4 at the same location. The curves represent variation of the projectile mass with fixed projectile impact velocity of 30m/s. The maximum stress peaks show minor variation with small variations of projectile mass. The influence on pulse duration is more significant.

Stresses at the same location as a function of time are plotted by varying the projectile impact velocity for fixed mass of 0.175 kg in Figure 6.6 and Figure 6.8, respectively for the numerical models with height 400mm and 250mm. The maximum stress peaks are considerably influenced by the velocities due to the energy increase.

Figure 6.9 and Figure 6.10 show contact pressure in the plate middle plane at the top surface. The pressure is plotted along a horizontal straight 50mm long path (from the mid plan) for analysis a10 and for the plates with height 400mm and 250mm respectively. The contact pressures are plotted for the time instants t=[12, 15, 18, 21, 24, 27, 30]10^{-6}s for both analyses.

Contour plots of the stress in vertical direction at the time instant t=$57 \cdot 10^{-6}$s are correspondingly plotted for analyses a10 in Figure 6.11 and Figure 6.12. The assumption of 2D behaviour seems acceptable based on the constant stresses through the thickness of the shear wall as can be seen in Figure 6.11 and Figure 6.12.

The numerical model in ABAQUS consists of 30880 (height 400mm) and 28000 (height 250mm) elements of type C3D8R. This is an 8-node linear brick solid element with reduced integration. The total number of nodes in the models are 35971 (height 400) and 32812 (height 250), with 107913 and 98436 variables for the respective FE models. The dynamic analyses are performed with the explicit solver.

Table 6.1: Description of the different FE analyses performed with ABAQUS. The described analysis scheme is performed for both numerical models.

	M_P=0.175kg	M_P=0.200kg	M_P=0.225kg	M_P=0.250kg
Impact velocity=30 m/s	a1	a2	a3	a4
Impact velocity=40 m/s	a5	a6	a7	a8
Impact velocity=50 m/s	a9	a10	a11	a12
Impact velocity=60 m/s	a13	a14	a15	a16
Impact velocity=70 m/s	a17	a18	a19	a20

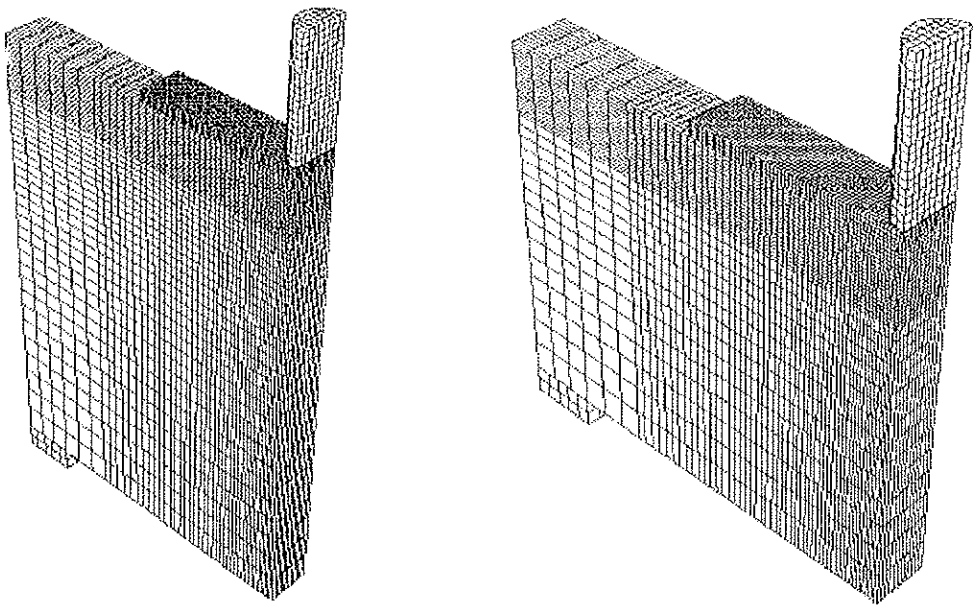

A) B)

Figure 6.2: Illustration of the numerical model used in the pre-calculations. A) is the 600x400 shear wall and B) is the 600x250 shear wall.

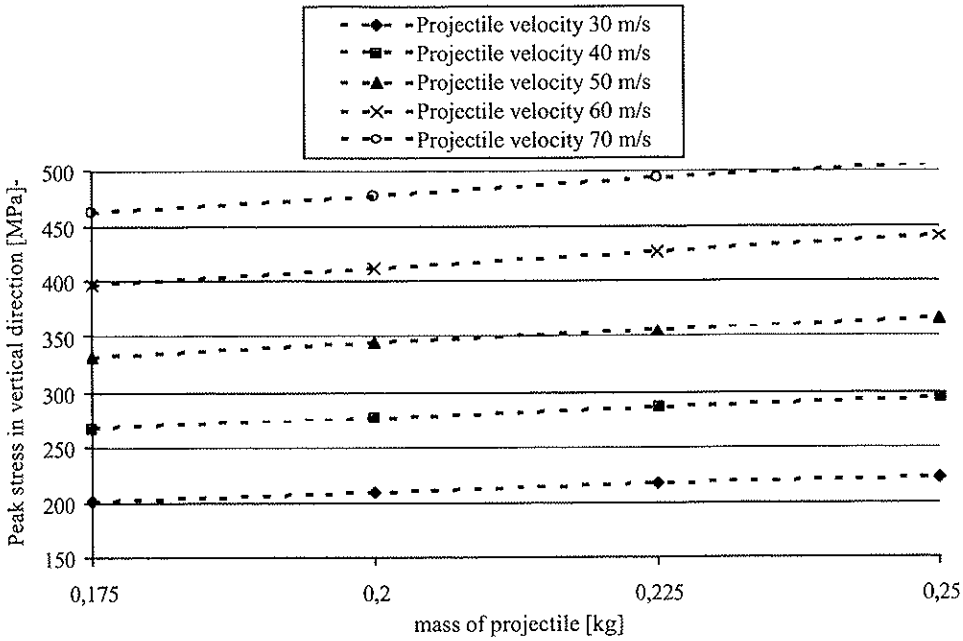

Figure 6.3: Plot of the peak stress in an element at the center of the top boundary of the shear wall versus projectile mass for the numerical model with height 400mm.

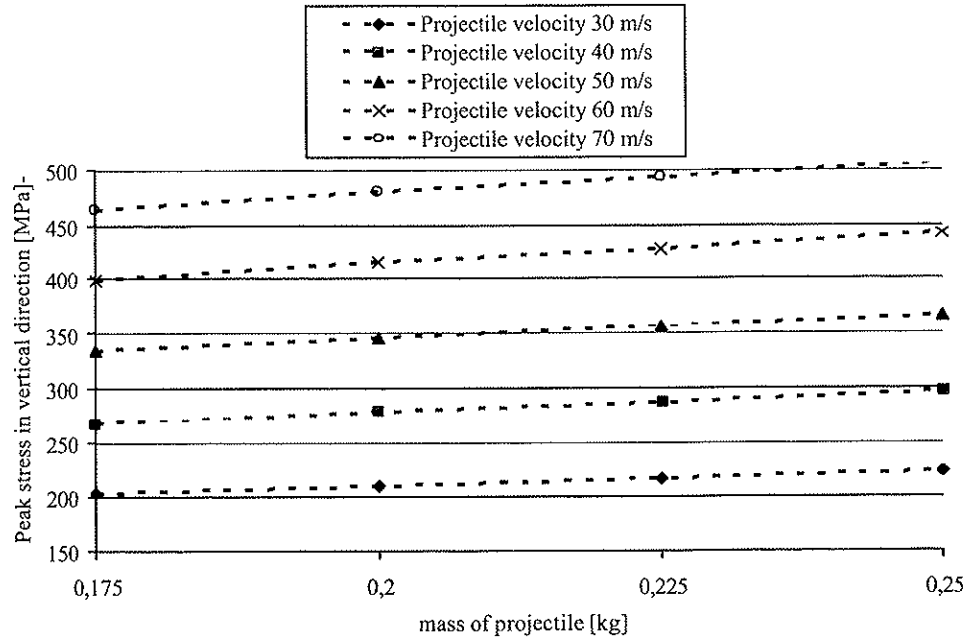

Figure 6.4: Plot of the peak stress in an element at the center of the top boundary of the shear wall versus projectile mass for the numerical model with height 250mm.

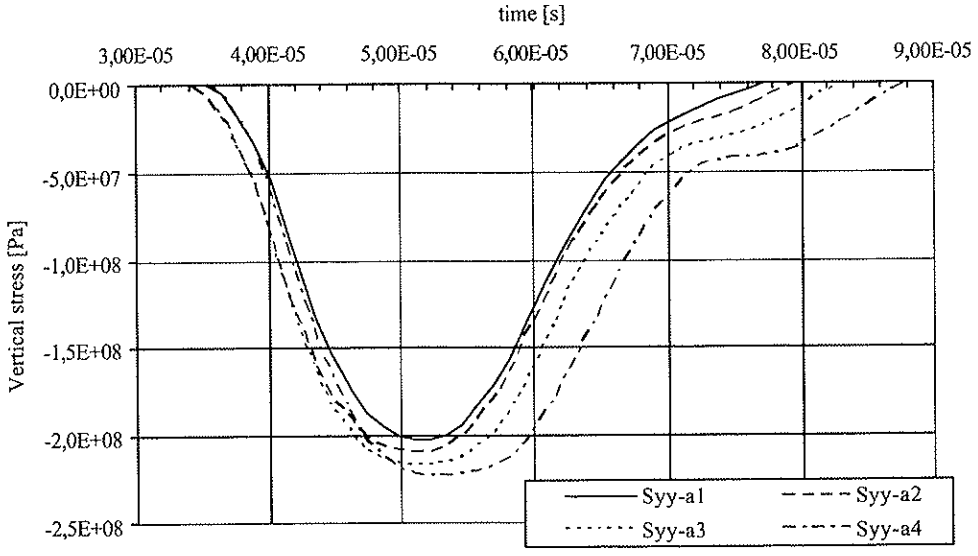

Figure 6.5: The curves show the vertical stress pulse for analyses a1 to a4 of the numerical model with height 400mm. The stresses are plotted for an element at the center of the upper boundary of the shear wall.

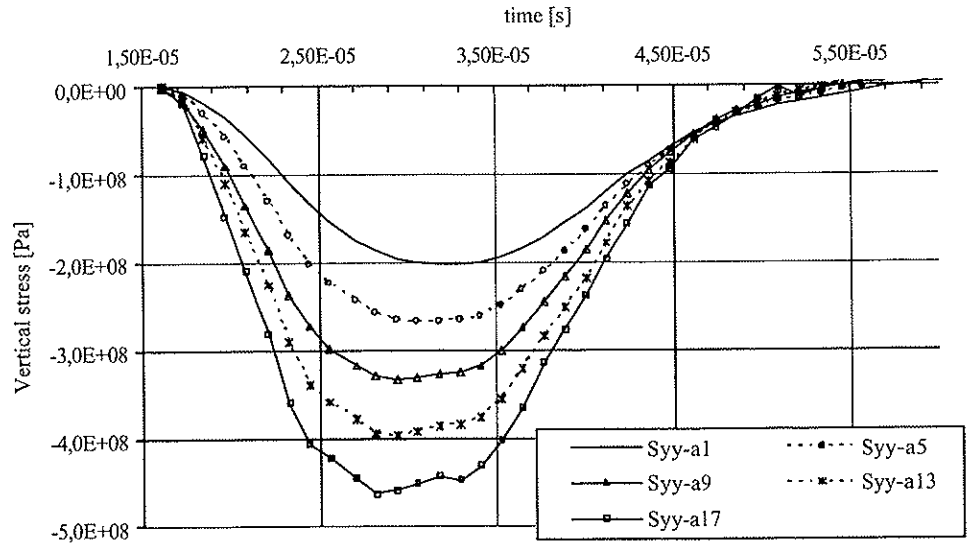

Figure 6.6: The curves show the vertical stress pulse for analyses a1, a5, a9, a13 and a17 of the numerical model with height 400mm. The stresses are plotted for an element at the center of the upper boundary of the shear wall.

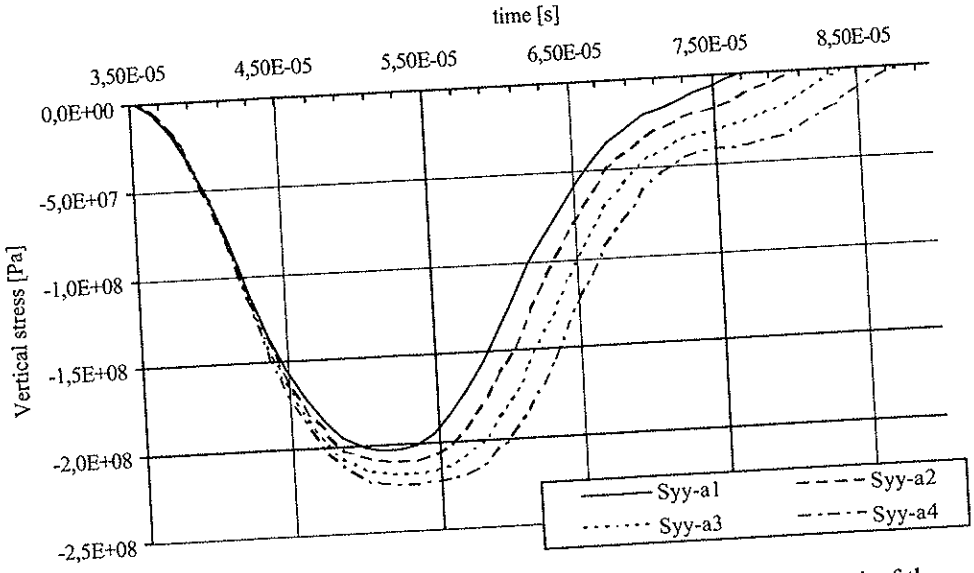

Figure 6.7: The curves show the vertical stress pulse for analyses a1 to a4 of the numerical model with height 250mm. The stresses are plotted for an element at the center of the upper boundary of the shear wall.

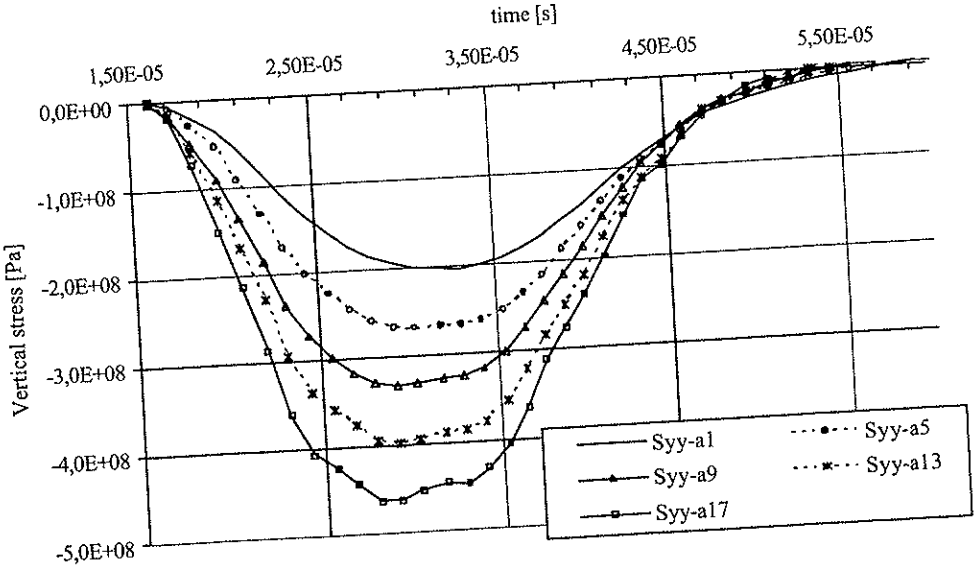

Figure 6.8: The curves show the vertical stress pulse for analyses a1, a5, a9, a13 and a17 of the numerical model with height 250mm. The stresses are plotted for an element at the center of the upper boundary of the shear wall.

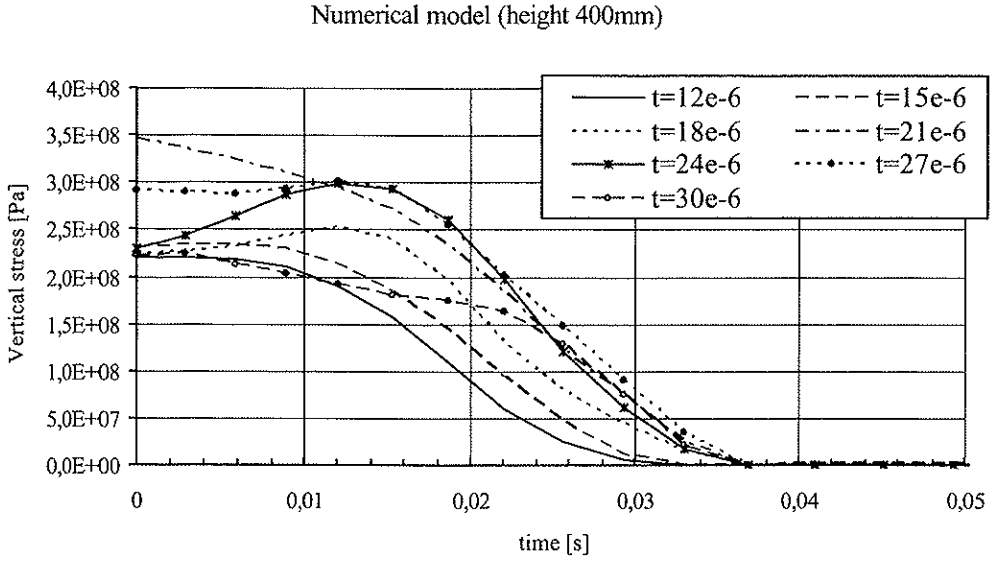

Figure 6.9 Plot of contact pressure in the plate middle plane at the top surface in horizontal direction for analysis a10 of the numerical model with height 400mm. The contact pressures are plotted for the time instants t=[12, 15, 18, 21, 24, 27, 30]10^{-6}s.

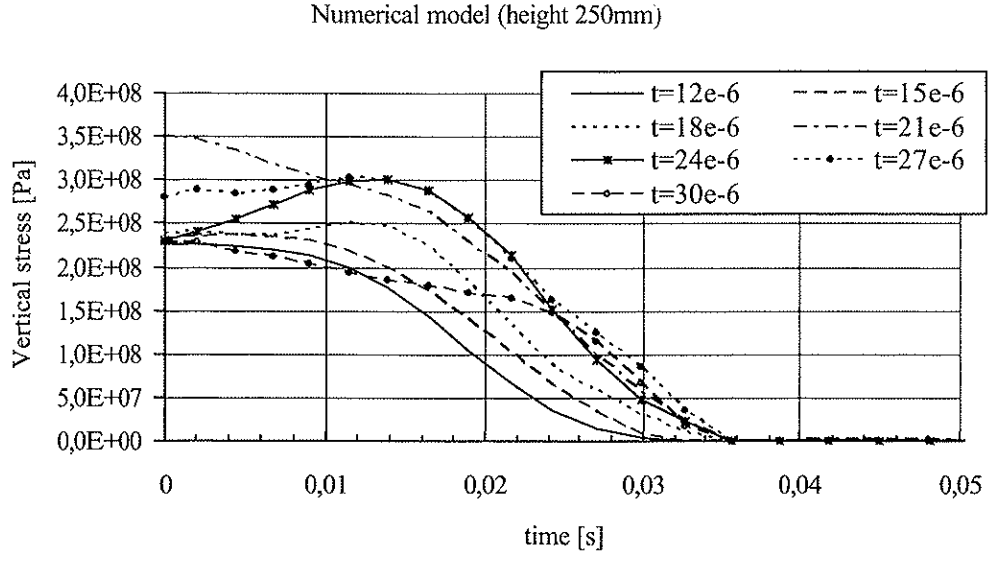

Figure 6.10: Plot of contact pressure in the plate middle plane at the top surface in horizontal direction for analysis a10 of the numerical model with height 250mm. The contact pressures are plotted for the time instants t=[12, 15, 18, 21, 24, 27, 30]10^{-6}s.

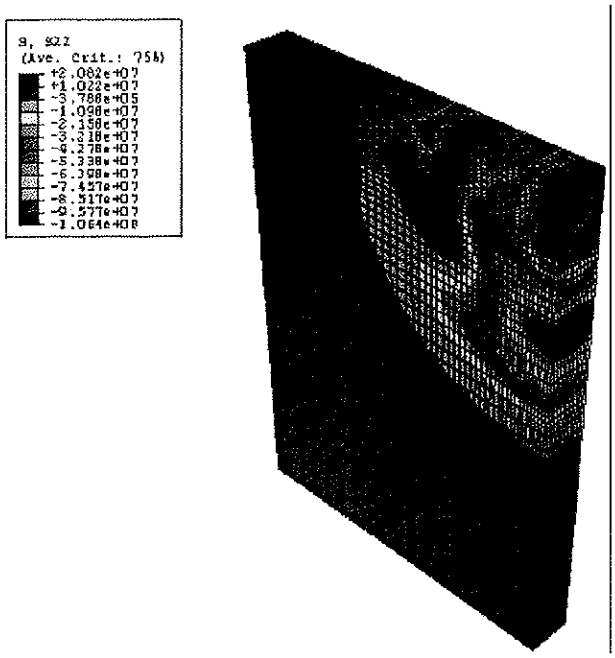

Figure 6.11: Contour plot of stress in vertical direction for Analysis a10 at the time instant $t=57\cdot10^{-6}$s, for the numerical model with height 400mm.

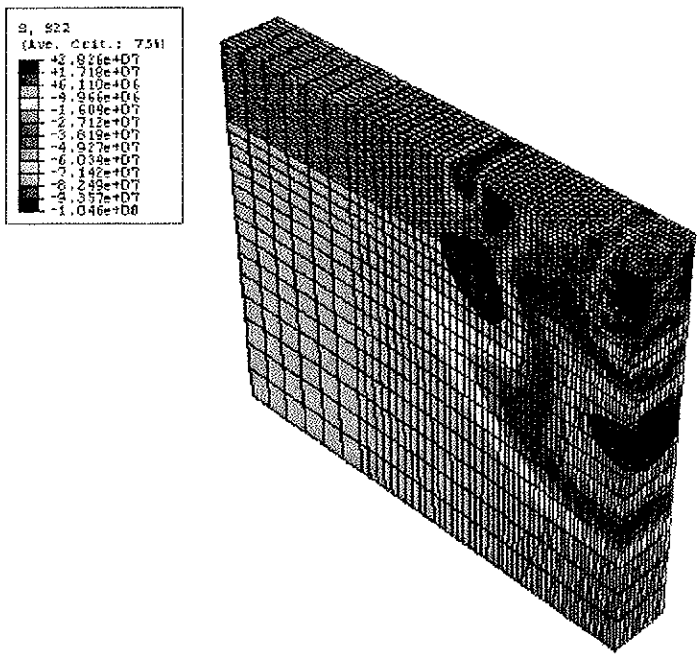

Figure 6.12: Contour plot of stress in vertical direction for Analysis a10 at the time instant $t=57\cdot10^{-6}$s, for the numerical model with height 250mm.

6.4 Crack propagation simulation with the EFG method and mixed mode fracture criterion

In this section the aim is to establish an EFG model of the shear wall based on the results from the calculations in the previous section. The simulations of the numerical models should result in crack patterns that can be verified by tests in the laboratory. The crack pattern from the EFG code is limited to contain one or two crack paths.

6.4.1 Numerical model characteristics

The concrete material parameters are the same as described in the previous section. In addition the dynamic fracture toughness will have the value $K_{Ic} = 0.8 MPa\sqrt{m}$, and the simulations will adopt a constant crack propagation velocity of 50 percent of the shear propagation velocity in the concrete. The constant fracture toughness is assumed based on the estimates given in Xu, S. and Reinhardt, H.W (1998).

The geometry of the shear wall and the node densities of the numerical models are varied in the different analyses as listed in Table 6.2 and Table 6.3 respectively for the numerical models with heights 400mm and 250mm. It is assumed that the crack starts at the mid section of the shear wall, since at this point the stress waves will cause the first exceedance of the concrete dynamic fracture toughness. The most likely location at the mid section for initiation of the crack propagation is investigated by a 10mm horizontal crack at different heights along the mid section of the shear wall. By comparing the mode I stress intensity factor between the different numerical calculations for the predefined 10mm horizontal cracks, the actual crack initiation is found.

The numerical models are plotted in Figure 6.13 and Figure 6.14. The length of the supports is approximately 50mm, and the width of the loading is approximately 30mm in all calculations. The width is calculated from the assumption that the loading area in the EFG numerical model should be equal to the loading area in the FE numerical model. This gives the loading width of 30mm in the EFG numerical model. The stress level of the loading is assumed constant over the width. This is a

simplification of the results from the FE analysis shown in Figure 6.9 and Figure 6.10. It is assumed to represent a close approximation. The assumption is based on the fact that the stress waves are circular and smooth when it reaches the crack propagation area, and since the energy is the important factor, the local intensity variations do not influence this picture significantly. The load intensity is given by:

$$\sigma(t) = \begin{Bmatrix} \sigma_1(T_1 - t)/T_p & \text{for } t \le T_1 \\ \sigma_1 = 0, & \text{for } t > T_1 \end{Bmatrix}$$

where $\sigma_1 = -250\text{MPa}$ and $T_1 = 1.0\text{ms}$ for the numerical model with height 400mm and $\sigma_1 = -300\text{MPa}$ and $T_1 = 1.0\text{ms}$ for the model with height 250mm. The pulse shape is assumed to have a triangular form, with the peak at t=0.0ms. The reason why T_1 is increased from the linear elastic impact simulated by ABAQUS, is the fact that the projectile will induce some ductile behavior at the top of the shear wall caused by the high peak stresses. The ductile behaviour and also other damping effects will tend to increase the pulse duration for a test in the laboratory. Time history plots of strain from the experiment will give the actual pulse shape and duration.

Table 6.2: Specifications of different EFG numerical models for the crack propagation analyses of the model with height 400mm.

Analysis name:	Length:	Height:	Node density:	Initial crack y-coordinate
A-600-400-a1	600mm	400mm	62 times 42 nodes	0mm from bottom
A-600-400-a2	600mm	400mm	62 times 42 nodes	50mm from bottom
A-600-400-a3	600mm	400mm	62 times 42 nodes	100mm from bottom
A-600-400-a4	600mm	400mm	62 times 42 nodes	150mm from bottom
A-600-400-a5	600mm	400mm	62 times 42 nodes	200mm from bottom
A-600-400-a6	600mm	400mm	62 times 42 nodes	250mm from bottom
A-600-400-a7	600mm	400mm	62 times 42 nodes	300mm from bottom

Table 6.3: Specifications of different EFG numerical models for the crack propagation analyses of the model with height 250mm.

Analysis name:	Length:	Height:	Node density:	Initial crack y-coordinate
A-600-250-a1	600mm	250mm	62 times 27 nodes	0mm from bottom
A-600-250-a2	600mm	250mm	62 times 27 nodes	15mm from bottom
A-600-250-a3	600mm	250mm	62 times 27 nodes	25mm from bottom
A-600-250-a4	600mm	250mm	62 times 27 nodes	35mm from bottom
A-600-250-a5	600mm	250mm	62 times 27 nodes	45mm from bottom
A-600-250-a6	600mm	250mm	62 times 27 nodes	55mm from bottom
A-600-250-a7	600mm	250mm	62 times 27 nodes	65mm from bottom
A-600-250-a8	600mm	250mm	62 times 27 nodes	75mm from bottom
A-600-250-a9	600mm	250mm	62 times 27 nodes	85mm from bottom
A-600-250-a10	600mm	250mm	62 times 27 nodes	120mm from bottom

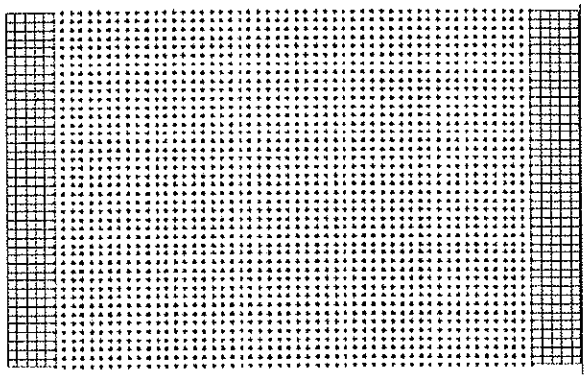

Figure 6.13: Plot of the numerical model for the analyses with height 400mm.

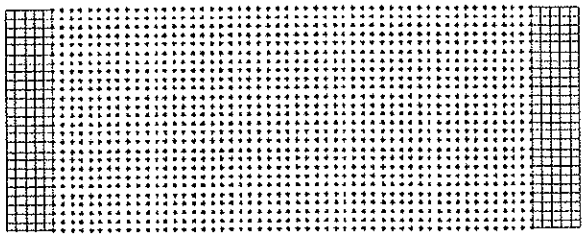

Figure 6.14: Plot of the numerical model for the analyses with height 250mm.

6.4.2 Results from EFG crack propagation simulation of the numerical model with height 400mm

The normalized mode I stress intensity factor for all the analyses with load intensity -250MPa and load duration 0.12ms of the numerical model with height 400mm are plotted in Figure 6.16. In Figure 6.17 are plotted normalized mode I stress intensity factors for the analyses with load intensity -250MPa with load duration 0.1ms.

The mode I stress intensity factor is calculated from the 10mm horizontal predefined crack at the mid section, i.e. no crack propagation. The purpose of these calculations is to identify the most likely location of the crack from which propagation will start in a numerical analysis. The crack starts to propagate at the location where the mode I stress intensity factor is larger than the material fracture toughness, K_{Ic}. The material fracture toughness has some dependence on the magnitude of the strain rates. In this study the material fracture toughness, K_{Ic}, is kept constant during the analyses.

As can be seen from Figure 6.16 (for the analyses with load intensity -250MPa and load duration 0.12ms) the location of the first crack to start propagation is at the bottom surface at the mid plan (SIF I-0cm, the solid line), where the normalized mode I stress intensity factor is greater than 1.0 for the first time at the time instant t=0.125ms. The normalized stress intensity factor is also grater than 1.0 at the time instant t=0.13ms for the predefined crack located at 205mm above the bottom surface (SIF I-20.5cm). For the case with load intensity -250MPa and load duration 0.1ms, the crack propagation starts at the horizontal crack 255mm above the bottom surface (SIF I-25.5cm) since the mode I stress intensity factor reaches the fracture toughness for the first time at this location. The crack starts to propagate at the time instant t=0.12ms. The vertical crack (SIF I-0cm, the solid line) is the second crack that starts to propagate, and the crack initiation is at the time instant t=0.125ms. The tendency for this load intensity is that for the shortest load duration the horizontal crack will start higher above the bottom surface than for the longer load duration. However, it can be expected that both the vertical and the horizontal crack will start almost at the same time instant after the projectile impact, and that the horizontal crack starts to propagate 200mm to 250mm above the bottom surface at the mid plane

The analysis where the crack propagation is allowed is performed with predefined cracks at the bottom surface and 205mm above the bottom surface at the mid cross section. The predefined cracks will have the possibility to propagate during the analysis. The applied load intensity is -250MPa. The finial crack pattern for this analysis is plotted in Figure 6.15 with red lines. Deformation plots of the model at different time instants are presented for analysis A-600-400-a5 in Appendix D. Contour plot of the normal stresses in y-direction (S_{22}) at corresponding time instants are also presented in Appendix D.

It can be observed that the final crack paths are not exactly symmetric about the mid cross section of the shear wall. The reason for this is shown in Figure 6.18 by the difference in the stress intensity factor curves for the left end (end 1) and the right end (end 2) points of the crack path. The mode I stress intensity factor should be the same for both end points, but the mode II stress intensity factor will have opposite signs for a idealized symmetric case. Since the vertical crack follows a zig zag path it would induce some non-symmetric stress waves which can cause the non-symmetric horizontal crack pattern. The solution is also sensitive to the artificial oscillations in the model after the first crack propagation starts. This is indicated also by the curves in Figure 6.18, which are almost identical before the crack starts to propagate (intersection with the red dotted line at 1.0) followed by deviations between the curves. Refinement of the nodes and especially shortening of the time intervals between updating of the stiffness matrix during crack growth will decrease the artificial oscillations (see section 5.2.5).

Figure 6.15 shows the final crack path for the analysis A-600-400-a5 with load magnitude -250MPa.

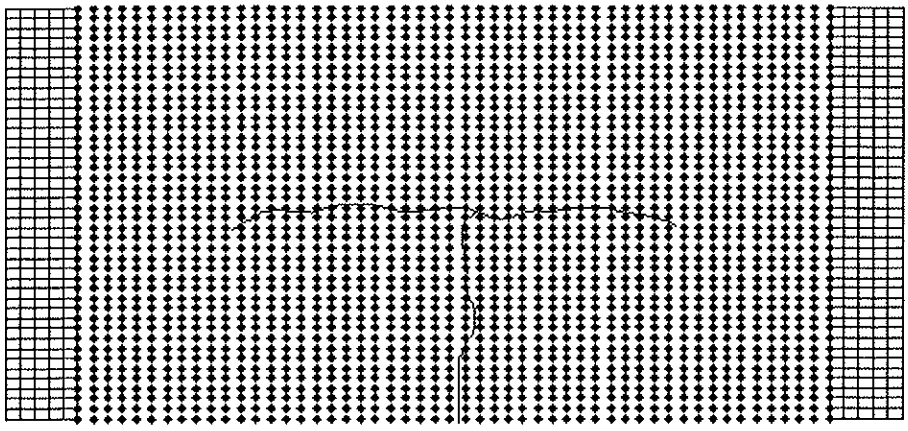

Figure 6.15: Plot of the final crack path for the analysis A-600-400-a5 with load intensity -250MPa and load duration 0.12ms.

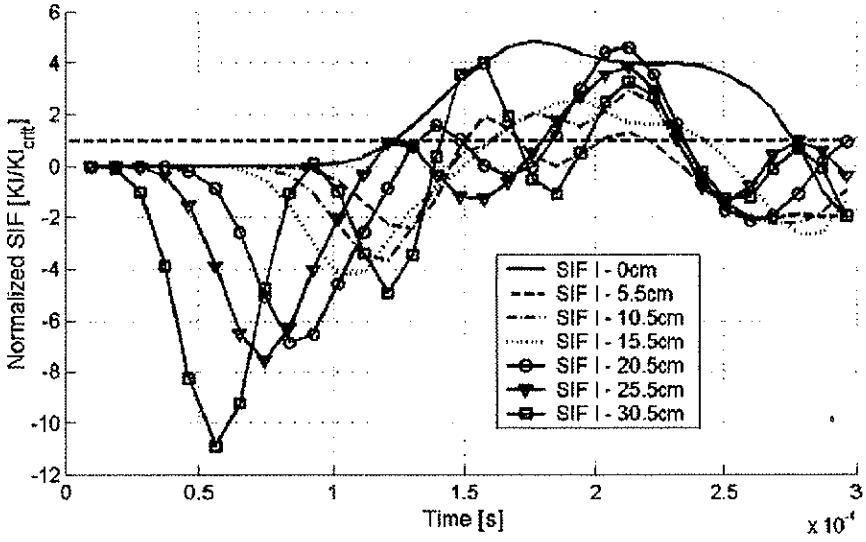

Figure 6.16: The curves show normalized mode I SIF for all the analyses of the numerical model with height 400mm and time history stress peak of 250MPa with load duration 0.12ms.

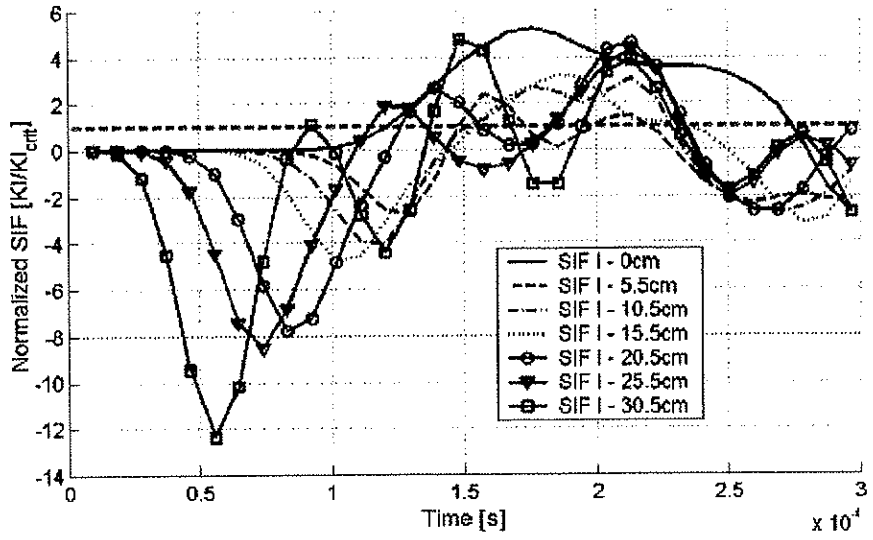

Figure 6.17: The curves show normalized mode I SIF for all the analyses of the numerical model with height 400mm and time history stress peak of 250MPa with load duration 0.1ms.

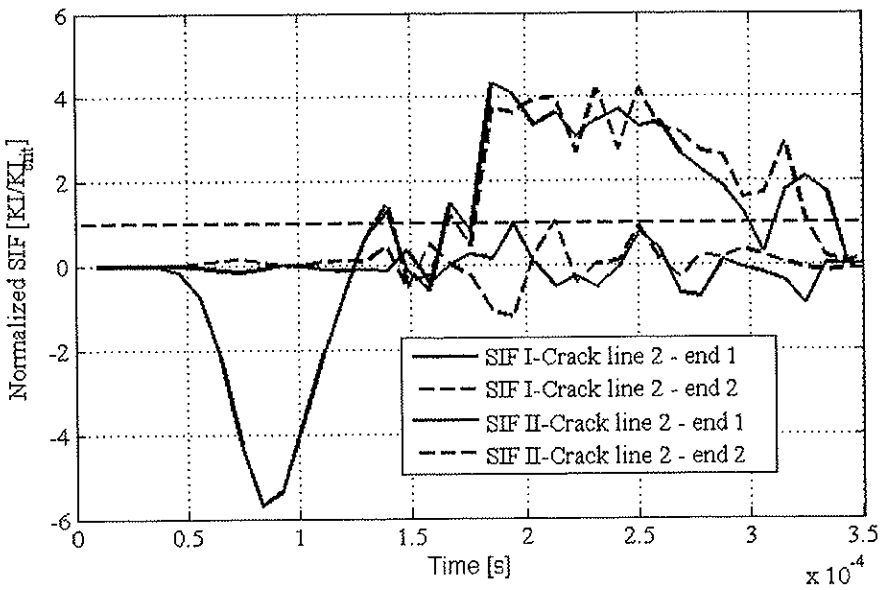

Figure 6.18: Plot of the normalized mode I and mode II stress intensity factors (SIF) for analysis A-600-400-a5 with load magnitude -300MPa at both ends of crack line 2 (200mm above bottom surface).

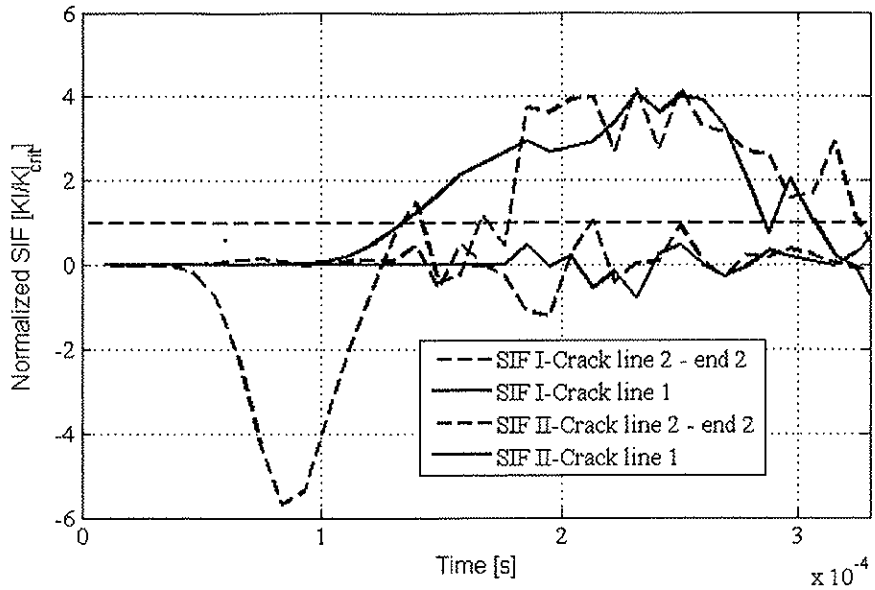

Figure 6.19: Plot of the normalized mode I and mode II stress intensity factors (SIF) for analysis A-600-400-a5 with load magnitude -300MPa for crack line 2 (200mm above bottom surface) at end 2 and crack line 1 (vertical crack from bottom surface at mid cross section).

6.4.3 Results from EFG crack propagation simulation for the model with height 250mm

The normalized mode I stress intensity factor for all the analyses of the numerical model with height 250mm are plotted in Figure 6.20. In Figure 6.21 and Figure 6.22 corresponding curves are plotted except for the crack at the bottom surface SIF I-0cm. The mode I stress intensity factors are calculated fom a 10mm horizontal predefined crack at the mid section, i.e. no crack propagation. The same arguments as for the simulation with shear wall height 400mm are valid for this simulation. The crack starts to propagate at the location where the mode I stress intensity factor is greater than the material fracture toughness, K_{Ic}. As can be seen in Figure 6.20 the location of the first crack propagation is at the bottom surface at the mid plan (SIF I-0cm, the solid line), where the normalized mode I stress intensity factor is greater than 1.0 for the first time at the time instant t=0.08ms. The normalized mode I stress intensity factor for the predefined crack 55mm above the bottom surface at the mid plane (SIF I-5.5cm) is the

second curve that intersects the red dotted line (at 1.0) at the time instant t=0.1035ms, see Figure 6.21 and Figure 6.22. It should be mention that the crack initiation can also start from a crack in the range from 45mm to 85mm measured from the bottom surface. This is because the mode I stress intensity factors in this range intersect the fracture toughness line at almost the same time instant (see Figure 6.22). Small disturbances of the loading or variations in material properties in an experiment may be enough to move the crack initiation from the 55mm location.

The aim of this experiment is to be able to predict a case with spalling from the bottom side of the shear wall, i.e. no vertical crack along the mid cross section. Reinforcement close to the bottom surface of the shear wall can hopefully avoid the vertical crack to dominate the crack pattern.

A simplified crack propagation simulation for the reinforcement case is performed with a predefined crack 55mm above the bottom surface at the mid cross section, and without any crack from the bottom surface. This is based on the assumption that the reinforcement prevents the vertical crack to evolve and that the reinforcement bars do not considerably disturb the stress waves propagation in the shear wall. The applied load magnitude is 300MPa. The finial crack pattern for this analysis is plotted in Figure 6.24 with red lines. Deformation plots of the model at different time instants are plotted for Analysis A-600-250-a6 in Appendix D. Contour plots of the normal stresses in y-direction (S_{22}) are plotted correspondingly in Appendix D.

It can also be observed that the final crack pattern is almost exactly symmetric about the mid section of the shear wall (see Figure 6.24). In more detail this is supported by the curves of the stress intensity factors in Figure 6.23. It is seen that the mode I stress intensity factor is almost equal for both endpoints of the crack path and that the mode II stress intensity factor has the same magnitude but with opposite sign. This is correct for the symmetric case. The small deviations in stress intensity factors for both end points may result from artificial oscillations.

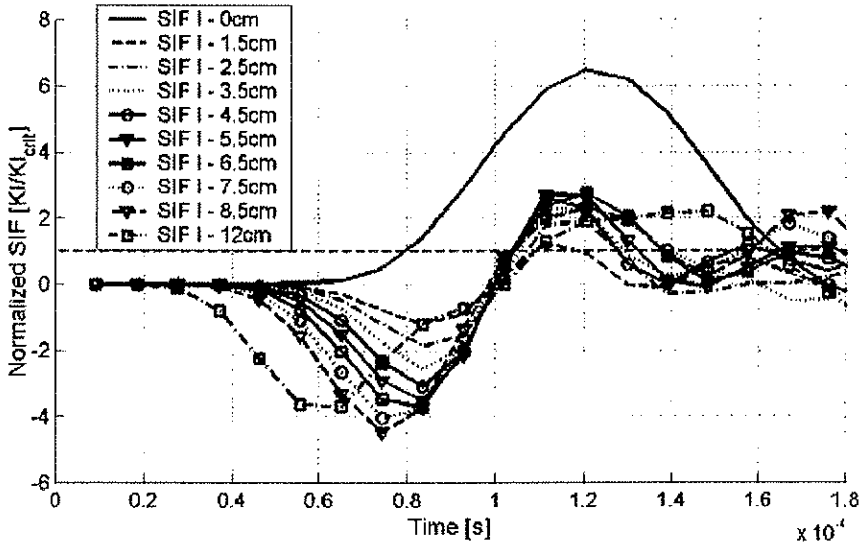

Figure 6.20: The curves show normalized mode I SIF for all the analyses of the numerical model with height 250mm, and the time history stress peak of 300MPa.

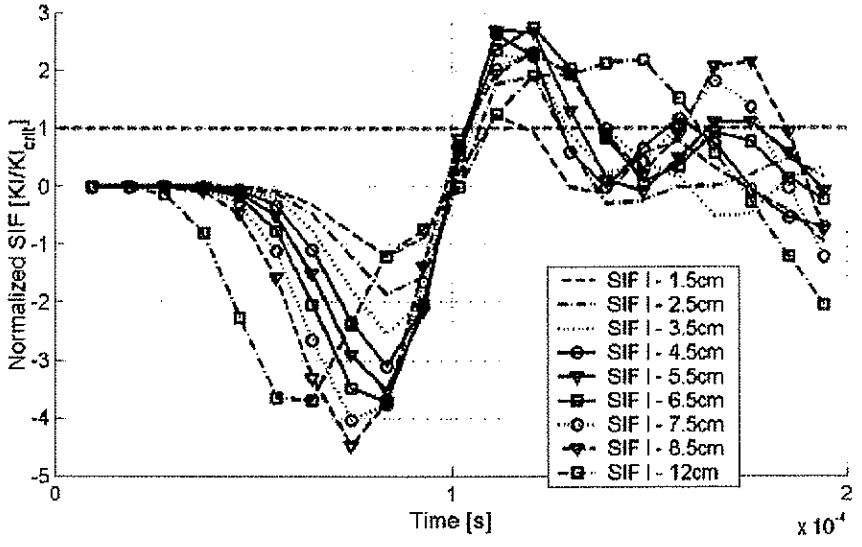

Figure 6.21: The curves show normalized mode I SIF for all the analyses of the numerical model with height 250mm (except SIF I-0cm), and time history stress peak of 250MPa.

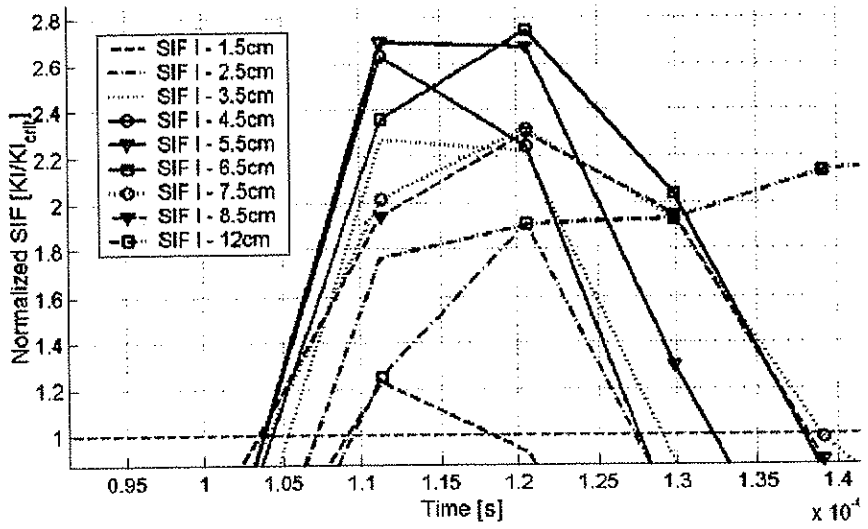

Figure 6.22: The curves show normalized mode I SIF for all the analyses of the numerical model with height 250mm (except SIF I-0cm), and time history stress peak of 250MPa.

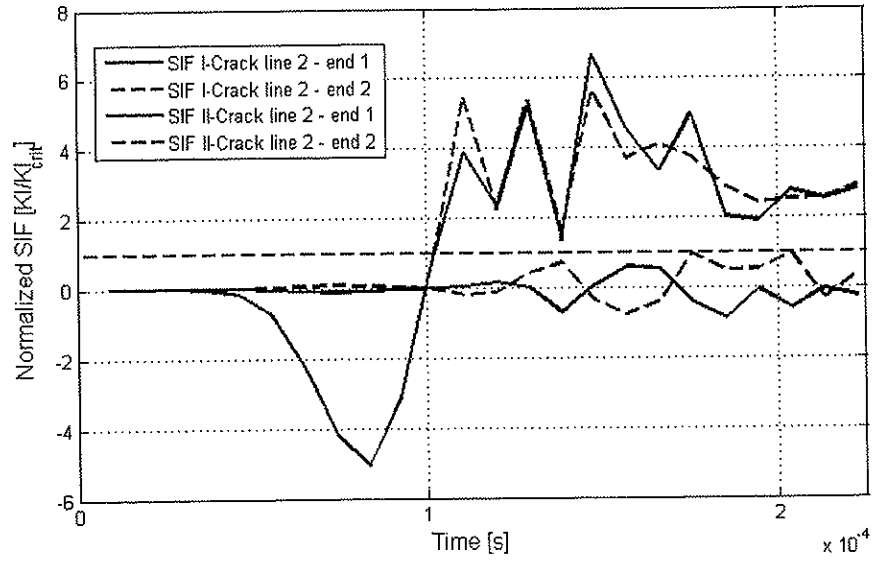

Figure 6.23: Plot of normalized mode I and mode II stress intensity factors (SIF) for Analysis A-600-250-a6 at both ends of the crack line 1. The left end corresponds to the solid line. The red dotted line is the fracture toughness limit.

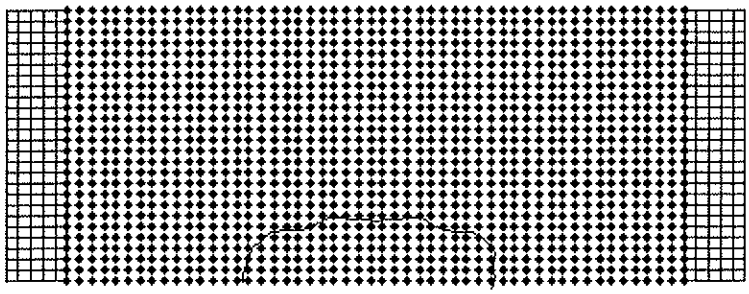

Figure 6.24: Plot of the final crack path for the A-600-250-a6 analysis.

6.5 Description of the experimental set-up

The experiments are based on the numerical simulations reported in the previous sections. Two series of experiments are conducted for shear wall heights 400mm (Experiment 1) and 250mm (Experiment 2) respectively.

The numerical simulations do not take into account any possible increase in the fracture toughness due to high strain rates. This could be a source of error and will be discussed in the next chapter. The effect of possible increase in the pulse duration due to yielding of the material or other damping effects is approximately accounted for by a duration increase of 0.5ms. The actual pulse duration will be measured in the experiment by strain gages.

Results from the experiments should verify the numerical simulations within the range of uncertainties comprised in the numerical modeling and the experiments

6.5.1 Experiment series 1

From the results obtained with ABAQUS (see Section 6.3) it is possible to estimate the impact velocity and projectile mass for the experiment. Figure 6.3 shows this relationship. An impact velocity of 35-45m/s for a mass of 0.2 kg corresponds to a load peak of -250MPa. It is expected that the horizontal crack starts to propagate approximately 200mm to 250mm above the bottom surface at the mid plane.

Based on the previous calculations the proposal for the experimental model is:

- shear wall length 600mm, height 400mm and thickness 40mm
- the impact velocity 35-45m/s and projectile mass approximately 0.2kg
- circular projectile impact area with diameter 40mm
- support extension 50mm at each side of the shear wall

6.5.2 Experiment series 2

For the crack pattern from the numerical simulation (see Section 6.4.3), a ridge shaped concrete part may loosen from bottom of the shear wall. The time history load peak was -300MPa. In this case the expected impact velocity and mass for the experiment is found in Figure 6.4. The curves give an impact velocity of 40-50m/s for a mass of 0.2 kg. For that impact velocity it is expected that the horizontal crack starts to propagate approximately 55mm above the bottom surface (or in the range between 45mm and 85mm, as discussed in Section 6.4.3).

Based on the previous calculations the proposal for the experiment set-up is:

- shear wall length 600mm, height 250mm and thickness 40mm
- impact velocity 40-50m/s, and projectile mass approximately 0.2kg
- circular projectile impact area with diameter 40mm
- support extension 50mm at each side of the shear wall

Chapter 7 Shear wall experiment

7.1 Introduction

This chapter discusses the shear wall experiments. The parameters for each test set-up are specified, and the corresponding results are reported. The experiments are also simulated with the EFG code based on the actual input parameters from the experiment.

The execution of the experiments is not a part of this study. They have been handled by the structural laboratory at NTNU.

7.2 Experiment I

The experiment is described in the next section, followed by listing of results in Section 7.2.2 and numerical results from the EFG code in Section 7.2.3.

7.2.1 Description of Experiment I

The experiment set-up is sketched in Figure 7.1. A digital picture from the structural laboratory of the shear wall test specimen, strain gages and the gas gun barrel opening is shown in Figure 7.2. A picture of the velocity measuring equipment (red lights) is shown in Figure 7.3.

The shear wall length is 600mm, the height is 400mm and the thickness is 40mm for the three test specimens of Experiment I. Material tests to determine the concrete material parameters were performed on the same day as the shear wall experiments for the actual test specimen. The Young's modulus and the Poisson's ratio are listed in Table 7.1. Tests of the fracture toughness and the crack propagation velocity were not performed.

The shear wall is supported at both ends over a length of 50mm, see Figure 7.1. On the shear wall side where the impact will take place, a 300mm long, 40mm wide and 10mm thick steel bar is embedded in the concrete. This steel bar is reducing crushing at the concrete surface when the steel projectile is impacting by distributing the contact pressure against the concrete. The projectile is cylindrical with a diameter of 40mm. It is made of steel and its weight is listed in Table 7.1.

Strain gauges are located on the shear wall surface at the points P_1 and P_2. Both points has a radial distance of 150mm from the center of the steel bar top surface (see Figure 7.1).

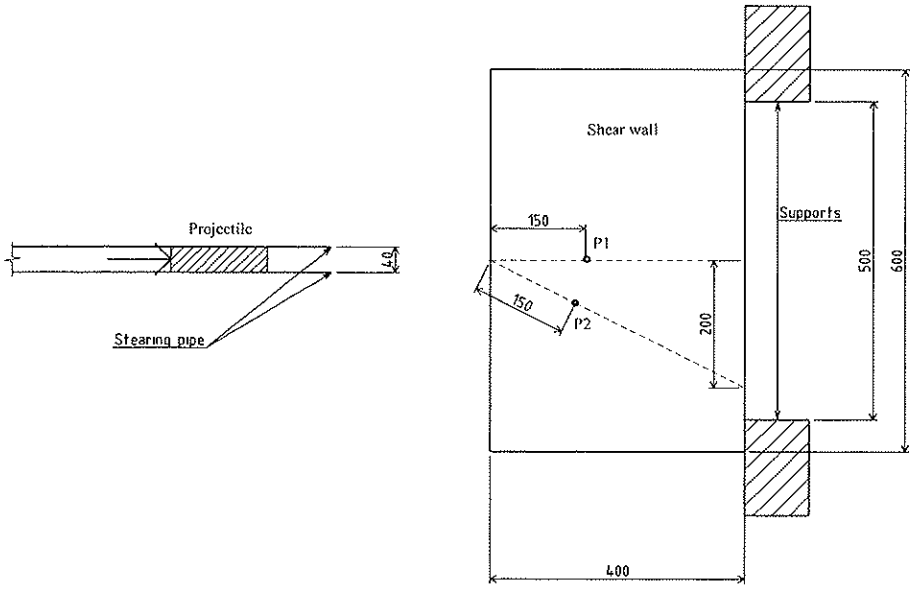

Figure 7.1: Sketch of the shear wall experiment set-up.

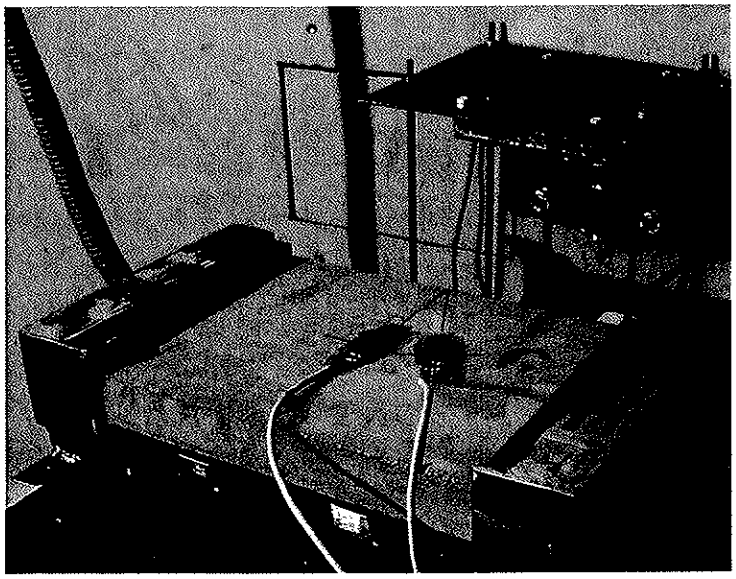

Figure 7.2: Picture from the testing chamber of the gas gun equipment with the shear wall, strain gages and the gas gun barrel opening.

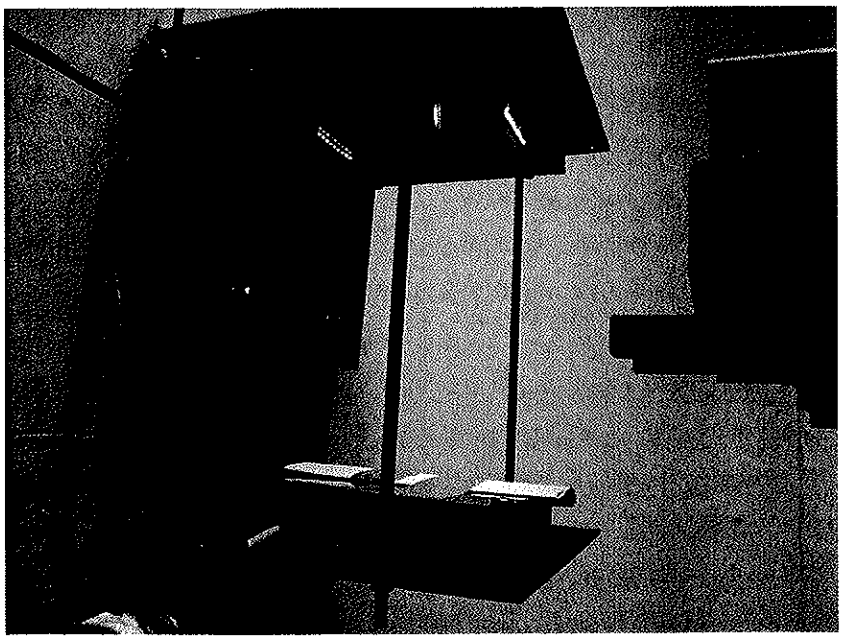

Figure 7.3: Picture of the gas gun barrel connection to the test chamber and the velocity measure equipment (red lights). Mounting of the test specimens to the right.

Table 7.1: Listing of parameters for each shear wall test case, for Experiment I.

Test	Mass projectile kg	Velocity projectile m/s	E-modulus shear wall GPa	ρ shear wall kg/m^3	ν shear wall
1	0.2102	40	31.4	2400	0.2
2	0.2225	51.4	31.4	2400	0.2
3	0.2193	47.2/39.8	31.4	2400	0.2

7.2.2 Results of Experiment I

The results of each test case of the shear wall Experiment I are presented as plots of the final crack patterns and time history curves of the vertical strain at P_1. Table 7.2 lists references to figures with results for each test case.

The vertical strain at P_1 has peaks from $0.5 \cdot 10^{-3}$ to $0.8 \cdot 10^{-3}$, and pulse durations from 0.08ms to 0.12ms for all tests. Figure 7.7 shows curves of the vertical strain time histories for Tests 1, 2 and 3 at point P_1. The most reliable result is from Test 1, because the results are from one single shot that resulted in the crack pattern shown in Figure 7.4. For Test 2 the plotted crack pattern given in Figure 7.5 is a result of 4 consecutive impacts. No cracking was seen from the first three impacts, but internal cracks have most likely occurred. The finial crack pattern for this test is different from Test 1. The projectile mass and velocity is higher for the last impact, which also can be a source of the difference in results between the two tests. From the digital picture of the test specimen, Figure 7.5, a larger area with plastic deformations in the vicinity of the impact together with higher level of plastification of the embedded steel bar at the top surface of the shear wall is observed. This is a result of significantly larger impact energy in Test 2 than for Test 1. The last test, Test 3, got a vertical crack at the first shot and a horizontal crack in the second shoot. This is also a different behaviour compared with what was observed in Test 1. A consequence of these results is that Test 1 gave the most reliable result, and will be the best test to compare with a numerical solution. It should, however be noticed that the crack patterns of the three tests are similar, see Figure 7.4, Figure 7.5 and Figure 7.6

The pictures of the crack pattern are taken when all the cracks have stopped propagating after the impact, and give no information of the crack path sequence. A short description of the three different cracking procedures is listed below:

- Test 1: the vertical crack length is approximately 150mm and the curved horizontal (horizontal at initiation) crack length is approximately 400mm and it intersects the mid plane approximately 200mm above the bottom surface. Both crack paths evolved simultaneously from one projectile impact. The crack pattern is almost symmetrical about the mid plane.
- Test 2: the vertical crack length is approximately 225mm and the inclined horizontal (horizontal initially) crack length is approximately 385mm. The horizontal crack intersects the mid plane approximately 223mm above the bottom surface. Both crack paths developed simultaneously at the second projectile impact.
- Test 3: the vertical crack length is approximately 116mm and the horizontal (at initiation) crack length is approximately 360mm. The horizontal crack intersects the mid plane approximately 165mm above the bottom surface. For the projectile impact velocity of 47.2m/s, the vertical cracks started to propagate. The horizontal cracking occurs for the next shot with projectile impact velocity of 39.8m/s.

Table 7.2: Reference to result plot for each test case.

Test:	Crack pattern:	Time history:
1	Figure 7.4	Figure 7.7
2	Figure 7.5	Figure 7.7
3	Figure 7.6	Figure 7.7

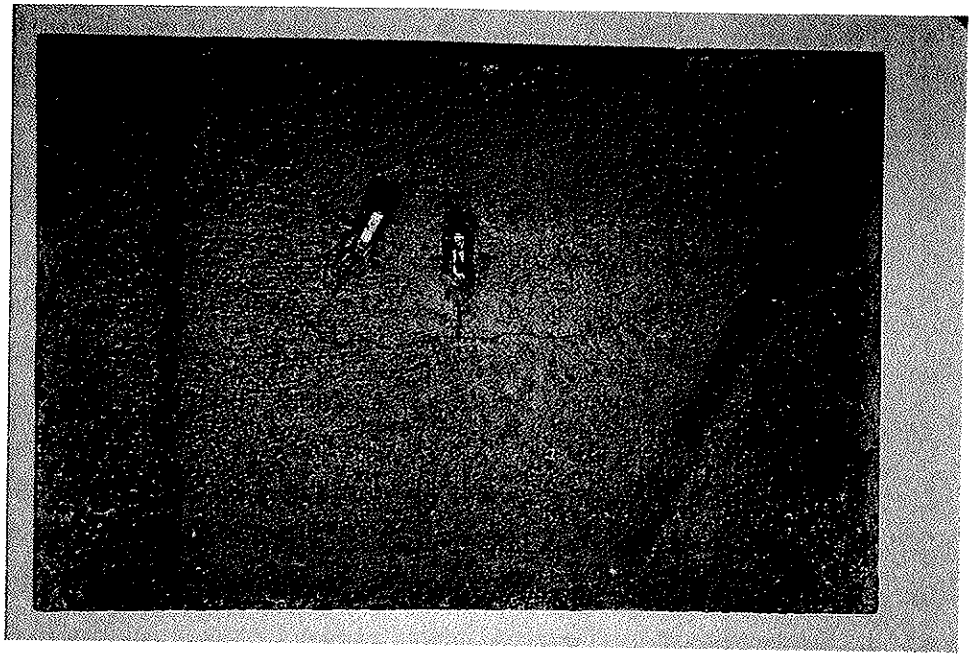

Figure 7.4: Digital picture of the final crack pattern for Test 1.

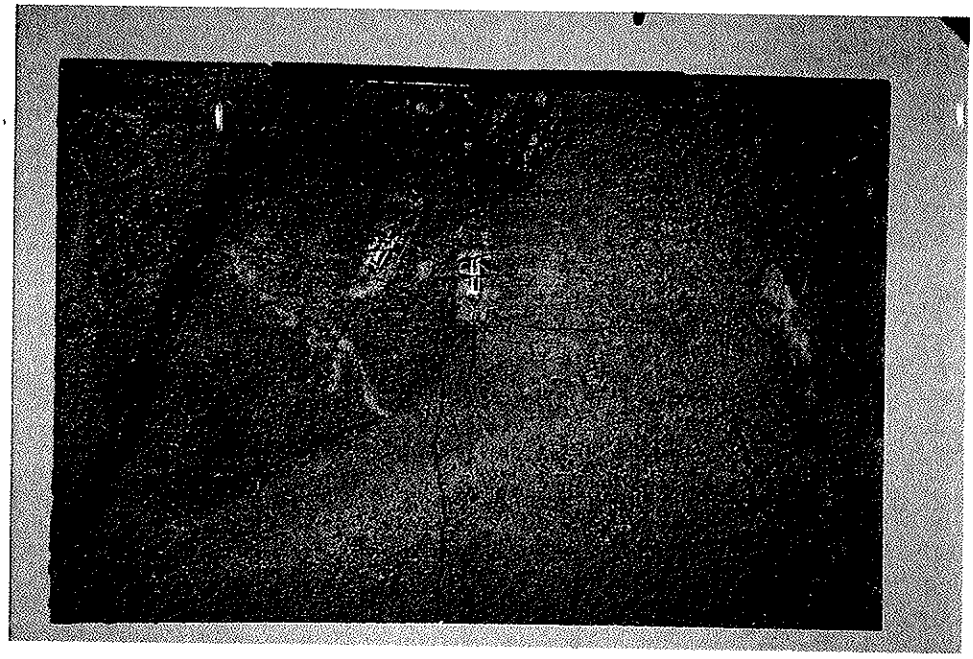

Figure 7.5: Digital picture of the final crack pattern for Test 2.

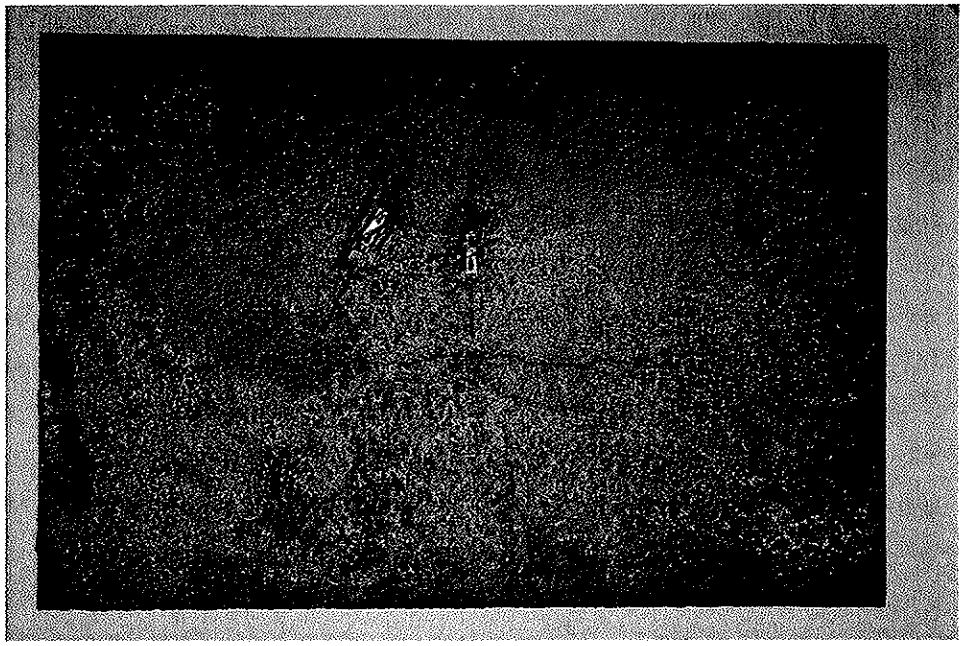

Figure 7.6: Digital picture of the final crack pattern for Test 3.

7.2.3 Numerical simulation of Experiment I with the EFG code

Based on the results from the shear wall Experiment I, only a few parameters are modified from the initial simulation. Table 7.3 lists the parameters that are changed in the numerical re-simulation of the shear wall. The time history parameters of the load intensity for the re-calculation are:

$$\sigma(t) = \begin{cases} \sigma_1 (T_1 - t)/T_1, & \text{for } t \le T_1 \\ \sigma_1 = 0, & \text{for } t > T_1 \end{cases}$$

where σ_1=-250(-350)MPa and T_1=0.12(0.10)ms. The load function parameters for the re-calculations are listed in Table 7.4. The correctness of this load can be valued by studying the vertical strain time history curves from the experiment plotted together with the corresponding strain curves from the initial numerical simulations, see Figure 7.7. This comparison shows that the elastic impact (F250-T12-ABAQUS) gives higher

strain magnitude and shorter pulse duration than measured for the experiments. This may be a result of the plastic impact, which is related to plastification of the steel plate and projectile together with the crushing of the concrete. The strain time history for the EFG simulation, F250-T12-EFG, has also too high strain magnitudes but the pulse duration is more like the measured pulse duration. If the measured values are correct the comparisons can indicate that the fracture toughness utilized in the numerical simulations is somewhat high, since the crack pattern is similar with too high strain magnitudes. It should be noticed that the raise-time of the strain time history for the EFG simulation is too long compared with the applied time history load, which indicates that the distance between nodes and the time increments could be reduced to obtain more accurate solutions. This has, however, not been done because of the uncertainties in the test parameters and the considerably increase of computer time for such simulations.

The crack pattern from the re-calculations with the above modified parameters is plotted in Figures 7.8 and 7.9. The crack patterns in the numerical simulations are similar to the crack pattern from the tests performed in the laboratory. The horizontal crack paths from the test cases curve slightly upwards, which differ from the numerical simulations where it curves downwards or is almost horizontal. For the simulations F250-T10-Vc05, F250-T10-Vc05 and F250-T10-Vc05 the downward curving is smaller. This indicates that shorter pulse duration and relatively high crack propagation speed bring the numerical results closer to the results from the laboratory tests. It should be emphasized that this is only an indication, and with the limited basis from the laboratory results and the performed numerical simulations there are still uncertainties.

Table 7.3: Experiment specification for both initial- and re-simulations.

Parameter:	**Initial simulation:**	**Re-simulations:**
Shear wall length	600mm	600mm
Shear wall height	400mm	400mm
Shear wall thickness	40mm	40mm
Shear wall support length	50mm	50mm
Shear wall E-module	30.0GPa	31.4GPa
Shear wall density, ρ	2400 kg/m^3	2400 kg/m^3
Shear wall ν	0.2	0.2
Steel bar E-module	210GPa	210GPa
Steel bar density, ρ	7850 kg/m^3	7850 kg/m^3
Steel bar ν	0.3	0.3

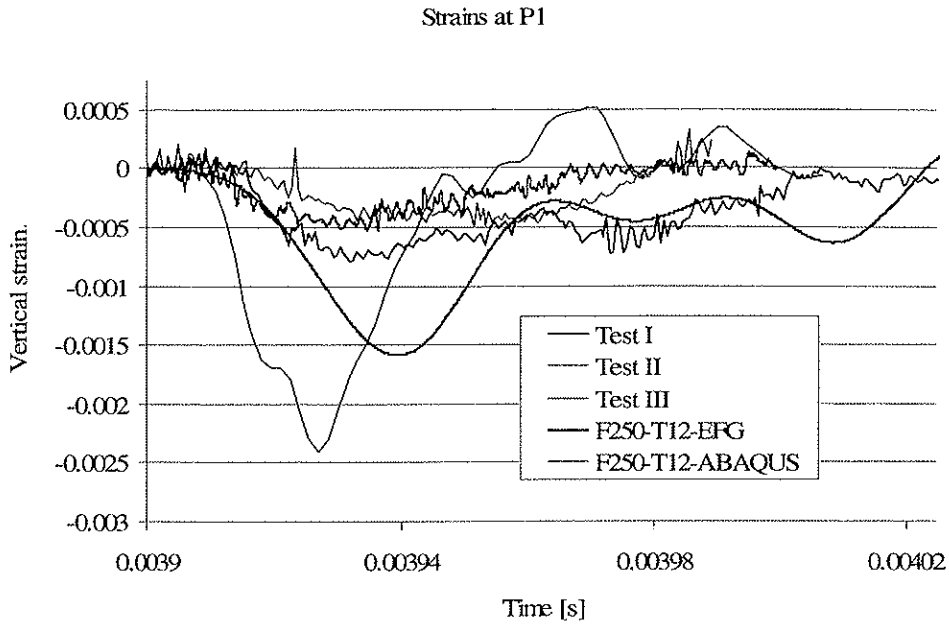

Figure 7.7: The curves show the time history of the vertical strain from the strain gages located at P_1 in the surface of the shear wall, and the vertical strain in P_1 from EFG and FE analysis with peak magnitude -250MPa respectively curves F250-T12-EFG and F250-T12-ABAQUS.

Table 7.4: Listing of the analysis name, load function parameters and crack speed utilized in the re-calculations.

Analysis name	**Magnitude on the surface load [MPa]**	**Duration time of the surface load [e-5s]**	**Crack speed [fraction of shear wave speed]**
F250-T10-Vc05	-250	10	0.5
F250-T12-Vc03	-250	12	0.3
F250-T12-Vc05	-250	12	0.5
F250-T12-Vc07	-250	12	0.7
F250-T12-Vc05	-350	12	0.5

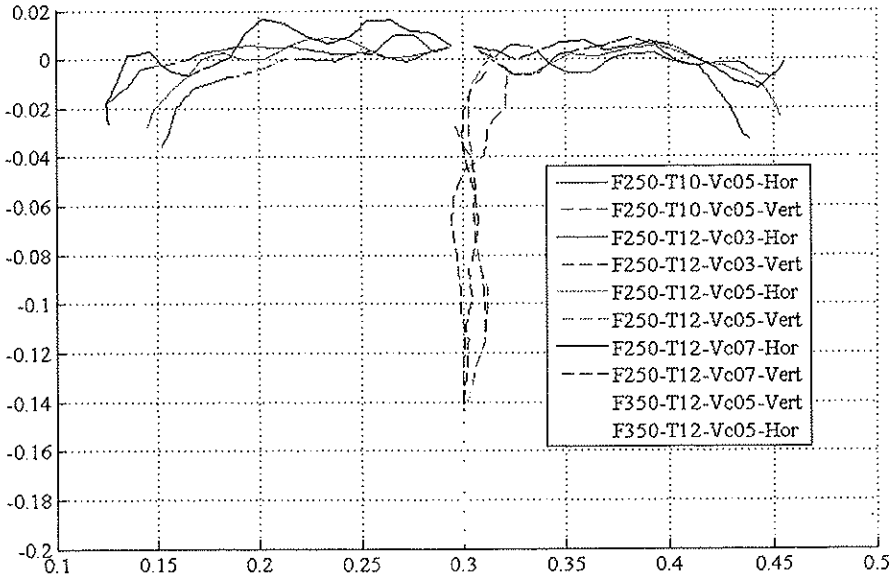

Figure 7.8: Plots of the final crack patterns for all the re-calculations.

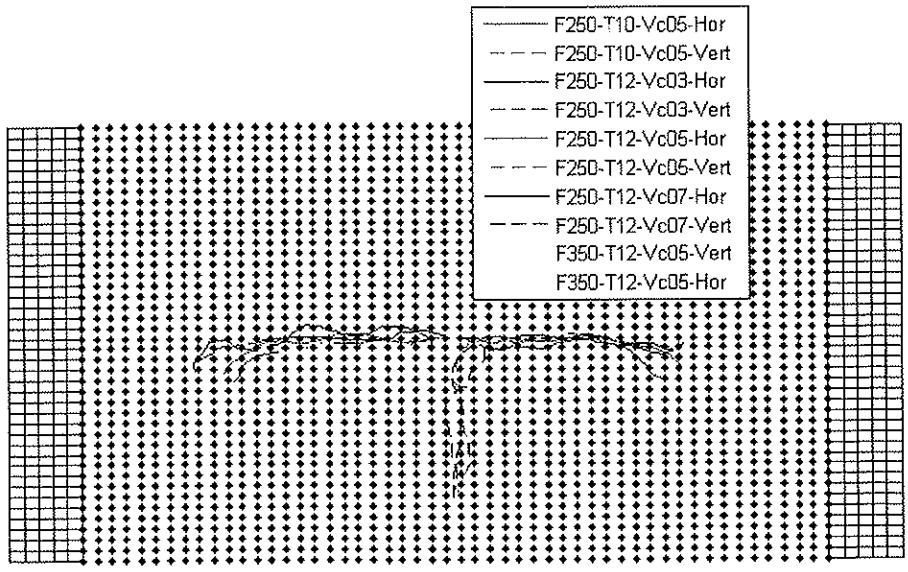

Figure 7.9: Plots of the final crack patterns and the shear wall node density for all the re-calculations.

7.3 Experiment II

The principal experiment set-up is the same as for Experiment I, but the test specimen dimensions are different: length 400mm, height 250mm and thickness 40mm. The experiment characteristics are given in Section 7.3.1, followed by listing of results in Section 7.3.2 and numerical calculations with the EFG code in Section 7.3.3.

7.3.1 Description of Experiment II

The set-up for Experiment II is the same as for Experiment I, which was sketched in Figure 7.1. Digital pictures from the structural laboratory of the shear wall, strain gages and the gas gun barrel opening are also given in the previous section in Figure 7.2, and a picture of the velocity measure equipment (red lights) is shown in Figure 7.3. These are taken with a test specimen from Experiment II.

The experiment deviates from Experiment I in test specimen dimensions. The main purpose of this second experiment is to obtain a different crack pattern (ridge-like spalling). In order to avoid the vertical crack at the mid plane, reinforcement is embedded horizontally near the bottom surface at a 100mm long region at the centerline of the shear wall. The reinforcement consists of 2 bars with diameter 8mm. The Young's modulus, Poisson's ratio, density of the shear wall and the projectile mass is listed in Table 7.5. Only one test is performed.

Strain gages are located on the shear wall surface at the points P_1 and P_2. Both points has a radial distance of 120mm from the center of the steel bar top surface (see Figure 7.1).

Table 7.5: Listing of parameters for the shear wall Test 1.

Test	Mass projectile kg	Velocity projectile m/s	E module shear wall GPa	ρ shear wall kg/m^3	ν shear wall
1	0.210	39.9	31.4	2400	0.2

7.3.2 Results of Experiment II

The results of Test 1 of the shear wall Experiment II are presented as plot of the final crack pattern shown in Figure 7.10. The vertical strain peak value at P1 is $1.1 \cdot 10^{-3}$, and the pulse duration is 0.1ms for Test 1. The strain time history curve has similar shape as the curves shown in Figure 7.7. The maximum magnitude measured is more like the EFG results for this experiment than was the case for Experiment I. This may indicate some uncertainties in the measurements.

The crack pattern did not give the expected ridge-shaped spalling. It seems that the reinforcement spreading was to short, with the result of initiation of a vertical crack at the right hand end of the reinforcement at the bottom surface. In addition a horizontal crack at the mid plane, approximately 60mm above the bottom surface was initiated. This is the crack that was expected to propagate down wards to the bottom surface to form a ridge-shaped spalling. Further discussion of the evolution of this crack pattern is given in the next section also based on additional numerical calculations. A brief listing of the measurements of the crack pattern is given below:

- Test 1: A horizontal crack 60mm above the bottom surface at the mid part of the shear wall is observed. At the right end of the horizontal crack a vertical crack goes straightly downwards to the bottom surface. From the left hand side of the horizontal crack a vertical crack goes up to the steel bar at the top surface.

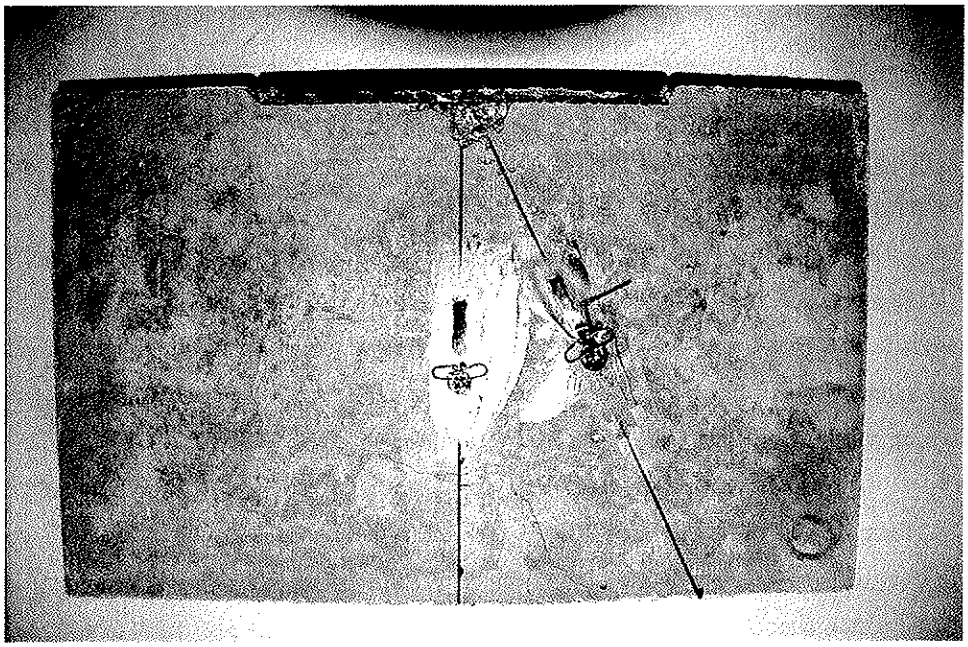

Figure 7.10: Digital picture of the final crack pattern for Test 1.

7.3.3 Numerical simulation related to Experiment II with the EFG code

Based on the results from the shear wall Experiment II, it is necessary to modify some of the parameters used in the initial simulation. Table 7.3 lists the parameters that are changed in the numerical simulations of the shear wall. The time history parameters of the load intensity for the re-calculation are:

$$\sigma(t) = \begin{Bmatrix} \sigma_1 (T_1 - t)/T_1, & \text{for } t \le T_1 \\ \sigma_1 = 0, & \text{for } t > T_1 \end{Bmatrix}$$

where σ_1=-250MPa and T_1=0.12ms. The correctness of this load is verified by studying the results from the strain gages. By recalling the results from Experiment I, see Figure 7.7, and the vertical strain peak value and the pulse duration from Experiment II (vertical strain peak value at P1 is $1.1 \cdot 10^{-3}$ and the pulse duration is 0.1ms) the chosen time history load is better correlated with the measured data than for Experiment I.

Since the shear wall dimensions differ between the model used in the initial calculations, an updated numerical model is established. The mode I stress intensity factors at different heights above the bottom surface at the mid plane for 10mm horizontal pre-cracks are calculated. This is done to predict where the horizontal crack is expected to initiate.

Figure 7.11 shows the mode I stress intensity factors, where it can be seen that the pre-crack located 55mm (SIF I - 5.5cm) above the bottom surface intersects the fracture toughness (red doted line) first. This indicates where the horizontal crack will be initiated. This is also in agreement with the horizontal crack from the laboratory test, which was located 60mm above the bottom surface.

If vertical crack initiation from the bottom surface should be avoided the reinforcement must be extended. This is avoided if the mode I stress intensity factor for the vertical pre-crack intersects the fracture toughness line at a delayed time at least equal to the time for the horizontal crack to propagate from the pre-crack to establish the complete spalling pattern. I.e. the time from the horizontal crack intersects the fracture toughness line until the ridge-shaped spalling is established. The time delay for the 10cm offset crack (SIF I - 8cm offset), see Figure 7.12, is 0.01ms. Within this time interval the horizontal crack will only advance 1-2cm which may result in initiation of the vertical crack. This is an approximate consideration since when the horizontal cracking is started it will disturb the mode I stress intensity factor at the bottom surface. Prior to possible further experimental verifications, numerical simulations must be run with one 10mm horizontal crack 55mm above the bottom surface at the mid plane, together with short vertical cracks with different offset distances from the mid plane. Then the necessary reinforcement extension can be decided.

Figure 7.13 shows the crack pattern from a simulation with only one 10mm long horizontal pre-crack 55mm above the bottom surface at the mid plane, this simulation gives the ridge-shaped spalling. Figure 7.14 shows the crack pattern from a numerical simulation of the experiment with the updated parameters listed in Table 7.6. A 10mm long horizontal pre-crack is located 55mm above the bottom surface at the mid plane of the shear wall and a 25mm long vertical pre-crack at the bottom surface is located with 50mm offset from the mid plane. This numerical simulation demonstrates some of the behaviour observed in the laboratory (see previous section).

Table 7.6: Experiment specification for initial- and re-simulations.

Parameter:	**Initial simulation:**	**Re-simulations:**
Shear wall length	600mm	400mm
Shear wall height	400mm	250mm
Shear wall thickness	40mm	40mm
Shear wall support length	50mm	50mm
Shear wall E-module	30.0GPa	31.4GPa
Shear wall density, ρ	2400 kg/m^3	2400 kg/m^3
Shear wall ν	0.2	0.2
Steel bar E-module	210GPa	210GPa
Steel bar density, ρ	7850 kg/m^3	7850 kg/m^3
Steel bar ν	0.3	0.3

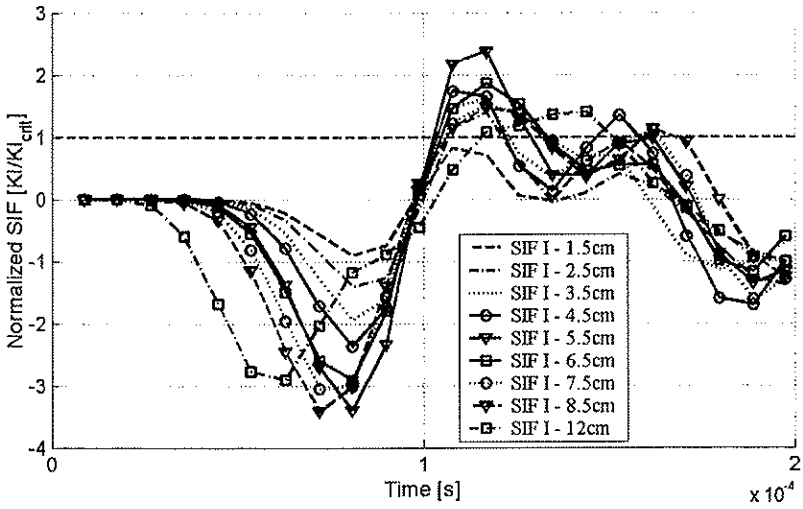

Figure 7.11: Mode I stress intensity factors at horizontal pre cracks at different heights above the bottom surface at the mid plane of the shear wall.

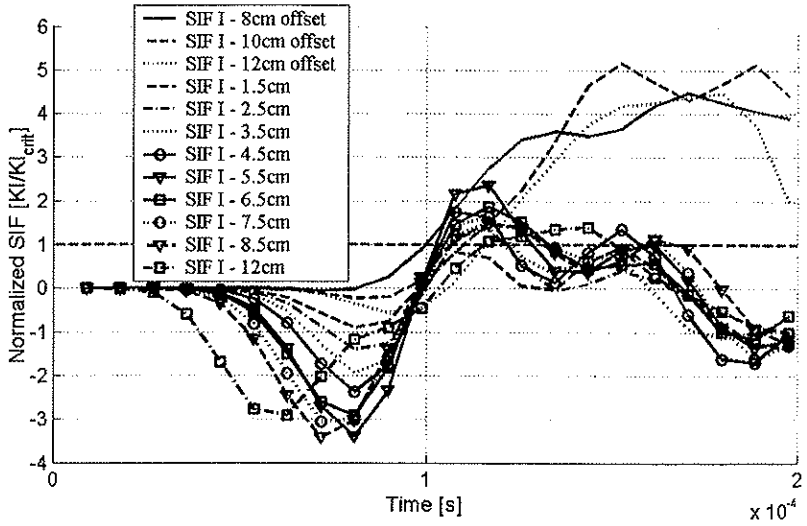

Figure 7.12: Mode I stress intensity factors at horizontal pre cracks at different heights above the bottom surface at the mid plane, and 25mm long vertical pre-cracks at the bottom surface with different offsets from the mid plane.

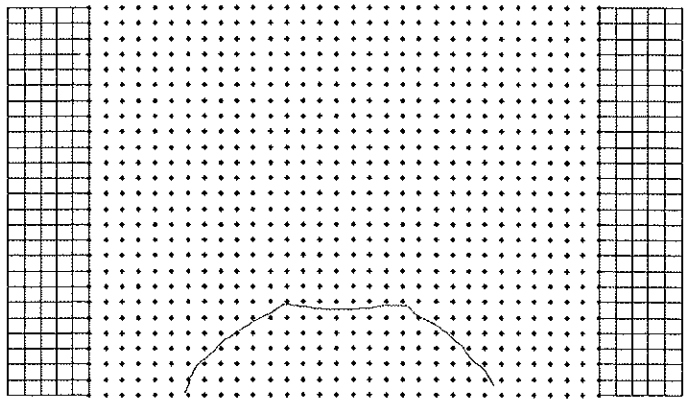

Figure 7.13: Plot of the final crack pattern for the numerical re-simulation with only one horizontal pre-crack located 55mm above the bottom surface at the mid plane.

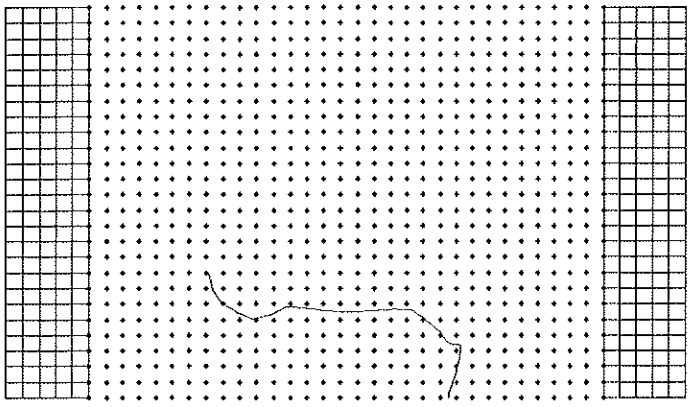

Figure 7.14: Plot of the final crack pattern for the numerical re-simulation with one horizontal pre crack located 55mm above the bottom surface at the mid plane, and a vertical 25mm long vertical pre crack located at the bottom surface at 50mm offset from the mid plane.

7.4 Conclusive remarks

In this section discussions of the laboratory experiments and the numerical initial- and re-calculations are listed.

For Experiment I, the shear wall with 600mm length and 400mm height, there is a good agreement between the results from the numerical simulations and the results from the laboratory tests. Classification of the agreement as good is of course considering the level of uncertainties in the parameters used for the numerical simulations, and the relatively coarse density of nodes and integration points in the numerical model. The most uncertain parameters are the shape and magnitude of the time history load function, fracture toughness of the concrete and the crack propagation velocity. Measurements with higher level of accuracy of the strain in the test specimens could reduce some of the uncertainties in the load function parameters. The fracture toughness could be found in standardized tests, and the crack velocity could be decided by special cameras. Unfortunately, this was not an option when the experiments were performed.

For Experiment II, the shear wall with 400mm length and 250mm height, only one test case is performed. The expected crack pattern was not completely obtained. The purpose of this test case was to obtain a ridge-shaped spalling, where vertical cracking from the bottom surface of the shear wall should be avoided by use of reinforcement. The reinforcement was located close to the bottom surface with endpoints approximately 50mm from the mid plane. This resulted in initiation of the vertical crack at the ends of the reinforcement, and thus changed the expected crack pattern.

The experiments were included to show that the numerical tools based on linear fracture mechanics and the Element Free Galerkin method, are suited for solving dynamic brittle fracture. It will be possible to tune the numerical solutions to obtain best-fit pre-simulations of the experiment and of course the confidence level of the experimental work. The main conclusions from this exercise is, however, that the numerical tools work properly for this type of problems, and that the work in this thesis show one possible way of predicting the crack initiation and its finial crack pattern for brittle fracture.

The numerical simulations also show that the values of the estimated fracture toughness and crack propagation speed have been reasonable, based on a simplified comparison of results between the numerical simulations and the laboratory tests.

Chapter 8 Conclusions and suggestions for further work

In this chapter the main conclusions of the thesis work are given in Section 8.1, followed in Section 8.2 by some suggestions for further work within associated areas.

8.1 Summary and conclusions

The EFG method is suited to solve problems with local discontinuous behaviour such as general crack growth. The applicability to this type of problems is rational as the connectivity between nodes in the numerical model is such that it can be updated during time stepping analyses. The displacement approximation that allow for updating the node connectivity during numerical simulations is based on minimizing the weighted quadratic difference between the local approximation and the nodal parameters for every node with non-zero influence domain. This method is called the moving least square method (MLS). Establishing the discrete equations based on the EFG displacement approximation is performed in a similar manner as for the finite element method, i.e. inserting the displacement approximation into the weak formulation of the problem. A disadvantage of the EFG formulation is that it is more computer time demanding than the finite element method for solving problems without local discontinuities. To utilize the advantages of each method they are coupled through interface elements. The coupling makes it possible to limit the domain where the EFG method is used to calculate the local discontinuities while the finite element method is exploited in the remaining domain of the numerical model. This results in cost effective calculations with respect to computer time.

To decide if a crack will initiate propagation, be arrested, will propagate further and in what direction, the linear elastic dynamic fracture mechanics theory is utilized. The energy release rate domain integral is performed for an area that contains the crack tip for calculation of the stress intensity factors. These are then compared to the fracture

criterion. In this work the maximum circumferential stress criterion is used as the fracture criterion for the actual material of the numerical model. If a crack initiates propagation or continue propagation, the crack path is updated stepwise during the simulation. This will release the connectivities between the nodes that the crack separates. Updating of the stiffness matrix is necessary. This is a process that is generally handled within a predefined domain (i.e. the EFG domain). The analyses that are performed show that the linear elastic dynamic fracture mechanics gives stable results also without very high node densities. Even relatively low node densities predict satisfactory estimates of the crack pattern and failure mode with robust algorithmic performance.

Part of the research within computational mechanics at the Department of structural engineering NTNU, has been directed towards nonlinear dynamic problems with application to protective structures. This identified a need for the ability to simulate problems where the material may fail in brittle fracture. This is often the case for concrete and rock. The combination of elastoplastic material behaviour and brittle fracture is also an important issue for welded metallic structures. Dynamic response of offshore pipelines is thus another field of application for numerical codes that can estimate brittle fracture and in combination with elastoplastic material behaviour. For research applications there was a need to obtain comprehensive knowledge of crack growth in brittle materials. In particular there was a requirement to know about accuracy, computational efficiency and not least robustness in obtaining reliable results. Among actual methods for crack growth estimation the EFG method was found to be promising for the purposes. Because commercial codes were not available the need to study the method comprehensively led to the decision of developing a prototype computer code on a MATLAB platform.

The code is limited to two-dimensional linear elastic dynamic fracture simulations, where explicit solution of the discrete equations in the time domain is applied. The development has emphasized handling of the coupling between the finite element description and the EFG description, and that general crack propagation of two independent cracks should be possible. For the purpose of analyzing protective

structures in rock, the possibility of including cavities with general shape has been implemented in the code. Optimizing the code with respect to computer time cost efficiency has not been emphasized. Several analyses of different reference problems have been run in order to verify and validate the code. The comparisons show a satisfactory level of accuracy and robustness in the solution for simulation of general crack growth for two-dimensional problems.

Sensitivity in estimated results and impact on computational efficiency from various EFG modeling parameters for linear elastic dynamic crack propagation problems were studied for 3-point bending of a concrete beam. Crack growth in the mid plane was studied. The parameter variations include variation of d (side length in a square defining the J-integral domain) , Δt (time increment), d_{max} (defining the size of the domain of influence), the number of Gauss cells, the frequency of updating the stiffness matrix, linear and quadratic coupling in the interface domain, explicit integration parameter β_1 and linear or extended basis. A set of parameters was adopted for further simulations based on the parameter study described above. The criterion for selection of parameters was that the results from the simulations should show satisfactory convergence with minimum use of computer time. The size of the EFG domain where crack growth is allowed, d_{max}, and the frequency of updating of the stiffness matrix to trace the crack growth are the most significant parameters that influence the total use of computer time. Oscillations induced from infrequent updating the stiffness matrix to trace the crack advancement, named artificial oscillations, were observed. More frequent updating gives lower oscillation amplitudes.

The simulations of two well-defined examples, the pendulum experiment by John R. and S.P. Shah (1990) and the cracking of a free plate of high strength steel by Kalthoff and Winkler (1987) were selected for verification of the present code. The results from these numerical simulations with the EFG method and use of linear elastic dynamic fracture mechanics as crack propagation criterion are also used by Organ (1996). This makes comparison of results easy. The comparison between the results obtained by Organ (1996) and results from the analyses with the present code showed good correlation between the simulations. This is a valuable indication and confirmation of

the accuracy obtainable with the present code. Some minor differences in the compared results are observed, but the overall estimated behaviour of the numerical models is in good agreement. Detailed information of the simulations by Organ is needed to conclude further on the differences. For the main purpose of studying the capabilities and robustness of the EFG method as implemented in the present code, the comparison with Organ is fully satisfactory.

Laboratory experiments and numerical initial- and re-calculations were also performed for validation of the EFG results. A concrete shear wall was impacted at the mid plane of the longest side by a steel projectile. The shear wall was supported at both ends opposite to the edge where the projectile hit. The results from Experiment I, a shear wall with 600mm length and 400mm height, is classified as good correspondence between the results from the numerical simulations and the results from the laboratory tests. It is, however, realized that each parameter entering the comparison may have significant uncertainties. For Experiment II, the shear wall with 400 mm length and 250mm height, there is only performed one test case. It did not completely obtain the expected crack pattern. The aim of this test case was to get a ridge shaped spalling, where vertical cracking from the bottom surface of the shear wall should be avoided by use of reinforcement. The reinforcement was located close to the bottom surface with endpoints approximately at 50mm offset from the mid plane. This resulted in initiation of a vertical crack at the endpoint of the reinforcement. This influenced the crack pattern.

The main conclusion of the present study is that the EFG method together with linear elastic dynamic fracture mechanics is well suited for simulation of general crack propagation in brittle materials. Since the EFG method is more computer time consuming than the finite element method it will be efficient to limit the EFG domain and base the rest of the numerical model on finite elements. Additional advantage is that all the well-documented possibilities of the finite element method are available in the numerical model outside the EFG domain. For this type of simulations to predict reliable results one should choose parameters carefully and with knowledge from this type of calculations. Combination of EFG and FEM modeling will also enable reliable

estimates of the performance of protective structures exposed to external explosive loading in the vicinity of the structure or inside the structure. One particular problem that can be solved is then the estimation of whether spalling will occur at rock cavern surfaces.

8.2 Suggestions for further work

Suggestion for further work is listed as:

- The EFG code is suited for parameter studies of incoming shock waves to rock tunnels and caverns and similar protective structures. It is possible to make calibration with results from full-scale tests. After calibration and with satisfactory results obtained, the EFG code can be used for design of tunnels and rock caverns. This direction of the research points to practical benefit and applications.

- An expansion of the EFG code to three-dimensional space is an obvious choice, since shock waves and the resulted crack pattern in rock tunnels and caverns is typical three-dimensional. This will also enable applications to combined fracture development and elastoplastic behaviour for offshore pipelines.

- If commercial codes that offer this type of calculations will be available in the future, this work can be a basis and useful reference for calibration. Since today's commercial codes offer coupling to computational fluid dynamics codes, calculations of the explosion phase and its resulting shock waves would directly be integrated with the numerical model of the structure. This could be the solution to the complete problem sketched in the introduction.

References:

ABAQUS Version 6.5, developed by Abaqus, Inc, Rhode Islands, USA, address: ABAQUS Inc. - Rising Sun Mills - 166 Valley Street - Providence, RI 02909-2499, USA, www.abaqus.com.

Belytshko, T., D. Organ, and Y. Krongauz (1995). *A coupled finite element - element-free Galerkin method.* Computational Mechanics 17, 186-195.

Dolbow, J., T. Belytschko. *An Introduction to Programming the Meshless Element Free Galerkin Method.* Computational Methods in Engineering, Vol. 5, 3, 207-241, (1998).

Dolbow, J. *Numerical Integration in Meshfree Methods.* Master of Science thesis, (1998), Northwestern University.

Flemming, M. A. *The Elment-Free Galerkin Method for Fatique and Quasi-static Fracture* (1997). Ph.D. thesis, Northwestern University.

Flemming, M., Y. A. Chu, B. Moran, and T. Belytshko (1997). *ENRICHED ELEMENT-FREE GALERKIN METHODS FOR CRACK TIP FIELDS.* Numerical methods in engineering, Vol., 40, 1483-1504.

Freund, L. B. (1998) *Dynamic fracture mechanics.* Cambridge Monographs on Mechanics and Applied Mathematics. CAMBRIDGE UNIVERSITY PRESS.

Hughes, T. J. R. (1997). *The Finite Element Method.* Englewood Cliffs, N. J.: Prentice Hall.

John, R. (1988). Mixed *Mode fracture of Concrete Subjected to Impact Loading.* Ph. D. thesis, Northwestern University.

John, R. and S. P. Shah (1990). *Mixed mode fracture of concrete subjected to impact loading.* ASCE Journal of Structural Engineering 116, 585-602.

J. F. Kalthoff and S. Winkler (1987). *Failure mode transition at high rates of shear loading.* International Conference on Impact Loading and Dynamic Behaviour of Materials, edited by C. Y. Chiem, H. D. Kunze and L. W. Meyer, pp 185-195.

Lancaster, P., and K. Salkauskas (1981). *Surfaces generated by moving least squares methods.* Mathematics of Computation 37, 141-158.

Xu, S. and Reinhardt, H.W. *Determination of the Double-K fracture parameters in standard three-point bending notched beams.* Fracture Mechanics of Concrete Structures, Volume 1, Fracture Properties and Parameters. AEDIFICATIO Publishers, 1998.

Organ, D., M. Flemming, T. Terry and T. Belytschko, *Continuous Meshless Approximations for Nonconvex Bodies by Diffraction and Transparency*, Comp. Mech., 18, 225-245, (1996).

Organ, D. *Numerical Solutions to Dynamic Fracture Problems Using the Element-Free Galerkin Method.* (1996) Ph.D. thesis, Northwestern University.

Appendix A

The first term in the asymptotic solution for stresses, displacements and velocities for mode I and mode II loading, are described with the formulas (A.1) to (A.18) (see Freund (1998)). The x and y variable in the field equations, are defined relative to the crack tip coordinate system as shown in Figure A.1. The function q and its material derivative are plotted in Figure A.2 - Figure A.1, it's plotted on the integration domain A, see Figure A.1. Figure A.5 to Figure A.14 illustrate the actual variable as a 3D surface plot above the integration domain A.

ASYMPTOTIC CRACK TIP FIELDS:

In Section 3.5 the definitions below where done:

$$\alpha_d = \sqrt{1-\frac{v^2}{c_d^2}}, \qquad \alpha_s = \sqrt{1-\frac{v^2}{c_s^2}} \tag{A.1}$$

$$D(v) = 4\alpha_d\alpha_s - (1+\alpha_s^2)^2 \tag{A.2}$$

To simplify the formulas in this Appendix, the following definitions are done:

$$r_d = \sqrt{x^2+\alpha_d^2 y^2}\,,\ r_s = \sqrt{x^2+\alpha_s^2 y^2}\,,\ \theta_d = \tan^{-1}\frac{\alpha_d y}{x},\ \theta_s = \tan^{-1}\frac{\alpha_s y}{x} \tag{A.3}$$

MODE I STRESS:

$$\sigma_{11} = \frac{K_I}{D\sqrt{2\pi}}\left[(\alpha_s^2+1)(2\alpha_d^2-\alpha_s^2+1)\frac{1}{\sqrt{r_d}}\cos\frac{\theta_d}{2} - 4\alpha_s\alpha_d\frac{1}{\sqrt{r_s}}\cos\frac{\theta_s}{2}\right] \quad (A.4)$$

$$\sigma_{22} = \frac{K_I}{D\sqrt{2\pi}}\left[-(\alpha_s^2+1)^2\frac{1}{\sqrt{r_d}}\cos\frac{\theta_d}{2} + 4\alpha_s\alpha_d\frac{1}{\sqrt{r_s}}\cos\frac{\theta_s}{2}\right] \quad (A.5)$$

$$\sigma_{12} = \frac{K_I}{D\sqrt{2\pi}}\left[2\alpha_d(\alpha_s^2+1)\frac{1}{\sqrt{r_d}}\sin\frac{\theta_d}{2} - 2\alpha_d(\alpha_s^2+1)\frac{1}{\sqrt{r_s}}\sin\frac{\theta_s}{2}\right] \quad (A.6)$$

MODE II STRESS:

$$\sigma_{11} = \frac{K_{II}}{D\sqrt{2\pi}}\left[2\alpha_s(\alpha_s^2-2\alpha_d^2-1)\frac{1}{\sqrt{r_d}}\sin\frac{\theta_d}{2} + 2\alpha_s(\alpha_s^2+1)\frac{1}{\sqrt{r_s}}\sin\frac{\theta_s}{2}\right] \quad (A.7)$$

$$\sigma_{22} = \frac{K_{II}}{D\sqrt{2\pi}}\left[2\alpha_s(\alpha_s^2+1)\frac{1}{\sqrt{r_d}}\sin\frac{\theta_d}{2} - 2\alpha_s(\alpha_s^2+1)\frac{1}{\sqrt{r_s}}\sin\frac{\theta_s}{2}\right] \quad (A.8)$$

$$\sigma_{12} = \frac{K_{II}}{D\sqrt{2\pi}}\left[4\alpha_d\alpha_s\frac{1}{\sqrt{r_d}}\cos\frac{\theta_d}{2} - (\alpha_s^2+1)^2\frac{1}{\sqrt{r_s}}\cos\frac{\theta_s}{2}\right] \quad (A.9)$$

MODE I DISPLACEMENT:

$$u_1 = \frac{K_I\sqrt{2}}{\mu D\sqrt{\pi}}\left[(\alpha_s^2+1)\sqrt{r_d}\cos\frac{\theta_d}{2} - 2\alpha_s\alpha_d\sqrt{r_s}\cos\frac{\theta_s}{2}\right] \tag{A.10}$$

$$u_2 = \frac{K_I\sqrt{2}}{\mu D\sqrt{\pi}}\left[-\alpha_d(\alpha_s^2+1)\sqrt{r_d}\sin\frac{\theta_d}{2} + 2\alpha_d\sqrt{r_s}\sin\frac{\theta_s}{2}\right] \tag{A.11}$$

MODE II DISPLACEMENT:

$$u_1 = \frac{K_{II}\sqrt{2}}{\mu D\sqrt{\pi}}\left[2\alpha_s\sqrt{r_d}\sin\frac{\theta_d}{2} - \alpha_s(\alpha_s^2+1)\sqrt{r_s}\sin\frac{\theta_s}{2}\right] \tag{A.12}$$

$$u_2 = \frac{K_{II}\sqrt{2}}{\mu D\sqrt{\pi}}\left[2\alpha_s\alpha_d\sqrt{r_d}\cos\frac{\theta_d}{2} - (\alpha_s^2+1)\sqrt{r_s}\cos\frac{\theta_s}{2}\right] \tag{A.13}$$

MODE I VELOCITY:

$$\dot{u}_1 = \frac{vK_I}{\mu D\sqrt{2\pi}}\left[-(\alpha_s^2+1)\frac{1}{\sqrt{r_d}}\cos\frac{\theta_d}{2} - 2\alpha_s\alpha_d\frac{1}{\sqrt{r_s}}\cos\frac{\theta_s}{2}\right] \tag{A.14}$$

$$\dot{u}_2 = \frac{vK_I}{\mu D\sqrt{2\pi}}\left[-\alpha_d(\alpha_s^2+1)\frac{1}{\sqrt{r_d}}\sin\frac{\theta_d}{2} + 2\alpha_d\frac{1}{\sqrt{r_s}}\sin\frac{\theta_s}{2}\right] \tag{A.15}$$

MODE II VELOCITY:

$$\dot{u}_I = \frac{vK_{II}}{\mu D\sqrt{2\pi}}\left[2\alpha_s \frac{1}{\sqrt{r_d}}\sin\frac{\theta_d}{2} - \alpha_s(\alpha_s^2+1)\frac{1}{\sqrt{r_s}}\sin\frac{\theta_s}{2}\right]$$

(A.16)

$$\dot{u}_I = \frac{vK_I}{\mu D\sqrt{2\pi}}\left[-2\alpha_s\alpha_d \frac{1}{\sqrt{r_d}}\cos\frac{\theta_d}{2} + (\alpha_s^2+1)\frac{1}{\sqrt{r_s}}\cos\frac{\theta_s}{2}\right] \qquad (A.17)$$

ACCELERATION:

The acceleration can be derived by applying the local steady state condition twice. Then the expression for the acceleration can be written as:

$$\ddot{u}_i = -v_{,t}u_{i,I} - v\dot{u}_{i,I} \qquad (A.18)$$

The first term in Eq. (A.18) is zero when constant crack growth is applied.

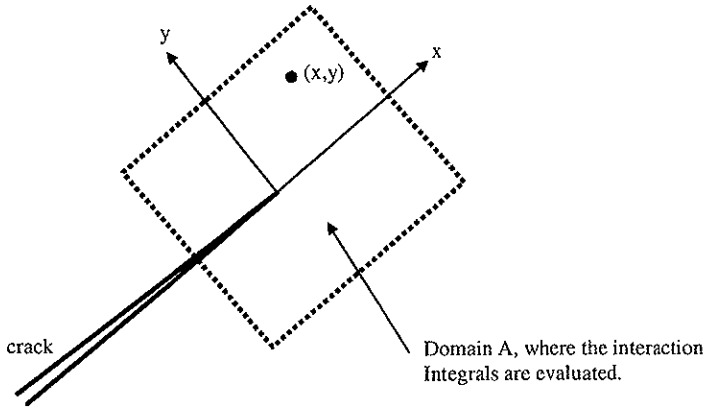

Figure A.1: Relations between the local coordinates x and y and the crack tip.

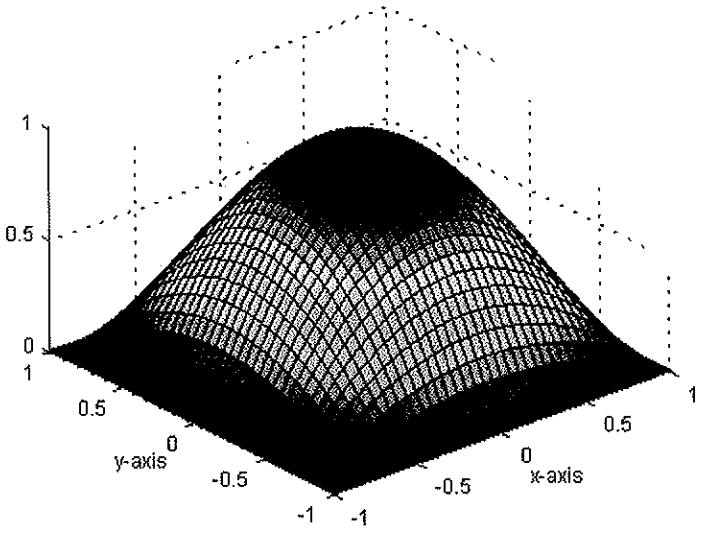

Figure A.2: The function q plotted over the integration domain A, axes and crack position as in the illustration in Figure A.1.

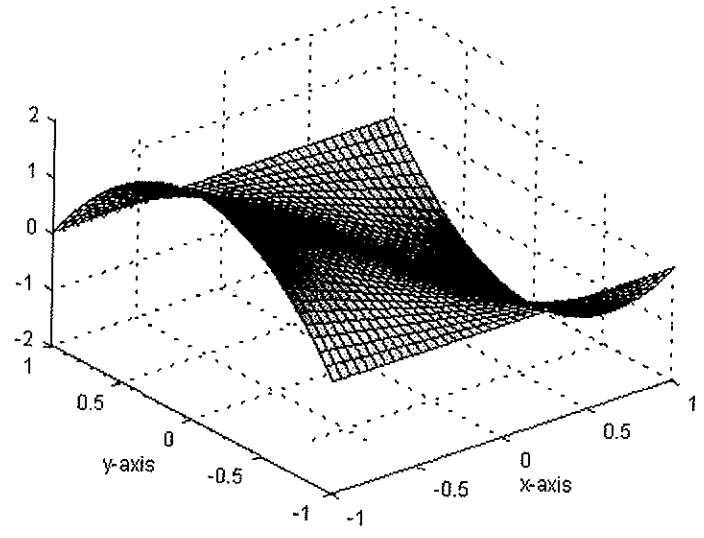

Figure A.3: The function $q_{,1}$ plotted over the integration domain A, axes and crack position as in the illustration in Figure A.1.

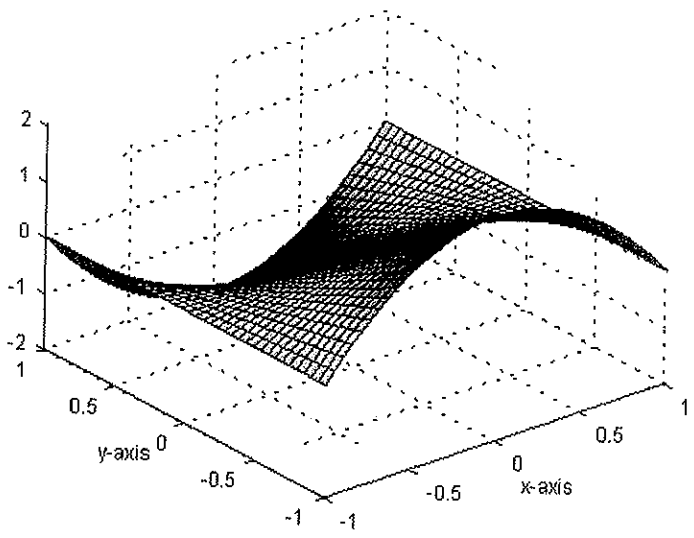

Figure A.4: The function $q_{,2}$ plotted over the integration domain A, axes and crack position as in the illustration in Figure A.1.

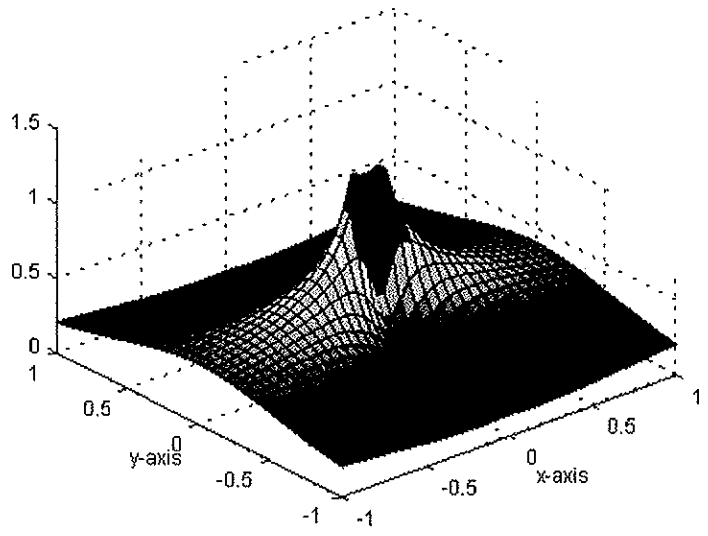

Figure A.5: The circumferential stress $\sigma_{11}^{(1)}$ from mode I loading, is plotted over the integration domain A, axes and crack position as in the illustration in Figure A.1.

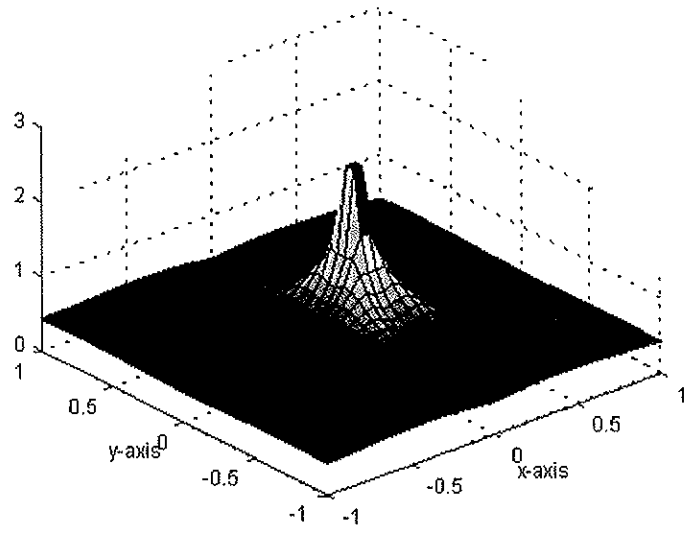

Figure A.6: The radial stress $\sigma_{22}^{(1)}$ from mode I loading, is plotted over the integration domain A, axes and crack position as in the illustration in Figure A.1.

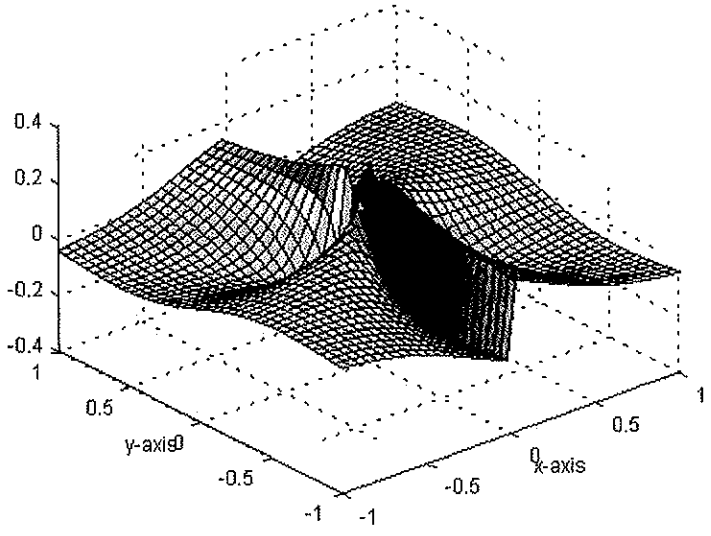

Figure A.7: The shear stress $\sigma_{12}^{(I)}$ from mode I loading, is plotted over the integration domain A, axes and crack position as in the illustration in Figure A.1.

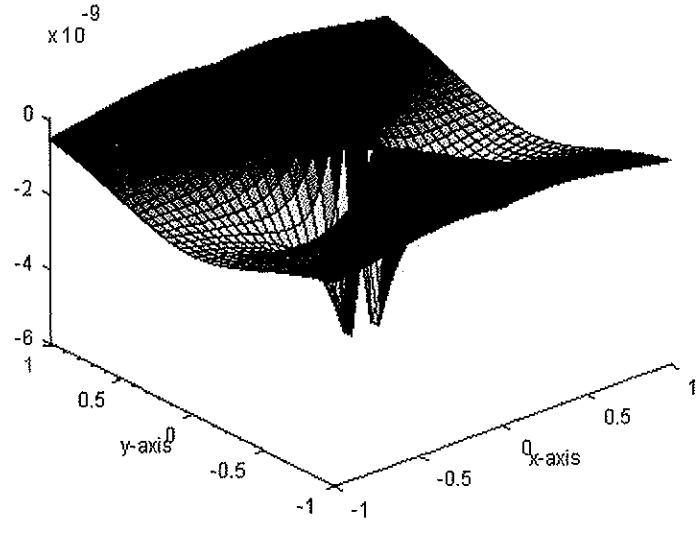

Figure A.8: $\dot{u}_i^{(I)}$ from mode I loading is plotted over the integration domain A, axes and crack position as in the illustration in Figure A.1.

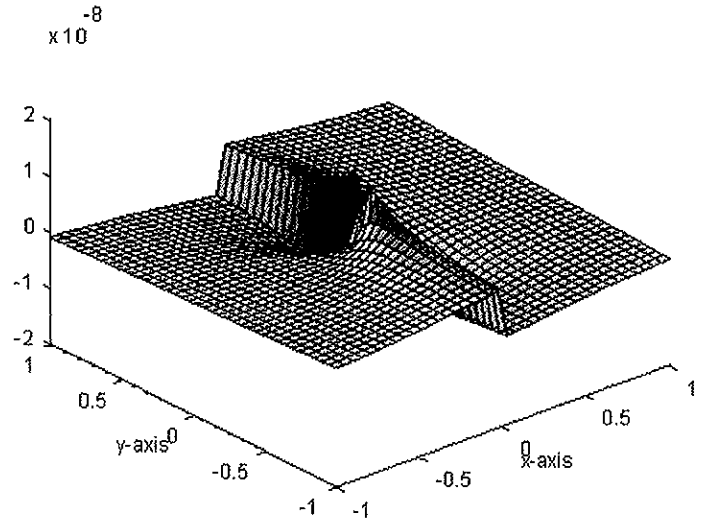

Figure A.9: $\dot{u}_2^{(1)}$ from mode I loading is plotted over the integration domain A, axes and crack position as in the illustration in Figure A.1.

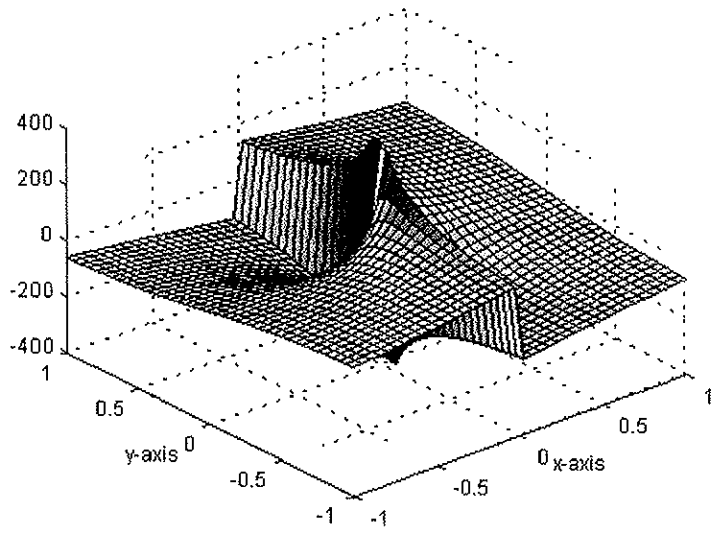

Figure A.10: The circumferential stress $\sigma_{11}^{(2)}$ from mode II loading, is plotted over the integration domain A, axes and crack position as in the illustration in Figure A.1.

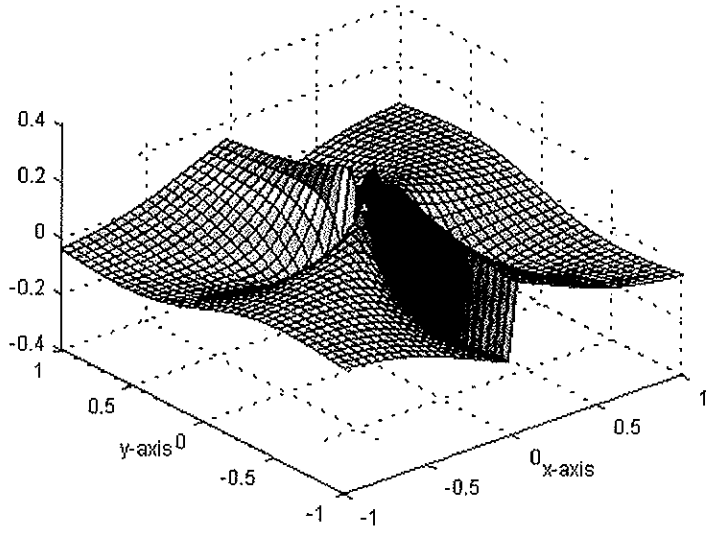

Figure A.11: The radial stress $\sigma_{22}^{(2)}$ from mode II loading, is plotted over the integration domain A, axes and crack position as in the illustration in Figure A.1.

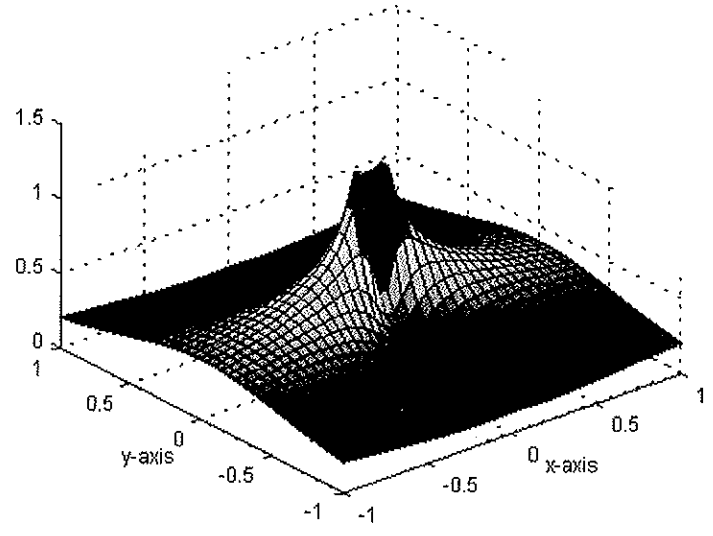

Figure A.12: The shear stress $\sigma_{12}^{(2)}$ from mode II loading, is plotted over the integration domain A, axes and crack position as in the illustration in Figure A.1.

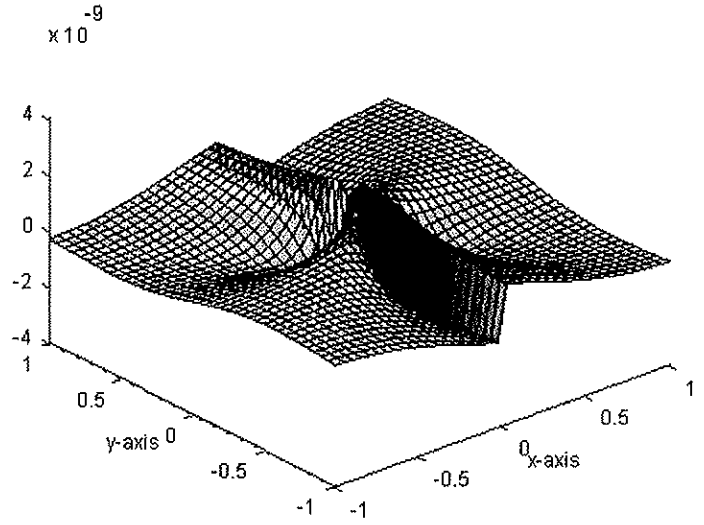

Figure A.13: $\dot{u}_1^{(2)}$ from mode II loading is plotted over the integration domain A, axes and crack position as in the illustration in Figure A.1.

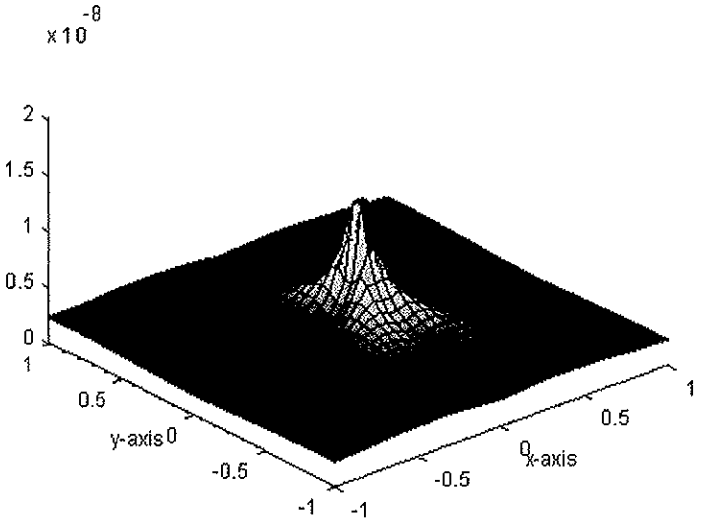

Figure A.14: $\dot{u}_2^{(2)}$ from mode II loading is plotted over the integration domain A, axes and crack position as in the illustration in Figure A.1.

Appendix B

In Section 4.2 the program structure was briefly described, with references to this appendix for more detailed descriptions of the main routines Kmat.m, CGKmat.m, and CG.m. In the following each routine structure is listed:

Kmat.m: establish the global stiffness matrix, unless for the xcrack region.

[K,Cxg] = Kmat(.....)
Definition of variables for use in this routine.
for gc = 1 **to** *(total number of Gauss points)*
    if *(the Gauss point is inside the Finite Element domain)*
        K = KFEM(....), *inserts the stiffness contribution from the Finite Element domain into the global stiffness matrix.*
    end if
    if *(the Gauss point is inside the EFG domain, but outside xcrack domain)*
        K = KEFG(....), *inserts the stiffness contribution from the Element Free Galerkin domain into the global stiffness matrix.*
    end if
    if *(the Gauss point is inside the interface domain)*
        K = Kinterface(....), *inserts the stiffness contribution from the interface domain into the global stiffness matrix.*
    end if
    if *(the Gauss point is inside xcrack domain)*
        Cxg = *(saving information of the Gauss points inside the xcrack domain)*
    end if
end for
end Kmat.m

CG.m: calculate the stress intensity factors, and checking the crack propagation criterion.

[**L**c, tc, ...] = CG(.....)

Definition of variables for use in this routine.

xc = *is the crack tip coordinates, where the crack propagation criterion is to be checked.*

xa = *define the corners in the domain integration range, where the stress intensity factors is to be calculated. See Section 3.9.2.*

for i = 1 **to** *(total number of points in* Cxg*)*

if *(the Gauss point is inside the domain defined by the corners in* **x**a*)*

St = *the stresses at the Gauss point. The stresses take into account, cracks by the visibility criterion (see 2.6.1), and the enriched basis (see Section 2.7).*

ut = *the displacement, velocity, and the acceleration similarly as for the stresses.*

Cg = *the variables in the auxiliary field to be used in the domain integration (see Section 3.8).*

GintI = *building up the interaction dynamic energy release rate integral, mode I (see Section 3.8).*

GintII = *building up the interaction dynamic energy release rate integral, mode II (see Section 3.8).*

end if

end for

Calculating the stress intensity factors with the Equations 3.39 and 3.40:

$$K_I = \left(\frac{E}{1-\nu^2}\right)\frac{\mathcal{G}_{int}^{(1)}}{2A_I}$$

$$K_{II} = \left(\frac{E}{1-\nu^2}\right)\frac{\mathcal{G}_{int}^{(2)}}{2A_{II}}$$

Checking the crack propagating criterion:

if (*crack propagate = ok)*

Lc = *adding the new crack segment to the previous crack path.*

tc = *1 (tells other routines that the crack has advanced)*

else

tc = *-1*

end if

end CG.m

CGKmat.m: establish the stiffness matrix for the xcrack region.

KEFGc = CGKmat(.....)

Definition of variables for use in this routine.

for i = 1 **to** *(total number of points in* Cxg*)*

if *(the Gauss point is inside the enriched/coupled domain (if enrichment of the basis is to be used, see Section 2.7) in the vicinity of the crack tip.*

Se = shape(....), *return the shape functions for the enriched/coupled domain.*

end if

if *(the Gauss point is outside the enriched domain)*

Sl = shape(....), *return the shape functions for the linear basis domain.*

end if

KEFGc = *building up the stiffness matrix KEFGc, on the basis of the shape functions, Gauss point information, and the material behaviour.*

end for

end CGKmat.m

Appendix C

In this Appendix C deformation plot for all the numerical simulations is presented, together with plots of the normal stress component in the x-direction, σ_{xx}, for some of the analyses. The stress plots are presented as a surface above the beam model and a contour plot of the stress surface below the beam model. These forms of plots are given for the simulations: G0705C and G0734V.

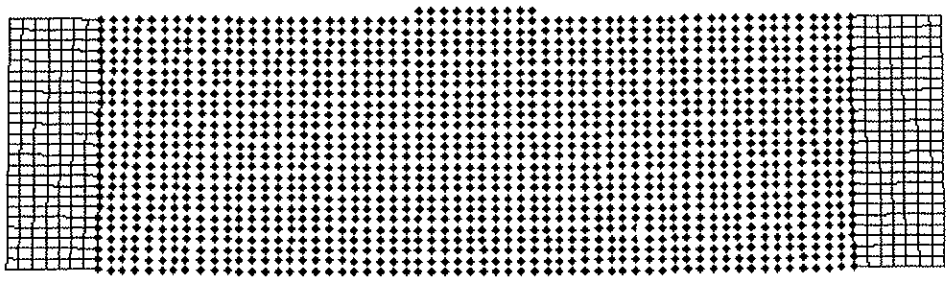

(a) Deformed numerical model from analysis G0672C (magnification factor 100) at the time instant 0.3 ms

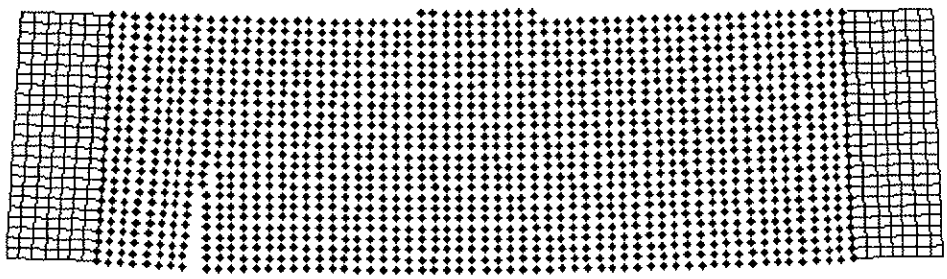

(b) Deformed numerical model from analysis G0672C (magnification factor 100) at the time instant 0.87 ms.

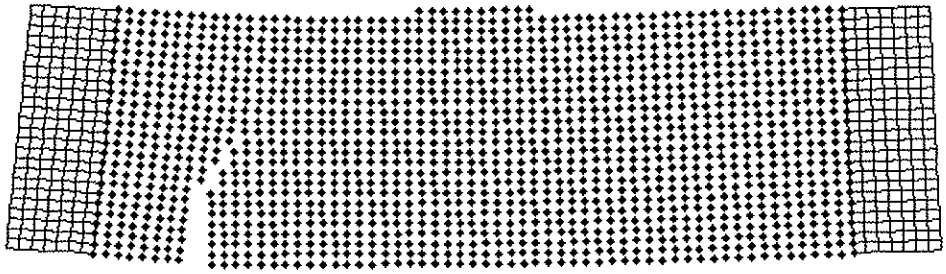

(c) Deformed numerical model from analysis G0672C (magnification factor 100) at the time instant 0.99 ms.

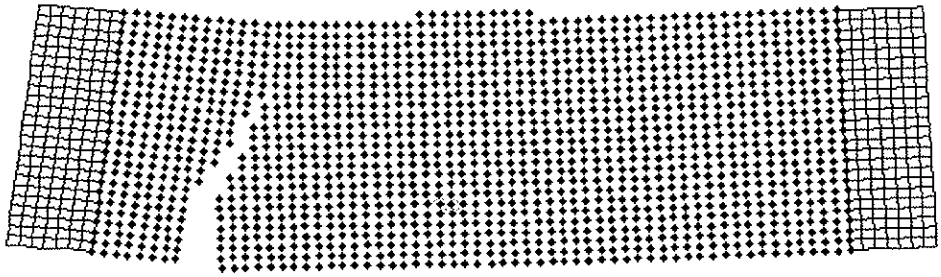

(d) Deformed numerical model from analysis G0672C (magnification factor 100) at the time instant 1.11 ms.

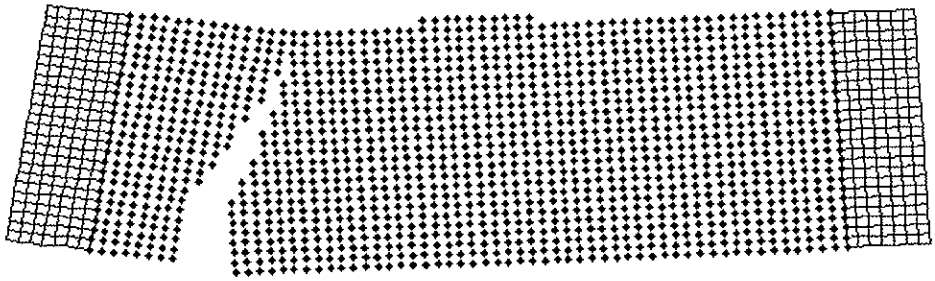

(e) Deformed numerical model from analysis G0672C (magnification factor 100) at the time instant 1.23 ms.

Figure C1: Plot of the deformed numerical models for simulation G0672C at time different time instants from a) 0.3ms to e) 1.23ms.

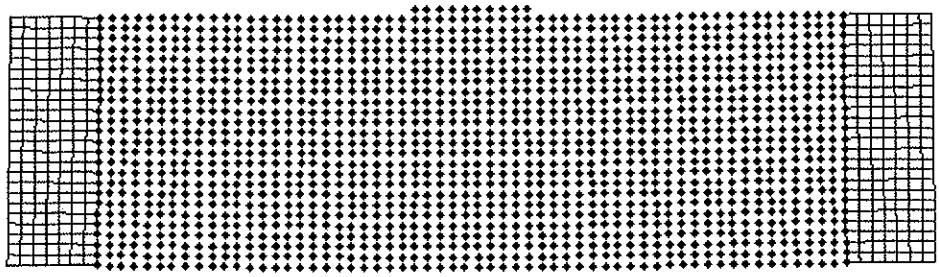

(a) Deformed numerical model from analysis G0705C (magnification factor 100).

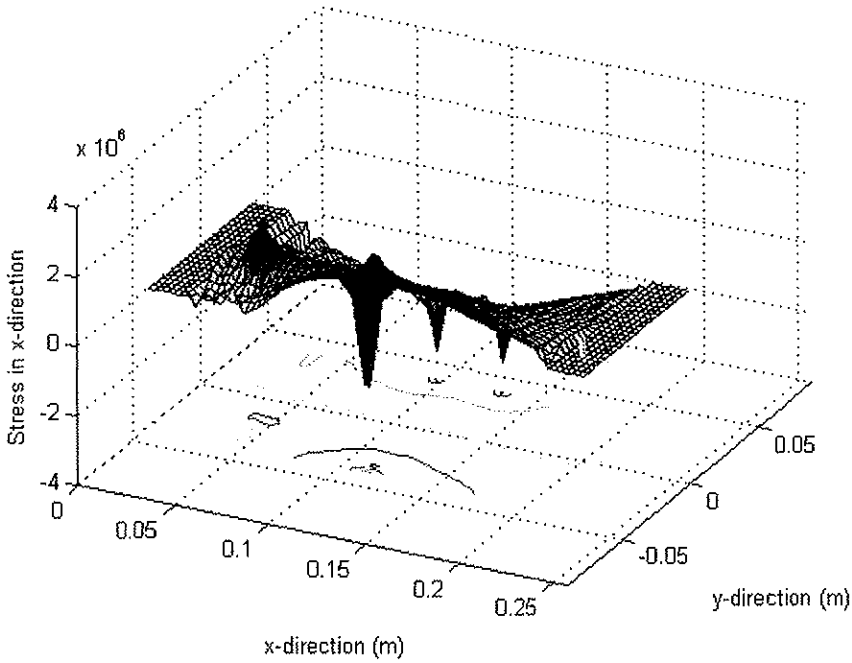

(b) 3D and contour stress plot of σ_{xx}, for the simulation G0705C.

Figure C2: (a) Plot of the deformed numerical model for simulation G0705C at time 0.3 ms. (b) 3D and stress contour plot of σ_{xx} for the same simulation and time instant as in (a).

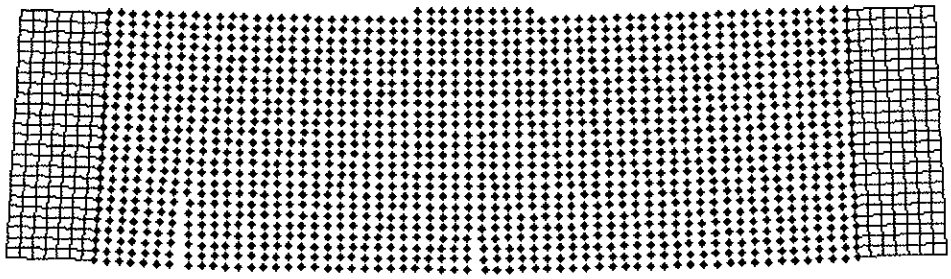

(a) Deformed numerical model from analysis G0705C (magnification factor 100).

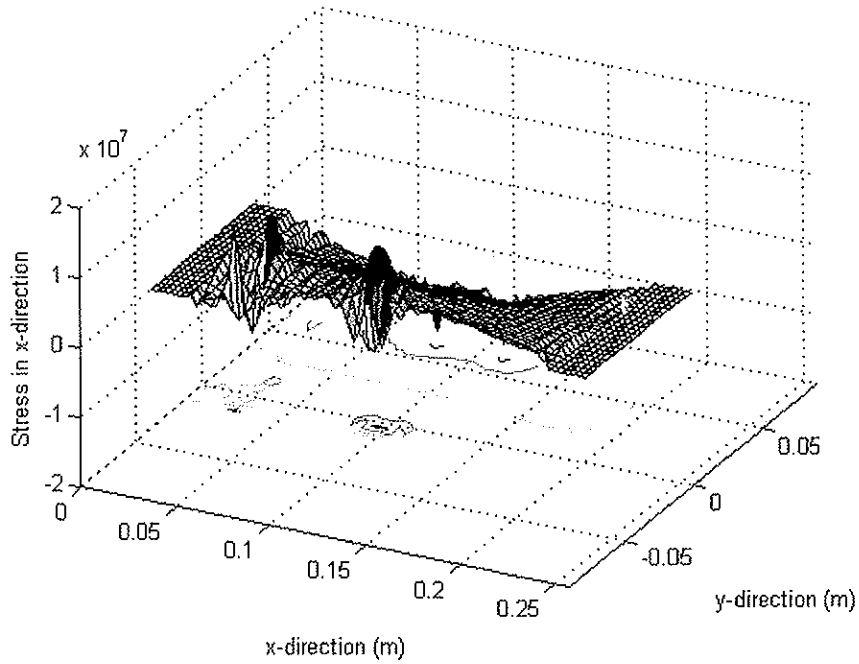

(b) 3D and contour stress plot of σ_{xx}, for the simulation G0705C.

Figure C3: (a) Plot of the deformed numerical model for simulation G0705C at time 0.96 ms. (b) 3D and stress contour plot of σ_{xx} for the same simulation and time instant as in (a).

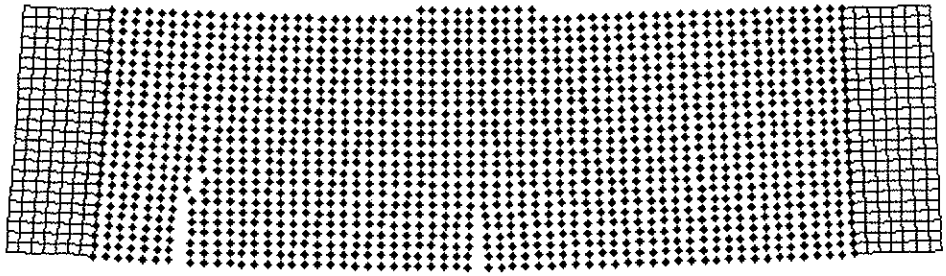

(a) Deformed numerical model from analysis G0705C (magnification factor 100).

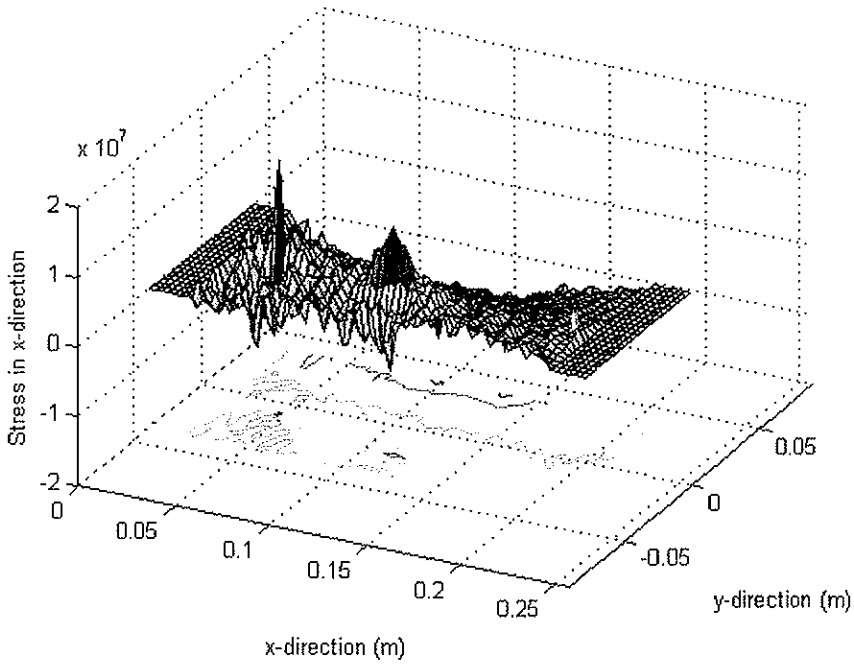

(b) 3D and contour stress plot of σ_{xx}, for the simulation G0705C.

Figure C4: (a) Plot of the deformed numerical model for simulation G0705C at time 1.02 ms. (b) 3D and stress contour plot of σ_{xx} for the same simulation and time instant as in (a).

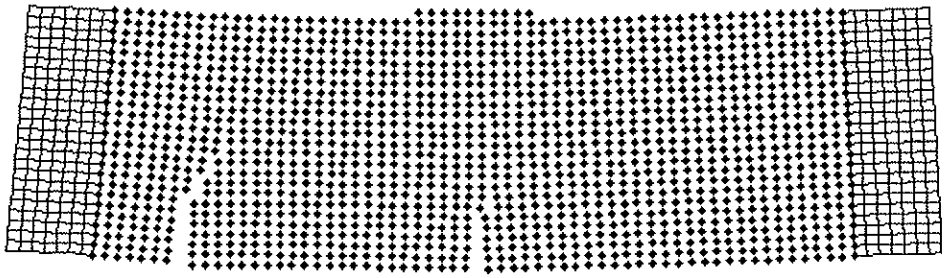

(a) Deformed numerical model from analysis G0705C (magnification factor 100).

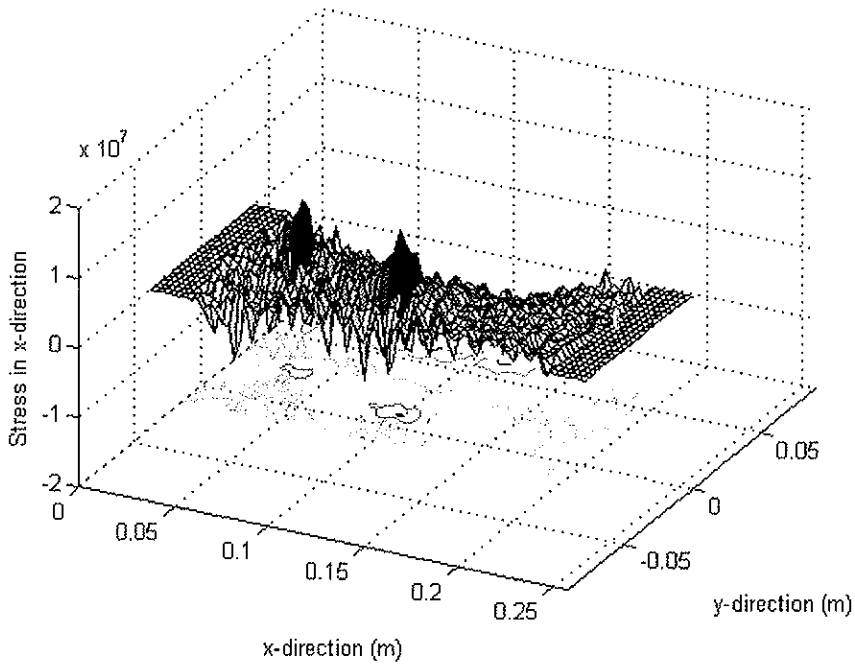

(b) 3D and contour stress plot of σ_{xx}, for the simulation G0705C.

Figure C5: (a) Plot of the deformed numerical model for simulation G0705C at time 1.08 ms. (b) 3D and stress contour plot of σ_{xx} for the same simulation and time instant as in (a).

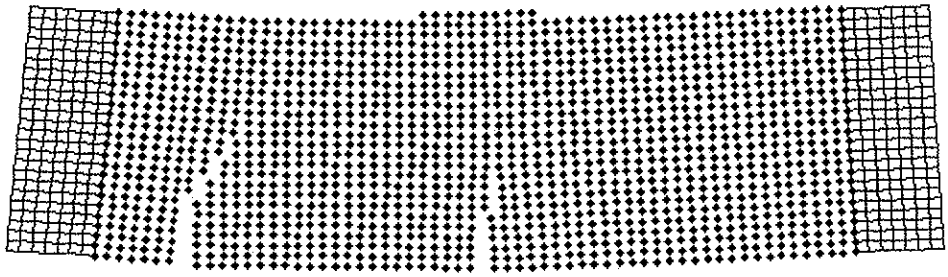

(a) Deformed numerical model from analysis G0705C (magnification factor 100).

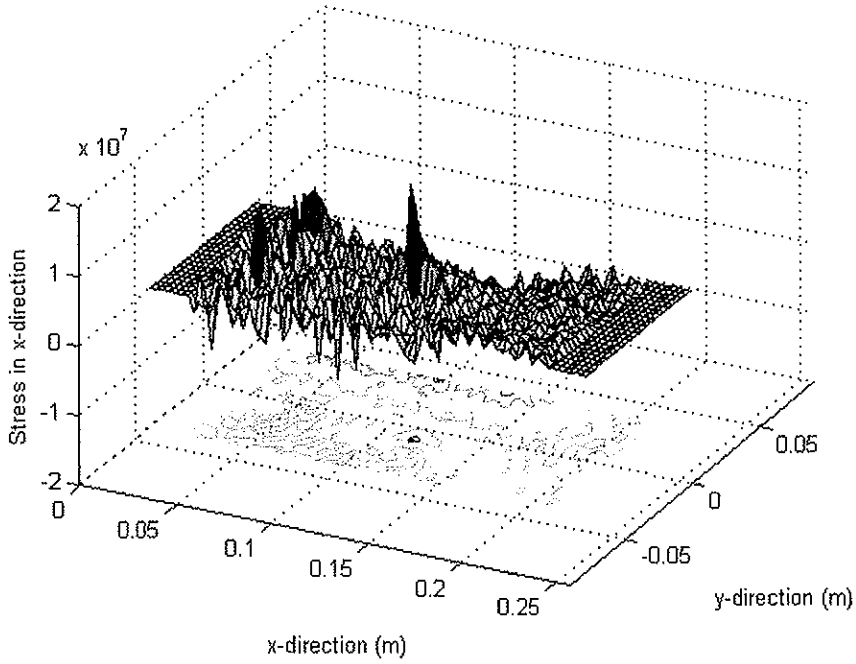

(b) 3D and contour stress plot of σ_{xx}, for the simulation G0705C.

Figure C6: (a) Plot of the deformed numerical model for simulation G0705C at time 1.14 ms. (b) 3D and stress contour plot of σ_{xx} for the same simulation and time instant as in (a).

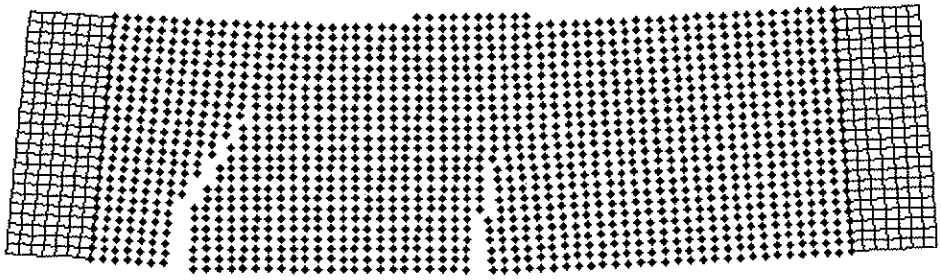

(a) Deformed numerical model from analysis G0705C (magnification factor 100).

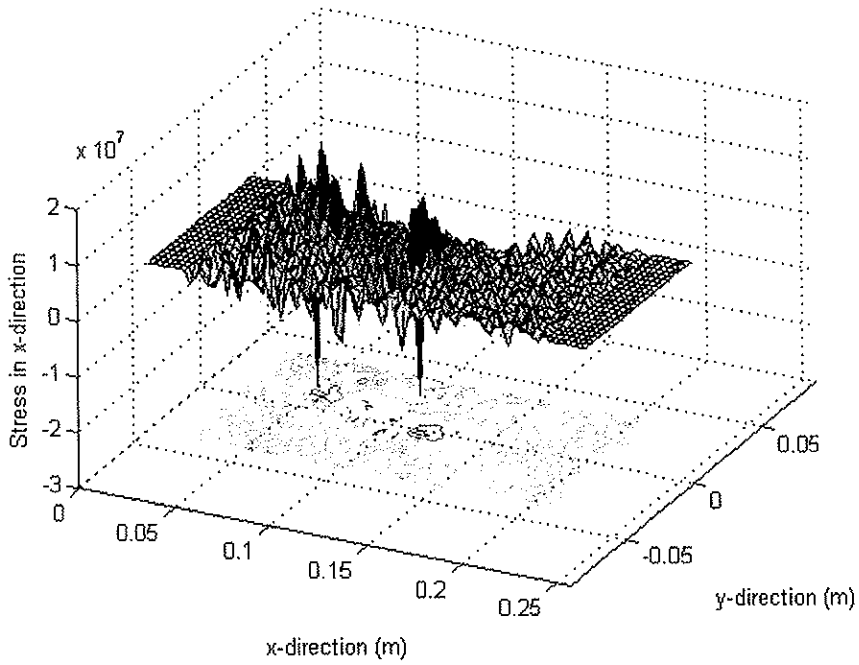

(b) 3D and contour stress plot of σ_{xx}, for the simulation G0705C.

Figure C7: (a) Plot of the deformed numerical model for simulation G0705C at time 1.2 ms. (b) 3D and stress contour plot of σ_{xx} for the same simulation and time instant as in (a).

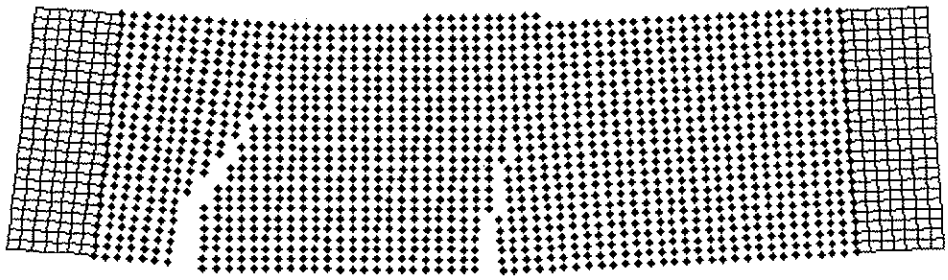

(a) Deformed numerical model from analysis G0705C (magnification factor 100).

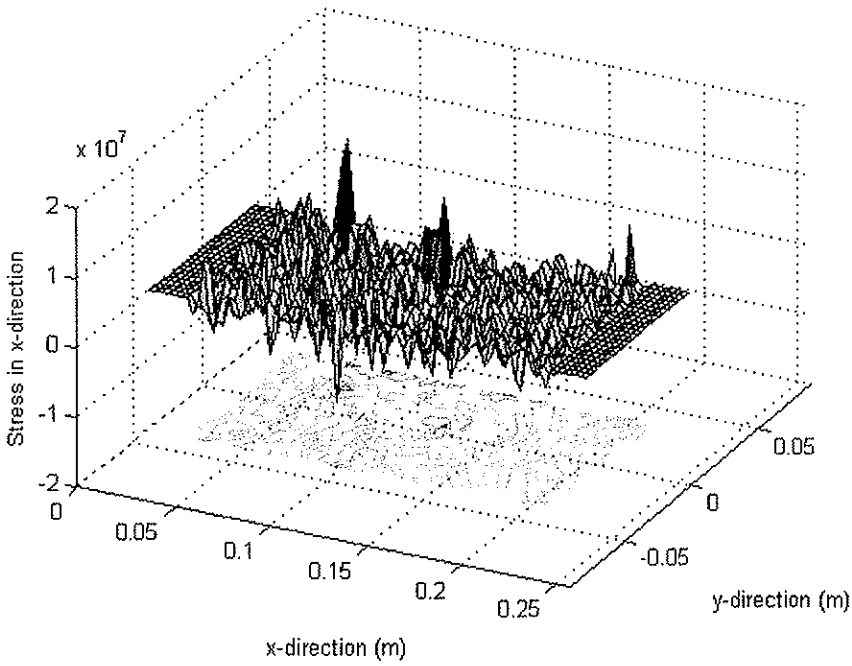

(b) 3D and contour stress plot of σ_{xx}, for the simulation G0705C.

Figure C8: (a) Plot of the deformed numerical model for simulation G0705C at time 1.26 ms. (b) 3D and stress contour plot of σ_{xx} for the same simulation and time instant as in (a).

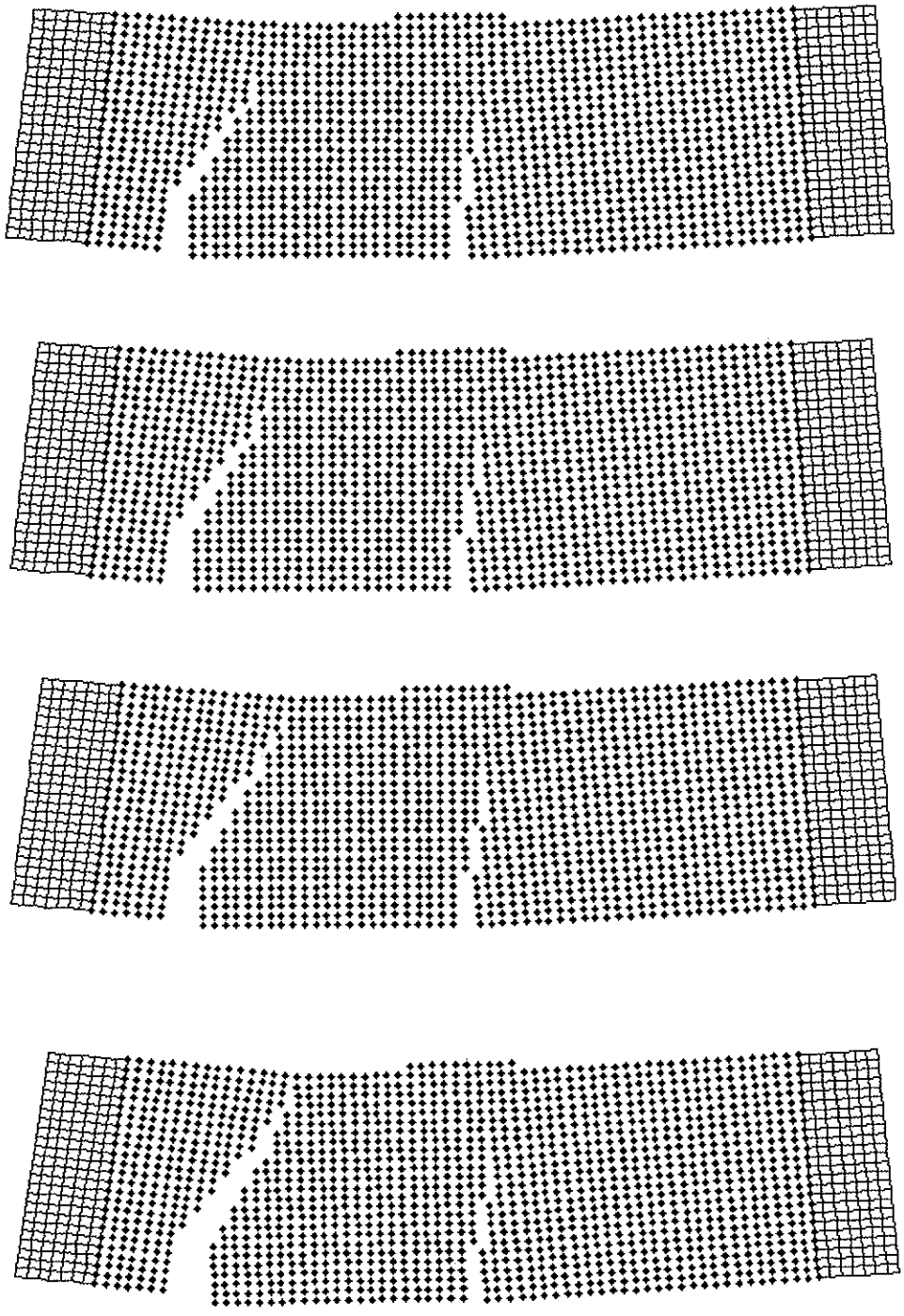

Figure C9: Deformed numerical models from analysis G0705C (magnification factor 100) for the time instants: 1.29, 1.35, 1.41, and 1.47 ms.

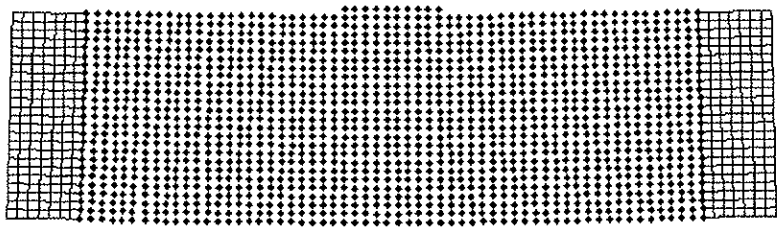

(a) Deformed numerical model from analysis G0734C (magnification factor 100) at the time instant 0.5 ms.

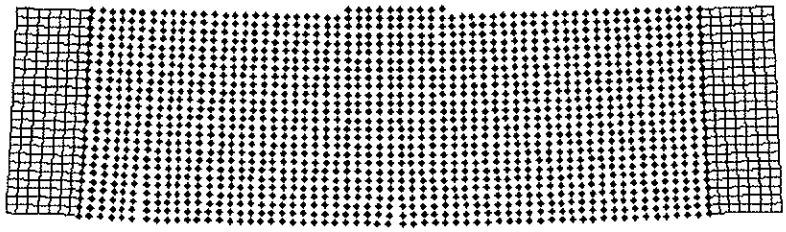

(b) Deformed numerical model from analysis G0734C (magnification factor 100) at the time instant 1.0 ms.

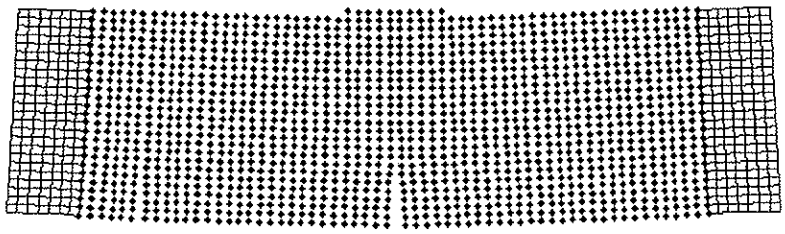

(c) Deformed numerical model from analysis G0734C (magnification factor 100) at the time instant 1.1 ms.

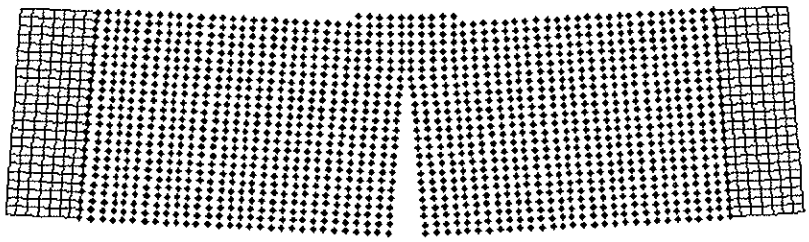

(d) Deformed numerical model from analysis G0734C (magnification factor 100) at the time instant 1.4 ms.

Figure C10: Plot of the deformed numerical models for simulation G0734C at time different time instants from a) 0.5ms to d) 1.4ms.

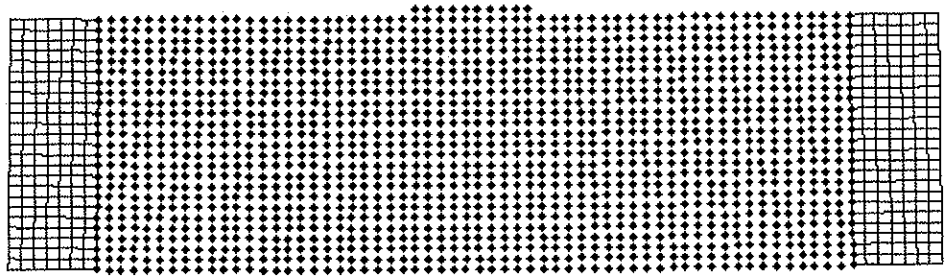

(a) Deformed numerical model from analysis G0734V (magnification factor 100).

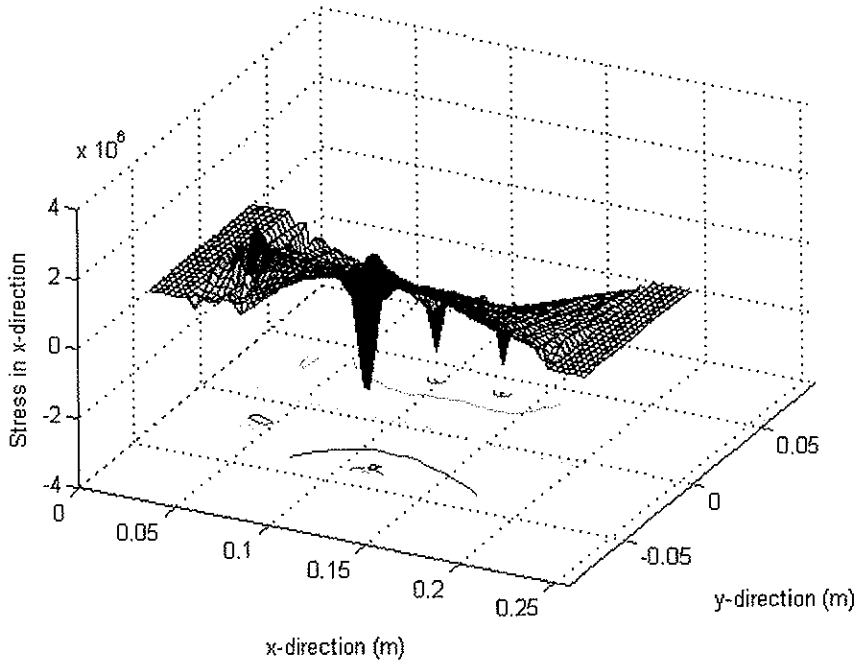

(b) 3D and contour stress plot of σ_{xx}, for the simulation G0734V.

Figure C11: (a) Plot of the deformed numerical model for simulation G0734V at time 0.3 ms. (b) 3D and stress contour plot of σ_{xx} for the same simulation and time instant as in (a).

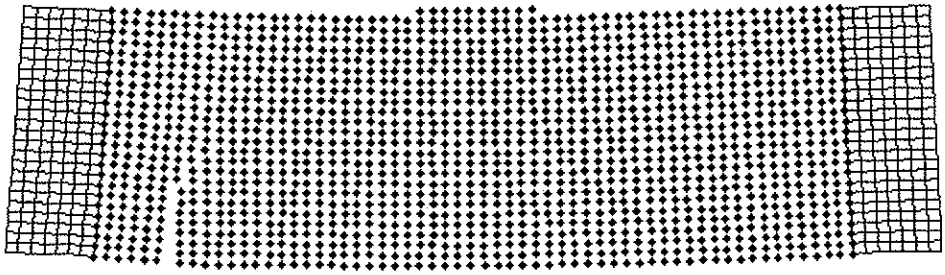

(a) Deformed numerical model from analysis G0734V (magnification factor 100).

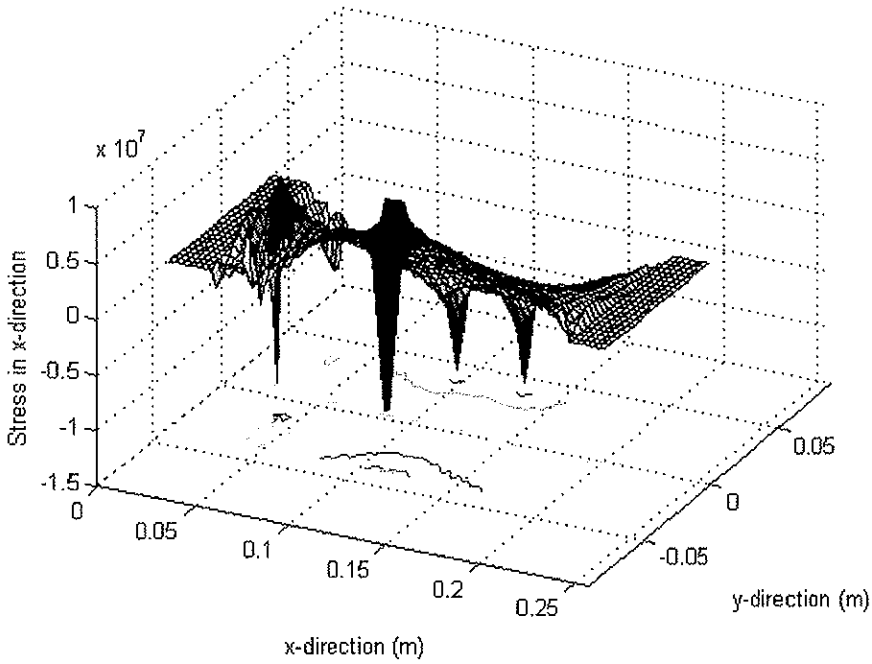

(b) 3D and contour stress plot of σ_{xx}, for the simulation G0734V.

Figure C12: (a) Plot of the deformed numerical model for simulation G0734V at time 1.08 ms. (b) 3D and stress contour plot of σ_{xx} for the same simulation and time instant as in (a).

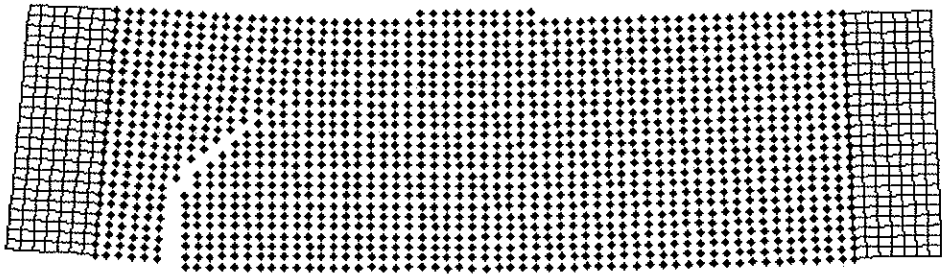

(a) Deformed numerical model from analysis G0734V (magnification factor 100).

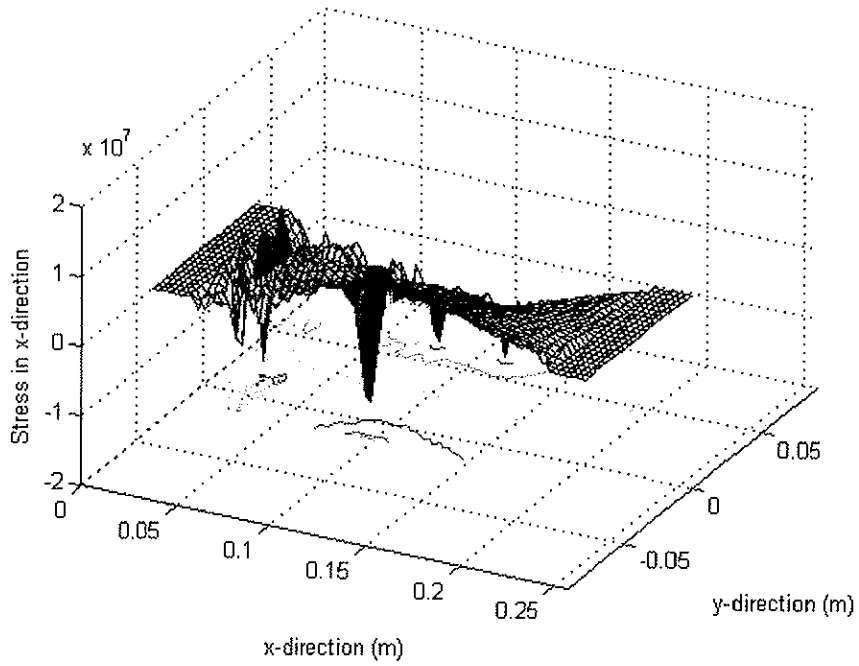

(b) 3D and contour stress plot of σ_{xx}, for the simulation G0734V.

Figure C13: (a) Plot of the deformed numerical model for simulation G0734V at time 1.11 ms. (b) 3D and stress contour plot of σ_{xx} for the same simulation and time instant as in (a).

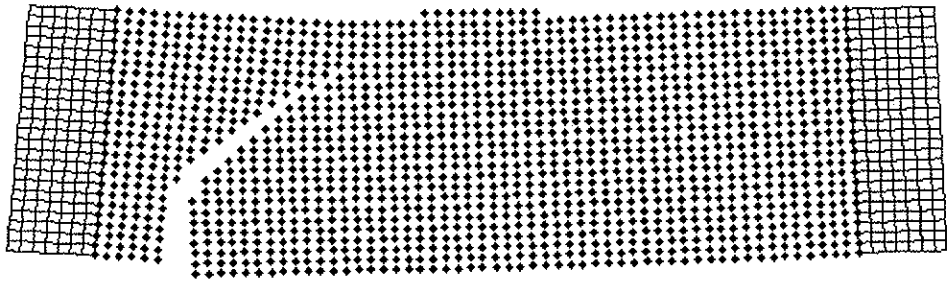

(a) Deformed numerical model from analysis G0734V (magnification factor 100).

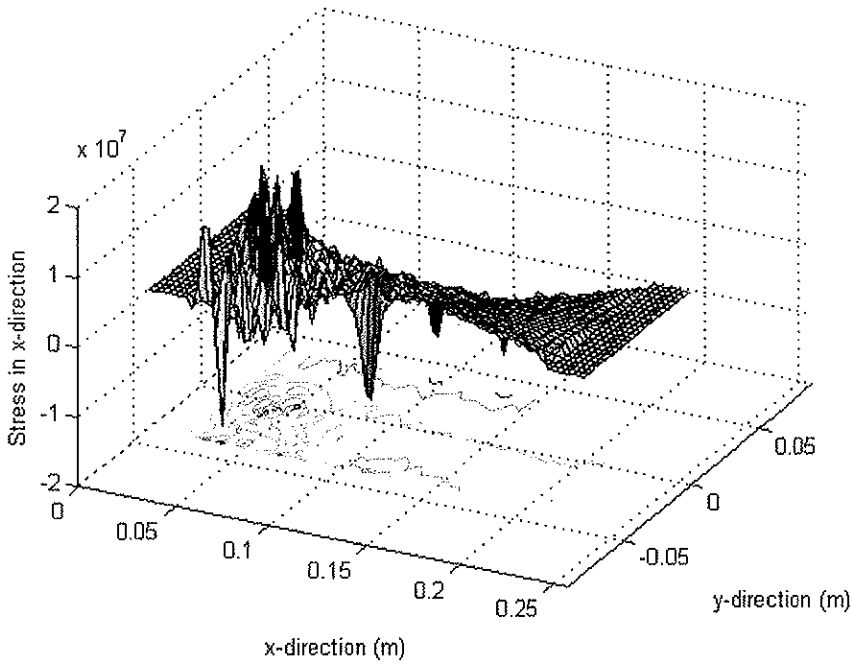

(b) 3D and contour stress plot of σ_{xx}, for the simulation G0734V.

Figure C14: (a) Plot of the deformed numerical model for simulation G0734V at time 1.14 ms. (b) 3D and stress contour plot of σ_{xx} for the same simulation and time instant as in (a).

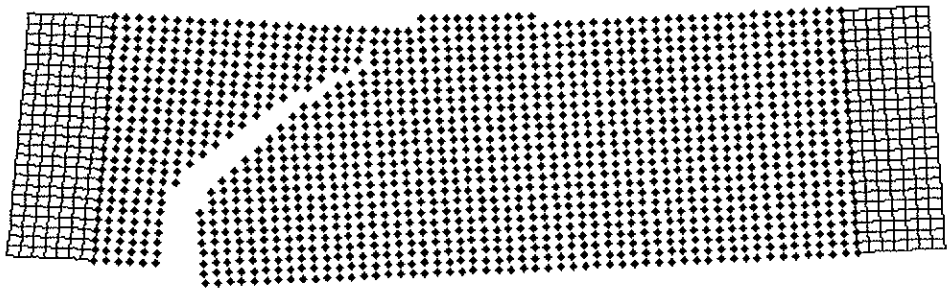

(a) Deformed numerical model from analysis G0734V (magnification factor 100).

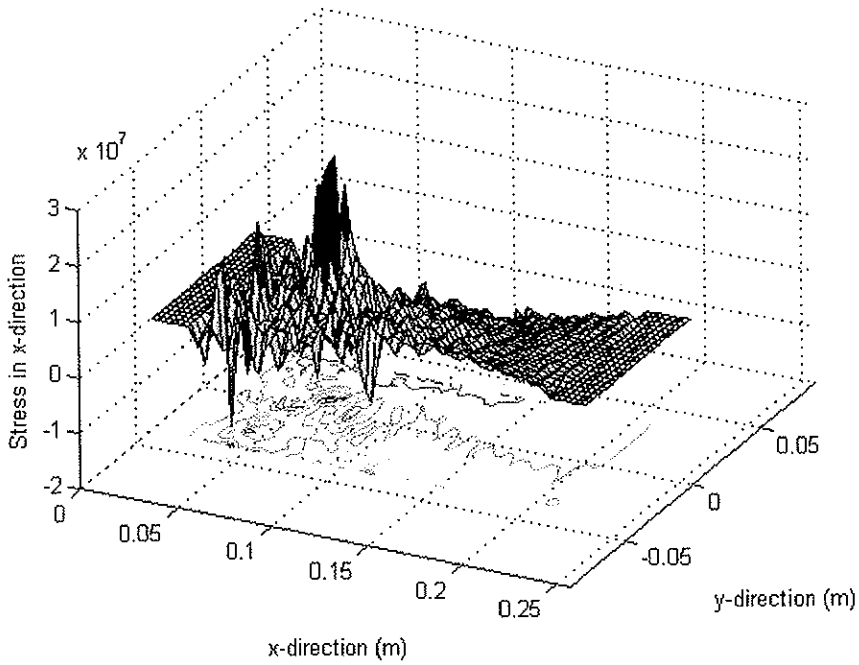

(b) 3D and contour stress plot of σ_{xx}, for the simulation G0734V.

Figure C15: (a) Plot of the deformed numerical model for simulation G0734V at time 1.17 ms. (b) 3D and stress contour plot of σ_{xx} for the same simulation and time instant as in (a).

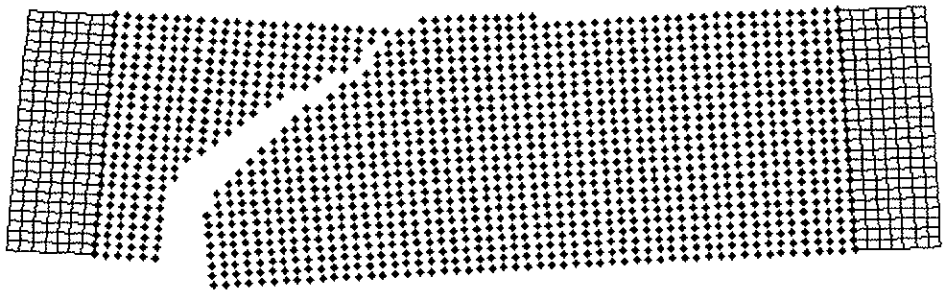

(a) Deformed numerical model from analysis G0734V (magnification factor 100).

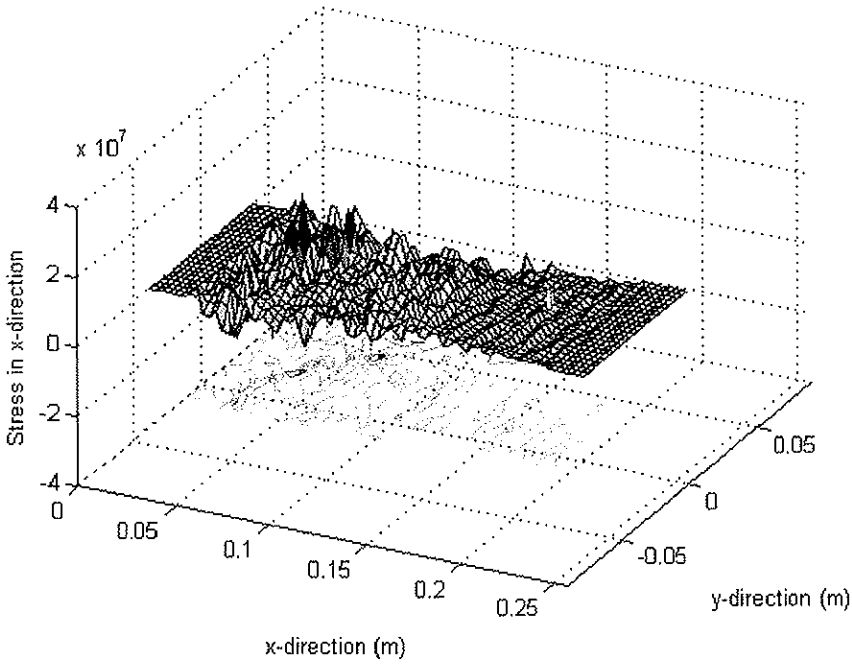

(b) 3D and contour stress plot of σ_{xx}, for the simulation G0734V.

Figure C16: (a) Plot of the deformed numerical model for simulation G0734V at time 1.20 ms. (b) 3D and stress contour plot of σ_{xx} for the same simulation and time instant as in (a).

Appendix D

In this Appendix the crack path evolution (deformed numerical model) during the numerical simulation and contour plots of stress in y-direction are plotted for analyses A-600-400-a5 and A-600-250-a6.

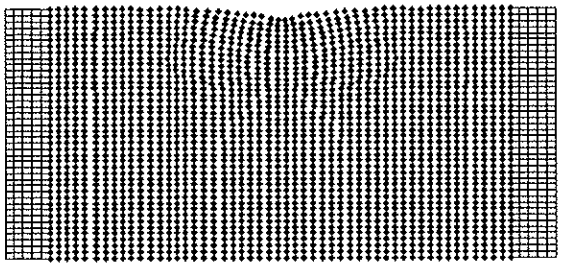

A) time instant t=0.05ms

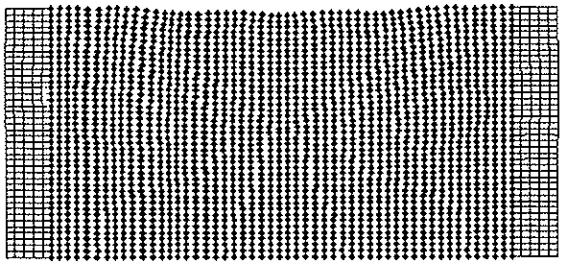

B) time instant t=0.1ms

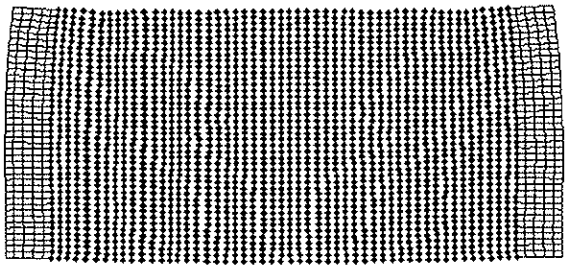

C) time instant t=0.15ms

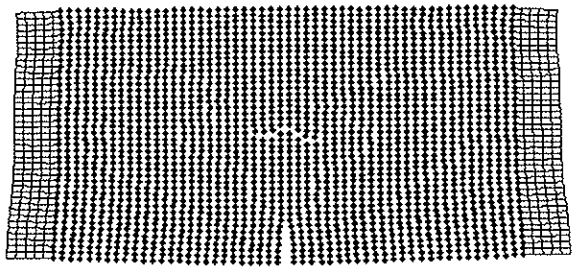

D) time instant t=0.2ms

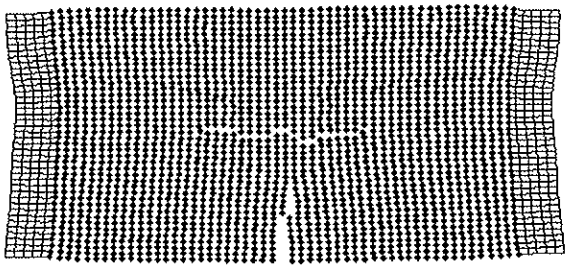

E) time instant t=0.25ms

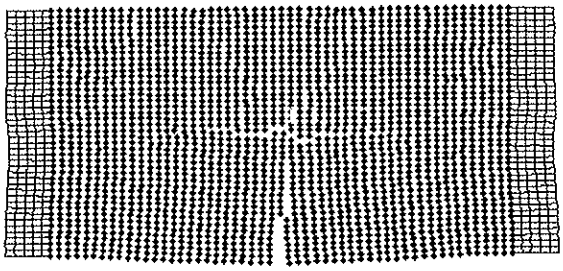

F) time instant t=0.3ms

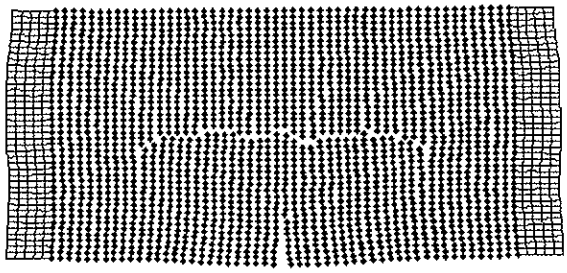

G) time instant t=0.35ms

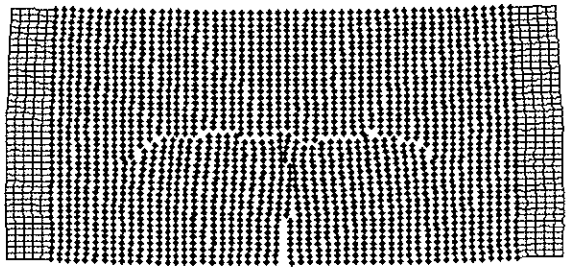

H) time instant t=0.4ms

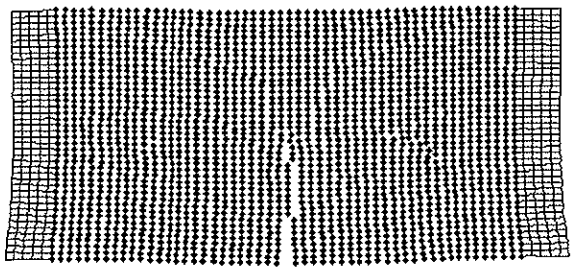

I) time instant t=0.45ms

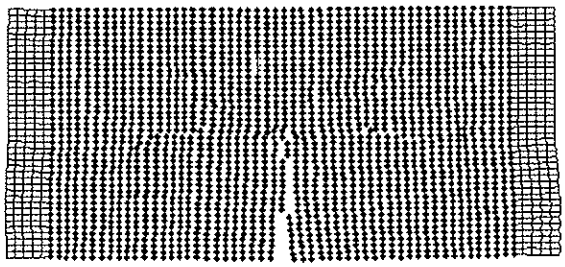

J) time instant t=0.5ms

Figure D.1: Deformation plots at different time instants for analysis A-600-400-a5. The displacement magnification factor is 50.

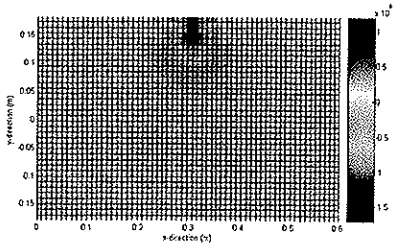

A) time instant t=0.05ms

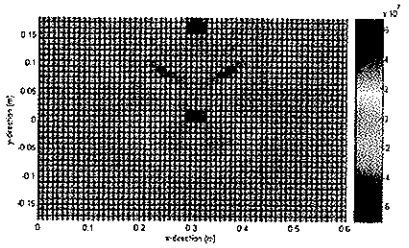

B) time instant t=0.1ms

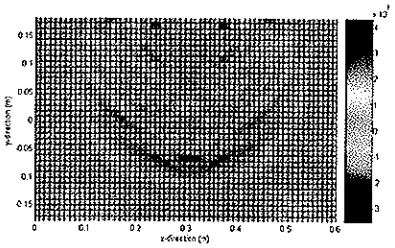

C) time instant t=0.15ms

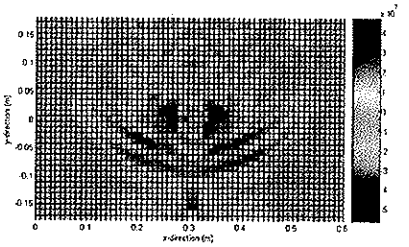

D) time instant t=0.2ms

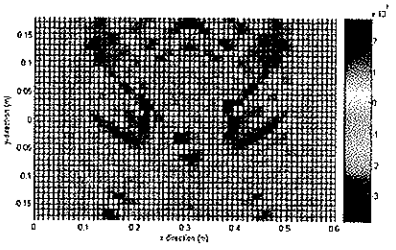

E) time instant t=0.25ms

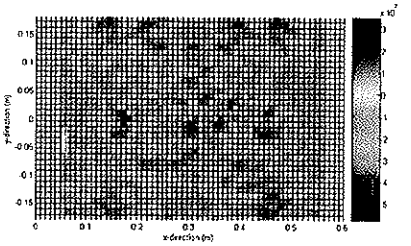

F) time instant t=0.3ms

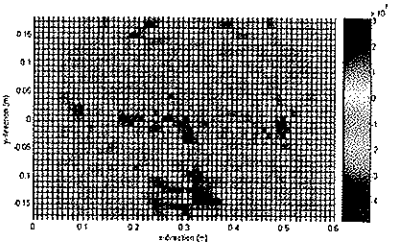

G) time instant t=0.35ms

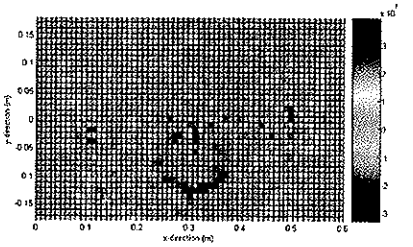

H) time instant t=0.4ms

Figure D.2: Contour plots of stresses in y-direction for analysis A-600-400-a5 at different time instants.

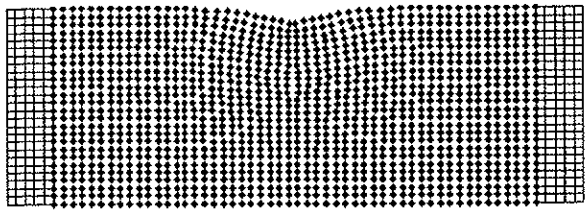

A) time instant t=0.05ms

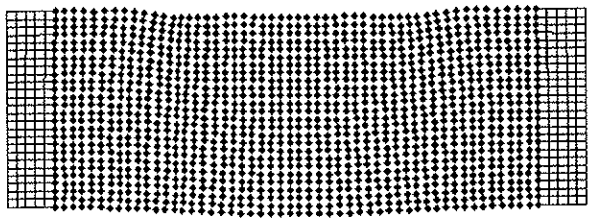

B) time instant t=0.1ms

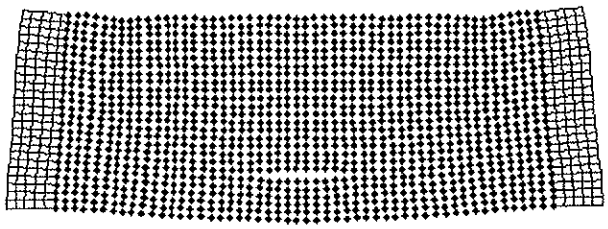

C) time instant t=0.15ms

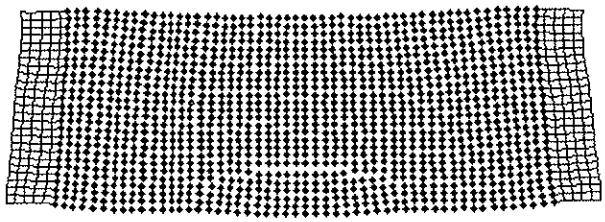

D) time instant t=0.2ms

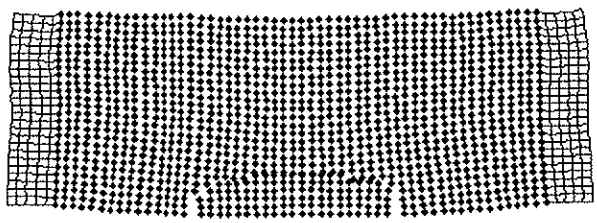

E) time instant t=0.25ms

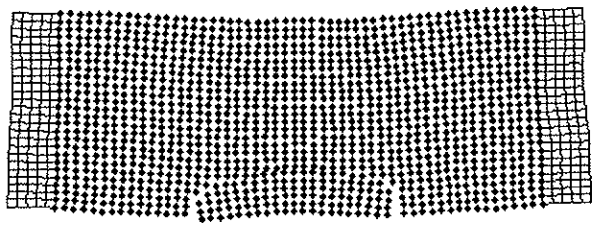

F) time instant t=0.3ms

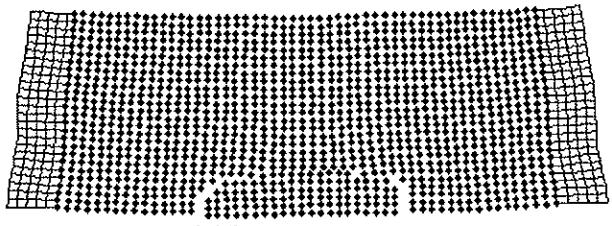

G) time instant t=0.35ms

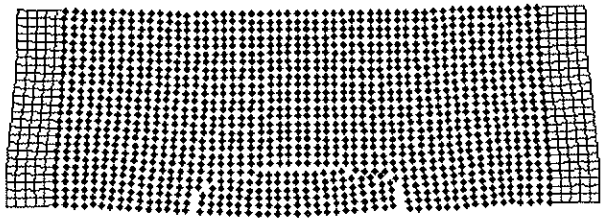

H) time instant t=0.4ms

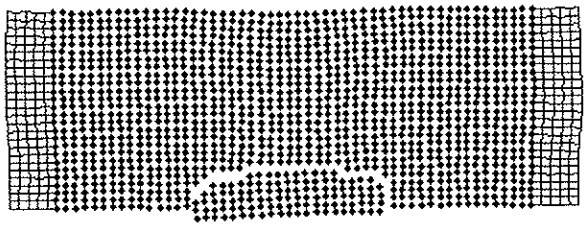

I) time instant t=0.5ms

Figure D.3: Deformation plots at different time instants for analysis A-600-250-a6. The displacement magnification factor is 50.

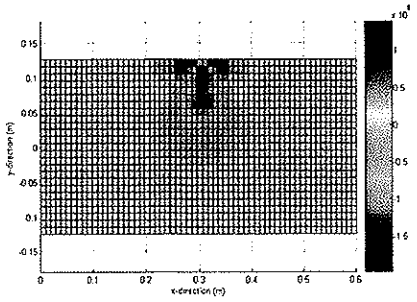

A) time instant t=0.05ms

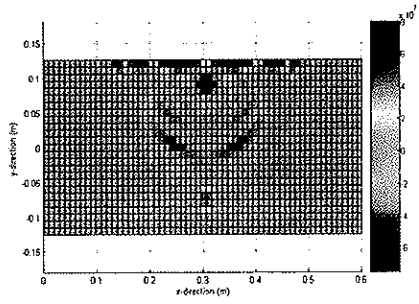

B) time instant t=0.1ms

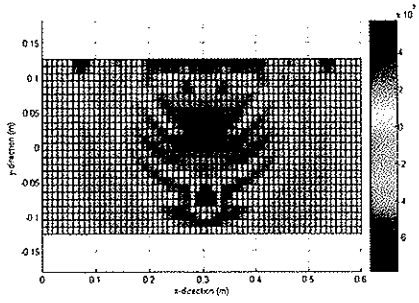

C) time instant t=0.15ms

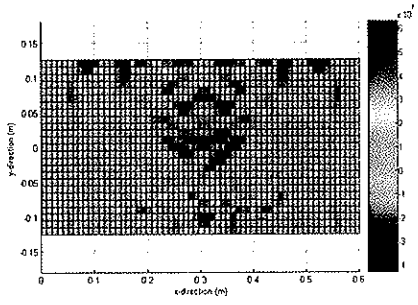

D) time instant t=0.2ms

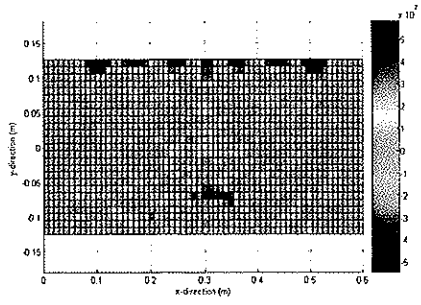

E) time instant t=0.25ms

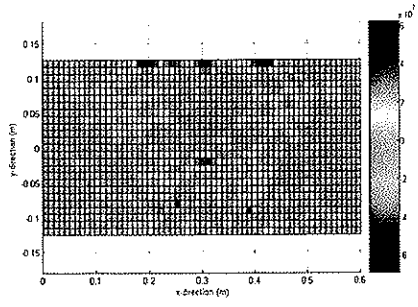

F) time instant t=0.3ms

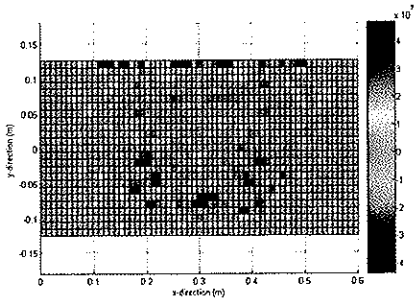

G) time instant t=0.35ms

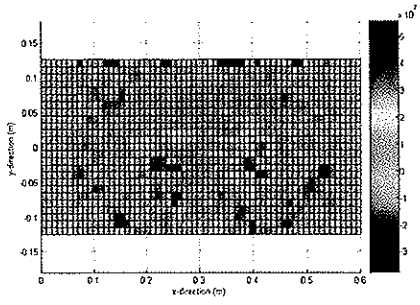

H) time instant t=0.4ms

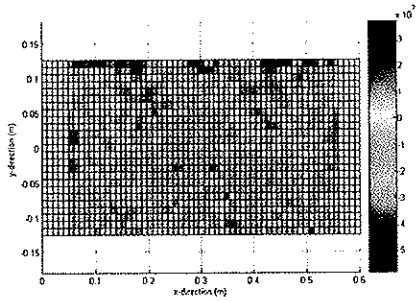

I) time instant t=0.5ms

Figure D.4: Contour plots of stresses in y-direction for analysis A-600-250-a6 at different time instants.

DEPARTMENT OF STRUCTURAL ENGINEERING
NORWEGIAN UNIVERSITY OF SCIENCE AND TECHNOLOGY

N–7491 TRONDHEIM, NORWAY
Telephone: +47 73 59 47 00 Telefax: +47 73 59 47 01

"Reliability Analysis of Structural Systems using Nonlinear Finite Element Methods",
C. A. Holm, 1990:23, ISBN 82-7119-178-0.

"Uniform Stratified Flow Interaction with a Submerged Horizontal Cylinder",
Ø. Arntsen, 1990:32, ISBN 82-7119-188-8.

"Large Displacement Analysis of Flexible and Rigid Systems Considering Displacement-Dependent Loads and Nonlinear Constraints", K. M. Mathisen, 1990:33, ISBN 82-7119-189-6.

"Solid Mechanics and Material Models including Large Deformations",
E. Levold, 1990:56, ISBN 82-7119-214-0, ISSN 0802-3271.

"Inelastic Deformation Capacity of Flexurally-Loaded Aluminium Alloy Structures",
T. Welo, 1990:62, ISBN 82-7119-220-5, ISSN 0802-3271.

"Visualization of Results from Mechanical Engineering Analysis",
K. Aamnes, 1990:63, ISBN 82-7119-221-3, ISSN 0802-3271.

"Object-Oriented Product Modeling for Structural Design",
S. I. Dale, 1991:6, ISBN 82-7119-258-2, ISSN 0802-3271.

"Parallel Techniques for Solving Finite Element Problems on Transputer Networks",
T. H. Hansen, 1991:19, ISBN 82-7119-273-6, ISSN 0802-3271.

"Statistical Description and Estimation of Ocean Drift Ice Environments",
R. Korsnes, 1991:24, ISBN 82-7119-278-7, ISSN 0802-3271.

"Properties of concrete related to fatigue damage: with emphasis on high strength concrete",
G. Petkovic, 1991:35, ISBN 82-7119-290-6, ISSN 0802-3271.

"Turbidity Current Modelling",
B. Brørs, 1991:38, ISBN 82-7119-293-0, ISSN 0802-3271.

"Zero-Slump Concrete: Rheology, Degree of Compaction and Strength. Effects of Fillers as Part Cement-Replacement",
C. Sørensen, 1992:8, ISBN 82-7119-357-0, ISSN 0802-3271.

"Nonlinear Analysis of Reinforced Concrete Structures Exposed to Transient Loading",
K. V. Høiseth, 1992:15, ISBN 82-7119-364-3, ISSN 0802-3271.

"Finite Element Formulations and Solution Algorithms for Buckling and Collapse Analysis of Thin Shells", R. O. Bjærum, 1992:30, ISBN 82-7119-380-5, ISSN 0802-3271.

"Response Statistics of Nonlinear Dynamic Systems",
J. M. Johnsen, 1992:42, ISBN 82-7119-393-7, ISSN 0802-3271.

"Digital Models in Engineering. A Study on why and how engineers build and operate digital models for decisison support", J. Høyte, 1992:75, ISBN 82-7119-429-1, ISSN 0802-3271.

"Sparse Solution of Finite Element Equations",
A. C. Damhaug, 1992:76, ISBN 82-7119-430-5, ISSN 0802-3271.

"Some Aspects of Floating Ice Related to Sea Surface Operations in the Barents Sea",
S. Løset, 1992:95, ISBN 82-7119-452-6, ISSN 0802-3271.

"Modelling of Cyclic Plasticity with Application to Steel and Aluminium Structures",
O. S. Hopperstad, 1993:7, ISBN 82-7119-461-5, ISSN 0802-3271.

"The Free Formulation: Linear Theory and Extensions with Applications to Tetrahedral Elements with Rotational Freedoms", G. Skeie, 1993:17, ISBN 82-7119-472-0, ISSN 0802-3271.

"Høyfast betongs motstand mot piggdekkslitasje. Analyse av resultater fra prøving i Veisliter'n",
T. Tveter, 1993:62, ISBN 82-7119-522-0, ISSN 0802-3271.

"A Nonlinear Finite Element Based on Free Formulation Theory for Analysis of Sandwich Structures", O. Aamlid, 1993:72, ISBN 82-7119-534-4, ISSN 0802-3271.

"The Effect of Curing Temperature and Silica Fume on Chloride Migration and Pore Structure of High Strength Concrete", C. J. Hauck, 1993:90, ISBN 82-7119-553-0, ISSN 0802-3271.

"Failure of Concrete under Compressive Strain Gradients",
G. Markeset, 1993:110, ISBN 82-7119-575-1, ISSN 0802-3271.

"An experimental study of internal tidal amphidromes in Vestfjorden",
J. H. Nilsen, 1994:39, ISBN 82-7119-640-5, ISSN 0802-3271.

"Structural analysis of oil wells with emphasis on conductor design",
H. Larsen, 1994:46, ISBN 82-7119-648-0, ISSN 0802-3271.

"Adaptive methods for non-linear finite element analysis of shell structures",
K. M. Okstad, 1994:66, ISBN 82-7119-670-7, ISSN 0802-3271.

"On constitutive modelling in nonlinear analysis of concrete structures",
O. Fyrileiv, 1994:115, ISBN 82-7119-725-8, ISSN 0802-3271.

"Fluctuating wind load and response of a line-like engineering structure with emphasis on motion-induced wind forces",
J. Bogunovic Jakobsen, 1995:62, ISBN 82-7119-809-2, ISSN 0802-3271.

"An experimental study of beam-columns subjected to combined torsion, bending and axial actions", A. Aalberg, 1995:66, ISBN 82-7119-813-0, ISSN 0802-3271.

"Scaling and cracking in unsealed freeze/thaw testing of Portland cement and silica fume concretes", S. Jacobsen, 1995:101, ISBN 82-7119-851-3, ISSN 0802-3271.

"Damping of water waves by submerged vegetation. A case study of laminaria hyperborea",
A. M. Dubi, 1995:108, ISBN 82-7119-859-9, ISSN 0802-3271.

"The dynamics of a slope current in the Barents Sea",
Sheng Li, 1995:109, ISBN 82-7119-860-2, ISSN 0802-3271.

"Modellering av delmaterialenes betydning for betongens konsistens",
Ernst Mørtsell, 1996:12, ISBN 82-7119-894-7, ISSN 0802-3271.

"Bending of thin-walled aluminium extrusions",
Birgit Søvik Opheim, 1996:60, ISBN 82-7119-947-1, ISSN 0802-3271.

"Material modelling of aluminium for crashworthiness analysis",
Torodd Berstad, 1996:89, ISBN 82-7119-980-3, ISSN 0802-3271.

"Estimation of structural parameters from response measurements on submerged floating tunnels",
Rolf Magne Larssen, 1996:119, ISBN 82-471-0014-2, ISSN 0802-3271.

"Numerical modelling of plain and reinforced concrete by damage mechanics",
Mario A. Polanco-Loria, 1997:20, ISBN 82-471-0049-5, ISSN 0802-3271.

"Nonlinear random vibrations - numerical analysis by path integration methods",
Vibeke Moe, 1997:26, ISBN 82-471-0056-8, ISSN 0802-3271.

"Numerical prediction of vortex-induced vibration by the finite element method",
Joar Martin Dalheim, 1997:63, ISBN 82-471-0096-7, ISSN 0802-3271.

"Time domain calculations of buffeting response for wind sensitive structures",
Ketil Aas-Jakobsen, 1997:148, ISBN 82-471-0189-0, ISSN 0802-3271.

"A numerical study of flow about fixed and flexibly mounted circular cylinders",
Trond Stokka Meling, 1998:48, ISBN 82-471-0244-7, ISSN 0802-3271.

"Estimation of chloride penetration into concrete bridges in coastal areas",
Per Egil Steen, 1998:89, ISBN 82-471-0290-0, ISSN 0802-3271.

"Stress-resultant material models for reinforced concrete plates and shells",
Jan Arve Øverli, 1998:95, ISBN 82-471-0297-8, ISSN 0802-3271.

"Chloride binding in concrete. Effect of surrounding environment and concrete composition",
Claus Kenneth Larsen, 1998:101, ISBN 82-471-0337-0, ISSN 0802-3271.

"Rotational capacity of aluminium alloy beams",
Lars A. Moen, 1999:1, ISBN 82-471-0365-6, ISSN 0802-3271.

"Stretch Bending of Aluminium Extrusions",
Arild H. Clausen, 1999:29, ISBN 82-471-0396-6, ISSN 0802-3271.

"Aluminium and Steel Beams under Concentrated Loading",
Tore Tryland, 1999:30, ISBN 82-471-0397-4, ISSN 0802-3271.

"Engineering Models of Elastoplasticity and Fracture for Aluminium Alloys",
Odd-Geir Lademo, 1999:39, ISBN 82-471-0406-7, ISSN 0802-3271.

"Kapasitet og duktilitet av dybelforbindelser i trekonstruksjoner",
Jan Siem, 1999:46, ISBN 82-471-0414-8, ISSN 0802-3271.

"Etablering av distribuert ingeniørarbeid; Teknologiske og organisatoriske erfaringer fra en norsk ingeniørbedrift", Lars Line, 1999:52, ISBN 82-471-0420-2, ISSN 0802-3271.

"Estimation of Earthquake-Induced Response",
Símon Ólafsson, 1999:73, ISBN 82-471-0443-1, ISSN 0802-3271.

"Coastal Concrete Bridges: Moisture State, Chloride Permeability and Aging Effects"
Ragnhild Holen Relling, 1999:74, ISBN 82-471-0445-8, ISSN 0802-3271.

"Capacity Assessment of Titanium Pipes Subjected to Bending and External Pressure",
Arve Bjørset, 1999:100, ISBN 82-471-0473-3, ISSN 0802-3271.

"Validation of Numerical Collapse Behaviour of Thin-Walled Corrugated Panels",
Håvar Ilstad, 1999:101, ISBN 82-471-0474-1, ISSN 0802-3271.

"Strength and Ductility of Welded Structures in Aluminium Alloys",
Miroslaw Matusiak, 1999:113, ISBN 82-471-0487-3, ISSN 0802-3271.

"Thermal Dilation and Autogenous Deformation as Driving Forces to Self-Induced Stresses in High Performance Concrete",
Øyvind Bjøntegaard, 1999:121, ISBN 82-7984-002-8, ISSN 0802-3271.

"Some Aspects of Ski Base Sliding Friction and Ski Base Structure",
Dag Anders Moldestad, 1999:137, ISBN 82-7984-019-2, ISSN 0802-3271.

"Electrode reactions and corrosion resistance for steel in mortar and concrete",
Roy Antonsen, 2000:10, ISBN 82-7984-030-3, ISSN 0802-3271.

"Hydro-Physical Conditions in Kelp Forests and the Effect on Wave Damping and Dune Erosion. A case study on Laminaria Hyperborea",
Stig Magnar Løvås, 2000:28, ISBN 82-7984-050-8, ISSN 0802-3271.

"Random Vibration and the Path Integral Method",
Christian Skaug, 2000:39, ISBN 82-7984-061-3, ISSN 0802-3271.

"Buckling and geometrical nonlinear beam-type analyses of timber structures",
Trond Even Eggen, 2000:56, ISBN 82-7984-081-8, ISSN 0802-3271.

"Structural Crashworthiness of Aluminium Foam-Based Components",
Arve Grønsund Hanssen, 2000:76, ISBN 82-7984-102-4, ISSN 0809-103X.

"Measurements and simulations of the consolidation in first-year sea ice ridges, and some aspects of mechanical behaviour", Knut V. Høyland, 2000:94, ISBN 82-7984-121-0, ISSN 0809-103X.

"Kinematics in Regular and Irregular Waves based on a Lagrangian Formulation",
Svein Helge Gjøsund, 2000-86, ISBN 82-7984-112-1, ISSN 0809-103X.

"Self-Induced Cracking Problems in Hardening Concrete Structures",
Daniela Bosnjak, 2000-121, ISBN 82-7984-151-2, ISSN 0809-103X.

"Ballistic Penetration and Perforation of Steel Plates",
Tore Børvik, 2000:124, ISBN 82-7984-154-7, ISSN 0809-103X.

"Freeze-Thaw resistance of Concrete. Effect of: Curing Conditions, Moisture Exchange and Materials", Terje Finnerup Rønning, 2001:14, ISBN 82-7984-165-2, ISSN 0809-103X

Structural behaviour of post tensioned concrete structures. Flat slab. Slabs on ground",
Steinar Trygstad, 2001:52, ISBN 82-471-5314-9, ISSN 0809-103X.

"Slipforming of Vertical Concrete Structures. Friction between concrete and slipform panel", Kjell Tore Fossâ, 2001:61, ISBN 82-471-5325-4, ISSN 0809-103X.

"Some numerical methods for the simulation of laminar and turbulent incompressible flows", Jens Holmen, 2002:6, ISBN 82-471-5396-3, ISSN 0809-103X.

"Improved Fatigue Performance of Threaded Drillstring Connections by Cold Rolling", Steinar Kristoffersen, 2002:11, ISBN: 82-421-5402-1, ISSN 0809-103X.

"Deformations in Concrete Cantilever Bridges: Observations and Theoretical Modelling", Peter F. Takâcs, 2002:23, ISBN 82-471-5415-3, ISSN 0809-103X.

"Stiffened aluminium plates subjected to impact loading", Hilde Giæver Hildrum, 2002:69, ISBN 82-471-5467-6, ISSN 0809-103X.

"Full- and model scale study of wind effects on a medium-rise building in a built up area", Jónas Thór Snæbjørnsson, 2002:95, ISBN82-471-5495-1, ISSN 0809-103X.

"Evaluation of Concepts for Loading of Hydrocarbons in Ice-infested water", Arnor Jensen, 2002:114, ISBN 82-417-5506-0, ISSN 0809-103X.

"Numerical and Physical Modelling of Oil Spreading in Broken Ice", Janne K. Økland Gjøsteen, 2002:130, ISBN 82-471-5523-0, ISSN 0809-103X.

"Diagnosis and protection of corroding steel in concrete", Franz Pruckner, 20002:140, ISBN 82-471-5555-4, ISSN 0809-103X.

"Tensile and Compressive Creep of Young Concrete: Testing and Modelling", Dawood Atrushi, 2003:17, ISBN 82-471-5565-6, ISSN 0809-103X.

"Rheology of Particle Suspensions. Fresh Concrete, Mortar and Cement Paste with Various Types of Lignosulfonates", Jon Elvar Wallevik, 2003:18, ISBN 82-471-5566-4, ISSN 0809-103X.

"Oblique Loading of Aluminium Crash Components", Aase Reyes, 2003:15, ISBN 82-471-5562-1, ISSN 0809-103X.

"Utilization of Ethiopian Natural Pozzolans", Surafel Ketema Desta, 2003:26, ISSN 82-471-5574-5, ISSN:0809-103X.

"Behaviour and strength prediction of reinforced concrete structures with discontinuity regions", Helge Brå, 2004:11, ISBN 82-471-6222-9, ISSN 1503-8181.

"High-strength steel plates subjected to projectile impact. An experimental and numerical study", Sumita Dey, 2004:38, ISBN 82-471-6281-4 (elektr. Utg.), ISBN 82-471-6282-2 (trykt utg.), ISSN 1503-8181.

"Alkali-reactive and inert fillers in concrete. Rheology of fresh mixtures and expansive reactions." Bård M. Pedersen, 2004:92, ISBN 82-471-6401-9 (trykt utg.), ISBN 82-471-6400-0 (elektr. utg.), ISSN 1503-8181.

"On the Shear Capacity of Steel Girders with Large Web Openings". Nils Christian Hagen, 2005:9 ISBN 82-471-6878-2 (trykt utg.), ISBN 82-471-6877-4 (elektr. utg.), ISSN 1503-8181.

"Behaviour of aluminium extrusions subjected to axial loading". Østen Jensen, 2005:7, ISBN 82-471-6872-3 (elektr. utg.) , ISBN 82-471-6873-1 (trykt utg.), ISSN 1503-8181.

"Thermal Aspects of corrosion of Steel in Concrete". Jan-Magnus Østvik, 2005:5, ISBN 82-471-6869-3 (trykt utg.) ISBN 82-471-6868 (elektr.utg), ISSN 1503-8181.

"Mechanical and adaptive behaviour of bone in relation to hip replacement." A study of bone remodelling and bone grafting. Sébastien Muller, 2005:34, ISBN 82-471-6933-9 (trykt utg.) (ISBN 82-471-6932-0 (elektr.utg), ISSN 1503-8181.

"Analysis of geometrical nonlinearities with applications to timber structures". Lars Wollebæk, 2005:74, ISBN 82-471-7050-5 (trykt utg.), ISBN 82-471-7019-1 (elektr. Utg.), ISSN 1503-8181.

"Pedestrian induced lateral vibrations of slender footbridges", Anders Rönnquist, 2005:102, ISBN 82-471-7082-5 (trykt utg.), ISBN 82-471-7081-7 (elektr.utg.), ISSN 1503-8181.

"Initial Strength Development of Fly Ash and Limestone Blended Cements at Various Temperatures Predicted by Ultrasonic Pulse Velocity", Tom Ivar Fredvik, 2005:112, ISBN 82-471-7105-8 (trykt utg.), ISBN 82-471-7103-1 (elektr.utg.), ISSN 1503-8181.

"Behaviour and modelling of thin-walled cast components", Cato Dørum, 2005:128, ISBN 82-471-7140-6 (trykt utg.), ISBN 82-471-7139-2 (elektr. utg.), ISSN 1503-8181.

"Behaviour and modelling of selfpiercing riveted connections", Raffaele Porcaro, 2005:165, ISBN 82-471-7219-4 (trykt utg.), ISBN 82-471-7218-6 (elektr.utg.), ISSN 1503-8181.

"Behaviour and Modelling og Aluminium Plates subjected to Compressive Load", Lars Rønning, 2005:154, ISBN 82-471-7169-1 (trykt utg.), ISBN 82-471-7195-3 (elektr.utg.), ISSN 1503-8181

"Bumper beam-longitudinal system subjected to offset impact loading", Satyanarayana Kokkula, 2005:193, ISBN 82-471-7280-1 (trykt utg.), ISBN 82-471-7279-8 (elektr.utg.), ISSN 1503-8181.

"Control of Chloride Penetration into Concrete Structures at Early Age", Guofei Liu, 2006:46, ISBN 82-471-7838-9 (trykt utg.), ISBN 82-471-7837-0 (elektr. utgave), ISSN 1503-8181.

"Modelling of Welded Thin-Walled Aluminium Structures", Ting Wang, 2006:78, ISBN 82-471-7907-5 (trykt utg.), ISBN 82-471-7906-7 (elektr.utg.), ISSN 1503-8181.

"Time-variant reliability of dynamic systems by importance sampling and probabilistic analysis of ice loads", Anna Ivanova Olsen, 2006:139, ISBN 82-471-8041-3 (trykt utg.), ISBN 82-471-8040-5 (elektr.utg.), ISSN 1503-8181.

"Fatigue life prediction of an aluminium alloy automotive component using finite element analysis of surface topography". Sigmund Kyrre Ås, 2006:25, ISBN 82-471-7791-9 (trykt utg.), ISBN 82-471-7791-9 (elektr.utg.), ISSN 1503-8181.

"Constitutive models of elastoplasticity and fracture for aluminium alloys under strain path change", Dasharatha Achani, 2006:76, ISBN 82-471-7903-2 (trykt utg.), ISBN 82-471-7902-4 (elektr.utg.), ISSN 1503-8181.